Probing and manipulating graphene physics at the atomic level.

Tesis presentada por

Héctor González Herrero

Para optar al Grado de Doctor en Ciencias Físicas

Director de Tesis

Iván Brihuega Álvarez

Departamento de física de la Materia Condensada

Universidad Autónoma de Madrid

Probing and manipulating graphene physics at the atomic level.

Resumen.

En los últimos 12 años, un campo dentro de la física de la materia condensada que ha experimentado un gran boom, ha sido el de los materiales bidimensionales. Todo esto ha sido posible gracias a la obtención en 2004 de la primera lámina de grafeno por Andre Geim y Konstantin Novoselov. Este nuevo material consistente en una lámina de grafito de un átomo de espesor, había sido estudiado desde un punto de vista meramente teórico en los años 40 prometiendo propiedades muy interesantes. Con su aparición en escena, comenzó la fiebre de los materiales 2D. Aunque su número y variedad de propiedades no deja de aumentar, la presente tesis está centrada única y exclusivamente en el estudio de sistemas tipo grafeno. Esta tesis, es de carácter puramente experimental, si bien a lo largo de su desarrollo el apoyo de cálculos teóricos para obtener una mejor comprensión de la física involucrada ha sido indispensable y muy enriquecedor.

La técnica experimental usada a lo largo de esta tesis, ha sido la microscopia de efecto túnel (STM). Esta técnica, desarrollada en 1981 por Gerd Binning y Heinrich Rohrer y que fue premiada con el premio nobel en 1986, marcó el inicio de las llamadas microscopias de sonda de barrido (SPM), que en los últimos 30-35 años se han convertido en herramienta indispensable para la física de superficies y caracterización de nuevos materiales. El STM, como veremos a lo largo del manuscrito, permite obtener imágenes de superficies con una alta resolución espacial. De igual forma, el STM es sensible a la densidad local de estados de la muestra y si se combina con baja temperatura (~5K en nuestro caso), proporciona también una alta resolución en energías. Como se muestra a lo largo del capítulo 1, todas estas capacidades del STM han contribuido al entendimiento de la física del grafeno a nivel atómico.

Desde su descubrimiento, el grado de entendimiento de las propiedades del grafeno y cómo modificarlas de forma controlada no ha dejado de aumentar. Sin embargo, todavía quedan huecos por rellenar para poder conocer realmente los límites de este extraordinario material. El punto de partida de esta tesis era estudiar la posibilidad de inducir y controlar momentos magnéticos en grafeno. Este es un campo todavía en desarrollo dentro de la física del grafeno y tiene mucha importancia, ya que la implementación del magnetismo en grafeno podría tener una gran repercusión en campos como la spintrónica. Al comienzo de mi doctorado, el número de trabajos sobre este tema era escaso y poco conclusivo. Medidas magnéticas en grafito irradiado o tras adsorber átomos de ciertos elementos apuntaban en la buena dirección, pero el origen de la señal magnética no era claro. Los experimentos sobre adsorción de átomos de hidrógeno en grafeno presentados en esta tesis, prueban de forma irrefutable que un átomo individual de hidrógeno induce un momento magnético en la capa de grafeno, ofreciendo así la posibilidad de obtener grafeno magnético. En esta tesis también

se han estudiado los mecanismos involucrados en la adsorción de átomos de hidrógeno en grafeno con el fin de alcanzar una mejor comprensión de los límites de la hidrogenación como forma de producir grafeno magnético.

Algo de sobra sabido es que al poner en contacto una capa de grafeno con diferentes substratos, las propiedades del grafeno se ven alteradas. Alcanzar un entendimiento completo de cómo interacciona el grafeno con cada substrato específico, proporcionaría la posibilidad de diseñar las propiedades de nuestras capas de grafeno para nuestro propio beneficio. Nuestros experimentos estudiando la transparencia selectiva del grafeno a los electrones túnel, muestran que es posible acceder a las propiedades electrónicas del grafeno y el substrato en la mima región y al mismo tiempo. Gracias a nuestra capacidad para elegir que elemento del sistema queremos estudiar (grafeno o substrato), hemos sido capaces de caracterizar de forma completa las propiedades electrónicas del sistema Gr/Cu(111). Esto también tiene una gran importancia desde el punto de vista teórico, ya que puede ayudar a comprender y mejorar los funcionales usados para la descripción de la interacción carbono/metal, y especialmente los que incluyen interacciones de tipo van der Waals. Dichas interacciones juegan un papel muy importante en la correcta descripción de sistemas grafeno/metal débilmente interactuantes. Finalmente, nuestro estudio de la interacción de defectos puntuales en capas de grafeno muestra que esta transparencia ajustable es clave para lograr un entendimiento detallado de las interacciones locales y en particular en las cercanías de partículas adsorbidas o intercaladas.

Abstract.

In the last 12 years, there has been a huge boom in the field of condensed matter around bidimensional materials. This has been possible thanks to the first isolation of graphene in 2004 by Andre Geim and Konstantin Novoselov. This new material, consisting in a monolayer of graphite, had been foreseen from a theoretical point of view in the late 40's promising tantalizing properties. With the appearance of graphene on stage, 2D materials were brought into focus, starting a bidimensional fever. While their number and the variety of properties they show is still growing, the present thesis is entirely focused on the study of graphene systems. The research is conducted from an experimental point of view. However, along the whole thesis we have been supported by theoretical calculations, which have allowed us to get a better comprehension of our results, enriching our understanding of the physics behind.

The experimental technique employed in the present thesis has been the scanning tunnelling microscopy (STM). This technique, developed by Gerd Binning and Heinrich Rohrer in 1981, and awarded with the Nobel prize in physics in 1986, started the development of the so called scanning probe microscopies (SPM), which in the last 30-35 years have greatly contributed to the advance in surface and materials science. The STM, as we will explain during the manuscript, allows to obtain high spatial resolution images of surfaces. It is highly sensitive to the local density of states of the sample and when combined with low temperatures (in the order of 5K in our case) provides high energy resolution of the electronic states of the sample. As we show in chapter 1, this capabilities have greatly contributed to deep into graphene physics at an atomic level.

Since its discovery, the degree of understanding of graphene properties and how to modify them in a controlled way using different approaches has risen. However, there are still some missing pieces to fully understand the limits of such an extraordinary material. The starting point of this thesis was the study of the possibility to induce and control magnetic moments on graphene. This is a still developing field regarding graphene physics and has great importance, since the implementation of magnetism in graphene, would have a huge impact in fields like spintronics. This could allow the development of new technology and devices based on graphene, something that has been envisioned for some years. At the beginning of my phD thesis, the number of works regarding this matter were scarce and not very conclusive. Experiments measuring magnetic signals on irradiated graphene systems or after the deposition of foreign species showed the possibility to generate magnetic moments, but the origin of the magnetic signal was not completely clear. The experiments on the adsorption of hydrogen atoms on graphene presented in this manuscript, indisputably prove that a single hydrogen atom induces a net magnetic moment on the graphene layer and offer a way to obtain magnetic graphene. In line with the adsorption of hydrogen on

graphene, we studied the mechanisms involved in the adsorption process to better understand the limits of hydrogenation as a way to produce magnetic graphene.

In addition, it is well known that the contact of graphene with different substrates, affects the properties of the graphene layer. Achieving a global understanding of how graphene interacts with a specific surface would provide the possibility to design in advance the properties that we want our graphene layer to exhibit. Our experiments about the tuneable transparency of graphene to tunnelling electrons show that it is possible to have access at the same time and at the same sample region to the electronic properties of the graphene layer and the surface underneath. Thanks to our ability to selectively choose what element (graphene or substrate) of the system we want to image, we were able to fully characterized the electronic properties of the Gr/Cu(111) system. From a theoretical point of view, this comprehension would help to improve the functionals describing the carbon/metal interactions, especially the ones regarding van der Waals interactions. This interactions are known to play an important role in the correct description of low interacting graphene/metallic systems. Finally, our results about the coupling of point defects on graphene layers show that, graphene's transparency is key to achieve a detailed understanding of the local interactions, in particular in the vicinity of intercalated or adsorbed particles.

Chapter 1: Using STM/STS to explore graphene physics at the atomic scale.

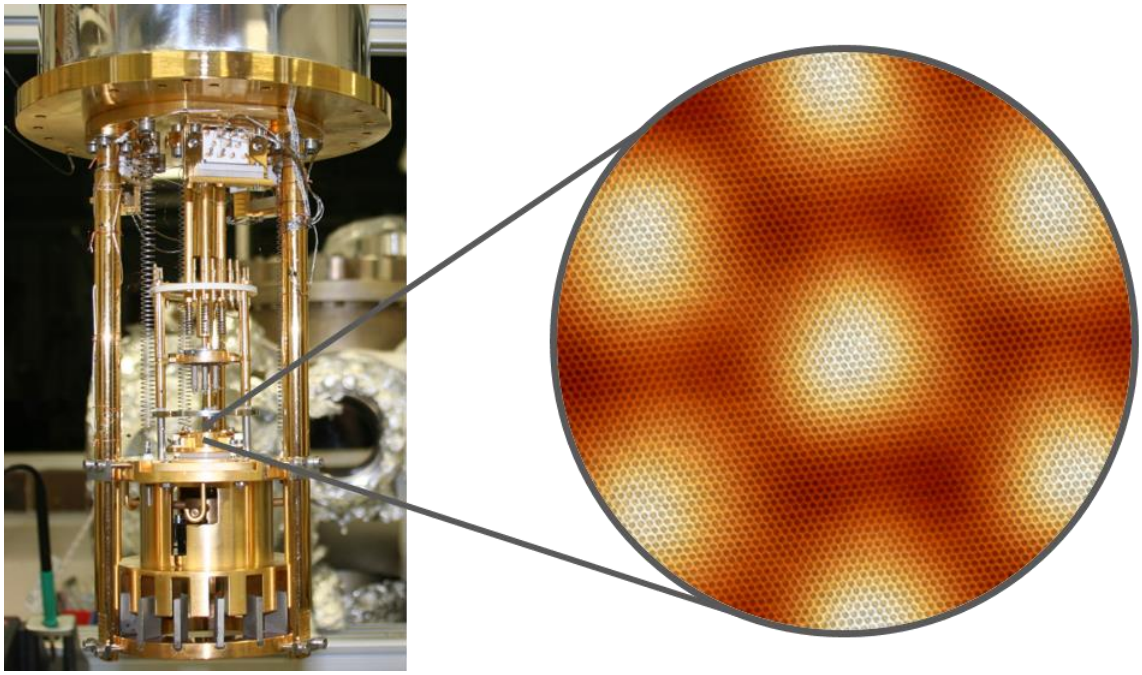

1.1 Introduction.

Scanning Tunnelling Microscopy (STM) is a technique that allows the study of surfaces with atomic precision. It was invented and developed by Gerd Binning and Heinrich Rohrer in 1982 [1, 2], invention that granted them the Physics Nobel prize in 1986 for their contribution to the understanding of surface science. The STM set the starting point of a new family of techniques called scanning probe microscopies (SPM). Prior to its invention, techniques such as Low Energy Electron Diffraction (LEED) and Near Edge X-ray Absorption Fine Structure (NEXAFS) were used to study surface morphology. Using LEED, information about the different periodicities present in the surface was accessible while NEFAXS offered information about the chemical bonds in the surface. To obtain information about the chemical composition of the surface, Auger Electron Spectroscopy (AES) was used and for the electronic structure photoemission techniques were employed. However, the information obtained by means of these techniques is a result of an average over micrometric regions of the sample. Therefore, the apparition of the STM made possible to gain information about surfaces at a really local scale with atomic resolution. Among its capabilities, STM has also shown the possibility to perform manipulations with atomic precision, allowing the study of single atoms and molecules. In addition, the STM has proven to operate under many different conditions: apart from atmospheric conditions, it can operate in ultra-high vacuum (UHV), high pressures of a certain gas or a mixture of gases and even under liquid conditions. It can also work in a wide range of temperatures, going from the mili-Kelvin regime up to temperatures close to 1000°C.

The aim of this thesis is to explore and manipulate the properties of graphene layers at the atomic scale. Graphene was the first bidimensional material ever isolated. Due to its bidimensionality, everything basically takes place on its surface. In that sense, scanning probe microscopies and specifically STM, appear as perfect candidates to study such novel material.

In this chapter, we will briefly describe the operation of an STM and the experimental set-up used during the present thesis to continue with an introduction to graphene and finish with an overview of the most important contributions of STM to the understanding of graphene. For a detailed description of the theory and development of STM see refs [3-6].

1.2 STM theory.

The working principle of an STM is based on a quantum mechanics effect: the tunnel effect. This effect, which had been predicted in the early 20th century, states that a particle with energy E that finds a potential barrier V (V>E) has a non-zero probability T to cross such barrier. This transmission probability T, decays exponentially with the width of the barrier. If a metallic tip is placed close enough to a metallic or semiconducting surface and a potential difference is applied between tip and sample, there will be a non-zero probability for electrons to flow from one to the other. In this way, an electric current is established. In the weak transmission limit, the transmission probability for electrons in an STM can be calculated using the following expression:

$$T(\vec{r}, E, eV) \backsimeq \exp\left(-2z\sqrt{\frac{2m}{\hbar^2}(\bar{\phi} - E)}\right) \quad (eq.1.1)$$

from which the exponential dependence of the tunnel current with the tip-sample distance can be observed. Indeed, it is thanks to this dependence that the STM has such a high spatial resolution: a reduction around ~1Å in the tip-sample distance, leads to an increment of the tunnel current of one order of magnitude.

The first realistic approximation to the tunnelling process of the STM was developed by Tersoff and Hamann [7, 8] using Bardeen's formalism. In their approximation they considered a spherical tip where the wave function was an s-type orbital, together with the limit of low voltage and temperature. From their assumptions, they obtained the following relation:

$$I \propto \sum_{v} |\psi_v(\overrightarrow{r_0})|^2 \, \delta(E_v - E_F) = LDOS(E_F, \overrightarrow{r_0}) \quad (eq.1.2)$$

where LDOS (Local Density of States) the density of states of the sample in $\overrightarrow{r_0}$ at the Fermi energy.

In order to obtain a more realistic expression where higher voltages and tip orbitals could be considered, Selloni et al. developed a more sophisticated formalism [9, 10]. The tunnel current in this approximation is expressed as

$$I(\vec{r}, V) \propto \int_{E_F}^{E_F + eV} dE \rho_T(E - eV)\, \rho_S(\vec{r}, E) T(\vec{r}, E, eV) \; (eq.1.3)$$

where $\rho_T(E_F)$ is the density of states of the tip at the Fermi energy.

Therefore, STM is sensitive to both the electronic structure of tip and sample, something that has to be kept in mind when interpreting STM data.

1.3 Operational modes of STM.

For the correct operation and extreme precision of STM, piezoelectric materials became really important. These materials experiment a mechanical strain when an electric field is applied. In such a way, controlled deformations of piezoelectric ceramics using different voltages will allow the precise motion of our STM. The experimental set-up of a STM can be observed in Figure 1.1. Thanks to piezoelectric ceramics, our metallic tip is approached towards the surface of the sample up to distances of a few nanometres. For distances of ~1nm and by applying a voltage difference called Bias voltage (V_B) between the tip and the sample, the tunnel current appears. Using the same ceramics or a similar set of them, the XY movement along the sample as well as the tip-sample distance can be controlled.

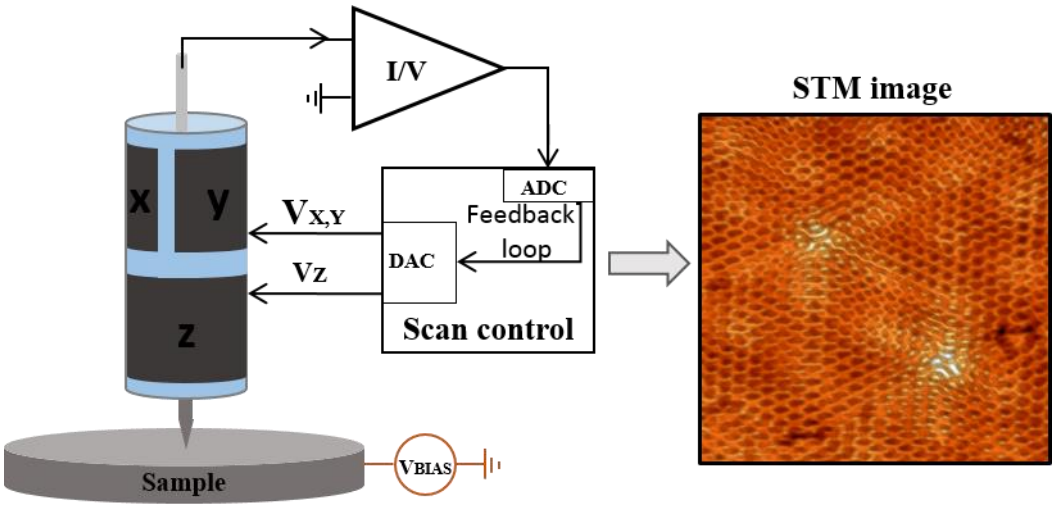

Figure 1.1: Scanning Tunneling Microscope. Diagram of a STM and the principal elements necessary for its operation.

1.3.1 Topography.

When acquiring topographic images using STM, we have to differentiate two modes. In both of them, the tip moves along the sample using the piezoelectric ceramics. The most commonly used mode is the so called constant current mode (see Figure 1.2 a). In this mode, the tip-sample distance is controlled by a feedback loop in such a way that the tunnel current is kept constant. The vertical movements of the tip during the sampling are registered, giving as a result a 3D map of the region. The second mode is the so called constant height mode (see Figure 1.2 b). As its name points out, in this mode the tip height is kept constant. In this mode, there is no need for a feedback loop and what we obtain is a current map of the sample's surface. The main advantage of this mode is that the absence of the feedback loop allows us to measure faster, although for highly corrugated samples it can lead to a crash of the tip with the sample. As we saw in the previous section, the tunnel current depends on the density of states of tip

and sample. Therefore, the heights measured in our images cannot be taken as the real corrugation of the sample, just a convolution of height and density of states.

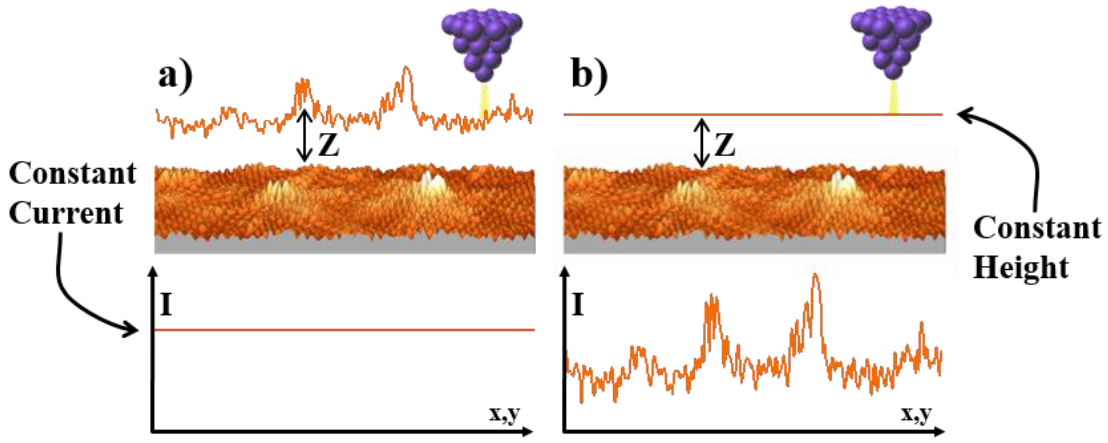

Figure 1.2: Operational modes of a STM. a) Constant current mode. b) Constant height mode.

1.3.2 Spectroscopy.

Scanning Tunnelling Spectroscopy (STS) allows us to study the electronic structure of our samples as a function of the energy thanks to the dependence of the tunnelling current with respect to the bias voltage. This technique has two main advantages compared with other spectroscopic techniques. First, as we already said in the introduction, is a local technique, it doesn't average over an area. In this sense, it is able to study, for example, single atoms or molecules on the surface. Moreover, it has access to both empty and occupy electronic states.

1.3.2.1 Local Density of States of the sample.

To study the electronic structure of a surface by means of STS is necessary the use of the differential conductance of the tunnel current. This quantity is defined as the derivative of the tunnel current with respect to the bias voltage (dI/dV). Taking equation 1.2 from Selloni et al., it follows the expression:

$$G = \frac{\partial I(\vec{r},V)}{\partial V} \propto \rho_T(E_F)\rho_S(\vec{r},E+eV)T(\vec{r},E_F+eV,eV) + \\ + \int_{E_F}^{E_F+eV} dE\rho_S(E)\frac{\partial \rho_T(\vec{r},E)}{\partial V}T(\vec{r},E,eV) + \\ + \int_{E_F}^{E_F+eV} dE\rho_T(E-eV)\,\rho_S(\vec{r},E)\frac{\partial T(\vec{r},E,eV)}{\partial V} \qquad \text{(eq. 1.4)}$$

Equation 1.4 can be simplified if the density of states of the tip and the transmission probability are considered approximately constant in the energy range eV. Therefore, the differential conductance G is equal to:

$$G = \frac{\partial I}{\partial V} \propto \rho_T(E_F)\rho_S(\vec{r}, E + eV)T(\vec{r}, E_F + eV, eV) \quad (eq. 1.5)$$

meaning that the differential conductance is proportional to the density of states of the sample in the point $\vec{r}$ of the sample.

The standard way to obtain an STS curve is the following: starting from a given voltage V_{est} and tunnelling current I_{est}, the feedback loop is disconnected and the tunnelling current I is recorded while the voltages varies from V_{ini} to a final voltage value V_{fin}. Afterwards, this I/V curve is differentiated (numerically or by lock-in) to obtain the differential conductance curve.

1.3.2.2 STS spatially resolved.

The highly spatial resolution of STM makes possible the acquisition of spectroscopic measurements spatially resolved. There are two main types of spatially resolved spectroscopic measurements, CITS (Current Imaging Tunneling Spectroscopy) and conductance maps (which along the present thesis has been the most commonly one used).

In a CITS, while we acquire a topography image consisting of N×N pixels, one (or various) I/V curve(s) is (are) acquire at each point. If the voltage sweep is made in M discrete steps, we will then obtain M current spatial maps $I_{xy}(V)$ that can be differentiated to obtain $(dI/dV)_{xy}(V)$. Due to all the curves performed during a CITS, their acquisition time can be rather long. An alternative and faster method is to directly obtain conductance maps at specific voltages using a lock-in.

1.3.3 Cu(111) surface state: An example of characterization of 2D states.

In this section we will briefly introduce show all the STM measurement modes that we have used in this thesis to facilitate its reading. For illustrative purposes we will use a Cu(111) surface, known to exhibit a surface state. This surface state is characterized by a 2D free-electron like behaviour with an isotropic parabolic band dispersion given by: $E = E_0 + \hbar^2 k^2 / 2m^*$, where E_0 is the band edge and m* is the effective mass (see Figure 1.3).

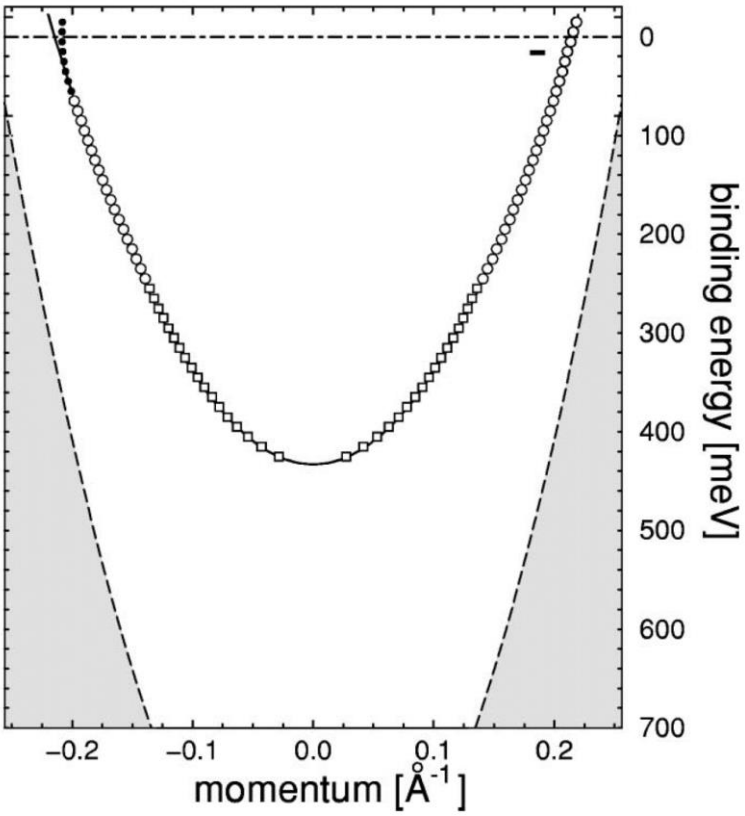

Figure 1.3: Cu(111) surface state. Dispersion of the Cu(111) surface state measured by photoemission (extracted from [11])

-**Topography image:** In Figure 1.4a we present a topography image of a terrace of Cu(111) measured using the constant current mode at 350 meV. The black circles are point defects in the surface, usually attributed to sulphur or antimony contaminants.

-**I/V and dI/dV curve:** If we now perform spectroscopic measurements far from the defects, we can study the local density of states of the Cu(111) surface. In Figure 1.4b we show an I/V curve (red line) acquired in the black cross marked in Figure 1.4a. If we now differentiate the spectrum, we obtain the dI/dV curve which is proportional to the LDOS (black line in Figure 1.4b). A sudden step appears around ~-440 mV from which the value of the band edge E_0 can be extracted.

-**STM image at low bias:** Figure 1.4c shows an STM image obtained at 10 mV. At this bias, the STM can be basically considered as a surface of constant local density of states at the Fermi energy (LDOS(E_F)). In this image we can observe the apparition of wave like patterns. These patterns are called standing waves and they arise from the scattering of the electrons of the Cu(111) surface state off defects (black dots in Figure 1.4 a and c). From the wavelength of these standing waves, the wave vector k at the Fermi energy can be recovered. However, there is another way to obtain the same information, and it consists on

performing the 2D Fast Fourier Transform (2D-FFT) of the image. The 2D-FFT presents a circle from which radius the value of the wave vector can be extracted (see Figure 1.4d).

-**Conductance map:** As we explained in the previous section, conductance maps give us information about the local density of states at a given energy $E=e\cdot V$. For each energy, the Cu(111) surface state has a given value for the wave vector which is reflected in a defined wavelength for the standing waves we observe in our images. By performing dI/dV maps at different energies and using the 2D-FFT, the energy dispersion k(E) for the Cu(111) surface state can be obtained (see Figures 1.4 e-f).

-**dI/dV curves along a line:** There is another way to gain spatially resolve information of the local density of states and measure the Cu(111) surface state energy dispersion: obtaining dI/dV curves along a line close to a straight step. In Figure 1.5a we can observe an atomic step and in Figure 1.5b we have a low bias image where the standing waves generated by the scattering of the electrons off the step can be seen. By performing a set of dI/dV curves along the line depicted in Figure 1.5b, a conductance map with respect to distance and energy [dI/dV(x, E)] is acquired (see Figure 1.5c). With this conductance map we can study both the local density of states and the extension of electronic states. If we perform a profile like the one depicted in Figure 1.5c, we recover the corresponding dI/dV curve in that spatial position (Figure 1.5e). If the profile is taken in the perpendicular direction, the intensity of the standing waves with the distance can be obtained and for example, study how that intensity decays (Figure 1.5f). In addition, if we perform the 1D-FFT of our map, the parabolic dispersion can be recovered (see Figure 1.5d).

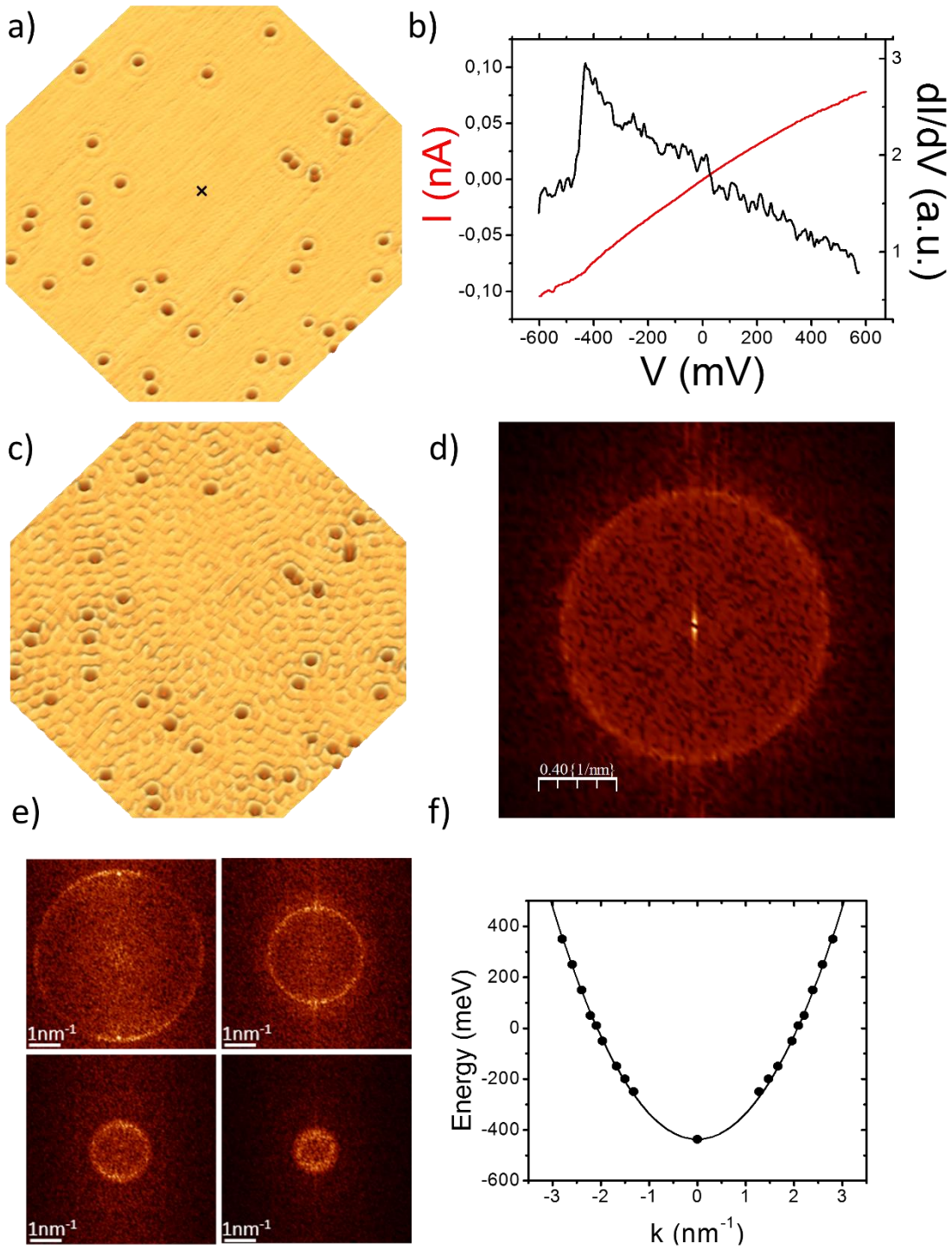

Figure 1.4: Measuring the surface state of Cu(111). a) STM image of a clean terrace at 350 meV. b) I/V and dI/dV curve obtained in the black cross in a). c) Low bias STM image of the terrace shown in a). d) 2D-FFT of Figure 1.4c. e) 2D-FFT of dI/dV maps of the terrace in a) acquired at 250,-200,-350 and -400 meV. f) Energy dispersion of the Cu(111) surface state obtained from our STM measurements.

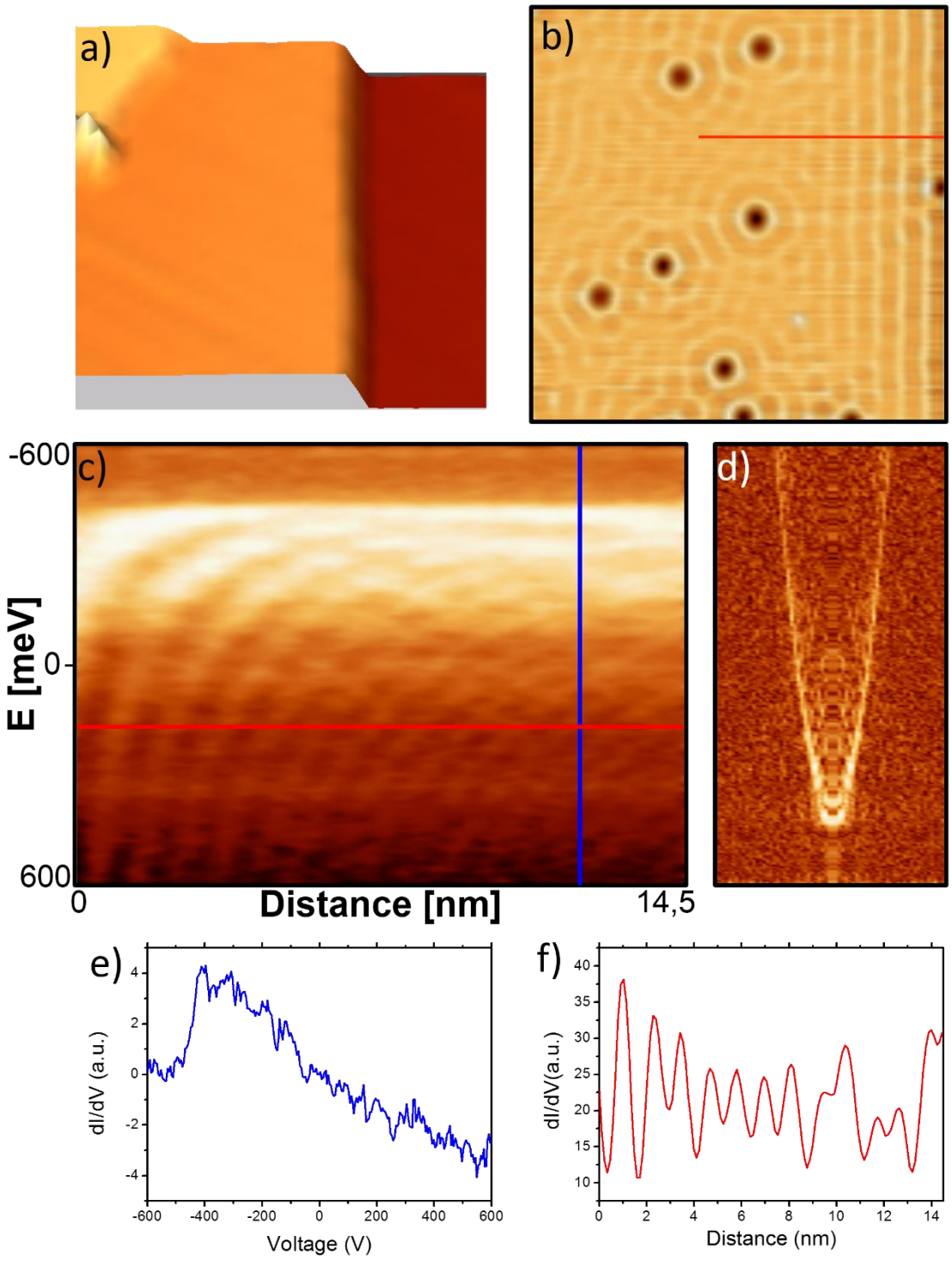

Figure 1.5: Using dI/dV(x,E) maps to characterize Cu(111). a) STM image of a Cu(111) region where an atomic step can be observed. b) Zoom in of image a) to observe the standing waves arising from the step. c) dI/dV(x,E) map obtained from the acquisition of dI/dV curves along the red line in b). d) 1D-FFT of c) showing the parabolic dispersion of the Cu(111) surface state. e) and f) Profiles along the red and blue lines in c).

1.4 Experimental set-up.

All the experimental results of the present thesis have been obtained in a home-made system consisting on a UHV chamber with a 4K STM. In the present section I will describe the main parts and characteristics of the experimental system.

The UHV chamber, as well as the STM have been designed and developed entirely in our group. It was constructed during Miguel Moreno Ugeda's phD thesis and a detailed description of the system can be found in his phD thesis [12]. Here we will just briefly mention the main elements to give a general overview of it. Our UHV system consists of two independent vacuum chambers (see Figure 1.6). One is used for preparing our samples and in the second one the low temperature STM and the liquid Helium cryostat are located. Both chambers are separated by a gate-valve and can be pumped separately. Samples are moved from one chamber to the other using cryogenic tweezers. The preparation chamber also counts with a pre-chamber in order to preserve the UHV conditions when introducing new samples in the system. To achieve our UHV conditions the system is first pumped using a turbo molecular pump assisted by a dry primary pump while baking the whole chamber. After ~48 hours, the base pressure of the system is on the order of $1 \cdot 10^{-9}$ Torr. Both chambers count with their own ion pump which can reduce this base pressure by a factor 2 and permit the disconnection of the turbo and dry pump, reducing the mechanical noise they generate. In the case the STM chamber, when measuring at LHe temperatures, the cryostat acts as a cryogenic pump, reaching estimated pressures below $1 \cdot 10^{-13}$ Torr.

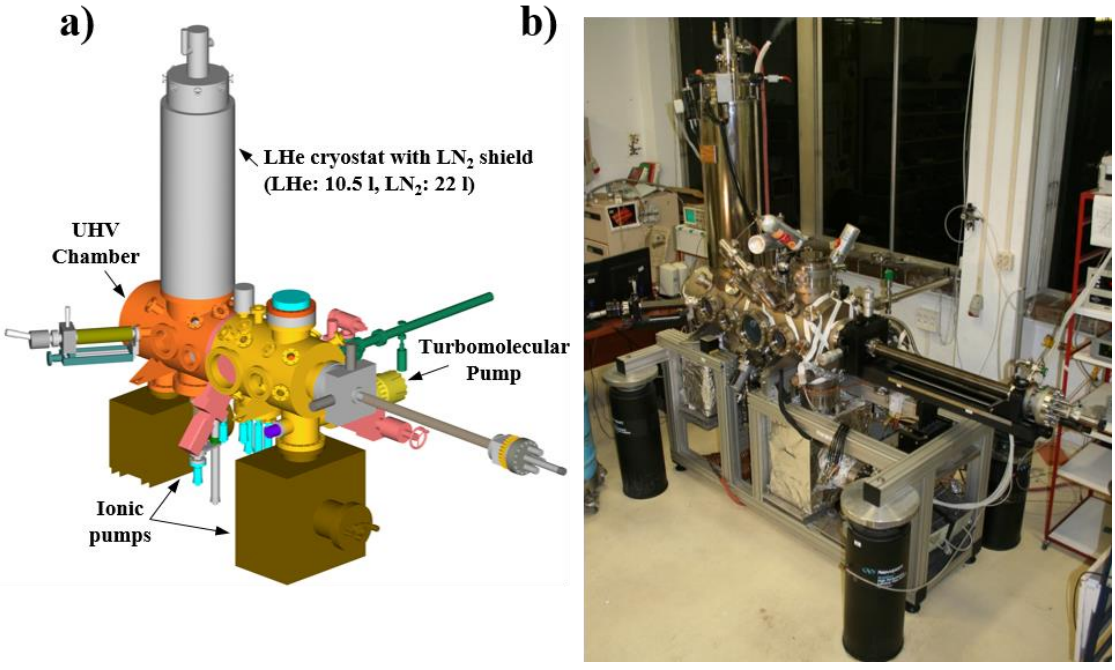

Figure 1.6: **UHV system.** a) 3D oblique perspective of the system where some parts of the system are tagged. c) Picture of the real system in our laboratory [12].

1.4.1 Preparation Chamber.

In this chamber, samples are cleaned and grown in UHV conditions. The samples can be sputtered, annealed and exposed to different atomic species and molecules. All these processes can be done while keeping our sample at temperatures from 40K to 300K. In Figure 1.7 we have a 3D representation of the chamber where all its main component can be seen.

-Horizontal cryogenic transfer bar: In order to prepare our samples and move them in our UHV system (from the Prep chamber to the STM chamber, for example), a translational manipulator was installed in the preparation chamber. This manipulator also counts with a continuous-flow cryostat which cold finger can reach 5K if liquid Helium is used allowing us to reach sample temperatures ~40K.

-**Heater, evaporator, tip cleaner:** The three of them are located in the same flange. In the centre we can find our electron bombardment heater. Our sputtering gun is pointing to the same focal point as well as one of the chamber's windows, where we place a pyrometer to control the temperature of the sample during annealing processes. In the left side an evaporator for low melting point temperature materials is located and in the right one a high voltage plate in order to prepare and clean new tips using field emission. A detailed description of these components can be found in the phD thesis of Dr. Óscar Custance [13].

-Vertical manipulator: This vertical manipulator is used to exchange tips and it has also been used to grab graphite exfoliators.

-Gas line: Our system counts with a high vacuum gas line. The line is connected with certain key points of the preparation chamber and they are controlled by different leak valves. It has space for up to 4 different gases, and thanks to its design, the bottles are easily interchangeable.

-Ion gun: In order to prepare some of our samples, we needed to use low energy ions (Ar^+ and C_2H_4). To do so, our system counts with an ion gun capable of supplying ions with energies from 100 to 3000 eV (PSP ISIS 3000).

-Hydrogen cracker: In chapters 2 and 3 we will study the adsorption of single hydrogen atoms in our graphene samples. In order to crack H_2 molecules, temperatures higher than 1600 °C are needed. Our home-made hydrogen cracker basically consists of a filament which can reach such high temperatures and a capillary through which H_2 gas flows. The cracker points to the same focal point as the ion gun.

-Quadrupole Mass Spectrometer (QMS): To prove the quality and chemical composition of our UHV vacuum, a QMS with a sweep interval from 1 uma to 200 uma was installed in the preparation chamber (Barlzers QMS 200).

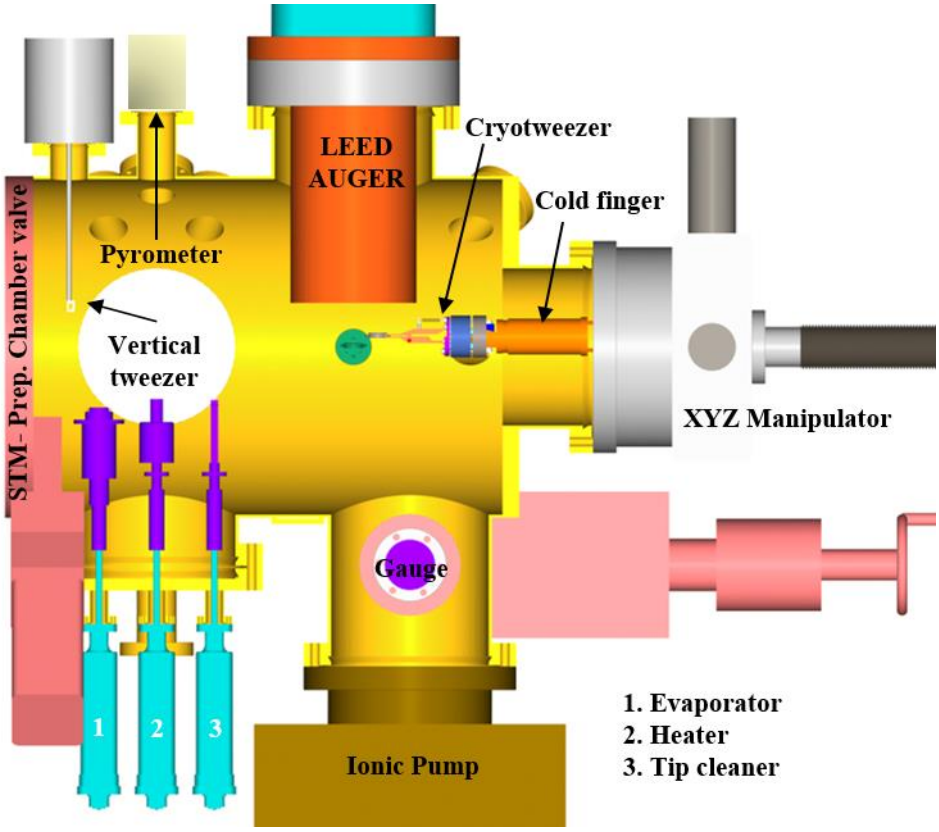

Figure 1.7: **Preparation chamber diagram.** Diagram of the preparation chamber where most of the equipment is highlighted [12].

1.4.2 LT-STM chamber.

The STM chamber contains the liquid helium bath cryostat where the STM head is located. In Figure 1.8 we can appreciate the arrangement of the cryostat and the STM in the chamber. The cryostat is composed of an outer and inner tanks. The outer one is filled with liquid nitrogen and acts as a radiation shield for the inner tank, which is filled with liquid helium. At the bottom of the LHe cryostat, a copper disc is place to act as cold finger with the structure where the STM is held. As in the case of the preparation chamber, it has an ion pump to maintain it in UHV conditions without the mechanical noise that a turbo molecular pump would induce. As we already commented, the final base pressure of this chamber is lower than the standard $1 \cdot 10^{-10}$ Torr once the cryostat is filled up with liquid Helium. This extremely low pressures are really convenient in this kind of systems since the samples can stay cleaner for longer periods of time. To take advantage of these pressures, a parking for the samples is located in the chamber. It is positioned in the space between the STM and the gate-valve of the preparation chamber and it has space up to 10 samples/tip holders/evaporators. In this

chamber we can find two more manipulators, one vertical and another one horizontal. The first one is used to drive the STM to its different positions (measure, tip change and cooling) while the second one is used when the STM tip needs to be changed.

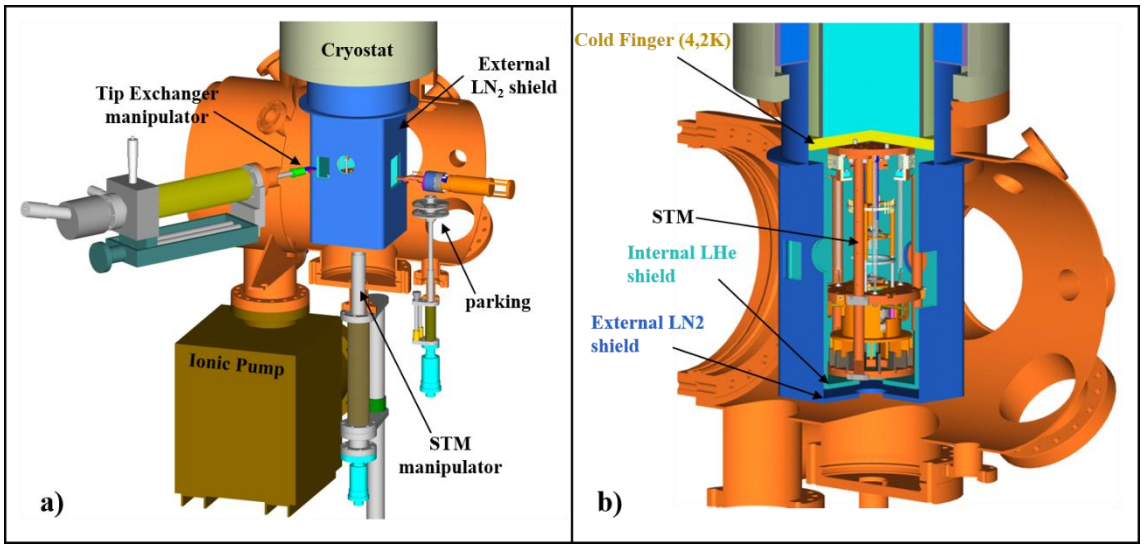

Figure 1.8: **STM Chamber.** a) Diagram of the STM where the principal components are indicated. b) Part sectional view of the cryostat to better appreciate the STM and shields [12].

The STM head is an inverted Beetle/Besocke design [14]. This kind of scanners are known to have high mechanical stability and a great thermal compensation due to its low size and radial symmetry. It consists of a cylindrical base where three outer piezoelectric ceramics are disposed in an equilateral triangle and a fourth one is in the centre. The three outer ceramics are responsible of the XY movement when measuring and they are also responsible of the STM approach towards the sample. The last ceramic only moves in the Z direction and has the STM tip attached to it together with the tunnel current wire. The STM temperature can be measured using a silicon diode attached to it. A diagram of the STM can be observed in Figure 1.9.

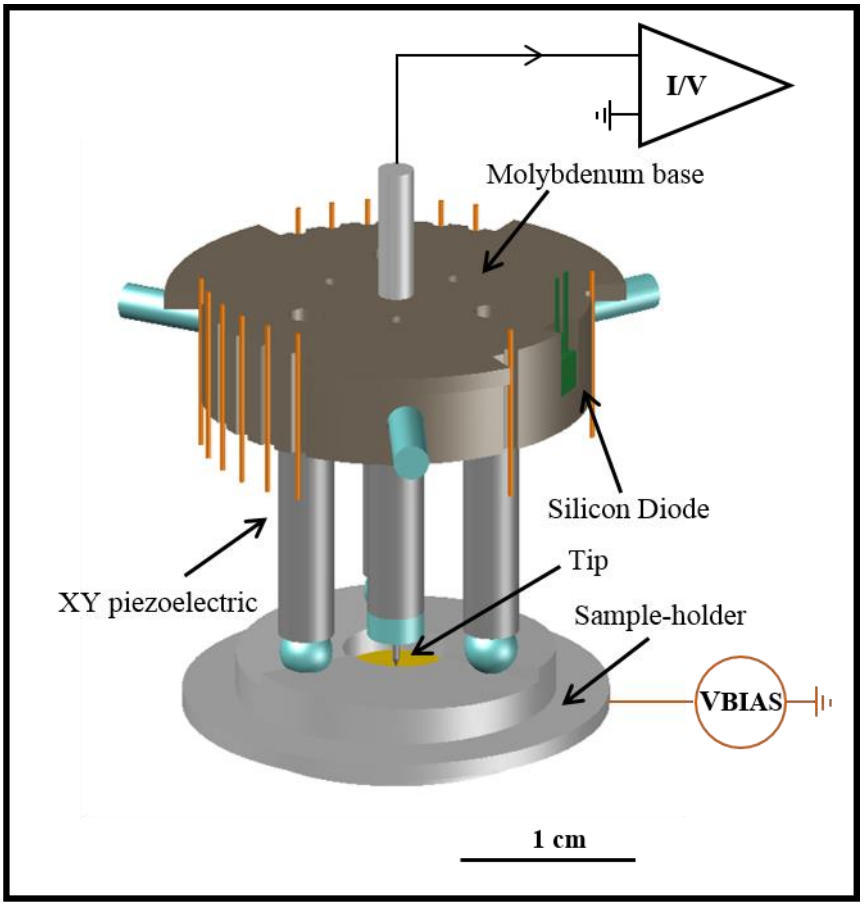

Figure 1.9: **4K-STM Head.** 3D design of the inverted beetle scanner used in our system [12].

1.5 What is graphene?

In the past decade an increasing interest in two-dimensional materials (2D) has arisen. The starting point was the first isolation of graphene in 2004 by A. Geim and K. Novoselov [15]. This discovery granted them the Nobel Prize in 2010. One of the main reasons why graphene's isolation was such a breakthrough was due to all the previous theoretical work stating the impossibility of the existence of truly 2D materials because of its thermodynamic instability [16-18]. For that reason, graphene research was only done from a theoretical point of view expecting graphene to exhibit interesting properties. Luckily, Geim and Novoselov showed the possibility of obtaining graphene layers with areas in the order of hundreds of square microns. Later experiments showed the possibility of suspending these graphene layers, demonstrating its stability [19]. From that moment, graphene has been extensively studied and characterized presenting fascinating attributes and opening a new path for seeking novel materials.

Graphene displays a great number of properties in diverse fields. It has great electronic and mechanical characteristics. The electron mobility measured in graphene is on the order of 200000 cm^2/Vs at room temperature [20, 21] and its thermal conductivity 5300 W/m·K [22]. The ambipolar field effect has also been measured in graphene making possible gating graphene layers when placed on top of a proper substrate [15]. It also exhibits ballistic transport, meaning that its carriers can move around without suffering any scattering due to its perfect lattice structure for long distances (~1 μm) [23]. From a mechanical point of view, it possesses a Young modulus up to 1TPa (5 times greater than steel) but it is very flexible at the same time [24-26]. In terms of optical properties, graphene presents an unexpectedly high opacity for an atomic monolayer, absorbing 2.3% of red light [27, 28]. Quantum Hall Effect at room temperature and an anomalous quantum Hall Effect have been measured in graphene too [29-32].

But what makes graphene such an amazing material? Most of graphene properties stem on the atomic structure of graphene. Graphene is basically a one atom thickness layer made of carbon atoms. It was the last carbon allotrope to be isolated and it consists of carbon atoms arranged in a honeycomb structure (see Figure 1.10a). In order to bind and form a planar configuration the carbon's 2s orbital hybridize with two of the three 2p orbitals (the p_x and p_y orbitals) to form 3 sp^2 orbitals (see Figure 1.10b). Therefore, each carbon atom can bind with its three first neighbour atoms *via* σ-bond. Sigma bonds are really strong, making the bidimensional sigma bond lattice the responsible for the incredible mechanical properties of graphene. The last electron, which is left in the p_z orbital, makes up a π-bond with the p_z orbitals of the neighbouring carbon atoms. These π-bonds are weaker than sigma bonds, and the electrons involved can jump from atom to atom giving rise to a delocalized band, the so called π-band, origin of the electronic properties of graphene (see Figure 1.10c).

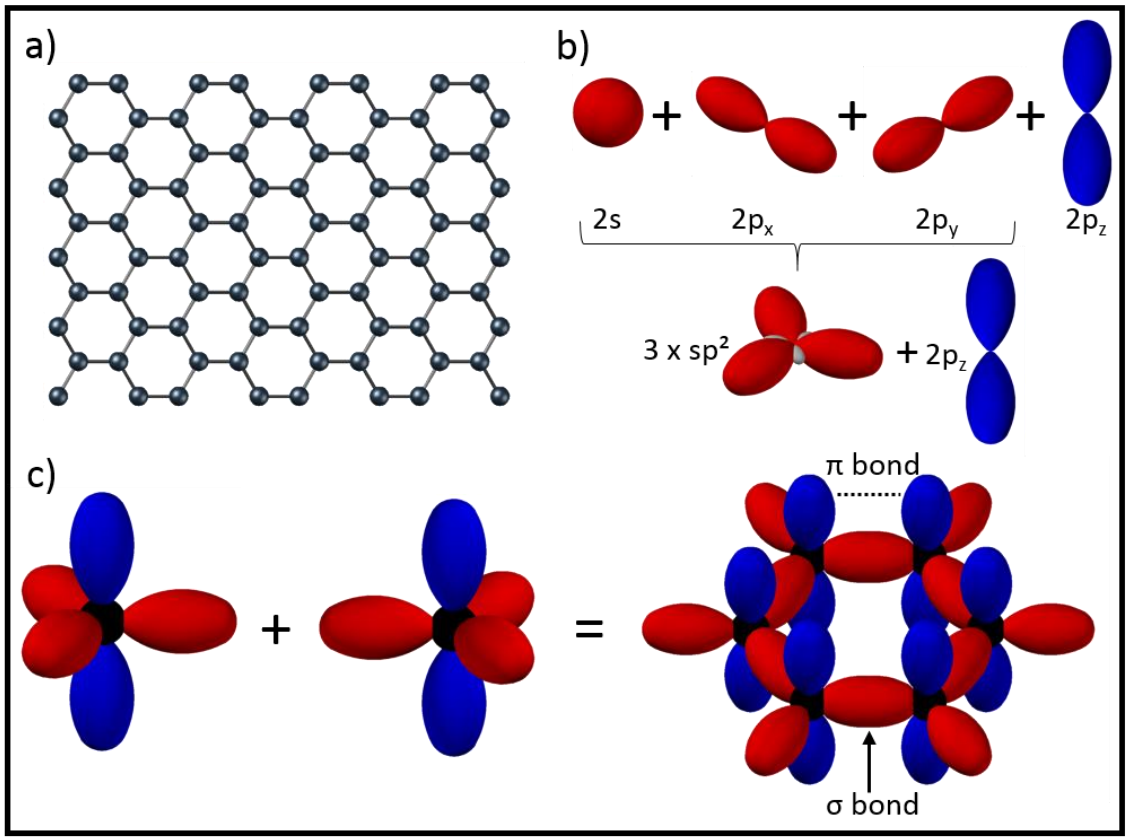

Figure 1.10: Graphene's lattice sketch. a) The hexagonal honeycomb lattice of graphene. b) sp² orbital hybridization. c) Formation of σ-bond and π-bond on graphene.

Therefore, to start understanding graphene attributes it is useful to take a look at its bandstructure. The π-band can be described using a tight binding model where only p_z orbitals are considered with an interaction with first and second nearest neighbours. However, the honeycomb lattice is not a Bravais lattice since two neighbouring sites are not equivalent. Nevertheless, graphene's lattice can be seen as two hexagonal sublattices A and B where the distance between nearest neighbour carbon atoms is 1.42 Å and the unit cell size is 2.46 Å (see Figure 1.11a). The energy bands derived from this approximation have the following expression [33, 34]:

$$E_{\pm}(\vec{k}) = \pm t\sqrt{3 + f(\vec{k})} - f(\vec{k}) \quad \text{(eq. 1.6)}$$

With

$$f(\vec{k}) = 2cos(\sqrt{3}k_y a) + 4cos\left(\frac{\sqrt{3}}{2}k_y a\right)cos\left(\frac{3}{2}k_x a\right) \quad \text{(eq. 1.7)}$$

Where depending on the square root sign we will obtain the upper band (π^*) for the plus sign and the lower band (π) for the minus sign. A 3D representation of these equation extracted from reference [33] shows the shape of graphene's bands (Figure 1.11c). As we can see, the conduction and valence band (π^* and π band respectively) only coincide in one point called the Dirac point. If the origin

of equation 1.6 is set to a K point applying a translation operation (k=K+q with |q|<<|K|) the band equation changes to:

$$E_{\pm}(\vec{q}) \approx \pm v_F|q| + O\left[\left(\frac{q}{K}\right)^2\right] \quad \text{(eq. 1.8)}$$

With $v_F = 3ta/2 \cong 10^6$m/s the Fermi velocity. In the vicinity of the Dirac point the last term can be neglected obtaining as a final result:

$$E_{\pm}(\vec{q}) \approx \pm v_F|q| \quad \text{(eq. 1.9)}$$

From this result important conclusions can be stated. Neutral graphene is a zero gap semiconductor where its valence and conduction bands present a linear dispersion around the neutrality point. This implies that the electron velocity is constant, independently of k, just like relativistic particles described by Dirac's equation. For that reason, graphene's carriers act as massless relativistic fermions. Here, the Fermi velocity of the electrons is around 300 times smaller than the speed of light, c.

However, it is important to mention that some of the exceptional properties of graphene do not arise from the linear dispersion around the Fermi level but from the existence of an additional quantum number, the pseudospin. This quantity is defined by the phase relation between the two sublattice components of the wave function of the quasiparticles. The pseudospin brings the necessity of introducing a new index that indicates whether the particle is in one sublattice or the other. To characterize the pseudospin of a particle we have to use an operator associated with an observable called helicity (or chirality) which is defined as the projection of the momentum $\vec{q}$ along the pseudospin direction. In graphene, the quasiparticle direction of the spin is parallel to its momentum for electrons, and antiparallel for holes. As a consequence, the chirality of electrons (holes) will be positive (negative). In Figure 1.11d we can find a sketch of the Dirac cones where the pseudospin direction has been represented using arrows. In summary, chirality states the fact that an electron with momentum q in graphene is linked with a hole with momentum –q since both have their origin on the same carbon sublattice.

Most of the extraordinary properties of graphene depend on the quality of the graphene layer. At the beginning of this chapter we described the operation of the scanning tunnelling microscope. This technique allows us to study the topography of the sample with atomic resolution and when performed at low temperature, the density of states of our surface with high energy resolution. Therefore, STM will become a powerful tool to study and characterize graphene systems and provide important information to improve our understanding of this material.

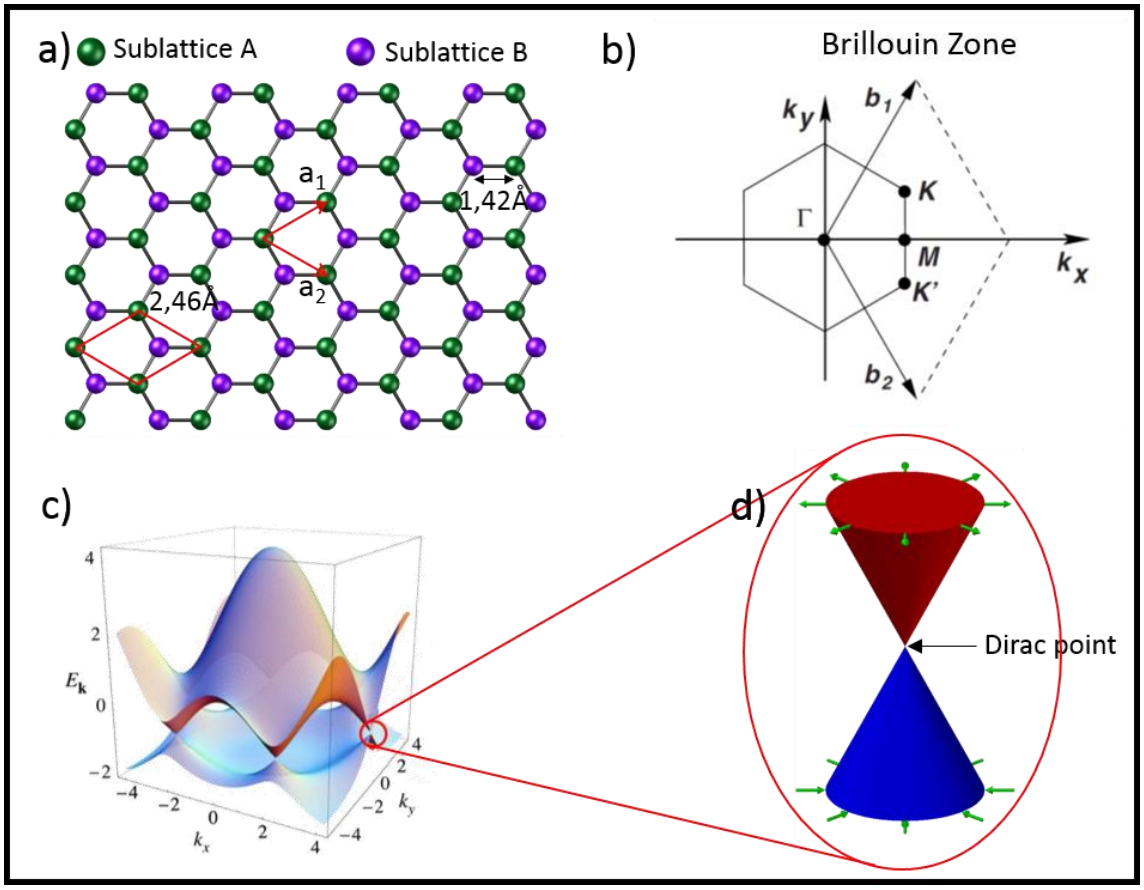

Figure 1.11: Tight binding approximation for graphene. a) Graphene lattice where the two sublattices A and B are differently coloured. The unit cell is highlighted with a red rhombus and the lattice unit vectors a_1 and a_2 as well. b) Brillouin zone of graphene. c) Tight binding approximation bands represented in 3D [33]. d) Dirac cones of graphene with the pseudospin represented as green arrows.

The aim of the following sections of this chapter is to present the contributions that STM has provided to the better understanding of graphene properties. To do so, I have selected the works that in my opinion have been more relevant and helped to shed light and give better insight of graphene's properties.

1.6 Graphene morphology with STM.

As we mentioned in the previous section, many of the extraordinary properties of graphene depend on the structural quality of the graphene layer. Therefore, ensuring the maximum perfection of our monolayer becomes a crucial issue. STM measurements have helped verifying the quality of graphene layers at the atomic scale as well as obtaining a better understanding of the conformation of graphene on different substrates.

The first graphene samples where its exceptional properties were experimentally measured were exfoliated graphene layers deposited on SiO_2 [15, 30, 35]. In those samples, one can find from single to multilayer graphene layers. STM images can help us discern whether we are measuring a monolayer or a multilayer region. This is possible thanks to the contrast change observed in the atomic structure, going from a honeycomb symmetry for the monolayer, to a threefold symmetry characteristic of AB stacking (as the one found on graphite samples) for multilayer graphene [35] (see Figure 1.12). Such atomic identifications are also possible in other graphene systems as shown in monolayer and bilayer graphene epitaxially grown on SiC substrates [36]. However it is important to notice that experiments have to be done carefully, since changes in the observed atomic structure can also depend on the tip's reactivity and its closeness to the surface. Theoretical calculations have shown that in graphite, in the near-contact regime, there is an inversion of the contrast where bright spots correspond to hollow sites instead of carbon atoms [37].

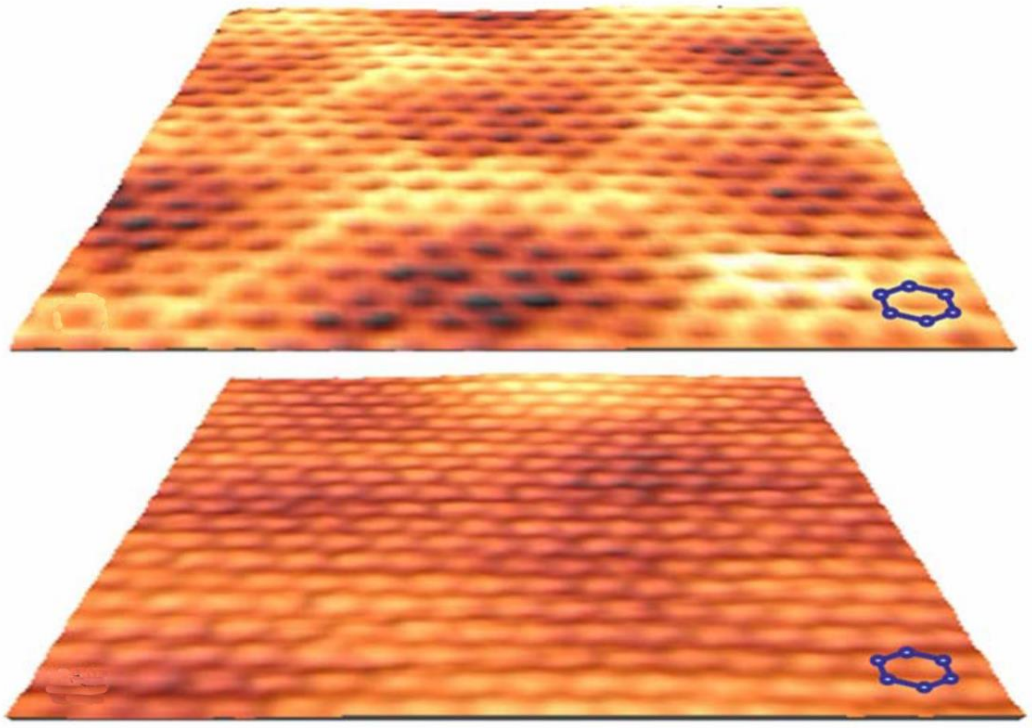

Figure 1.12: Monolayer vs. Bilayer graphene and contrast inversion. Top-bottom: 4×4 nm² 3D view of a monolayer and bilayer graphene terrace respectively [36].

Another critical parameter for the actual quality of the graphene layers stems in its corrugation. Transmission electron microscopy studies on suspended graphene found out of plane deformations in the order of 1nm [19]. STM measurements show that when transferred onto a Si wafer capped with SiO_2, graphene exhibits a smaller roughness at a bigger scale (around 0.5 nm) [38] while the hexagonal lattice is preserved when obtaining small scale images [35]. The corrugation observed in these samples is attributed to the partial accommodation of the graphene layer on the rough surface of the SiO_2. As a result of this disorder, the Dirac point of the graphene sample will vary along the sample, leading to graphene regions with different doping level [39] which can be directly visualized in STM experiments [40-42] as we will discuss in detail in section 1.7.

One way to reduce graphene's corrugation is to deposit it on top of an exfoliated boron nitride layer placed on the commonly used SiO_2 substrates. STM measurement of these samples have shown a decrease on the apparent height corrugation measured down to 20-30 pm [43, 44]. In Figure 1.13 we can observe two images of graphene: one transferred onto SiO_2 (left) and the other one on boron nitride (right) using the same colour scale to appreciate the difference on corrugation.

Graphene can also be grown epitaxially on SiC crystals or by chemical vapour deposition (CVD) on different metallic substrates [36, 45-50]. In these systems graphene shows the appearance of a moiré pattern due to the graphene/substrate lattice mismatch. In those samples, the corrugation found critically depends on the graphene/substrate interaction and values ranging from few picometers up to 1 angstrom can be found [51, 52].

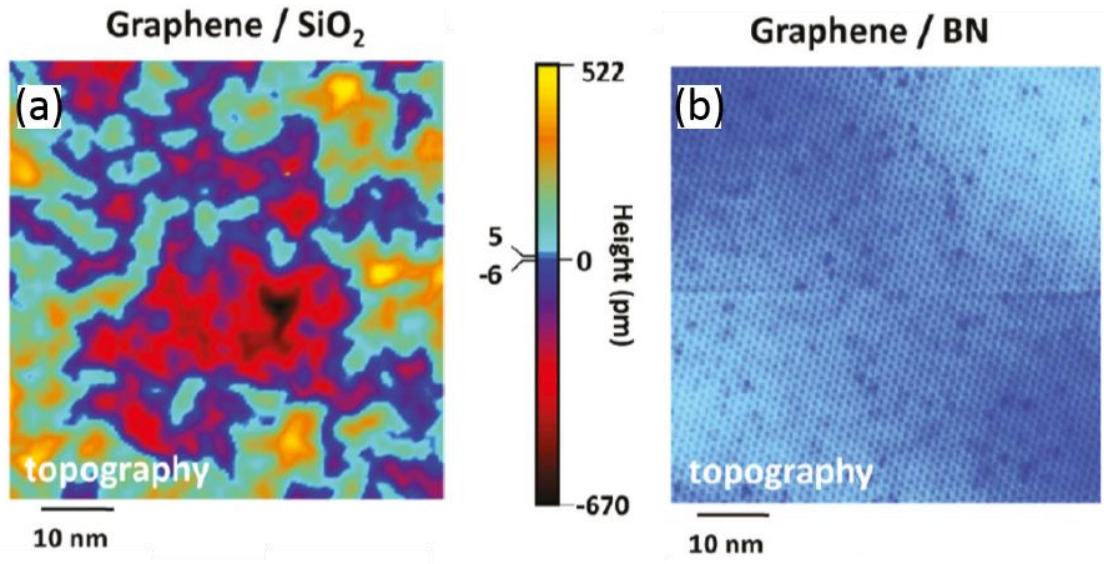

Figure 1.13: Graphene corrugation on different substrates. a) STM image of graphene transferred on top of silicon oxide. b) STM image of graphene transferred on top of boron nitride. A colour scale in the middle allows us to appreciate the difference in corrugation between both systems [43].

1.7 Dirac-point mapping: e-h puddles on graphene.

As we already commented in section 1.6, previous results on graphene on SiO_2 showed the existence of charge inhomogeneities that affected transport measurements of these samples [39]. As a result of these inhomogeneities, the Dirac point (and therefore the doping level) vary along the sample. One way to follow the changes of the Dirac point is by STS spectra. The linear dispersion of graphene around the Dirac point, leads to a V-like shape of the density of states centred on it. Therefore, single spectrum can tell us the doping level of a certain region of the sample in a very local way. In Figure 1.23 we can observe two different spectrum of a neutral graphene sample and a p-doped one. However, if we want to study the shape and extension of the regions with different doping levels, one should use the so called Dirac-point mapping. Dirac-point mapping is a technique that uses CITS maps to study the changes in energy of the Dirac point due to doping variations in graphene. Using this technique, the study of charge inhomogeneities such as e-h puddles on graphene on SiO_2 with an electron-density spatial resolution two orders of magnitude higher than scanning single-electron transistor microscopy was possible. Changes in the energy position of the Dirac point can be studied locally with dI/dV curves, but a more complete way would be the acquisition of the so called Dirac-point maps, where a single dI/dV curve is taken in every point of the image to obtain the energy position of E_D on each spatial spot [40-42]. These maps, $E_D(x,y)$, can be converted into charge-density maps using the relation:

$$n(x,y) = \frac{1}{\pi}\frac{E_D^2(x,y)}{\hbar^2 v_F^2} \qquad \text{(eq. 1.10)}$$

where v_f is the Fermi velocity of graphene.

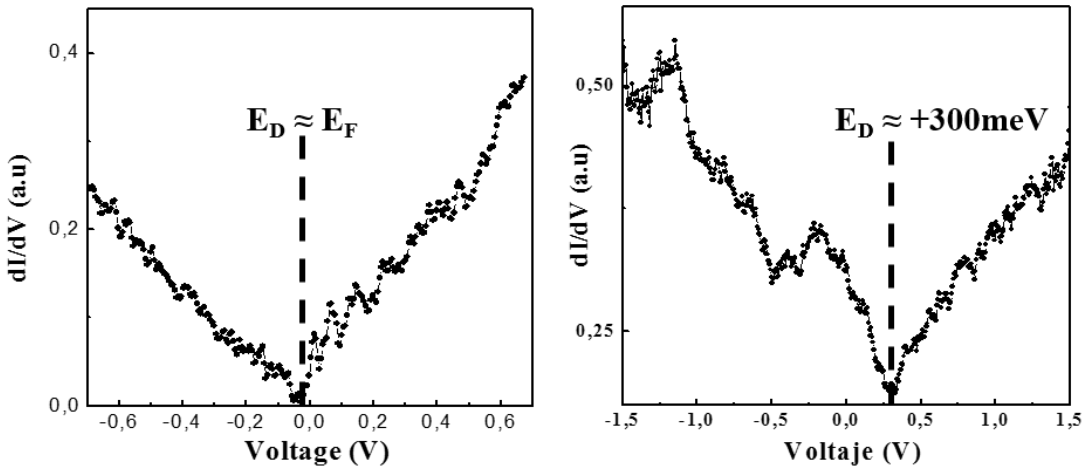

Figure 1.23: STS and Dirac point of graphene. Left spectrum: dI/dV curve taken on multilayer graphene grown on SiC(000-1) where the Dirac point is approximately at the Fermi level. Right spectrum: dI/dV curve taken on graphene grown on Pt(111) where the p-doping of the graphene layer can be observed [12].

Another way to investigate charge puddles is by measuring dI/dV maps for bias voltages slightly below E_D [40]. This reduces the acquisition time and gives a map of E_D, up to a multiplicative factor (see Figure 1.15c). This also allows the obtainment of bigger images to study larger areas. From all those measurements, the absence of correlation between charge puddle shape and graphene corrugation, points to a different origin of the charge impurities rather than morphology of the sample. From the study of many charge puddles, the origin of these inhomogeneities seems to come from air molecules trapped between the graphene and the SiO_2 substrate.

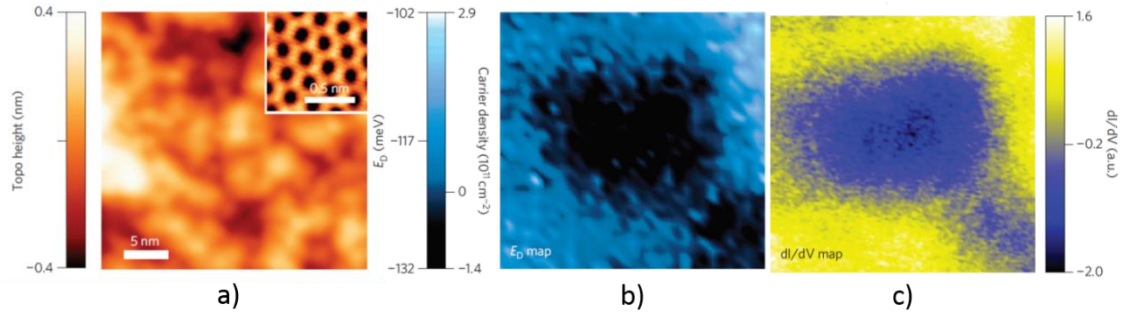

Figure 1.15: Dirac mapping on graphene: a) STM topography image of a graphene on a SiO_2 substrate region. Inset: Close-up image of the graphene honeycomb lattice. b) Dirac-point energy (E_D) map of a single charge puddle lying in the same area as a). c) Fixed-bias dI/dV map of the same area as a) and b) showing the same puddle shape [40].

Same experiments using boron nitride as substrate show a significant reduction of the charge inhomogeneity compared with the one measured in SiO_2 (see Figure 1.16a-b) [43]. Charge puddles also act as scattering sites for graphene quasiparticles leading to interference patterns. Here, the scattering occurs as a consequence of the quasiparticles scattering from a disordered potential (see Figure 1.16c).

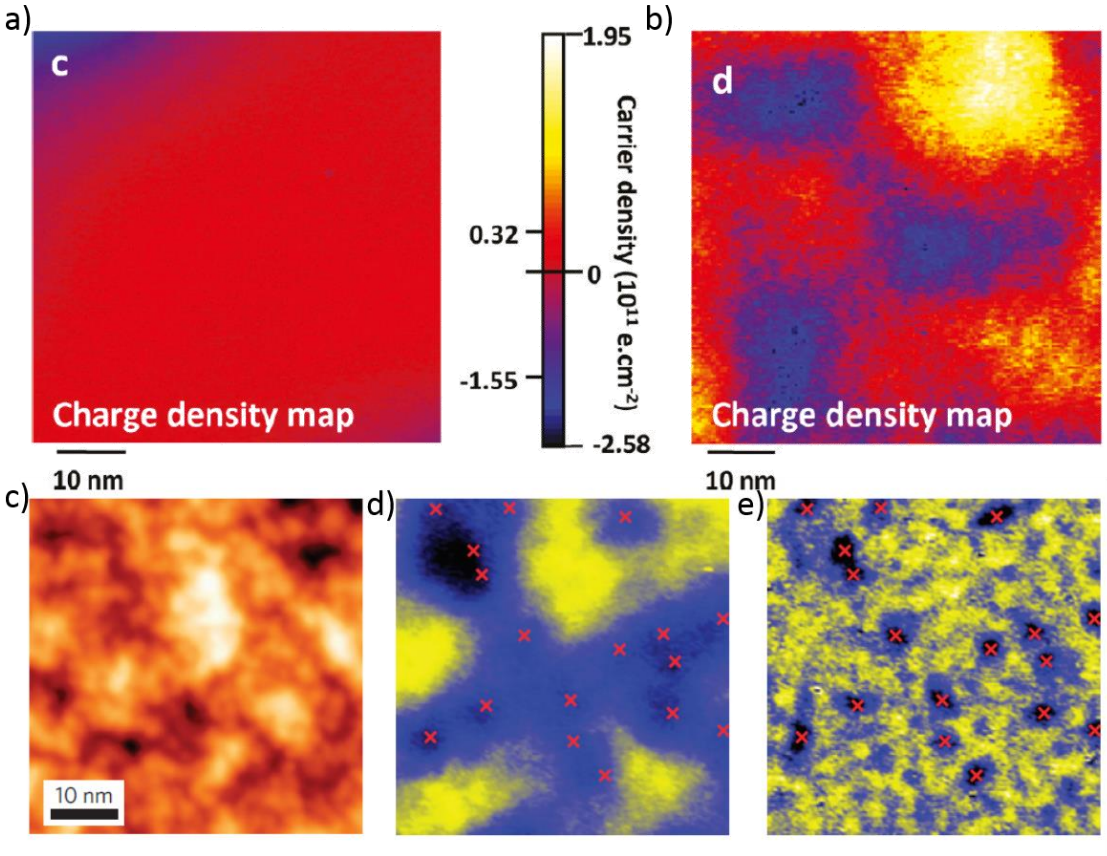

Figure 1.16: Dirac mapping on graphene over BN. a-b) Charge density maps of graphene on BN *vs.* graphene on SiO_2. c) STM topography of a graphene area. d) Same region as c). dI/dV map at bias near Dirac point showing electron puddles due to charge. Red crosses indicate the location of quasiparticle scattering-centre impurities observed in d. e) dI/dV map of the same area at larger bias revealing impurity scattering centres charge-density puddles (red crosses) [40, 43].

1.8 Pseudospin and quasiparticle scattering on graphene.

Scattering processes in metals have been studied for quite a long time. The electrons of the surface state of some metals like gold or copper are known to scatter from defects or steps leading to standing wave patterns [53, 54] which have been used to locally characterize the energy dispersion of surface states or to learn about the actual scattering of quasiparticles from the different defects naturally found or intentionally build on these metal surfaces. In graphene, due to its bidimensionality, the quasiparticles are naturally located on the surface and will also be sensitive to defects.

Scattering from defects within the graphene's lattice give rise to interference patterns on STM images like the ones in Figure 1.17A [55]. To explore the scattering vectors that define the patterns observed, it's useful to study the 2D constant-energy contours in reciprocal space using the Fourier transform of dI/dV maps. In the case of graphene, these constant-energy contours have circular shape with radius k as long as we are not too close to the Dirac point (as we get closer to the Dirac point these contours will get smaller until we get 6 dots) or we use energies where the Dirac cones start to warp and the linear dispersion of graphene disappears. On graphene, two kind of scattering processes are present: elastic electron scattering processes between the two non-equivalent Dirac cones at K_+ and K_- (intervalley scattering) together with elastic scattering processes between states located on the same Dirac cone (intravalley scattering) Figure 1.17D. These scattering processes appear as circles in the Fast Fourier Transform of our dI/dV maps. By measuring the radius of those circles at different energies, the energy dispersion of monolayer and bilayer graphene have been measured and the Fermi velocity extracted (Figure 1.17G).

As we commented in the introduction, due to the bipartite nature of graphene, a new degree of freedom absent in other conventional 2D metals emerges: the pseudospin. This quantity is crucial to understand many of the fundamental properties of graphene as the Anomalous Quantum Hall Effect or Klein paradox. It is defined by the phase relation between the two sublattice components of the wave function and has a great impact on the scattering processes of graphene quasiparticles.

Interestingly pseudospin was predicted to prevent backscattering processes in monolayer graphene from a theoretical point of view [56]. This prediction was proven by STM measurements on bilayer and monolayer graphene on SiC(0001) where intravalley scattering was only observed in the bilayer (Figure 1.18) [57, 58].

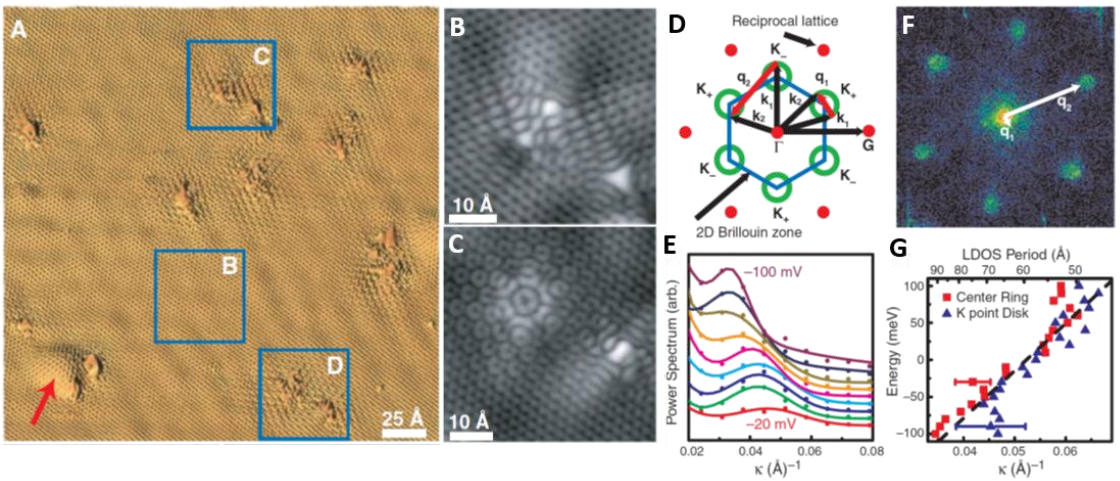

Figure 1.17: Scattering on graphene. A) STM topographic images of defects in the bilayer epitaxial graphene sample. B-C) Higher-magnification images from the boxed regions in (A) are shown: a complex scattering patterns around type defects [(C) and (D)]. D) Schematic of the 2D Brillouin zone (blue lines), constant energy contours (green rings) at the K± points, and the two kind of scattering vectors that create the interference patterns. F) Fast Fourier transform obtained from a dI/dV map. (E) Angular averages of the central ring q_1. G) Linear dispersion extracted from the ring's radius [55].

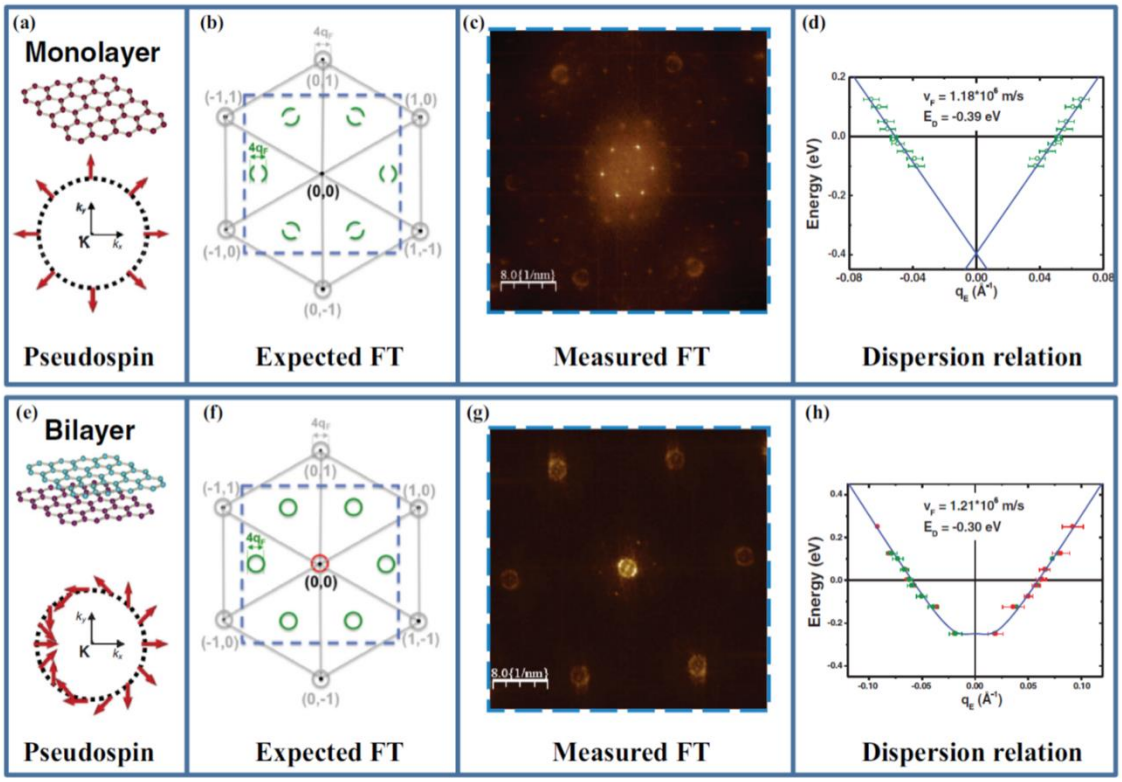

Figure 1.18: Pseudospin in monolayer and bilayer graphene. (a) Schematic pseudospin texture of ML. (b) Schematic FT LDOS map taking into account the Fermi surface topology and the pseudospin of ML. (c) FT LDOS map obtained from STM measurements on ML graphene on SiC(0001) at 5 K. (d) Dispersion relation derived from the STM data on ML. (e)–(h) same as (a)–(d) but for BL graphene. Note the correspondence between (f) and (g): the pseudospin has no significant impact for the BL, contrary to the ML case [58].

1.9 Landau levels on graphene.

The quantum Hall effect, the production of transverse conductivity when applying a magnetic field, has been observed in graphene. There are usually two main quantities measured when performing these conductance experiments: the Hall conductivity (σ_{xy}) and the longitudinal resistivity (ρ_{xx}). The Hall conductivity shows plateaus at values $\sigma_{xy} = \pm N\frac{e^2}{h}$ but in contrast to other 2D systems like silicon or gallium arsenide, the sequence of steps followed by graphene is $\sigma_{xy} = \pm 4(N + 1/2)\frac{e^2}{h}$ (see Figure 1.19). Because of this ½ shift in the sequence, there is no Hall plateau at N=0 and we talk about anomalous quantum Hall effect in graphene. For high enough magnetic fields fractional quantum Hall effect has also been measured in graphene. Related with the quantum Hall effect are the Landau levels.

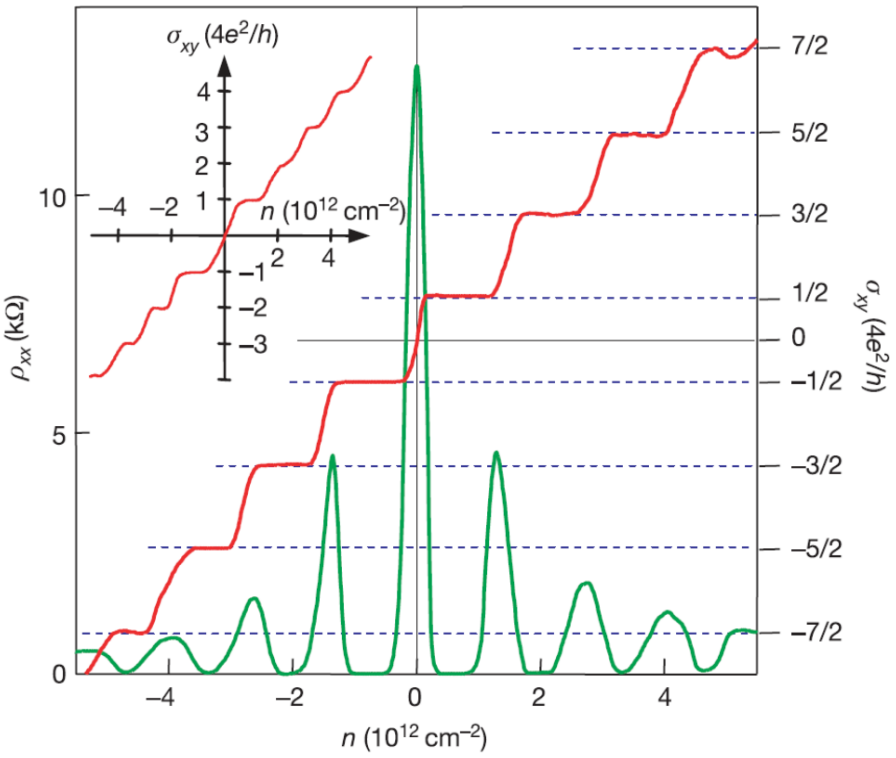

Figure 1.19: QHE for massless Dirac fermions. Hall conductivity σ_{xy} and longitudinal resistivity ρ_{xx} of graphene as a function of their concentration at B=14 T and T=4K. $\sigma_{xy} \equiv (4e^2/h)\nu$ is calculated from the measured dependences of $\rho_{xy}(V_g)$ and $\rho_{xx}(V_g)$ as $\sigma_{xy} = \rho_{xy}/(\rho_{xy}^2 + \rho_{xx}^2)$. Inset: σ_{xy} in 'two-layer graphene' where the quantization sequence is normal and occurs at integer n. The latter shows that the half-integer QHE is exclusive to 'ideal' graphene [30].

Due to the magnetic field applied, the electrons will move in circular orbits (cyclotron orbits). When treated using quantum mechanics, the result is that the energy of these orbits will be discretized. For parabolic energy bands where $E=E_{\pm}\pm\hbar^2k^2/2m^*$ the Landau levels when applying a perpendicular magnetic field follow the equation:

$$E_n = E_{\pm} \pm \hbar\omega_c(n + 1/2) \quad \text{(eq. 1.11)}$$

Where $\hbar$ is Planck's constant, n= 1,2,3…, $\omega_c = eB/m^*$ the cyclotron frequency and e the electron charge. In the special case of graphene, the energy bands are linear and the Landau level spectrum is different following the equation:

$$E_n = \pm\hbar\omega_G\sqrt{|n|},\ \omega_G = \frac{\sqrt{2}v_F}{l_B} \quad \text{(eq. 1.12)}$$

Here, n= … -2, -1, 0, +1, 0, +1, +2 … is the index of the Landau level, ω_G is the cyclotron energy for graphene and $l_B = \sqrt{\frac{\hbar}{eB}}$ is the magnetic length.

These Landau levels are no longer equally spaced, they don't depend linearly with the magnetic field and they contain a zero energy level (for n=0). Landau levels are highly degenerate, the degeneracy per unit area being equal to $4B/\phi_0$. Here B/ϕ_0 is the orbital degeneracy with $\phi_0 = h/e$ the flux quantum and $4 = g_s \cdot g_s$, where g_s and g_v ($g_s = g_v = 2$) are the spin and valley degeneracy, respectively.

Figure 1.20 shows a representation of the quantized Landau levels. The conical dispersion of graphene is transformed into a sequence of Landau levels in the presence of a magnetic field, corresponding to electron carriers above the Dirac point (DP) and holes below it. Represented on the left side we have the Landau levels in a 2DEG.

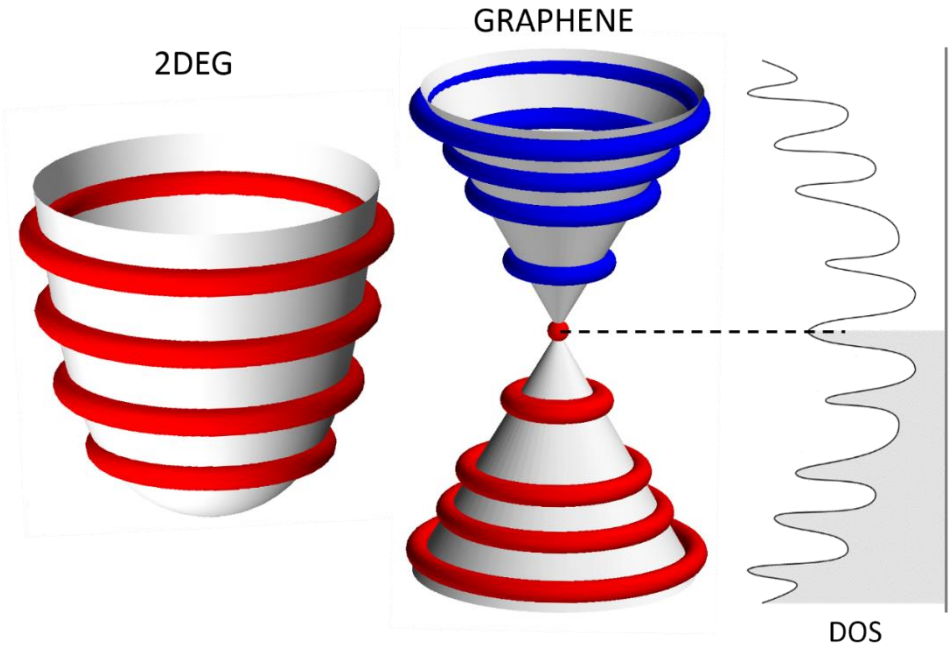

Figure 1.20: Illustration of quantized Landau levels. Right side: Dirac cone where the discrete Landau levels that appear under a magnetic field are depicted: red rings for electrons, blue rings for holes. Left side: Parabolic dispersion typical of 2DEG where the discrete Landau levels that appear under a magnetic field are depicted.

Landau levels can be observed using STS. They appear as peaks in the density of state of dI/dV curves. Previous to the measurement of the Landau levels in graphene, they had been measured in InAs or HOPG [59, 60].

Indeed, measurements of Landau levels on HOPG showed the coexistence of both massless and massive Dirac fermions on the surface [61]. In Figure 1.21a we can observe several dI/dV curves obtained at different magnetic fields and the appearance of different peaks associated with different Landau levels. If they are plot as a function of B or $B^{1/2}$ we can discern which ones are related with the massive particles or with the massless ones. From the fitting, the Fermi velocity can be extracted as well. This also allows to discern the degree of coupling of the topmost graphite layers with the underlying ones.

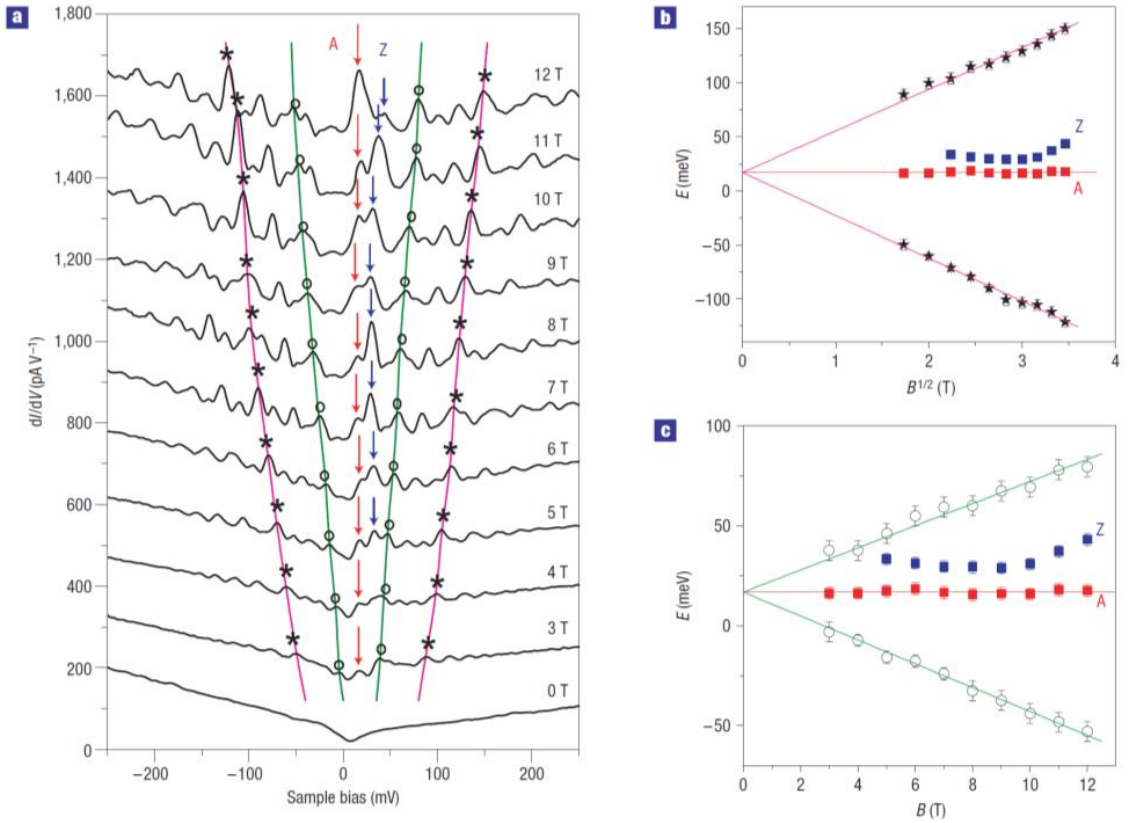

Figure 1.21: Tunnelling spectra on graphite. a) Magnetic-field dependence of tunnelling spectra on a graphite surface. All peaks, except the two labelled A and Z, show strong field dependence, shifting away from zero bias with increasing field. b) Landau levels marked with stars in a) show the square-root field dependence expected for massless carriers. c) Landau levels marked with circles in a) show linear field dependence as expected for massive carriers [61].

The previous data were obtained at 4K. If the same experiment is done at temperatures around 10mK the degeneracy of the Landau levels arise and the appearance of a quadruplet of the Landau levels can be observed [62].

Landau level spectra can also give information about many-body effects such as electron-phonon interactions which produce a normalization of the Fermi

velocity or electron-electron interactions which influences the lifetime of graphene’s quasiparticles.

1.10 Graphene on metals.

As we have seen, in order to access graphene's properties and due to its bidimensional nature, graphene needs to be placed or grown on top of another substrate. This substrate will interact with the graphene layer influencing its characteristics depending on the interplay between them. We already saw the e-h puddles on graphene on SiO_2 or boron nitride, but in this section we will focus on graphene grown on metallic substrates. The growth and understanding of the properties of graphene grown on metallic surfaces is important because of the interest on integrating graphene on future devices where metals play an important role. Growing graphene on different metals can lead to various changes as we move from weak to strong interacting substrates. For weak interacting substrates, the main observed effect is doping (both n- and p-type) while for strong interacting ones the apparition of gaps and the complete distortion of the π-bands together with the loss of the linear dispersion have been measured [49, 63-65]. Thanks to these interactions, the possibility to engineer graphene properties for our own interests is opened.

The growth of graphene on metals has been mostly centred in the thermal decomposition of hydrocarbons on the surface; being the chemical vapour deposition (CVD) the most used for this purpose. When growing graphene on metals, the metallic surface acts as a catalyser making the graphene growth to stop, in some cases, once the full monolayer has been achieved [66]. On single crystal metals, graphene has been grown epitaxially on the (111) face of Iridium, Platinum, Palladium, Rhodium, Nickel, Copper, Silver and Gold, the (0001) face of Ruthenium, Rhenium and Cobalt and the (110) face of Fe [50, 67-80].

All these graphene/metal systems have been measured by STM showing crystalline order and the appearance of moiré patterns due to the graphene/substrate lattice mismatch and graphene metal lattice relative orientation. In Figure 1.22 we have gathered STM images of all these systems. These STM images, show the perfect order of the hexagonal moiré over long distances, pointing to a coherent graphene layer over several terraces.

The existence of these moiré patterns in graphene/metal systems, has a geometric and an electronic origin. As we commented in section 1.6, depending on the graphene/metal interaction the corrugation of the graphene layer can vary from few picometers to 1 angstrom. The high quality and extension of these hexagonal moiré lattices has been used as a template to deposit metallic clusters of different materials. In that direction, cluster lattices of Ir, Rh, Pt, W and Re on graphene/Ir(111) and Pt on graphene/Ru(0001) have been reported [81-84]. The adsorption of clusters modifies the electronic properties of the graphene layer, leading to anisotropy in the Dirac cone, changes in the reactivity and changes in

the graphene/metal interaction. Moreover, these clusters exhibit high stability even at room temperature and higher.

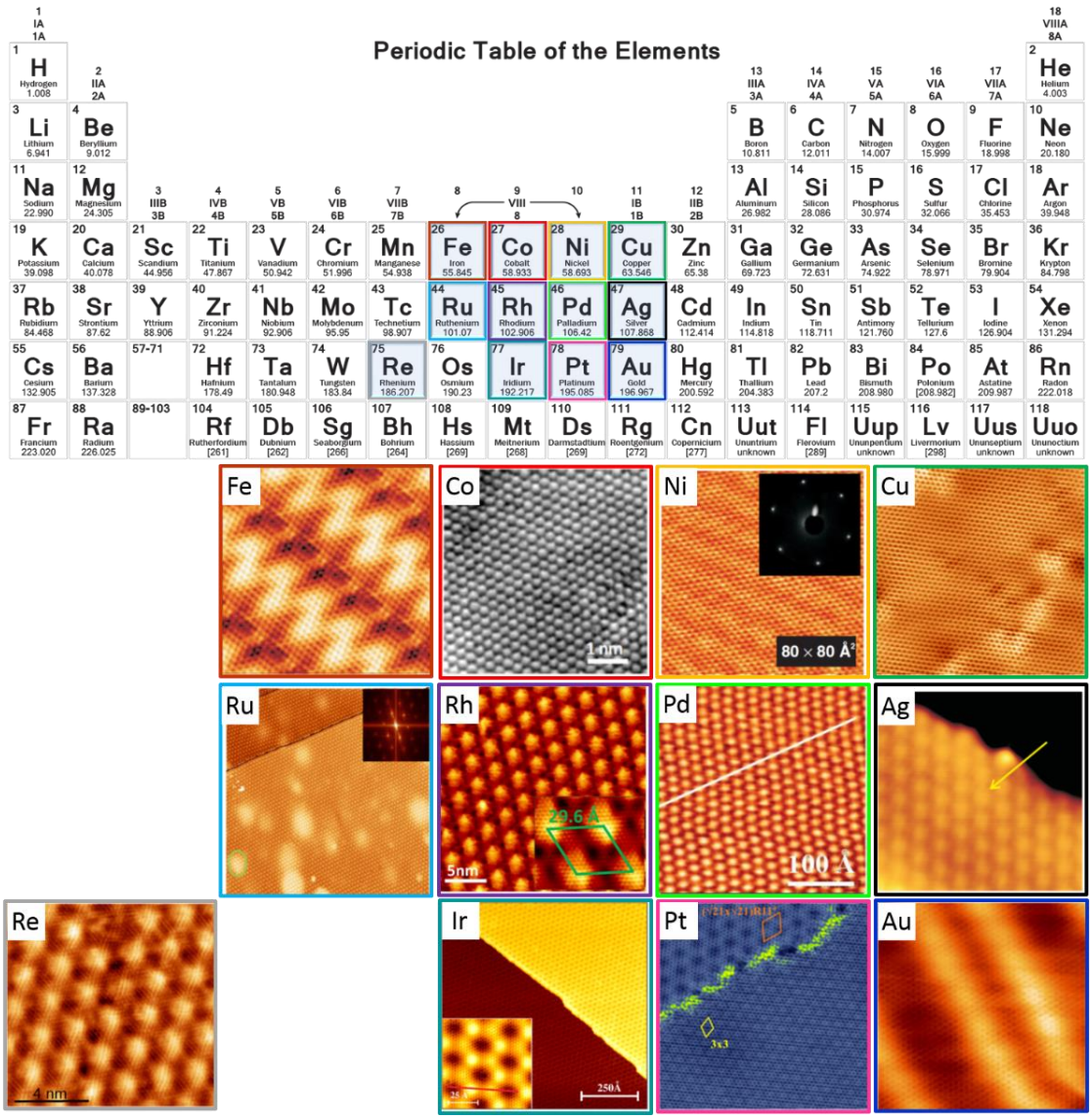

Figure 1.22: Graphene on metals. Upper part presents a periodic table where all the metals where graphene have been grown are highlighted. Lower part shows an STM image of all the graphene/metal systems. From top to bottom and from left to right, graphene grown on: Cobalt, Nickel, Copper, Ruthenium, Rhodium, Palladium, Silver, Rhenium, Iridium, Platinum and Gold [67-69, 71, 72, 74, 76-80].

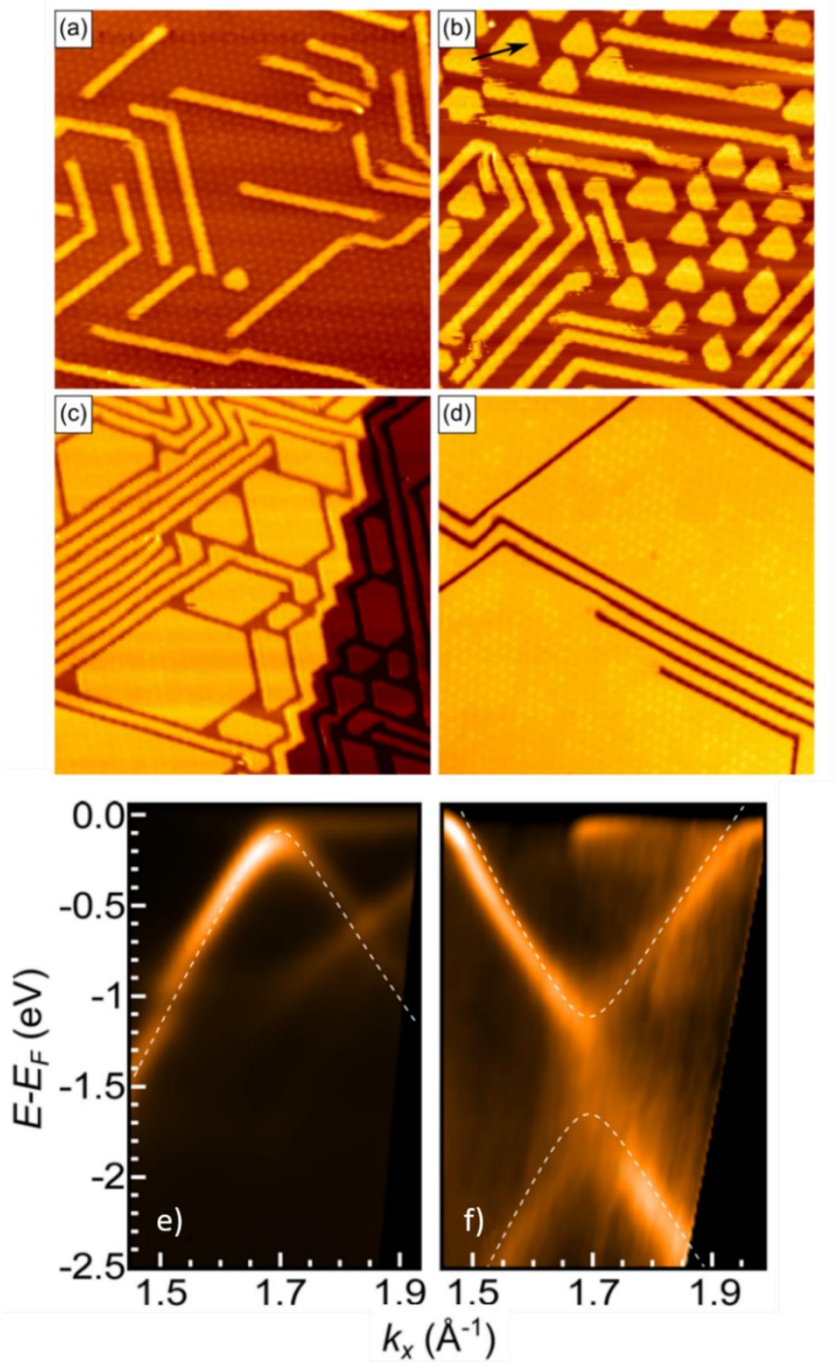

Figure 1.23: Europium intercalation measured with ARPES and STM. (a)–(d) STM topography images after intercalation of Eu resulting in successively larger intercalation coverage of (c) 18% ML, (d) 39% ML, (e) 72% ML, and (f) 89% ML. e-f) ARPES spectra taken in ΓKM direction for (a) Gr/Ir(111). (b) Gr/Ir(111) after exposure to 25% ML Eu at 720 K resulting in a complete Gr/Eu/Ir(111) layer [85, 86].

A different approach to change the interaction between graphene and the metallic substrate underneath which has been extensively studied in the late years has been the intercalation of different species underneath the graphene layer. Previous intercalation experiments on SiC(0001) showed the recovery of the linear bands of graphene with just a doping effect. In that sense, different elements have been used (oxygen, gold, lithium, germanium or fluor) proving the

possibility to get different doping levels [87-93]. Intercalation has been proven to work as well on graphene on metals. In the last years numerous works intercalating different elements, especially on Gr/Ir(111) and Gr/Ru(0001) have been published [94-97]. To get a deeper understanding of the mechanisms involved during intercalation, the capability of STM to image regions with atomic resolution comes very handy. For example in Figure 1.23, we can observe various images of Europium intercalated on Gr/Ir(111) together with some ARPES spectra [85, 86]. While ARPES averages on the sample, the STM images show the inhomogeneity of some terraces that would lead to different doping levels locally. STM measurements have also helped to understand the mechanism that leads some materials to intercalate. For example, elements like oxygen seem to need the partial coverage of the sample in order to penetrate underneath the graphene layer while for some others, full coverage doesn't prevent intercalation [95, 98].

1.11 Point defects on graphene

As we have seen along this chapter, the quality of our graphene layers can vary depending on the method used to obtain it. Intrinsic disorder and different defects are known to influence graphene's properties. For example it's known that carriers are affected by defects showing transport changes and also the mechanical properties of graphene are greatly influenced by the amount of defects [99, 100]. In addition, by inducing defects in a controlled way, some characteristics can be tuned in interesting ways. In this section we will focus on the effect of point defects on graphene's properties, concretely on vacancies, adatoms and substitutional species. The final result of all these modifications will depend on the graphene/substrate interaction. As we will see in chapter 4, STM can provide important information for the characterization and understanding of these interactions.

1.11.1 Carbon vacancies.

Carbon vacancies have been extensively studied both from a theoretical and experimental point of view. A carbon vacancy consists in the extraction of one carbon atom from the graphene lattice. The most common way to create carbon vacancies is the irradiation of the sample with low energy ions (Ar^+ or Ne^+ commonly). The main reason for this interest around the carbon vacancy comes from the theoretical prediction of the apparition of a magnetic moment induced by this defect [101, 102]. The first trace of such a magnetic moment was measured on irradiated HOPG samples with SQUID (superconducting quantum interferometer device) and magnetic force microscopy [103], but the first proof which could be indisputably attributed to a single C vacancy was only possible by STM/STS studies performed in our laboratory [104]. Later experiments using spin transport and SQUID have also confirmed the magnetic properties of vacancies [105-107]. In Figure 1.24a we can observe the topography image of four carbon vacancies on HOPG created by Ar^+ irradiation. When a spectra is taken on top of it (Figure 1.24c), the appearance of a localized state at the Fermi energy is revealed confirming the previous hypothesis. Carbon vacancies have also been induced in other graphene systems such as graphene/Pt(111). In this system, and due to the different interaction between the graphene layer and the substrate, the vacancies had a different shape, and no magnetic moment was expected [68].

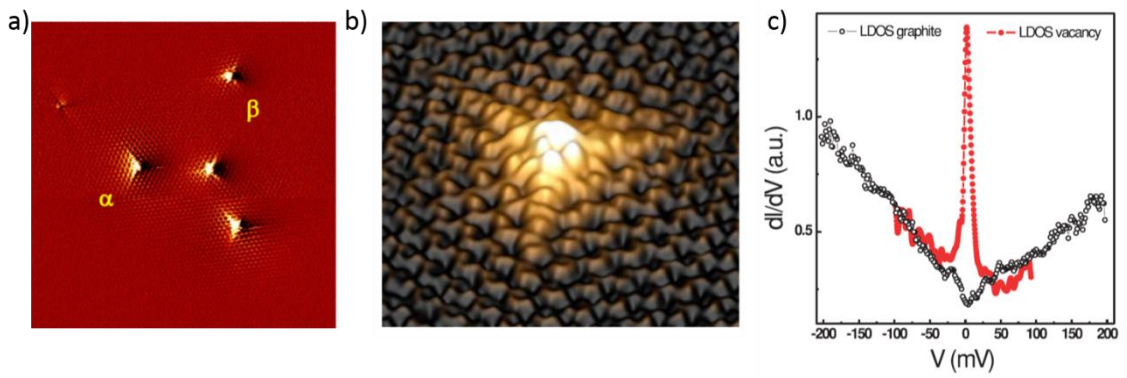

Figure 1.24: The carbon vacancy on graphene. a) STM image showing 4 carbon vacancies on HOPG b) 3D view of a single isolated vacancy. c) STS measurements of the LDOS on top of a single vacancy and on bare graphite. Black circles correspond to spectra measured on pristine graphite and red circles correspond to spectra on top of the single vacancy [104].

1.11.2 Adatoms.

In the previous section we saw how intercalated atoms affected the electronic properties of graphene. In a similar way, the deposition of foreign atoms on the other graphene face, i.e. on top of the graphene layer, also alter graphene's properties. For example, the electronic conductivity of graphene has been proven to decrease as potassium or transition metals such as titanium, iron and platinum are deposited on the surface [108, 109]. STM experiments on single adatoms on graphene have mostly focused on transition metals deposited on graphene grown on top of different substrates and the interaction of its magnetic moment with graphene [110-118]. While Ni atoms exhibit non-magnetic moments on graphene [112-114], Co atoms are still magnetic on graphene grown on the (111) face of Pt and Ir, and the (0001) face of Ru and SiC. However, its magnetic moment and anisotropy vary from one system to the other (see Figure 1.25) [112, 113, 117, 118]. In the case of Fe atoms, they are also magnetic, but in corrugated graphene like the one grown on Ru(0001), their adsorption site affects their properties [112, 115].

Another typical adatom which has been extensively studied on graphene and HOPG is hydrogen. However, since this manuscript has two chapters devoted to the study of the electronic properties and adsorption process of hydrogen atoms on graphene, we will not include it in this section.

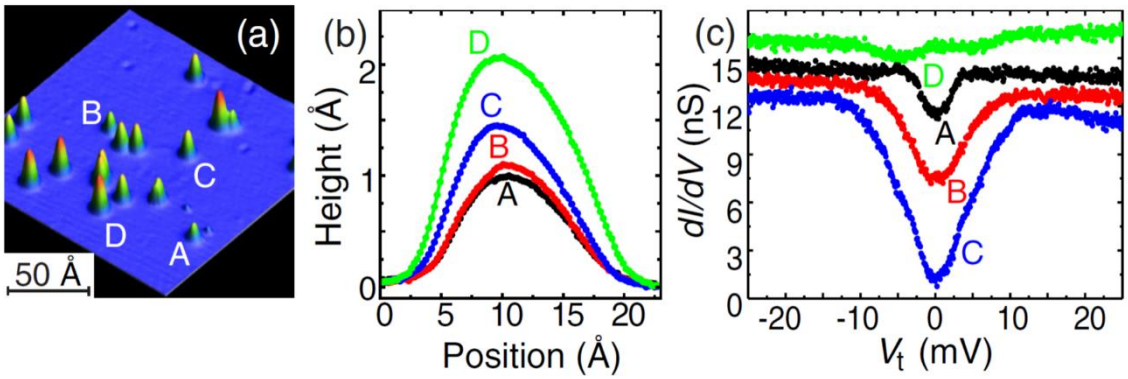

Figure 1.25: Co adatoms on Gr/Pt(111). (a),(b) Distinct apparent heights for clean Co (D), CoH (C), CoH2 (B), and CoH3 (A). (c) Characteristic inelastic conductance steps of the four species. While adatoms B and C show no Zeeman splitting, atoms the steps in the conductance for adatoms A and D show a clear Zeeman splitting proving their magnetic origin [118].

1.11.3 Substitutional species.

Another way to modify the electronic properties of graphene using point defects, is introducing atoms of other elements in the graphene lattice. Depending on the element, the possibility of introducing charge acceptors/donors in the graphene lattice has been studied. This has an enormous importance for electronics applications. Even more, some of these systems also exhibit an enhanced catalytic properties [119, 120].

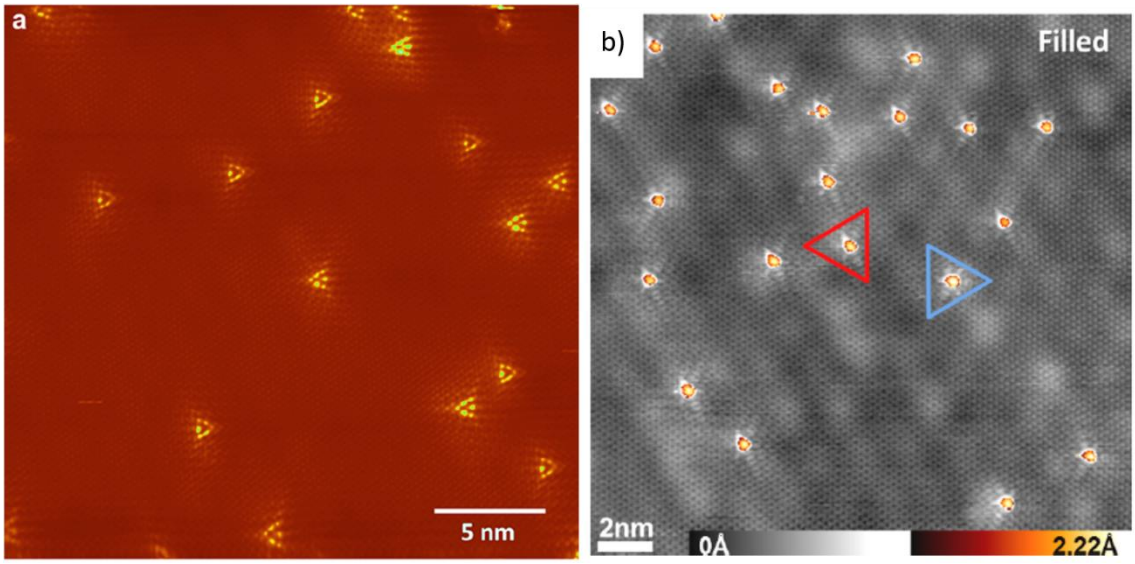

Figure 1.26: Nitrogen and Boron defects on graphene. a) STM image of a N-doped bilayer graphene on 6H-SiC(0001). b) STM image of a B-doped bilayer graphene on 6H-SiC(0001) [121, 122].

The two main species studied are Nitrogen and Boron, resulting on p- and n-doping respectively. There are different techniques for the implantation of substitutional species: CVD, plasma treatment and ion implantation. These methods result in different kind of defects which may have a different impact on the electronic properties. For example, the so called graphitic Nitrogen leads to

n-type doping while piridinic Nitrogen has the opposite effect. Therefore, the development of a reproducible technique which controls the type of defect created is really important and is still being studied [71, 121-125]. In Figure 1.26 we can observe different STM images of B and Ni substitutional atoms on graphene grown on SiC(0001).

1.12 Van Hove singularities and Fermi velocity renormalization on graphene.

At the beginning of my phD thesis, I worked on an alternative route for modifying graphene's band structure which is to exploit the rotation between two stacked graphene layers [126]. The consequence of rotating two identical periodic lattices with respect to each other is the apparition of a superlattice called moiré pattern. The relation between the length of the new supperlattice and the rotation angle between the graphene layers is:

$$L = \frac{a}{2\sin\frac{\theta}{2}} \quad \text{(eq. 1.13)}$$

Where L is the period of the moiré pattern, θ the rotation angle and a the lattice parameter of our mesh (a=2.46 Å for graphene). This moiré patterns can be considered as a superimposed periodic potential, which according to some studies, could lead to interesting changes in graphene's properties [127, 128].

In momentum space, the rotation of the corresponding Dirac cones will take place in a similar way (see Figure 1.27b). The distance separating the cones will be given by:

$$\Delta K = \frac{4\pi}{3a}\sin\frac{\theta}{2} \quad \text{(eq. 1.14)}$$

The crossing of the Dirac cones leads to a hybridization of the bands giving rise to the apparition of a saddle point called van Hove singularity.

According to calculations, for large angles ($\theta \geq 15°$) the low energy band structure of graphene should be preserved [129-131]. For intermediate angles ($1° \leq \theta \leq 15°$), it is predicted that while the linear dispersion persists in the vicinity of the Dirac points of both layers, the band velocity is depressed and the van Hove singularities appear (vHs) in the density of states (DOS) [126, 132-137] . For smaller angles ($\leq 1°$) weakly dispersive bands appear at low energy [138, 139] with sharp DOS peaks very close to the Dirac point [135, 137].

For intermediate angles ($1° \leq \theta \leq 15°$) , the van Hove singularities appear in the STM spectra as two peaks (see Figure 1.27b) where their separation in energy follows the expression [135, 140]:

$$\Delta E_{vHs} = 2\hbar v_F \Gamma K \sin(\theta/2) - 2t_\theta \quad \text{(eq. 1.15)}$$

being v_F the Fermi velocity for monolayer graphene, $\Gamma K = 1.703\ \text{Å}^{-1}$ the wave vector of the Dirac point in monolayer graphene, and t_θ the modulus of the amplitude of the main Fourier components of the interlayer potential.

The first experimental evidence of van Hove singularities were reported by G. Li et al. [132] when they measured three different moiré patterns demonstrating the dependence of the singularities with the angle. At the beginning of my phD thesis, those were the only STM experiments concerning the existence of VHs on graphene rotated layer. Thus, we decided to measure van Hove singularities in multilayer graphene samples grown on SiC(000-1), in collaboration with a French group from the CNRS in Grenoble . These samples presented a wide variety of rotational angles, allowing us to measure van Hove singularities for angles ranging from 1.4° to 9.6° (the first measurements were 1.16°,1.79° and 3.5° [132]). In Figure 1.27d, we show 5 spectra obtained in 4 different moirés of our SiC(000-1) sample, where the dependence of the van Hove singularity energy separation with the angle can be appreciated. In Figure 1.27e we show all the experimental data we gathered together. From our linear fitting and equation 1.15, a value of 1.12×10^6 m/s for the Fermi velocity was extracted together with a value of 0.108 eV for the interlayer potential t_θ .

Our results conclusively demonstrated the existence of vHs for rotational angles between 1° and 10° and from our STS data, the Fermi velocity and the effective interlayer coupling parameter could be determined. Finally, we proved the robustness of these vHs against perturbations in the interlayer distance or the stacking of the underlying layers [141].

The Fermi velocity of graphene was predicted to decrease for small angles ($\theta \leq 15°$). The slope of the Dirac cone is influenced by the van Hove singularity leading to a renormalized Fermi velocity following the equation [126]:

$$\frac{v_F(\theta)}{v_F^0} = 1 - 9\left(\frac{t_\perp^\theta}{\hbar v_F^0 \Delta K}\right)^2 \qquad \text{(eq. 1.16)}$$

Where v_F^0 is the bare velocity, $v_F(\theta)$ is the renormalized value at a given angle θ; the interlayer coupling is $t_\perp^\theta \approx 0.4\, t_\perp$ and $t_\perp$ is the interlayer coupling in the Bernal stacked bilayer.

This renormalization has been measured in twisted bilayer samples using the change in energy of the Landau levels to extract the Fermi velocity of regions with different moiré patterns (see Figure 1.28 c) [142]. In Figure 1.28 we can observe the STS under magnetic field with the Landau levels of two regions, one with a 4.0 nm moiré and the other region with no moiré. At zero magnetic field the moiré region exhibits a van Hove singularity while the other shows a normal V shape spectrum.

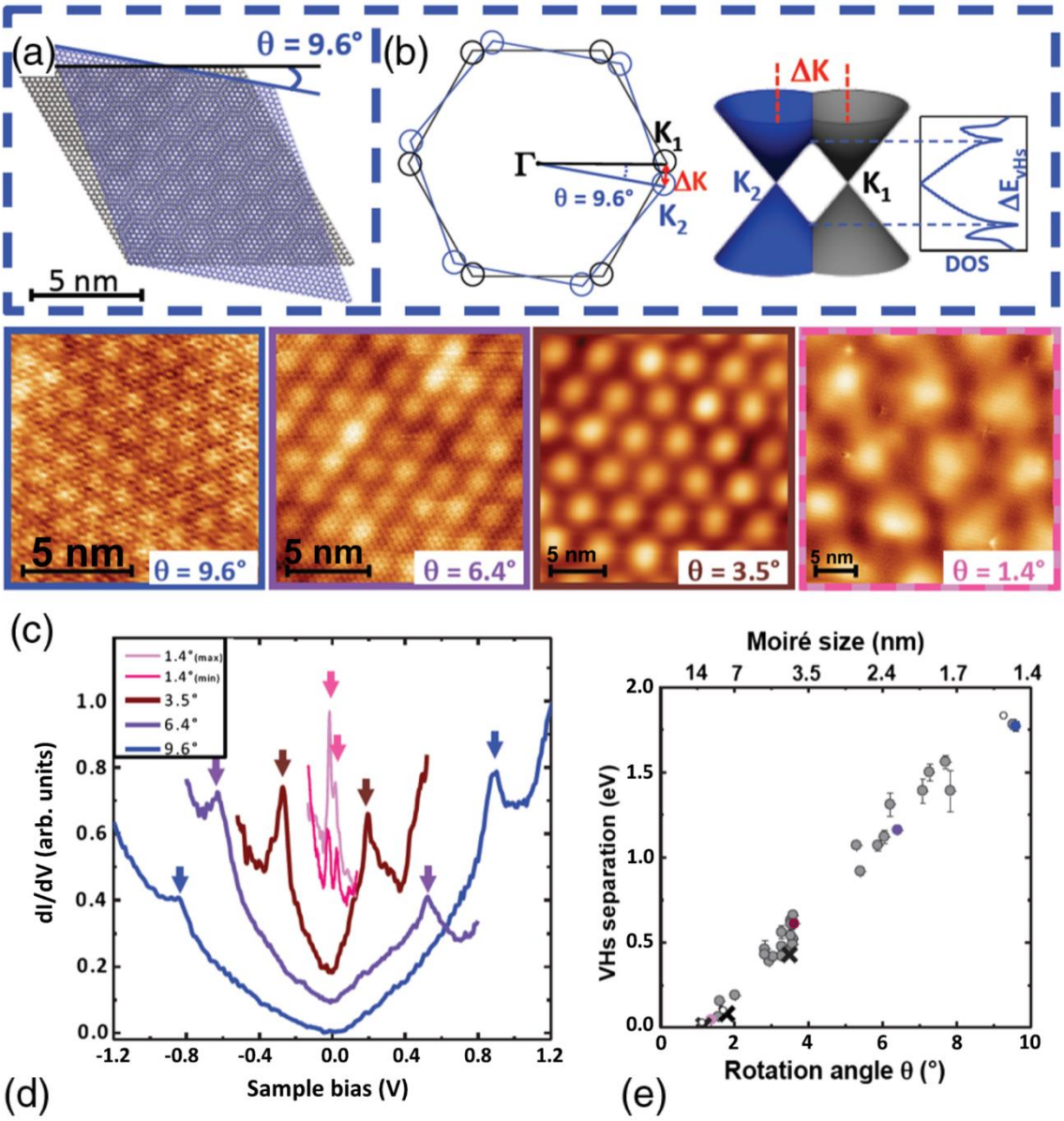

Figure 1.27: van Hove singularities on twisted bilayer graphene. (a) Illustration of a moiré pattern (MP) arising from a rotation angle $\theta = 9.6°$. (b) Emergence of vHs as a consequence of the rotation in reciprocal space. (c) STM images of several MP with differentθ. The scale bar is 5.0 nm. (d) LDOS spectra taken on the MP shown in (c). The curves are shifted vertically for clarity. The arrows point to the vHs. For $\theta = 1.4°$, max (min) indicates a spectrum taken on a bright (dark) area. (e) vHs separation as a function of θ. Colored dots refer to the spectra displayed in (c) [141].

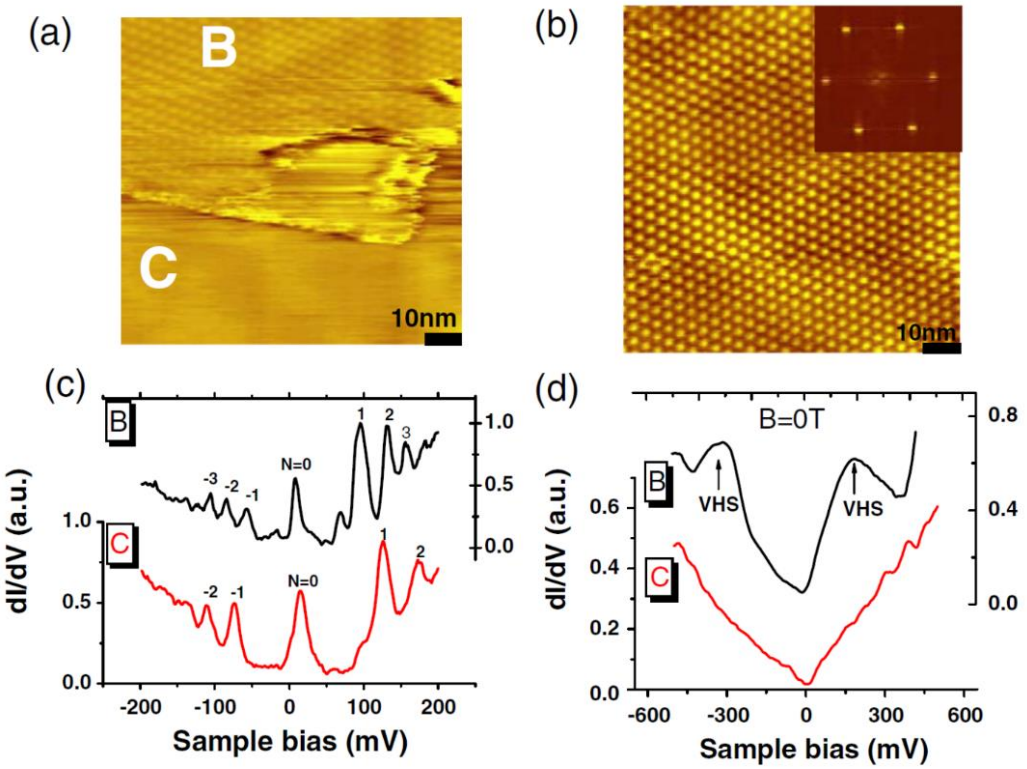

Figure 1.28: Fermi velocity renormalization. a) Large area topography showing two regions, one with a moiré pattern (B) and region C, which is featureless. b) Topography in the center of the area with moiré pattern with period 4 nm. Inset: Fourier transform of the main panel (c) High field (6 T) tunneling spectra taken at B and C in a). d) Zero field tunneling spectra taken at B and C in (a) [142].

1.13 STM lithography on graphene.

So far we have just discussed about the ability of STM to get topographic information and measure the electronic properties of our sample thanks to the relationship between the tunnelling current and the local density of states. But thanks to its extraordinary spatial resolution and under the right circumstances, the possibility to manipulate atoms and perform controlled lithography can be achieved using the STM tip.

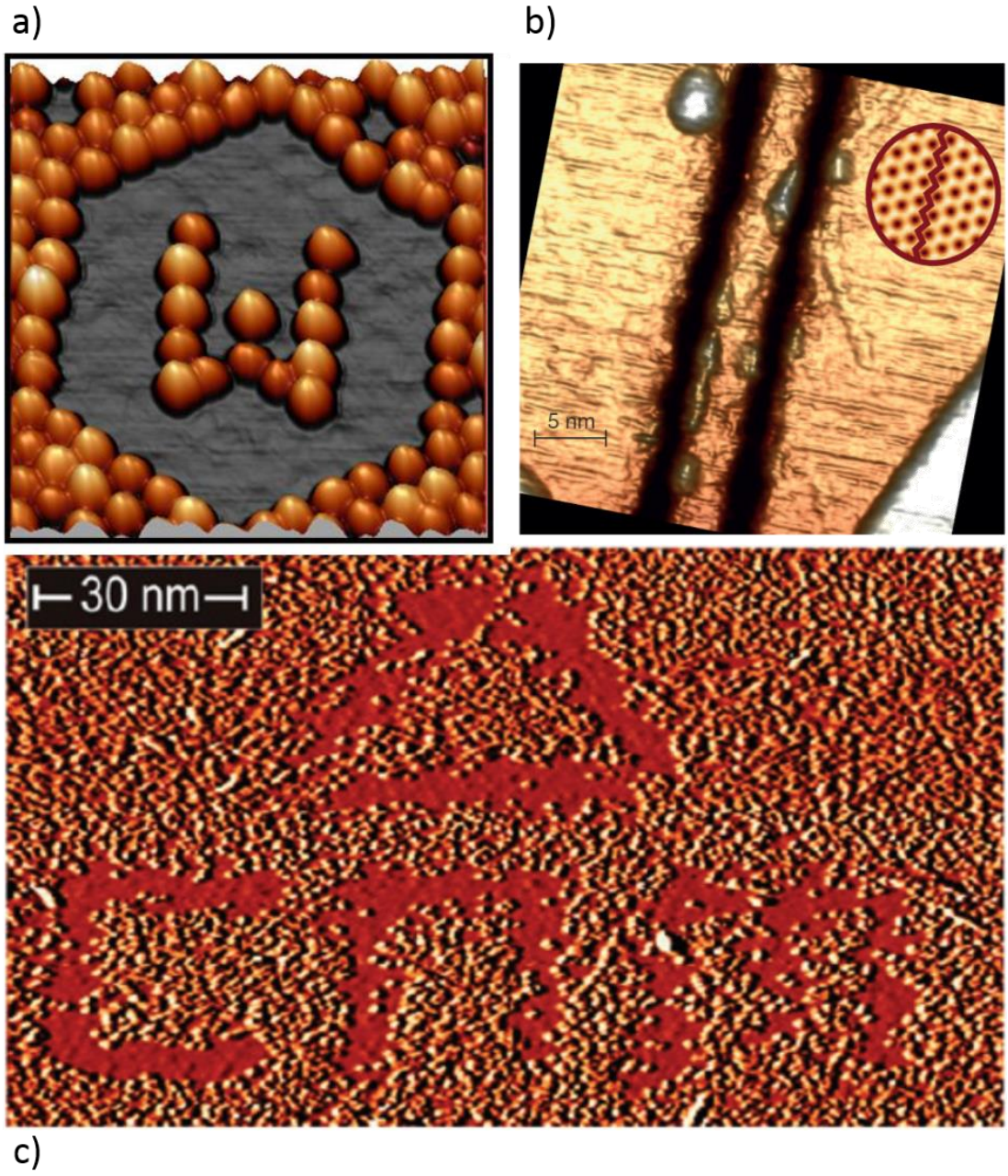

Figure 1.29: STM lithography on graphene. a) STM image where a W has been drawn using Tungsten clusters on graphene grown on Ir (111) [143]. b) STM image of a 6.5-nm-wide nanoribbon with zigzag edges created using STM lithography [144]. c) Lithography made using voltage pulses on hydrogenated graphene [145].

Although we have some extraordinary examples of manipulation experiments by STM in other materials [146], the number of works on STM manipulation on graphene samples is surprisingly scarce. As we saw in section 1.10 the deposition of metallic clusters using the moiré pattern can lead to changes in the electronic properties of our graphene layer [147]. Also the deposition of hydrogen atoms on SiC or graphene/Ir(111) has shown the apparition of a gap in the band structure [148]. However, we can go one step further and by selectively removing some of those metallic clusters (or hydrogen atoms) using our STM tip, create covered or uncovered regions making plausible the design of devices [73]. This has been proven by creating different arrangements of Ir or W clusters on graphene/Ir(111) or by removing hydrogen atoms and observing the recovery of graphene's dI/dV signature as hydrogen was desorbed (Figure 1.29 a and c) [143, 145].

In those previous examples, the authors were able to remove something that they previously deposited on the graphene surface deliberately. Still, the authors from reference [149], were able to perform graphene lithography, creating different shapes and arrangements by "cutting" the graphene layer using the STM tip, showing the possibility to create carbon nanoribbons of different shapes and sizes at will (see Figure 1.29b).

1.14 Two summarizing examples.

I would like to conclude this chapter by briefly describing two experiments that I personally find particularly interesting since they combine most of the STM abilities that we have discussed so far together with the particular physics of graphene. The first one is the atomic collapse in artificial nuclei on graphene, where the relativistic behaviour of the charge carriers in graphene is used to prove a prediction from nuclear physics. The second one is the creation of artificial molecular graphene-like lattices in order to demonstrate how many of the properties found in graphene are a consequence of its honeycomb structure and can be extended to artificial honeycomb lattices.

1.14.1 Atomic collapse in artificial nuclei on graphene

According to relativistic quantum-mechanics, the stability of the positive charge of a nuclei and the negative charge of its surrounding electrons breaks down above a threshold charge of the nucleus of 170 protons. At this point, atomic collapse occurs and the electrons fall into the nucleus. This phenomenon, first predicted in the 1930s had never been observed experimentally due to the large atomic number necessary. However, due to the relativistic nature of charge carriers on graphene, it has been predicted that charged impurities could show resonances corresponding to this atomic collapse [150-152]. For this system, the critical charge threshold is considerably lower than for atomic nuclei of atoms.

The first experimental proof of atomic collapse on graphene was observed using transferred CVD grown graphene onto a boron nitride flake on top of a SiO_2 surface. To create the charged impurities, Ca dimers were used as building blocks [153]. As Ca dimers were gathered together using the STM tip to create artificial nuclei, dI/dV spectra were obtained. As can be seen in Figure 1.30 A-E there is an apparition of a resonance-like structure for clusters formed by 3 or more Ca dimers. Dependence of the resonance state with the doping level showed that for decreasing p-doping the resonance energy shifted downwards while for n doping the resonance peak intensity decreased and essentially disappeared (Figure 1.30F).

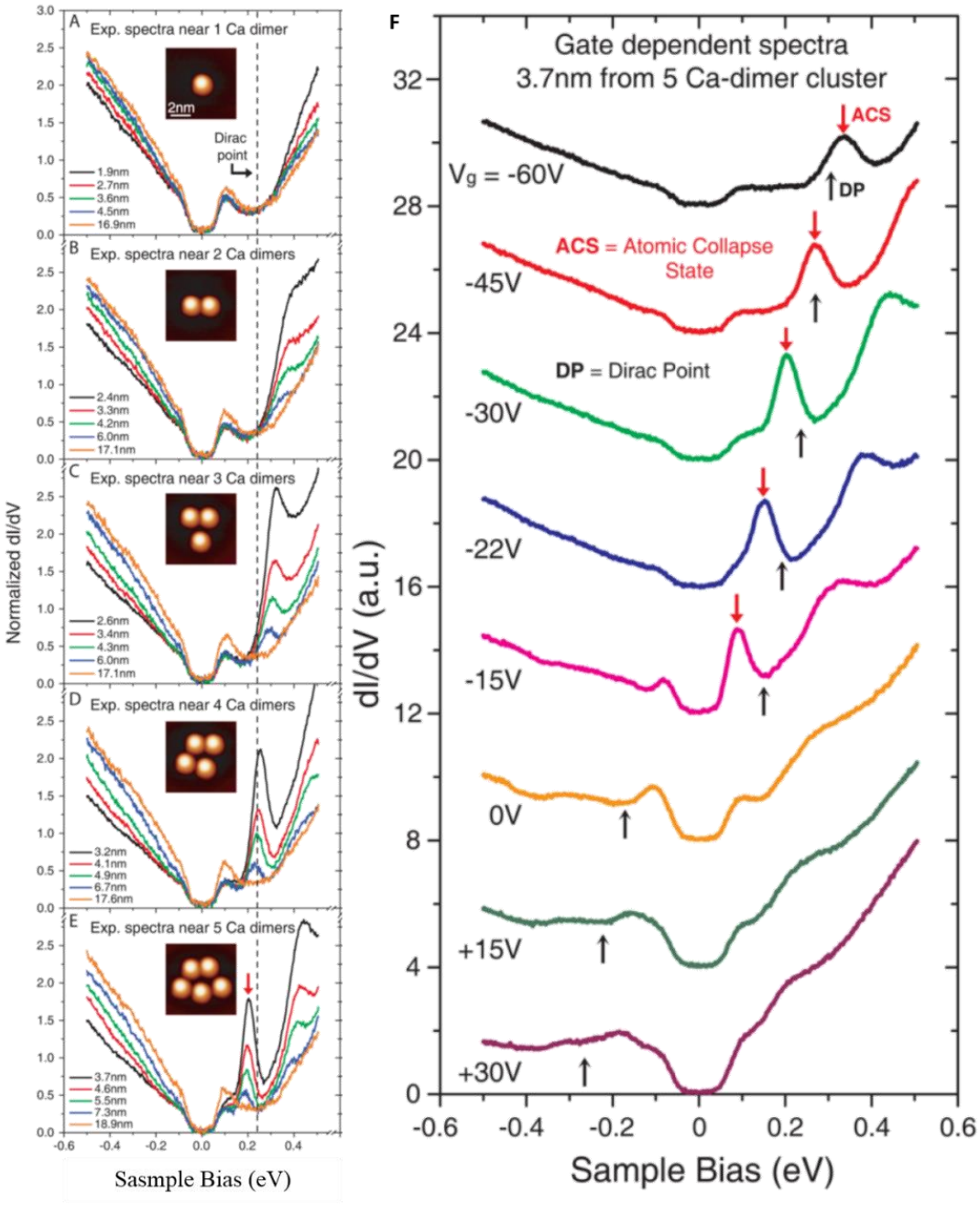

Figure 1.30: Atomic collapse on graphene. A-E: Evolution of dI/dV spectra measured at different distances from the center of Ca-dimer clusters (i.e., artificial nuclei) composed of 1-5 dimers. (Insets) STM topographs of atomically fabricated Ca-dimer clusters. F: Dependence of atomic collapse state on doping. Gate dependent spectra acquired at a lateral distance of 3.7 nm from the center of a five-dimer Ca cluster. The atomic collapse state intensity is quenched in the n-doped regime [153].

Atomic collapse has also been recently observed on carbon vacancies created on two graphene layers deposited on a SiO_2 substrate where boron nitride thin flakes were exfoliated onto [154]. The removal of a carbon atom and its relaxation, induce a positively charged vacancy. By applying bias pulses, the authors were able to build up enough charge on the vacancy, observing the appearance of the atomic collapse signature in the dI/dV curves.

1.14.2 Artificial graphene lattices.

Most of the amazing properties of graphene arise from its honeycomb atomic lattice together with its bidimensionality. While the two-site tight-binding model captures the natural physics of graphene, this description is more general and can thus be used to describe any group of atoms presenting a honeycomb atomic arrangement.

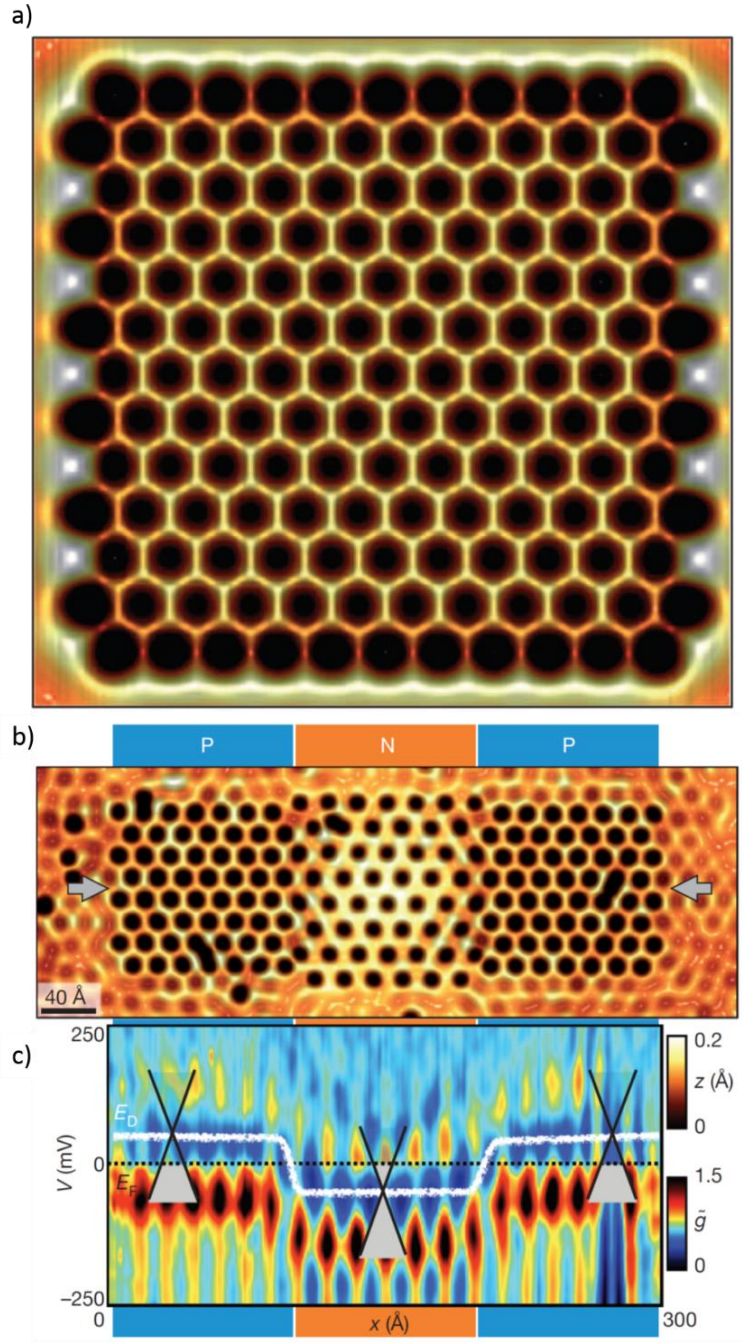

Figure 1.31: Artificial honeycomb lattices. a) Topograph of a molecular graphene lattice composed of 149 CO molecules. b) Topograph of a p–n–p lattice made of CO molecules. c) Intensity colour plot of the conductance spectra, where x denotes the distance along the centre line. The white line is the locus of the Dirac point in the conductance spectra. The dashed line marks the Fermi energy (EF) [155].

This was the idea that lead the authors of ref [155, 156] to create a hexagonal lattice of CO molecules on top of a Cu(111) crystal. By manipulating ~ 100-1000 CO molecules, they created “molecular graphene” of different sizes. In Figure 1.31a we can observe an example of molecular graphene. The high reproducibility and control of CO manipulation, allowed the authors to create graphene-like regions where the lattice parameter was modified. This changes in the lattice parameter lead to different values of the Dirac point energy permitting the creation of p-n junctions at desire (see Figure 1.31 b-c).

Thanks to the precision that STM provides for atomic manipulation, the authors were also able to generate and study different kind of defects, strained graphene and new arrangements that remained as a purely theoretical abstraction for standard graphene.

References.

1. Binnig, G., et al., *Tunneling through a controllable vacuum gap.* Applied Physics Letters, 1982. **40**.
2. Binnig, G., et al., *7 × 7 Reconstruction on Si(111) Resolved in Real Space.* Physical Review Letters, 1983. **50**: p. 120.
3. Chen, C.J., *Introduction to Scanning Tunneling Microscopy.* Oxford, 2008. **2nd Edition**.
4. Stroscio, J.A. and W.J. Kaiser, *Scanning Tunneling Microscopy*. 1993, San Diego: Academic Press.
5. Bonnell, D.A., Ed., *Scanning Probe Microscopy and Spectroscopy. Theory, Techniques, and Applications, 2nd ed.* 2001: Wiley-VCH.
6. Wiesendanger, R., *Scanning Probe Microscopy and Spectroscopy: Methods and Applications*. 1994, Cambridge: Cambridge University Press.
7. Tersoff, J. and D.R. Hamann, *Theory and Application for the Scanning Tunneling Microscope.* Physical Review Letters, 1983. **50**(25): p. 1998-2001.
8. Tersoff, J. and D.R. Hamann, *Theory of the Scanning Tunneling Microscope.* Physical Review B, 1985. **31**(2): p. 805-813.
9. Selloni, A., et al., *Voltage-Dependent Scanning-Tunneling Microscopy of a Crystal-Surface - Graphite.* Physical Review B, 1985. **31**(4): p. 2602-2605.
10. Lang, N.D., *Spectroscopy of Single Atoms in the Scanning Tunneling Microscope.* Physical Review B, 1986. **34**(8): p. 5947-5950.
11. Reinert, F., et al., *Direct measurements of the L-gap surface states on the (111) face of noble metals by photoelectron spectroscopy.* Physical Review B, 2001. **63**(11): p. 115415.
12. Ugeda, M.M. 2011, Universidad Autónoma de Madrid: Madrid. p. Doctoral Thesis.
13. Custance, O., *Estudio de procesos dinámicos a nivel atómico en los sistemas Pb/Si(111) y Sn/Si(111) mediante microscopía de efecto túnel de temperatura variable*. 2002, Universidad Autónoma de Madrid: MADRID.
14. Besocke, K., *An easily operable scanning tunneling microscope.* Surface Science, 1987. **181**(1-2): p. 145-153.
15. Novoselov, K.S., et al., *Electric field effect in atomically thin carbon films.* Science, 2004. **306**(5696): p. 666-669.
16. Peierls, R.E., *Quelques propriétés typiques des corps solides.* Ann. I. H. Poincare, 1935. **5**.
17. Landau, L.D., *Zur Theorie der Phasenumwandlungen II.* Phys. Z. Sowjetunion, 1937. **11**.
18. Mermin, N.D., *Crystalline order in two dimensions.* Physical Review, 1968. **176**.
19. Meyer, J.C., et al., *The structure of suspended graphene sheets.* Nature, 2007. **446**(7131): p. 60-63.
20. Bolotin, K.I., et al., *Ultrahigh electron mobility in suspended graphene.* Solid State Communications, 2008. **146**(9-10): p. 351-355.
21. Bolotin, K.I., et al., *Temperature-dependent transport in suspended graphene.* Physical Review Letters, 2008. **101**(9).
22. Balandin, A.A., *Thermal properties of graphene and nanostructured carbon materials.* Nature Materials, 2011. **10**(8): p. 569-581.
23. Mayorov, A.S., et al., *Micrometer-Scale Ballistic Transport in Encapsulated Graphene at Room Temperature.* Nano Letters, 2011. **11**(6): p. 2396-2399.
24. Lee, C., et al., *Measurement of the elastic properties and intrinsic strength of monolayer graphene.* Science, 2008. **321**(5887): p. 385-388.
25. Poot, M. and H.S.J. van der Zant, *Nanomechanical properties of few-layer graphene membranes.* Applied Physics Letters, 2008. **92**(6).
26. Gomez-Navarro, C., M. Burghard, and K. Kern, *Elastic properties of chemically derived single graphene sheets.* Nano Letters, 2008. **8**(7): p. 2045-2049.

27. Mak, K.F., et al., *Measurement of the Optical Conductivity of Graphene.* Physical Review Letters, 2008. **101**(19).
28. Nair, R.R., et al., *Fine structure constant defines visual transparency of graphene.* Science, 2008. **320**(5881): p. 1308-1308.
29. Zhang, Y.B., et al., *Experimental observation of the quantum Hall effect and Berry's phase in graphene.* Nature, 2005. **438**(7065): p. 201-204.
30. Novoselov, K.S., et al., *Two-dimensional gas of massless Dirac fermions in graphene.* Nature, 2005. **438**(7065): p. 197-200.
31. Novoselov, K.S., et al., *Room-temperature quantum hall effect in graphene.* Science, 2007. **315**(5817): p. 1379-1379.
32. Novoselov, K.S., et al., *Unconventional quantum Hall effect and Berry's phase of 2 pi in bilayer graphene.* Nature Physics, 2006. **2**(3): p. 177-180.
33. Castro Neto, A.H., et al., *The electronic properties of graphene.* Reviews of Modern Physics, 2009. **81**(1): p. 109-162.
34. Wallace, P.R., *The Band Theory of Graphite.* Physical Review, 1947. **71**.
35. Stolyarova, E., et al., *High-resolution scanning tunneling microscopy imaging of mesoscopic graphene sheets on an insulating surface.* Proceedings of the National Academy of Sciences of the United States of America, 2007. **104**(22): p. 9209-9212.
36. Mallet, P., et al., *Electron states of mono- and bilayer graphene on SiC probed by scanning-tunneling microscopy.* Physical Review B, 2007. **76**(4).
37. Ondráček, M., et al., *Forces and Currents in Carbon Nanostructures: Are We Imaging Atoms?* Physical Review Letters, 2011. **106**(17): p. 176101.
38. Geringer, V., et al., *Intrinsic and extrinsic corrugation of monolayer graphene deposited on SiO2.* Physical Review Letters, 2009. **102**(7).
39. Martin, J., et al., *Observation of electron-hole puddles in graphene using a scanning single-electron transistor.* Nature Physics, 2008. **4**(2): p. 144-148.
40. Zhang, Y.B., et al., *Origin of spatial charge inhomogeneity in graphene.* Nature Physics, 2009. **5**(10): p. 722-726.
41. Deshpande, A., et al., *Spatial Mapping of the Dirac Point in Monolayer and Bilayer Graphene.* Ieee Transactions on Nanotechnology, 2011. **10**(1): p. 88-91.
42. Deshpande, A., et al., *Mapping the Dirac point in gated bilayer graphene.* Applied Physics Letters, 2009. **95**(24).
43. Decker, R., et al., *Local Electronic Properties of Graphene on a BN Substrate via Scanning Tunneling Microscopy.* Nano Letters, 2011. **11**(6): p. 2291-2295.
44. Xue, J.M., et al., *Scanning tunnelling microscopy and spectroscopy of ultra-flat graphene on hexagonal boron nitride.* Nature Materials, 2011. **10**(4): p. 282-285.
45. Berger, C., et al., *Ultrathin epitaxial graphite: 2D electron gas properties and a route toward graphene-based nanoelectronics.* Journal of Physical Chemistry B, 2004. **108**(52): p. 19912-19916.
46. Forbeaux, I., J.M. Themlin, and J.M. Debever, *Heteroepitaxial graphite on 6H-SiC(0001): Interface formation through conduction-band electronic structure.* Physical Review B, 1998. **58**(24): p. 16396-16406.
47. Marchini, S., S. Gunther, and J. Wintterlin, *Scanning tunneling microscopy of graphene on Ru(0001).* Physical Review B, 2007. **76**(7).
48. N'Diaye, A.T., et al., *Two-dimensional Ir cluster lattice on a graphene moire on Ir(111).* Physical Review Letters, 2006. **97**(21): p. 215501.
49. Sutter, P., J.T. Sadowski, and E. Sutter, *Graphene on Pt(111): Growth and substrate interaction.* Physical Review B, 2009. **80**(24).
50. Martinez-Galera, A.J., I. Brihuega, and J.M. Gomez-Rodriguez, *Ethylene Irradiation: A New Route to Grow Graphene on Low Reactivity Metals.* Nano Letters, 2011. **11**(9): p. 3576-3580.

51. Batzill, M., *The surface science of graphene: Metal interfaces, CVD synthesis, nanoribbons, chemical modifications, and defects.* Surface Science Reports, 2012. **67**(3-4): p. 83-115.
52. de la Torre, B., et al., *Atomic-Scale Variations of the Mechanical Response of 2D Materials Detected by Noncontact Atomic Force Microscopy.* Physical Review Letters, 2016. **116**(24): p. 245502.
53. Crommie, M.F., C.P. Lutz, and D.M. Eigler, *Confinement of Electrons to Quantum Corrals on a Metal-Surface.* Science, 1993. **262**(5131): p. 218-220.
54. Crommie, M.F., C.P. Lutz, and D.M. Eigler, *Imaging Standing Waves in a 2-Dimensional Electron-Gas.* Nature, 1993. **363**(6429): p. 524-527.
55. Rutter, G.M., et al., *Scattering and interference in epitaxial graphene.* Science, 2007. **317**(5835): p. 219-222.
56. Ando, T. and T. Nakanishi, *Impurity scattering in carbon nanotubes - Absence of back scattering.* Journal of the Physical Society of Japan, 1998. **67**(5): p. 1704-1713.
57. Brihuega, I., et al., *Quasiparticle Chirality in Epitaxial Graphene Probed at the Nanometer Scale.* Physical Review Letters, 2008. **101**(20): p. 4.
58. Mallet, P., et al., *Role of pseudospin in quasiparticle interferences in epitaxial graphene probed by high-resolution scanning tunneling microscopy.* Physical Review B, 2012. **86**(4): p. 14.
59. Wildoer, J.W.G., C. Harmans, and H. vanKempen, *Observation of Landau levels at the InAs(110) surface by scanning tunneling spectroscopy.* Physical Review B, 1997. **55**(24): p. 16013-16016.
60. Matsui, T., et al., *STS observations of landau levels at graphite surfaces.* Physical Review Letters, 2005. **94**(22).
61. Li, G. and E.Y. Andrei, *Observation of Landau levels of Dirac fermions in graphite.* Nature Physics, 2007. **3**(9): p. 623-627.
62. Song, Y.J., et al., *High-resolution tunnelling spectroscopy of a graphene quartet.* Nature, 2010. **467**(7312): p. 185-189.
63. Preobrajenski, A.B., et al., *Controlling graphene corrugation on lattice-mismatched substrates.* Physical Review B, 2008. **78**(7).
64. Sutter, P., et al., *Electronic Structure of Few-Layer Epitaxial Graphene on Ru(0001).* Nano Letters, 2009. **9**(7): p. 2654-2660.
65. Pletikosic, I., et al., *Dirac Cones and Minigaps for Graphene on Ir(111).* Physical Review Letters, 2009. **102**(5): p. 056808.
66. Wintterlin, J. and M.L. Bocquet, *Graphene on metal surfaces.* Surface Science, 2009. **603**(10-12): p. 1841-1852.
67. N'Diaye, A.T., et al., *Structure of epitaxial graphene on Ir(111).* New Journal of Physics, 2008. **10**.
68. Ugeda, M.M., et al., *Point Defects on Graphene on Metals.* Physical Review Letters, 2011. **107**(11).
69. Kwon, S.Y., et al., *Growth of Semiconducting Graphene on Palladium.* Nano Letters, 2009. **9**(12): p. 3985-3990.
70. Martin-Recio, A., et al., *Tug-of-war between corrugation and binding energy: revealing the formation of multiple moire patterns on a strongly interacting graphene-metal system.* Nanoscale, 2015. **7**(26): p. 11300-11309.
71. Martín-Recio, A., *Estudio del crecimiento, difusión, intercalación y dopaje en grafeno/Rh(111) mediante STM en condiciones de UHV.* Universidad Autónoma de Madrid, July 2016.
72. Dedkov, Y.S., et al., *Rashba effect in the graphene/Ni(111) system.* Physical Review Letters, 2008. **100**(10).
73. Gonzalez-Herrero, H., et al., *Graphene Tunable Transparency to Tunneling Electrons: A Direct Tool To Measure the Local Coupling.* Acs Nano, 2016. **10**(5): p. 5131-5144.

74. Jolie, W., F. Craes, and C. Busse, *Graphene on weakly interacting metals: Dirac states versus surface states.* Physical Review B, 2015. **91**(11): p. 8.
75. Tesch, J., et al., *Structural and electronic properties of graphene nanoflakes on Au(111) and Ag(111).* Scientific Reports, 2016. **6**: p. 9.
76. Leicht, P., et al., *In Situ Fabrication Of Quasi-Free-Standing Epitaxial Graphene Nanoflakes On Gold.* Acs Nano, 2014. **8**(4): p. 3735-3742.
77. Borca, B., et al., *Electronic and geometric corrugation of periodically rippled, self-nanostructured graphene epitaxially grown on Ru(0001).* New Journal of Physics, 2010. **12**.
78. Tonnoir, C., et al., *Induced Superconductivity in Graphene Grown on Rhenium.* Physical Review Letters, 2013. **111**(24): p. 5.
79. Eom, D., et al., *Structure and Electronic Properties of Graphene Nanoislands on Co(0001).* Nano Letters, 2009. **9**(8): p. 2844-2848.
80. Vinogradov, N.A., et al., *Formation and Structure of Graphene Waves on Fe(110).* Physical Review Letters, 2012. **109**(2).
81. Rusponi, S., et al., *Highly Anisotropic Dirac Cones in Epitaxial Graphene Modulated by an Island Superlattice.* Physical Review Letters, 2010. **105**(24).
82. Cavallin, A., et al., *Local Electronic Structure and Density of Edge and Facet Atoms at Rh Nanoclusters Self-Assembled on a Graphene Template.* Acs Nano, 2012. **6**(4): p. 3034-3043.
83. Donner, K. and P. Jakob, *Structural properties and site specific interactions of Pt with the graphene/Ru(0001) moire overlayer.* Journal of Chemical Physics, 2009. **131**(16): p. 164701.
84. N'Diaye, A.T., et al., *A versatile fabrication method for cluster superlattices.* New Journal of Physics, 2009. **11**: p. 103045.
85. Schumacher, S., et al., *Strain in Epitaxial Graphene Visualized by Intercalation.* Physical Review Letters, 2013. **110**(8).
86. Schumacher, S., et al., *The Backside of Graphene: Manipulating Adsorption by Intercalation.* Nano Letters, 2013. **13**(11): p. 5013-5019.
87. Riedl, C., et al., *Quasi-Free-Standing Epitaxial Graphene on SiC Obtained by Hydrogen Intercalation.* Physical Review Letters, 2009. **103**(24).
88. Oida, S., et al., *Decoupling graphene from SiC(0001) via oxidation.* Physical Review B, 2010. **82**(4).
89. Gierz, I., et al., *Electronic decoupling of an epitaxial graphene monolayer by gold intercalation.* Physical Review B, 2010. **81**(23).
90. Virojanadara, C., et al., *Epitaxial graphene on 6H-SiC and Li intercalation.* Physical Review B, 2010. **82**(20).
91. Emtsev, K.V., et al., *Ambipolar doping in quasifree epitaxial graphene on SiC(0001) controlled by Ge intercalation.* Physical Review B, 2011. **84**(12).
92. Wong, S.L., et al., *Quasi-Free-Standing Epitaxial Graphene on SiC (0001) by Fluorine Intercalation from a Molecular Source.* Acs Nano, 2011. **5**(9): p. 7662-7668.
93. Walter, A.L., et al., *Highly p-doped epitaxial graphene obtained by fluorine intercalation.* Applied Physics Letters, 2011. **98**(18).
94. Meng, L., et al., *Silicon intercalation at the interface of graphene and Ir(111).* Applied Physics Letters, 2012. **100**(8).
95. Granas, E., et al., *Oxygen Intercalation under Graphene on Ir(111): Energetics, Kinetics, and the Role of Graphene Edges.* Acs Nano, 2012. **6**(11): p. 9951-9963.
96. Jin, L., et al., *Pb intercalation underneath a graphene layer on Ru(0001) and its effect on graphene oxidation.* Physical Chemistry Chemical Physics, 2011. **13**(37): p. 16655-16660.
97. Romero-Muniz, C., et al., *Strong dependence of flattening and decoupling of graphene on metals on the local distribution of intercalated oxygen atoms.* Carbon, 2016. **101**: p. 129-134.

98. Schumacher, S., et al., *Europium underneath graphene on Ir(111): Intercalation mechanism, magnetism, and band structure.* Physical Review B, 2014. **90**(23).
99. Hao, F., D.N. Fang, and Z.P. Xu, *Mechanical and thermal transport properties of graphene with defects.* Applied Physics Letters, 2011. **99**(4).
100. Lopez-Polin, G., et al., *Increasing the elastic modulus of graphene by controlled defect creation.* Nature Physics, 2015. **11**(1): p. 26-31.
101. Yazyev, O.V., *Emergence of magnetism in graphene materials and nanostructures.* Reports on Progress in Physics, 2010. **73**(5): p. 056501.
102. Yazyev, O.V. and L. Helm, *Defect-induced magnetism in graphene.* Physical Review B, 2007. **75**(12): p. 125408.
103. Esquinazi, P., et al., *Induced magnetic ordering by proton irradiation in graphite.* Physical Review Letters, 2003. **91**(22).
104. Ugeda, M.M., et al., *Missing Atom as a Source of Carbon Magnetism.* Physical Review Letters, 2010. **104**(9).
105. Nair, R.R., et al., *Dual origin of defect magnetism in graphene and its reversible switching by molecular doping.* Nature Communications, 2013. **4**: p. 2010.
106. Nair, R.R., et al., *Spin-half paramagnetism in graphene induced by point defects.* Nature Physics, 2012. **8**(3): p. 199-202.
107. McCreary, K.M., et al., *Magnetic Moment Formation in Graphene Detected by Scattering of Pure Spin Currents.* Physical Review Letters, 2012. **109**(18): p. 186604.
108. Pi, K., et al., *Electronic doping and scattering by transition metals on graphene.* Physical Review B, 2009. **80**(7).
109. Chen, J.H., et al., *Charged-impurity scattering in graphene.* Nature Physics, 2008. **4**(5): p. 377-381.
110. Brar, V.W., et al., *Gate-controlled ionization and screening of cobalt adatoms on a graphene surface.* Nature Physics, 2011. **7**(1): p. 43-47.
111. Wang, Y., et al., *Mapping Dirac quasiparticles near a single Coulomb impurity on graphene.* Nature Physics, 2012. **8**(9): p. 653-657.
112. Eelbo, T., et al., *Adatoms and Clusters of 3d Transition Metals on Graphene: Electronic and Magnetic Configurations.* Physical Review Letters, 2013. **110**(13): p. 5.
113. Eelbo, T., et al., *Influence of the degree of decoupling of graphene on the properties of transition metal adatoms.* Physical Review B, 2013. **87**(20): p. 4.
114. Gyamfi, M., et al., *Orbital selective coupling between Ni adatoms and graphene Dirac electrons.* Physical Review B, 2012. **85**(16).
115. Gyamfi, M., et al., *Fe adatoms on graphene/Ru(0001): Adsorption site and local electronic properties.* Physical Review B, 2011. **84**(11).
116. Barla, A., et al., *Complex Magnetic Exchange Coupling between Co Nanostructures and Ni(111) across Epitaxial Graphene.* Acs Nano, 2016. **10**(1): p. 1101-1107.
117. Donati, F., et al., *Tailoring the Magnetism of Co Atoms on Graphene through Substrate Hybridization.* Physical Review Letters, 2014. **113**(17): p. 6.
118. Donati, F., et al., *Magnetic Moment and Anisotropy of Individual Co Atoms on Graphene.* Physical Review Letters, 2013. **111**(23): p. 5.
119. Wang, Y., et al., *Nitrogen-Doped Graphene and Its Application in Electrochemical Biosensing.* Acs Nano, 2010. **4**(4): p. 1790-1798.
120. Wang, H.B., T. Maiyalagan, and X. Wang, *Review on Recent Progress in Nitrogen-Doped Graphene: Synthesis, Characterization, and Its Potential Applications.* Acs Catalysis, 2012. **2**(5): p. 781-794.
121. Telychko, M., et al., *Electronic and Chemical Properties of Donor, Acceptor Centers in Graphene.* Acs Nano, 2015. **9**(9): p. 9180-9187.
122. Telychko, M., et al., *Achieving High-Quality Single-Atom Nitrogen Doping of Graphene/SiC(0001) by Ion Implantation and Subsequent Thermal Stabilization.* Acs Nano, 2014. **8**(7): p. 7318-7324.

123. Usachov, D., et al., *The Chemistry of Imperfections in N-Graphene.* Nano Letters, 2014. **14**(9): p. 4982-4988.
124. Koch, R.J., et al., *Growth and electronic structure of nitrogen-doped graphene on Ni(111).* Physical Review B, 2012. **86**(7).
125. Zhao, L.Y., et al., *Visualizing Individual Nitrogen Dopants in Monolayer Graphene.* Science, 2011. **333**(6045): p. 999-1003.
126. dos Santos, J., N.M.R. Peres, and A.H. Castro, *Graphene bilayer with a twist: Electronic structure.* Physical Review Letters, 2007. **99**(25): p. 4.
127. Park, C.H., et al., *New generation of massless Dirac fermions in graphene under external periodic potentials.* Physical Review Letters, 2008. **101**(12): p. 126804.
128. Park, C.H., et al., *Anisotropic behaviours of massless Dirac fermions in graphene under periodic potentials.* Nature Physics, 2008. **4**(3): p. 213-217.
129. Hass, J., et al., *Why multilayer graphene on 4H-SiC(000(1)over-bar) behaves like a single sheet of graphene.* Physical Review Letters, 2008. **100**(12): p. 125504.
130. Latil, S., V. Meunier, and L. Henrard, *Massless fermions in multilayer graphitic systems with misoriented layers: Ab initio calculations and experimental fingerprints.* Physical Review B, 2007. **76**(20).
131. Shallcross, S., S. Sharma, and O.A. Pankratov, *Quantum interference at the twist boundary in graphene.* Physical Review Letters, 2008. **101**(5).
132. Li, G.H., et al., *Observation of Van Hove singularities in twisted graphene layers.* Nature Physics, 2010. **6**(2): p. 44-48.
133. Shallcross, S., et al., *Electronic structure of turbostratic graphene.* Physical Review B, 2010. **81**(16).
134. Suarez Morell, E., et al., *Flat bands in slightly twisted bilayer graphene: Tight-binding calculations.* Physical Review B, 2010. **82**(12).
135. Lopes dos Santos, J.M.B., N.M.R. Peres, and A.H. Castro Neto, *Continuum model of the twisted graphene bilayer.* Physical Review B, 2012. **86**(15).
136. de Laissardiere, G.T., D. Mayou, and L. Magaud, *Localization of Dirac Electrons in Rotated Graphene Bilayers.* Nano Letters, 2010. **10**(3): p. 804-808.
137. de Laissardiere, G.T., D. Mayou, and L. Magaud, *Numerical studies of confined states in rotated bilayers of graphene.* Physical Review B, 2012. **86**(12).
138. Bistritzer, R. and A.H. MacDonald, *Moire bands in twisted double-layer graphene.* Proceedings of the National Academy of Sciences of the United States of America, 2011. **108**(30): p. 12233-12237.
139. San-Jose, P., J. Gonzalez, and F. Guinea, *Non-Abelian Gauge Potentials in Graphene Bilayers.* Physical Review Letters, 2012. **108**(21).
140. Li, G., et al., *Observation of Van Hove singularities in twisted graphene layers.* Nature Physics, 2010. **6**(2): p. 109-113.
141. Brihuega, I., et al., *Unraveling the Intrinsic and Robust Nature of van Hove Singularities in Twisted Bilayer Graphene by Scanning Tunneling Microscopy and Theoretical Analysis.* Physical Review Letters, 2012. **109**(19): p. 196802.
142. Luican, A., et al., *Single-Layer Behavior and Its Breakdown in Twisted Graphene Layers.* Physical Review Letters, 2011. **106**(12).
143. Martinez-Galera, A.J., et al., *Towards scalable nano-engineering of graphene.* Scientific Reports, 2014. **4**: p. 6.
144. Magda, G.Z., et al., *Room-temperature magnetic order on zigzag edges of narrow graphene nanoribbons.* Nature, 2014. **514**(7524): p. 608-+.
145. Sessi, P., et al., *Patterning Graphene at the Nanometer Scale via Hydrogen Desorption.* Nano Letters, 2009. **9**(12): p. 4343-4347.
146. Hla, S.W., *Scanning tunneling microscopy single atom/molecule manipulation and its application to nanoscience and technology.* Journal of Vacuum Science & Technology B, 2005. **23**(4): p. 1351-1360.

147. Schumacher, S., et al., *The Backside of Graphene: Manipulating Adsorption by Intercalation.* Nano Letters, 2013. **13**(11): p. 5013-5019.
148. Balog, R., et al., *Bandgap opening in graphene induced by patterned hydrogen adsorption.* Nature Materials, 2010. **9**(4): p. 315-319.
149. Tapaszto, L., et al., *Tailoring the atomic structure of graphene nanoribbons by scanning tunnelling microscope lithography.* Nature Nanotechnology, 2008. **3**(7): p. 397-401.
150. Pereira, V.M., J. Nilsson, and A.H.C. Neto, *Coulomb impurity problem in graphene.* Physical Review Letters, 2007. **99**(16).
151. Shytov, A.V., M.I. Katsnelson, and L.S. Levitov, *Atomic collapse and quasi-Rydberg states in graphene.* Physical Review Letters, 2007. **99**(24).
152. Shytov, A.V., M.I. Katsnelson, and L.S. Levitov, *Vacuum polarization and screening of supercritical impurities in graphene.* Physical Review Letters, 2007. **99**(23).
153. Wang, Y., et al., *Observing Atomic Collapse Resonances in Artificial Nuclei on Graphene.* Science, 2013. **340**(6133): p. 734-737.
154. Mao, J., et al., *Realization of a tunable artificial atom at a supercritically charged vacancy in graphene.* Nat Phys, 2016. **12**(6): p. 545-549.
155. Gomes, K.K., et al., *Designer Dirac fermions and topological phases in molecular graphene.* Nature, 2012. **483**(7389): p. 306-310.
156. Polini, M., et al., *Artificial honeycomb lattices for electrons, atoms and photons.* Nat Nano, 2013. **8**(9): p. 625-633.

Chapter 2: Atomic-scale control of graphene magnetism by using hydrogen atoms.

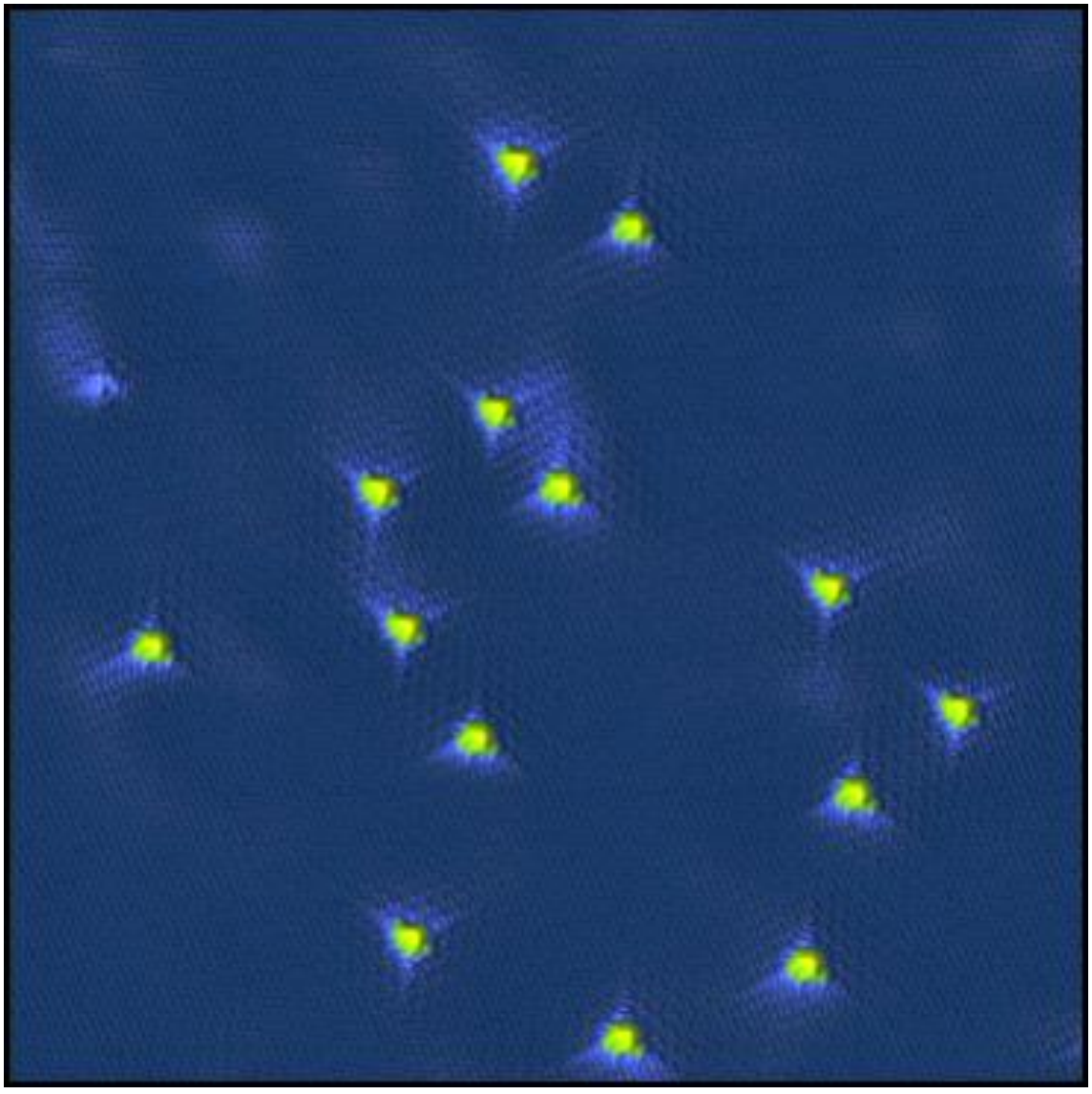

2.1 Introduction.

Since the discovery of graphene, the possibility to induce magnetic moments in this material has been pursued. In nature, the materials that exhibit magnetic order possess partially filled electron shells where the existence of unpaired electrons lead to a net magnetic moment. Among these materials we have iron, cobalt, nickel and gadolinium at room temperature, and other elements from the 3d or 4f series in the periodic table at lower temperatures. However, graphene is made of carbon atoms which electrons tend to form covalent bonds, hindering the possibility to develop any magnetic moment. Despite this tendency to form covalent bonds, achieving the use of spin as an additional degree of freedom would represent a tremendous boost to the versatility of graphene based devices. On one side, spin information transfer or spin diffusion phenomena are favoured by the expected long spin relaxation times of graphene carriers [1, 2]. In particular, inducing ferromagnetism in graphene remains one of the most challenging tasks and promising achievements. Ferromagnetism is expected to emerge in the pi bands [3, 4] and feature a very high Curie temperature [5]. Since charge transport also takes place in these pi bands, potential spintronics applications can be anticipated. In table 1 (extracted from [6]) spin-dependent properties of graphene, metals and semiconductors measured by spin-valve experiments are shown. From these values, it is clear that graphene is a great candidate for spintronics and the necessity of the control of graphene's magnetism.

Spin channel	Spin lifetime	Spin diffusion lengths	Spin signals
Metals			
Cu (refs 15,131)	~42 ps at 4.2 K ~11 ps at 300 K	~1 μm at 4.2 K ~0.4 μm at 300 K	~1 mΩ at 4.2 K ~0.5 mΩ at 300 K
Al (ref. 108)	~100 ps at 4.2 K ~45 ps at 300 K	~0.6 μm at 4.2 K ~0.4 μm at 300 K	~12 mΩ at 4.2 K ~0.5 mΩ at 300 K
Ag (ref. 132)	~20 ps at 5 K ~10 ps at 300 K	~1 μm at 5 K ~0.3 μm at 300 K	~9 mΩ at 5 K ~2 mΩ at 300 K
Semiconductors			
Highly doped Si (refs 129,154)	~10 ns at 8 K ~1.3 ns at 300 K	~2 μm at 8 K ~0.5 μm at 300 K	~30 mΩ at 8 K ~1 mΩ at 300 K
GaAs (ref. 155)	24 ns at 10 K 4 ns at 70 K	6 μm at 50 K	~30 mΩ at 50 K
Highly doped Ge (ref. 130)	~1 ns at 4 K ~300 ps at 100 K	~0.6 μm at 4 K	1 Ω at 4 K ~0.02–0.1 Ω at 200 K
Graphene[6,8–10,42]	0.5–2 ns at 300 K 1–6 ns at 4 K	3–12 μm at 300 K (~100 μm fit from local MR data)	130 Ω at 300 K (1 MΩ for local MR at 1.4 K)

Table 1: Spin-dependent properties of graphene, metals and semiconductors measured by spin-valve measurements [6]**.**

From a theoretical point of view, there is a clear understanding of how to produce and manipulate π-ferromagnetism in graphene layers; zigzag edges, graphene clusters, grain boundaries, and atomic defects being the main building blocks [7-11]. The basics of achieving graphene ferromagnetism are rather simple. The removal of a single p_z orbital from the π-graphene system creates a single π -state at the Fermi energy (E_F) around the missing orbital. The double

occupation of this state by two electrons with different spins is forbidden by the electrostatic Coulomb repulsion; namely, once an electron occupies the state, a second one with opposite spin needs to "pay" an extra energy U. This leaves a single electron occupying the state and therefore a net magnetic moment [7, 9, 11-13]. The strength of U, which determines the spin-splitting, depends on the spatial localization of the state since this defines the proximity between the electrons (see Figure 2.1). Contrary to magnetic moments of strong localized atomic character commonly found in magnetic materials, these induced moments are predicted to extend over several nanometers, anticipating a strong direct coupling between them at unusually long distances. The coupling rules between the induced magnetic moments are also expected to be simple. Because of the bipartite atomic structure of graphene— which consists of two equivalent triangular sublattices, labeled A and B—and according to Lieb's theorem [14], the ground state of the system possesses a total spin given by $S=1/2\times |N_A-N_B|$, where N_A and N_B are the number of p_z orbitals removed from each sublattice [8-10]. Thus, to generate a net magnetic moment in a particular graphene region, a different number of p_z orbitals from each sublattice needs to be locally removed.

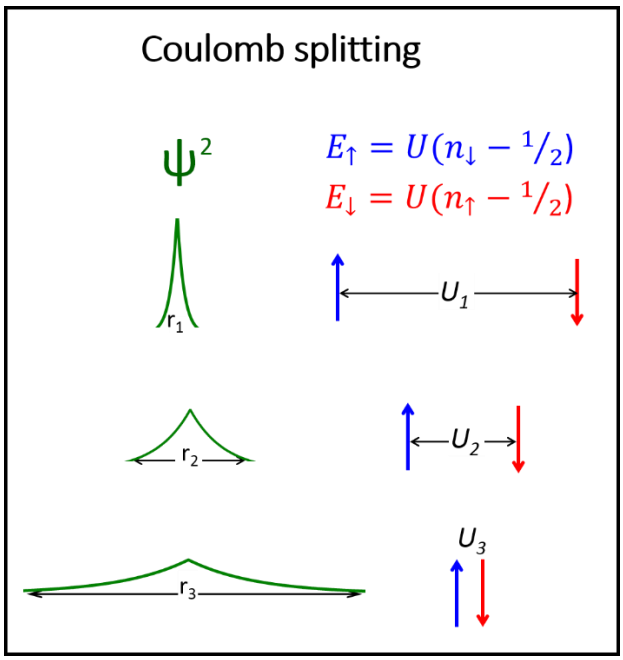

Figure 2.1: Coulomb splitting. Illustration of the origin of the spin-split state in terms of its spatial localization, given by the square of its wave function $|\psi|^2$, and the corresponding electrostatic Coulomb repulsion *U*. Arrows indicate the energy position of spin-up and spin-down levels. For a fully polarized one-electron state the majority level spin is filled and the minority one is empty; therefore $n_\uparrow=1$ and $n_\downarrow=0$, and the energy splitting ($E_\downarrow$-$E_\uparrow$) is given by *U*.

Experimentally, the removal of p_z orbitals from the π system has been achieved by randomly creating atomic vacancies or adsorbing adatoms [15-19]. The first one is usually called vacancy defect and the second one hydrogen chemisorption defect. Since both of them result in the removal of a p_z orbital, these two types of defect are also referred as p_z vacancies.

The development of a magnetic moment due to atomic vacancies was briefly mentioned in chapter 1, although no real discussion was put forward. The case of vacancies is quite interesting and puzzling at the same time. From an experimental point of view, the first measurements on this matter appeared in 2003. The group of P. Esquinazi was able to induce magnetic order in graphite at room temperature after irradiating it with high energy protons (2.25 MeV [20-22]. This magnetism would arise because of the mixture of sp^2, sp^3 hybrids carbon atoms on the surface. These results were measured using superconducting quantum interference device (SQUID) and magnetic force microscopy MFM. However, the experimental evidences at that time were controversial due to the low value of the magnetic signal in order to correctly determine the real origin of the magnetic moments. More recent experiments by the group of I.V. Grigorieva have studied the magnetic properties of irradiated HOPG samples. Their SQUID measurements of the magnetization curves have proven that irradiated HOPG samples exhibit paramagnetic properties associated with non-interacting spins with S=1/2 [16]. In addition, they also perform SQUID measurements on chemically doped samples, finding a reduction of ~50% of the magnetization [18]. Another experimental technique to measure magnetic moments in graphene used by the group of R.K. Kawakami consists on spin transport experiments. Their non-local magnetoresistance curves on argon irradiated samples, present a dip at zero field which points out to the formation of a magnetic moment in graphene [17]. On the other hand, the total magnetic moment associated with a single vacancy has been and still is a topic of great debate. The removal of a carbon atom from the graphene lattice takes away not only the pi orbital, but also breaks the three sigma bonds with its first neighbours. The vacancy then overcomes a reconstruction where two of the neighbouring carbon atoms form a bond leaving an empty sigma bond which also contributes to the magnetic moment of the vacancy (Figure 2.2 b). Because of this reconstruction, a self-doping effect appears, partially suppressing the p-state from the pi orbital. The overall magnetic moment per vacancy defect has been predicted to have a value going from 1.12 μ_B up to 2 μ_B depending on the calculation and density of vacancies [9]

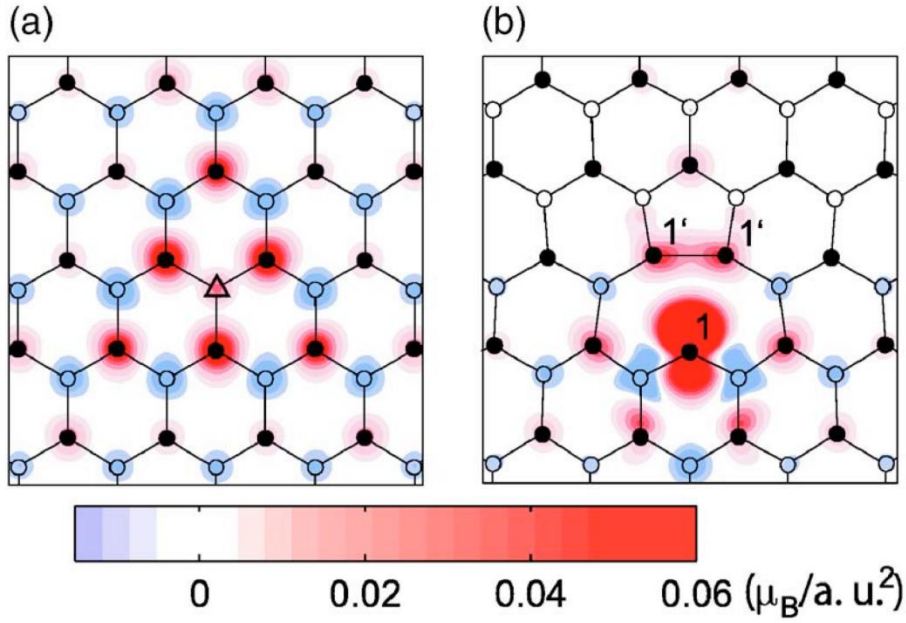

Figure 2.2: Spin-density projection around a H atom and a carbon vacancy. a) Hydrogen chemisorption defect. b) Vacancy defect. Carbon atoms corresponding to the α sublattice and β sublattice are distinguished by ○ and ● respectively [9].

In the case of hydrogen or light elements chemisorption defects, the existence of a softer reconstruction makes things easier to understand (see Figure 2.2 a). The foreign atom binds to the p_z orbital of the carbon atom, removing it from the π-graphene system, leading to the apparition of a magnetic moment of 1 μ_B. Experimentally, the group of I.V. Grigorieva proved, using SQUID, that fluorine adatoms have magnetic moments with spin S=1/2. However, as in the case of vacancies no magnetic order was observed and only paramagnetism was measured [16]. Spin transport measurements by the group of R.K. Kawakami have also demonstrated the formation of magnetic moments on hydrogenated graphene samples [17]. Hydrogen adsorption has also proven to enhance the spin-orbit interaction of graphene by three orders of magnitude allowing the observance of the spin Hall effect [19].

The results we have discussed so far were mainly obtained using techniques which average over microscopic regions. In our group, the electronic impact of point defects on graphene have been studied using STM, a really local technique. Indeed, in previous experiments, single atomic vacancies on graphite and graphene grown on Platinum, as well as divacancies on SiC(0001) had been studied. In the first case, the observation of a sharp resonance around the Fermi level was measured for the first time, confirming previous theoretical works [15]. For the vacancies on graphene grown on platinum a much broader resonance was found around the Dirac point but no magnetic moment was expected due to the interaction between the vacancy and the metal underneath leading to the quenching of the magnetic moment associated with the vacancy [23]. In the case of divacancies, the existence of an electronic resonance was also found, with no

magnetic character as in the case of graphene on Pt(111) [24]. With the idea of going one step further in our understanding of point defects and the possibility to induce local magnetic moments on it, we decided to use the STM capabilities to study hydrogen chemisorption at the single atom scale. In this chapter we will present our main results about the impact of single H atoms on the graphene properties.

2.2 Sample preparation.

All the samples used in the experiments of this chapter, were grown on SiC crystals by our French collaborators from the Neel Institute in Grenoble, Dr. Jean Yves Vellouin and Dr. Pierre Mallet. These crystals exhibit a wurtzite or hexagonal structure (see Figure 2.3 a) and due to its polar nature, they present two different crystallographic orientations. The so called SiC(0001) or silicon face and the SiC(000-1) or carbon face. In both faces, multiple layers of graphene can be grown by graphitization. In the present case, we used samples prepared on the carbon face. The reason why this substrate was chosen, is the fact that as we commented in the previous chapter when we discussed about van Hove singularities, the rotational disorder in the alignment of the layers leads to the decoupling of the topmost layer, which will behave as ideal graphene [25-29]. This has also been probed by photoemission experiments, where the linear dispersion of the graphene is preserved (see Figure 2.3 b) [30].

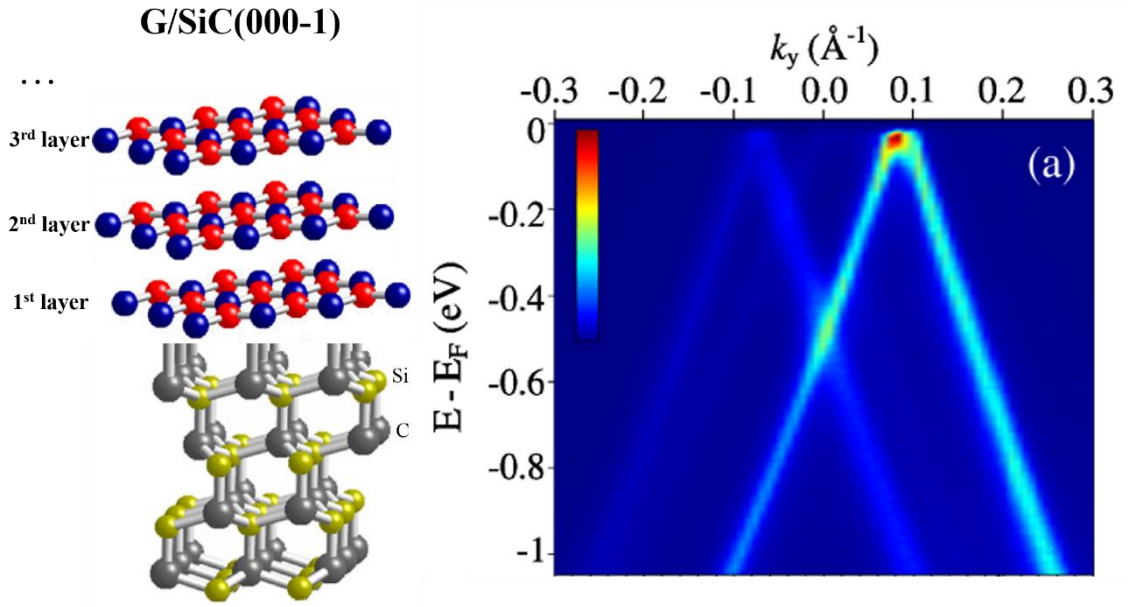

Figure 2.3: SiC (000-1). a) Atomic structure of graphene grown on the carbon face of SiC [31]. b) Photoemission measurement of the Dirac cone on multilayer graphene grown on SiC(000-1) [30].

The SiC(000-1) samples were prepared under UHV by graphitization of a 6H-SiC(000-1) surface [32, 33]. This surface presents the coexistence of two reconstructions: the 3x3 and $(2x2)_C$ where the subsequent layers will grow. The preparation procedure is as follows: the substrate surface is cleaned under a Si flux and subsequently annealed at 950-1000°C to get the 6H-SiC(000-1) (3x3) surface reconstruction. Further annealing at higher temperature induces the growth of graphene layers on this surface [32]. The onset of graphitization is detected by LEED measurements [33]. The average number of graphene layers on the surface is governed by the annealing temperature/time and is controlled by Auger electron spectroscopy with a precision of ± 1 monolayer. The final

number of layers will determine the position of the Dirac point of the graphene sheet. This is due to the occurrence of interfacial charge transfer between the substrate and the graphene layer. For low number of layers, the resulting graphene will be n-doped until we reach ~5 or more layers, where the Dirac point locates around the Fermi level. Since we were interested in studying the impact of single hydrogen atoms on the most realistic graphene we could get, the samples we used were prepared to obtain 5-7 layers and ensure graphene's neutrality. However, in the last part of the chapter we will discuss some results obtained in two doped graphene samples: one where 2-3 layers were grown, resulting in a n-doped graphene, and a 5-7 layers sample where p-doping was obtained after many cycles of H deposition and further annealing. In the following, unless specifically expressed, the discussed results will be about the 5-7 layers neutral sample. In Figure 2.4 we can observe a large scale image of the sample and how the different moirés appear in our images.

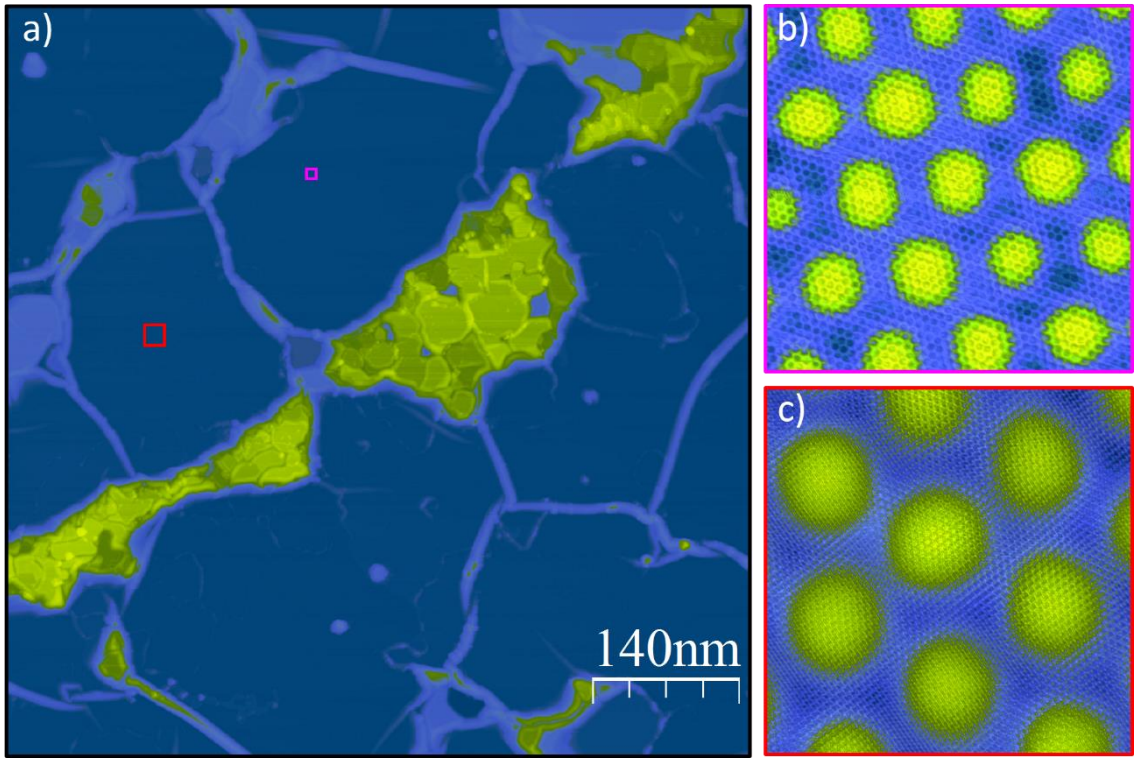

Figure 2.4: General morphology of the Gr/SiC(000-1) sample measured by STM. a) 700×700 nm² image showing multiple terraces. b-c) 10×10 nm² and 20×20 nm² images showing different moiré patterns present in our sample. Tunneling parameters: a) 0.4V, 0.2 nA; b-c) 0.15 V, 0.1 nA.

The quality of the SiC(000-1) samples is checked during its growth by our French collaborators in the UHV-STM system. After they are sure that the samples have the quality needed for our experiments, they send them to us by standard post service. Once the samples arrive to our laboratory and prior to the deposition of hydrogen on top of them, they are annealed to 700-800°C in order to degas them. After this process, the samples present the same quality as they had before been exposed to air. This method to receive our samples, has been

successfully used in our group since 2007. The deposition of atomic hydrogen was done following the procedure of refs [34-36], i.e. by the thermal dissociation of H_2 on a home-made hot hydrogen atom beam source. A molecular H_2 beam is passed through a hot W filament held at 1900K. The pristine graphene substrate is placed 10 cm away from the filament, held at RT during atomic H deposition and subsequently cooled down to 5K, the temperature at which we carried out all STM/STS experiments presented here. H_2 pressure is regulated by a leak valve and fixed to 3·10-7 torr as measured in the preparation chamber. The atomic H coverage was adjusted by changing the deposition times between 200-60s which corresponded to final coverages between 0.10-0.03 H atoms/nm² (or equivalently, 0.0026-0.0008ML; 1ML= 38 atoms/nm² = $3.8 \cdot 10^{15}$ atoms/cm², referred to carbon atoms in graphene layers).

After the H deposition the graphene surface presents several point defects (see Figure 2.5). As control experiments, to ensure our assignment of the nature of the new bright features as H atoms on graphene, we repeated exactly the same preparation procedure but either with the W filament off (i.e. H_2 pressure = $3 \cdot 10^{-7}$ torr; time =10 min, Temperature W filament =RT –the same holds for $T_{filament}$ < 1500K-) or without H_2 gas (i.e. H_2 pressure = 0 torr; time =10 min, temperature W filament = 1900K -we went up to $T_{filament}$ >2000K-). In both cases graphene samples looked identical to the pristine ones and no traces of H could be found on the substrates, confirming our identification of H atoms.

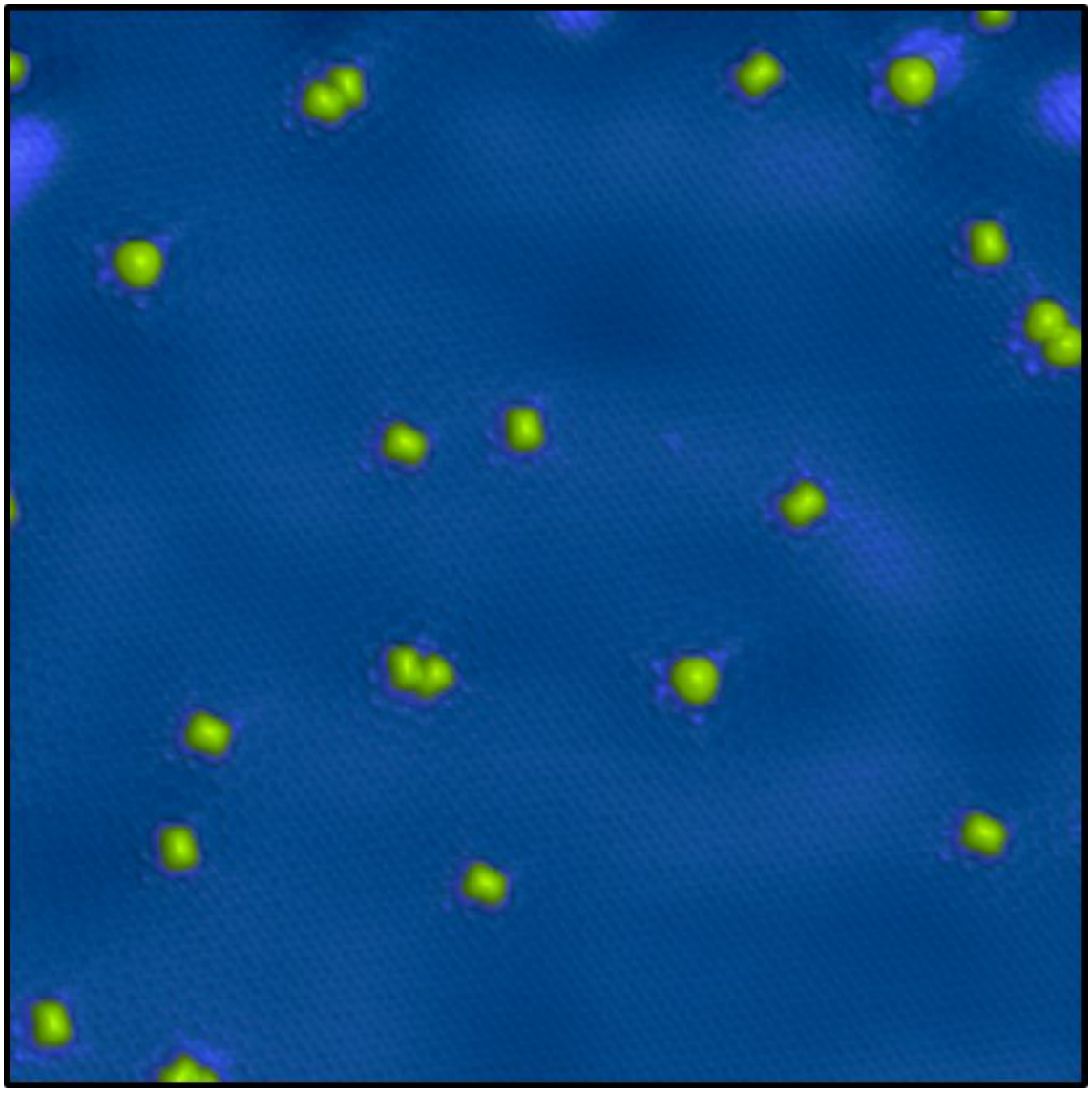

Figure 2.5: Gr/SiC(000-1) after hydrogen deposition. 20x20 nm² image of our graphene sample after hydrogen deposition. Different bright protrusion, attributed to hydrogen atoms, are observed. Tunneling parameters: 0.4V, 0.05 nA.

2.3 Theoretical methods.

2.3.1 Theoretical methodology for H on graphene.

All the calculations shown in this chapter were carried out by the group of Prof. Juanjo Palacios and Prof. Félix Yndurain.

In order to study the geometrical and electronic structure of the different defects in graphene, the first principles density functional [37, 38] SIESTA code [39, 40], which uses localized orbitals as basis functions was used [41]. A double ξ basis set, non-local norm conserving pseudopotentials was employed and for the exchange correlation functional the local density approximation (LDA) was used. The results have being checked with generalized gradient approximation (GGA) calculations [42]. The calculations are performed with stringent criteria in the electronic structure convergence (down to 10^{-5} in the density matrix), 2D Brillouin zone sampling (up to 1600 k-points), real space grid (energy cut-off of 400 Ryd) and equilibrium geometry (residual forces lower than 3×10^{-2} eV/Å). Due to the rapid variation of the density of states at the Fermi level, a polynomial smearing method was used [43].

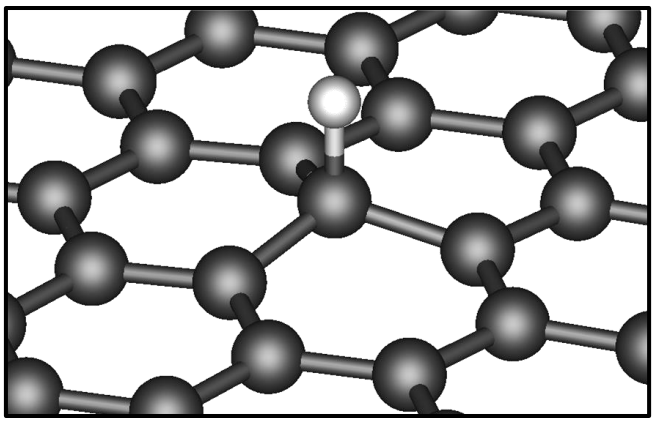

Figure 2.6: DFT atomic model of the hydrogen atom chemisorption on graphene.

In the fully relaxed geometry, not only the carbon atom, which binds directly to the hydrogen one, but the three surrounding ones move up to favour the process. The carbon-hydrogen distance becomes 1.20 Å, with the central carbon moved 0.35 Å upwards and the three surrounding around 0.08 Å. The sp^3 hybridization advantages the elongation of the hydrogenated graphene, and thus the lift of the carbon atoms, see Figure 2.6. The calculated adsorption energy of the Hydrogen on graphene is around 1 eV as can be seen fin Figure 2.7. This adsorption curve is quite interesting and it will be explained in more detail in the next chapter.

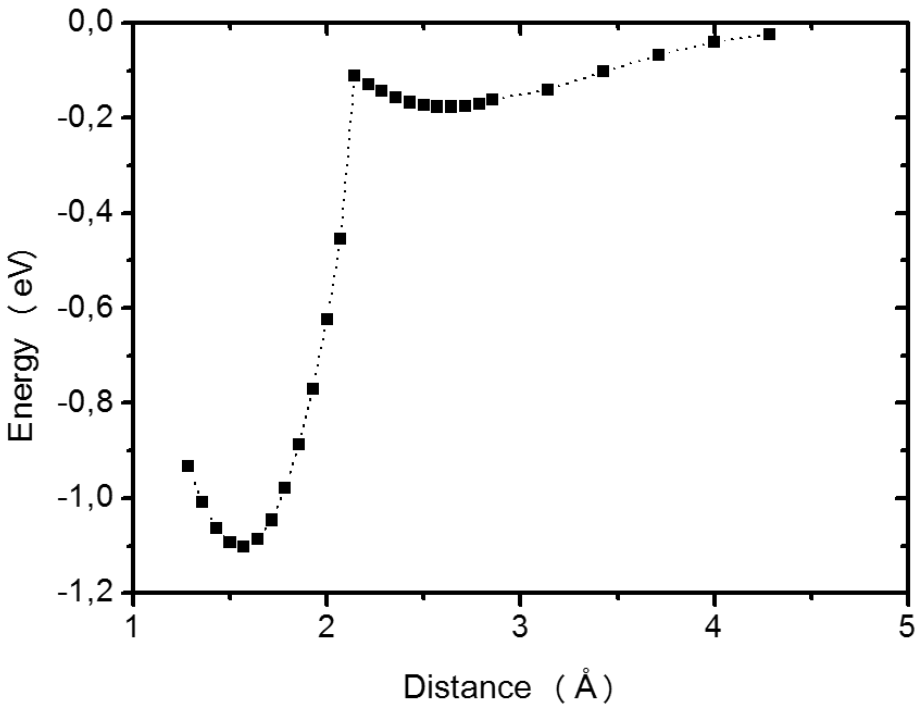

Figure 2.7: Adsorption curve of a single H atom on top of graphene.

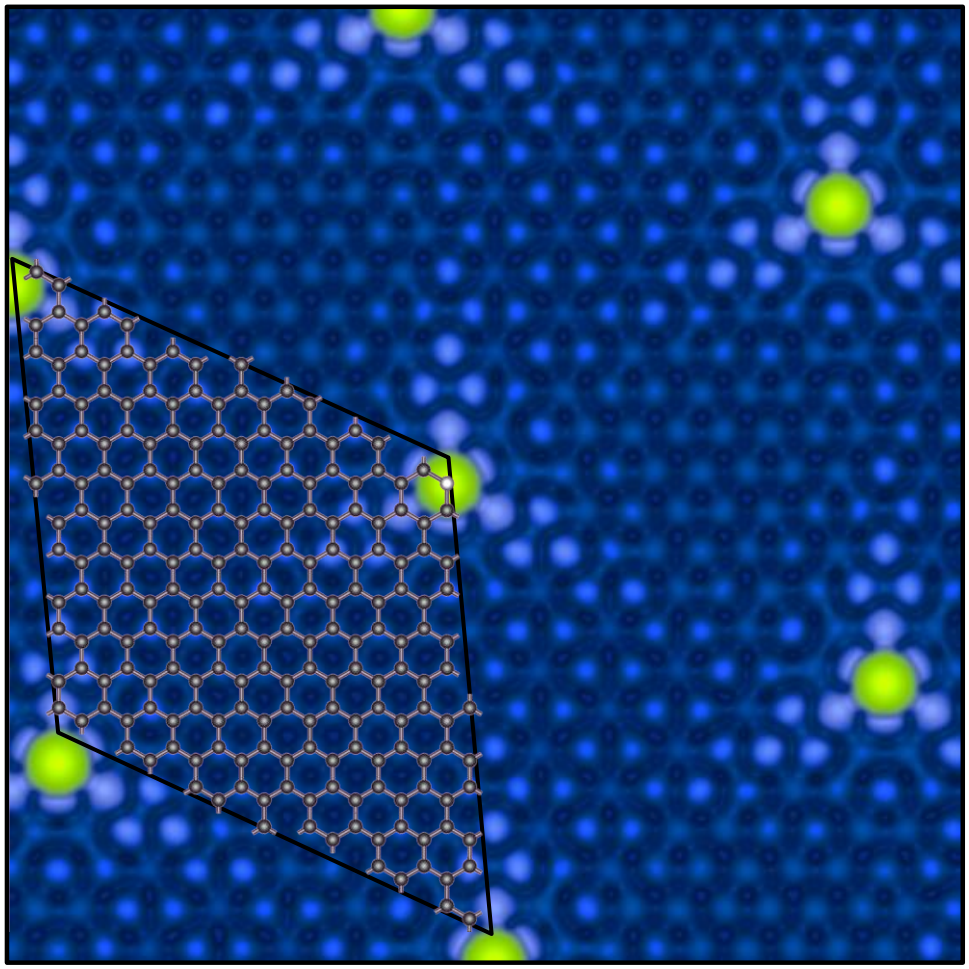

Figure 2.8: Graphene unit cell. Simulated STM image, within the Tersoff-Hamann approximation, of a hydrogen atom in a 218 atoms graphene unit cell. The atomic model is superimposed to outline the (5,7) “skewed" character of the unit cell.

To study defects the super cell approximations was used in the way that they ended up with an interaction between defects in the repeated unit cell. To minimize this interaction, different unit cells sizes were used and, in addition, “skewed" unit cells were used in a way that the lattice vector did not coincide with graphene symmetry directions. In this way, interactions along the zig-zag and armchair chains of atoms are minimized, see Figure 2.8.

2.3.2 Band structure and density of states calculated by DFT.

In Figure 2.9 the results of a non spin-resolved calculation of one hydrogen atom in a 218 atoms graphene unit cell are shown. We immediately realize the existence of an essentially half occupied extremely narrow peak at the Dirac point. The charge transfer between hydrogen and graphene being of the order of a few hundredths of electron.

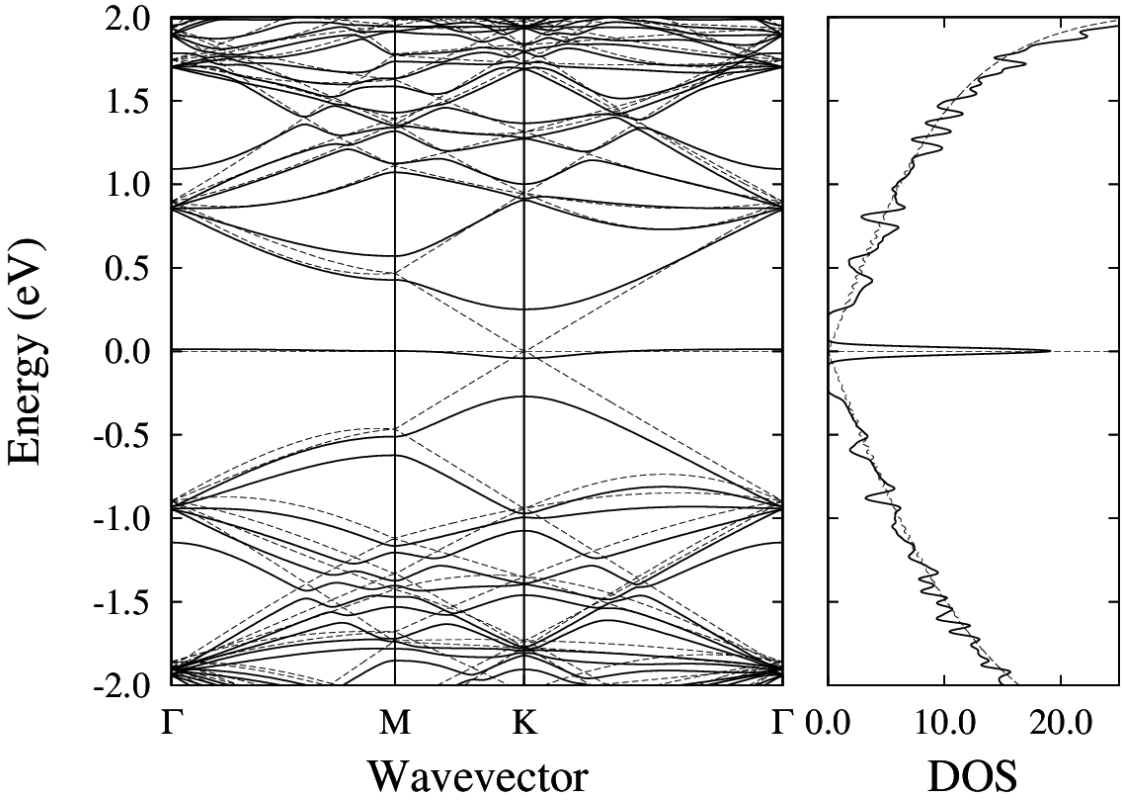

Figure 2.9: Non spin-resolved calculations. Non spin-resolved band structure (left panel) and density of states (right panel) of a hydrogen atom in a 218 atoms graphene unit cell (Figure 2.8). The horizontal dotted line indicates the Fermi energy. A small (0.025 eV) gaussian broadening is included in the density of states for presentation purposes. The dash line indicates the defect free graphene results.

Results of the corresponding spin resolved calculations are shown in Figure 2.10. We immediately notice the spin-up spin-down splitting of the hydrogen-induced state at the Dirac point. This is clearly reflected in the DOS as two sharp peaks, one above the Fermi energy and the second one below it. These peaks

are the fingerprint of the magnetic moment arising. Due to the sensitivity of STM to the LDOS, our main goal is to be able to measure them.

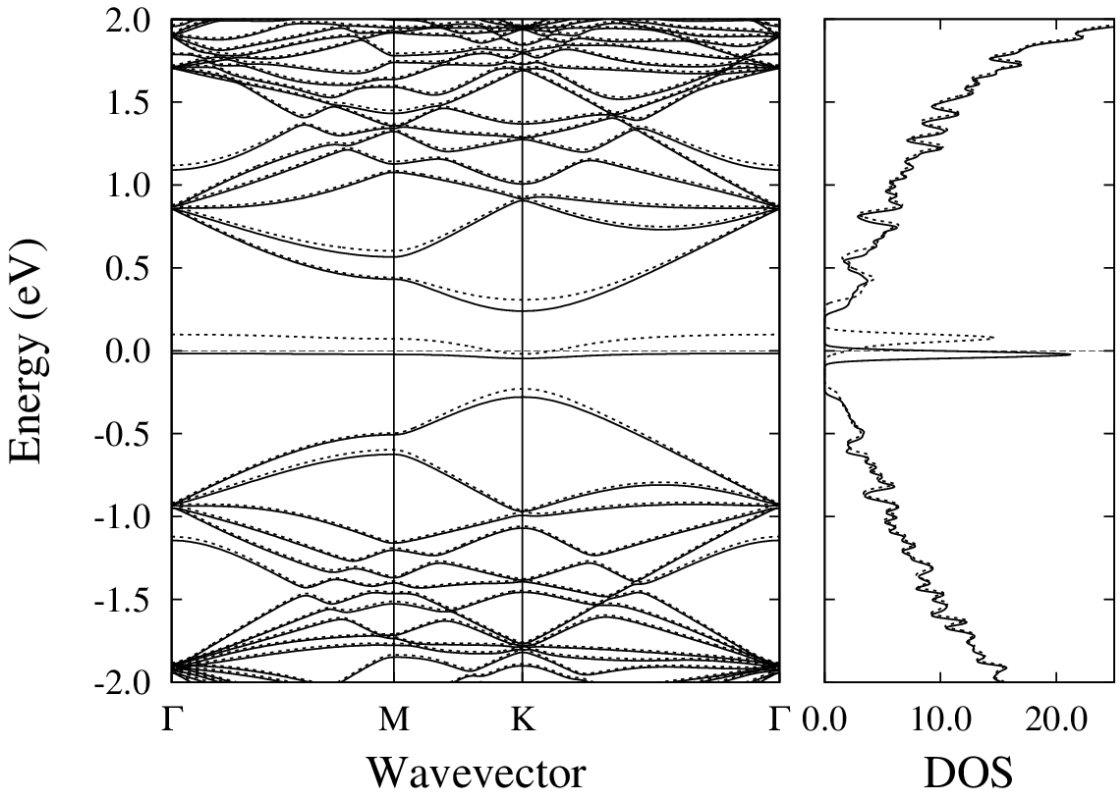

Figure 2.10: Spin-resolved calculations. Spin-resolved band structure (left panel) and density of states (right panel) of a hydrogen atom in a 218 atoms graphene unit cell. Solid and broken lines indicate spin up and spin down states respectively. The horizontal dotted line indicates the Fermi energy. A small (0.025 eV) gaussian broadening is included in the density of states for presentation purposes.

2.4 A single H atom on Gr/SiC(000-1): Emergence of a local magnetic moment in graphene.

2.4.1 Topography identification.

Previous experiments on hydrogen deposition on graphene have shown that hydrogen atoms can form different kind of arrangements when adsorbed on graphene [36, 44]. Therefore, a relevant part of our experiment will be the localization and identification of single hydrogen atoms on our sample. The exact atomic location of H atoms with respect to the graphene lattice can be inferred from our STM images. Scanning tunneling microscopy (STM) visualizes single H atoms as a bright protrusion (apparent height, ~2.5 Å) surrounded by a complex threefold $\sqrt{3}\times\sqrt{3}$ pattern that is rotated 30° degrees with respect to the graphene lattice (see Figure 2.11 A) [45, 46] . This complex R3 scattering pattern presents three "arms" at 120° each. Thanks to this triangular symmetry, the exact identification of the H adsorption site becomes quite simple; it is just given by the intersection of the three lines which goes along the three "arms" at 120° each generated by each H atom, see Figure 2.11C.

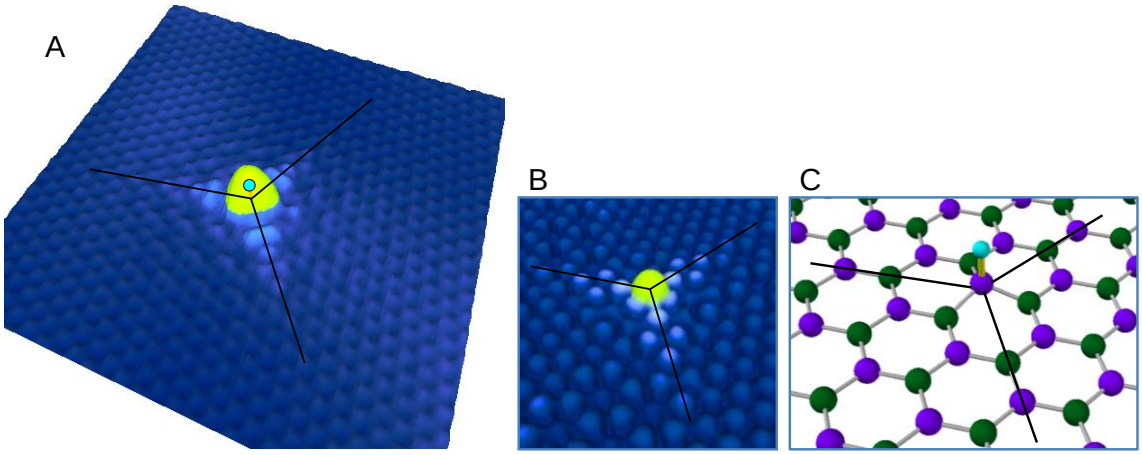

Figure 2.11: Identification of single H atoms. A) STM topography of a single H atom chemisorbed on graphene (0.2V, 0.1nA, 7x7nm²). B) DFT simulated STM image. C) Schematic diagram showing the corresponding H adsorption site (blue ball) on graphene (purple and green balls). The three lines, at 120° each, outlined in each panel correspond to the threefold ($\sqrt{3}\times\sqrt{3}$) patterns generated on graphene by the H atom. The simulated image is calculated at the same energy as the corresponding experimental one.

In this way, when several H atoms are present (at a distance > 0.5nm), the determination of their relative position with respect to the graphene sub-lattice, key for the present work, becomes trivial: H atoms chemisorbed on different sublattices show the three arms pointing in opposite directions, see Figure 2.11. The comparison of our atomically resolved STM images of these defects with density functional theory (DFT)–simulated STM images (see Figure 2.11 B and 3.12) calculated by our theoretical collaborators, confirms that these defects correspond to single H atoms chemisorbed on graphene.

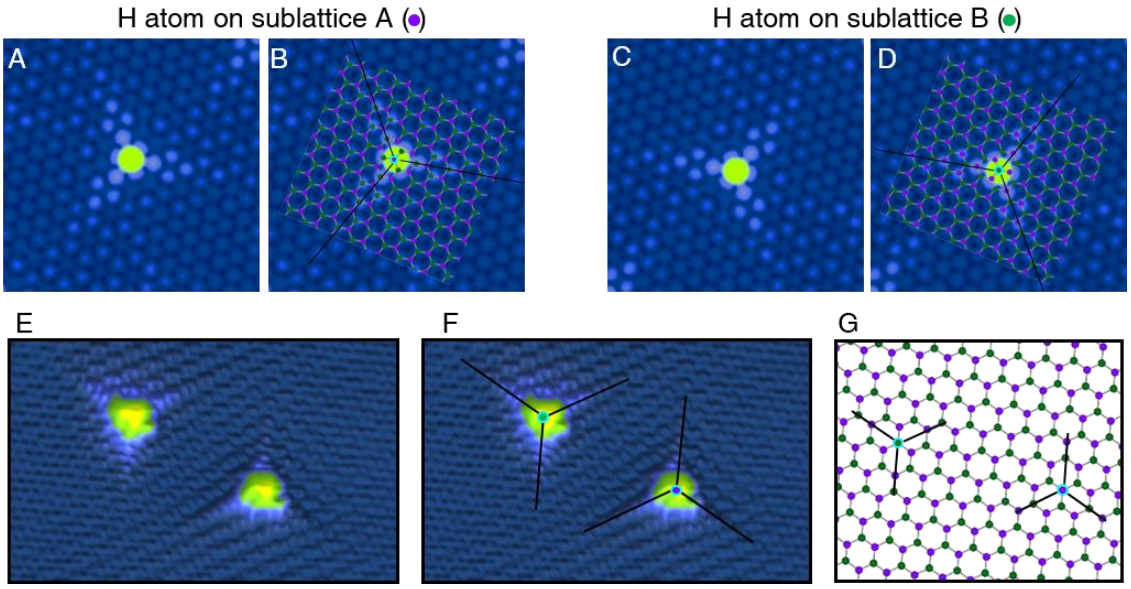

Figure 2.12: Identifying various H atoms. A) Simulated STM image of a hydrogen atom chemisorbed on graphene. B) Same calculated image as A) with a schematic diagram of the graphene lattice superimposed. Three black lines are also outlined along the three "arms" at 120° each generated by each H atom to illustrate that their intersection identify the H adsorption site. C, D) same as A, B to show that a H atom in the complementary graphene sublattice has the three "arms" pointing in the opposite direction. E) Experimental STM image with two H atoms adsorbed on different sublattices (8.8x5.5 nm², Vbias =0.4V, It=0.03nA). F) Same image as E where three black lines are outlined along the three "arms" at 120° each generated by each H atom identify the H adsorption site. G) Schematic diagram showing the corresponding H adsorption sites (blue rings) on graphene (purple and green balls) for the two H atoms shown in E, F (note that the actual experimental H-H distance is much larger).

2.4.2 Spectroscopic signature of the graphene magnetic moment induced by single H atoms: Spin-split state.

As discussed in the introduction of this chapter, graphene magnetic moments induced by H adsorption should be reflected in the appearance of a spin-polarized state at E_F, which, according to DFT calculations, should be characterized by two narrow peaks in the density of states (DOS) (Figure 2.13 D) [9]. Differential conductance spectra (dI/dV) probe the energy-resolved local DOS under the STM tip position and thus are ideal for investigating this question. Figure 2.13 B shows two dI/dV spectra, measured at 5 K, one measured on top of the hydrogen atom in Figure 2.13 A and the other on bare graphene. The dI/dV spectra measured on clean graphene, located far enough away from the hydrogen atom, have the characteristic featureless V shape of graphene, with a minimum at E_F indicating the position of the Dirac point E_D. On the other hand, the dI/dV spectra measured on top of the single H atoms have two narrow peaks, one below and one above E_F, separated in energy by a splitting of ~20 meV. We attribute these two features to the spin-polarized state, in which the Coulomb repulsion is large enough to fully separate the two spin components. The observed charge neutrality (the splitting is essentially symmetric around E_F) and

the well-defined peak splitting indicate the complete spin polarization of the state. DFT calculations show that the magnetic moment associated with the unpaired electron that is left over in the graphene system after H adsorption would be 1 bohr magneton. Our interpretation of the experiment is fully supported by DFT calculations, as can be seen in Figure 2.13 D, which shows the expected DOS for a single H atom in a graphene super cell containing 218 carbon atoms. The theoretical energy splitting showed here is bigger than the experimental one.

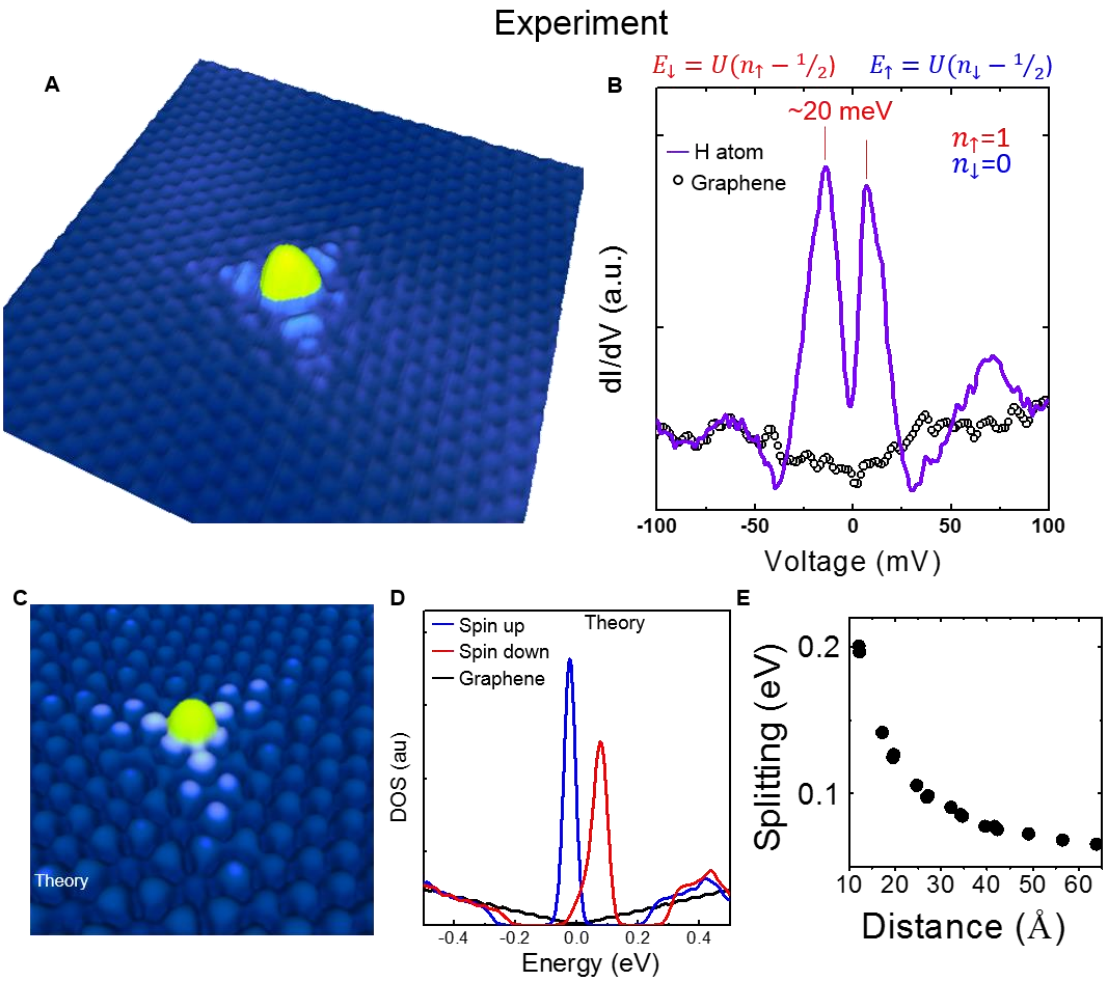

Figure 2.13: Spin split state induced by atomic H on graphene. (A) STM topography of a single H atom chemisorbed on neutral graphene (0.2V, 0.1nA, 7x7nm²). (B) dI/dV spectrum on the H atom, showing the appearance of a fully polarized peak at E_F, and of bare graphene far from the H atom. The spectra were acquired at a nominal junction impedance of 2 GΩ (-100 mV, 50 pA). (C, D) DFT simulated STM image (C) and DOS (D) of a H atom chemisorbed on neutral graphene. (E) Super-cell calculation of the energy splitting between spin up and spin down peaks and its dependence on the distance between hydrogen atoms in adjacent cells.

However, it is known that the energy splitting of the state depends on the size of the graphene super cell [11]. Our theoretical collaborators studied the spin-up spin-down peaks splitting depending on the size of the super-cell used in the calculation and therefore on the localization of the hydrogen induced state at the Fermi level as well as on the parasitic interaction between adjacent cells.

Results of the calculations are shown in Figure 2.13 E. We notice that, as expected [9], the splitting decreases with the size of the super-cell. As the size of the super-cell increases the state is more delocalized, the effective electron-electron interaction U decreases and the energy splitting of the state is smaller (see the sketch of Figure 2.1). The calculations were performed with super-cell sizes up to a 26x26- (1352+1 atoms).The results indicate that the energy splitting extrapolates to a finite non-zero value, which is in agreement with the experimental observations.

In the following sections, we aim to provide further experimental proofs confirming our assignment of the dI/dV signal as a consequence of a local magnetic state where the spin-splitting arises due to coulomb repulsion. If this hypothesis is correct, the magnetic state should fulfil two conditions due to its origin and the low value of the splitting energy of the two peaks:

- It has to be a really extended state.
- The value of the splitting has to depend on $n_{\downarrow}$ and $n_{\uparrow}$, i.e. it has to change with the doping level.

2.4.3 Spatial extension of the H induced graphene polarized state.

As we showed in Figure 2.1, as the value of U decreases, the state gets more delocalized. In the previous section we found a value for U in the order of 20 meV. Now the question is: How large is this value compared to other materials? Elements exhibiting magnetic properties like Co or Fe (from the 3d series) present a value of the Coulomb repusion in the order of 3-5 eV and localized states with a radious around ~1-2 Å. In comparison, the low value of the splitting observed in our measurements points out to a highly delocalized magnetic state. To check the validity of our hypothesis (the two peaks observed in our dI/dV curves have a magnetic origin), we studied with atomic precision the spatial extension of the spin-polarized electronic state induced by a H atom in graphene. To measure this spatial extension we performed the following experiment. First, we found a single isolated hydrogen atom (see Figure 2.14 B). Next, we performed several dI/dV curves (128) along the ~6 nm profile draw by a discontinous line and crossing the H atom and one of the three “arms”. By doing so, and thanks to the high spatial resolution of the STM, we obtained the LDOS in the 128 points of the profile. Now, to better appreciate the extension of the spin-polarized electronic state, we plotted a conductance map with respect to distance and energy [dI/dV(x, E)] than can be seen in Figure 2.14 A. In this conductance map, every vertical line is one dI/dV curve, where the heigh of the spectrum is converted to a colour code, allowing us to follow regions of the same DOS (see Figure 2.14 C). Supperimposed to the conductance map, we have the carbon atoms present along the profile. The green (purple) balls mark the position

of the C atoms in the same (opposite) sublattice to that of the adsorbed single H atom (blue ball). The state extends several nanometers away from the H atom, confirming that it is a quasi-localized graphene state [12]. It presents strong atomic-scale modulations of the peak intensities, with maxima (bright yellow features in the conductance map) corresponding to carbon atoms in the sublattice opposite to the one on which H is chemisorbed (purple balls). On carbon sites in the same sublattice as H chemisorption (green balls), the peaks vanish almost completely. To better appreciate this critical sublattice dependence, we have plotted the dI/dV curves acquired on two neighboring C atoms (m and n) belonging to different sublattices, which we have extracted from the vertical dashed lines outlined in the LDOS(x,E) map of Figure 2.14 A (see Figure 2.14 D). As we said, the spin-polarized state only emerges in the C atom belonging to opposite (purple) sublattice showing no significant weight on the C atom from the same (green) sublattice. The calculated projected density of states (PDOS) for those two particular C atoms shown in Figure 2.14 E, is in very good agreement with our experimental findings.

The experimental dI/dV data obtained here is formed by both spin-up and spin-down contributions. However, since in this system the spin-split state is fully polarized, this is enough to get information about the relative magnetization of each graphene site. Our DFT calculations show that the height of the occupied LDOS peak measured on a carbon atom is very closely correlated with its local magnetic moment. In Figure 2.14 F we compared the local magnetic moment calculated by DFT with the projected density of states (PDOS) peak height on top of some carbon atoms at different distances of the H atom. This is further illustrated in Figure 2.14 G, which shows that the magnetic moment is essentially induced on the carbon atoms in the graphene sublattice opposite to the locus of H chemisorption. Thus, by measuring the spatial evolution of the dI/dV occupied peak height, we can experimentally map the spatial distribution of the local magnetic moment induced by the atomic H chemisorption. This is further plotted in Figure 2.13 H presenting the magnetic moment distribution along the dashed line drawn in Figure 2.14 B, which is extracted from the dI/dV(x,-10meV) horizontal dotted line outlined on the conductance map of Figure 2.14 A. Our data show that the magnetic moment is essentially induced on the carbon atoms belonging to the graphene sublattice opposite to H adsorption.

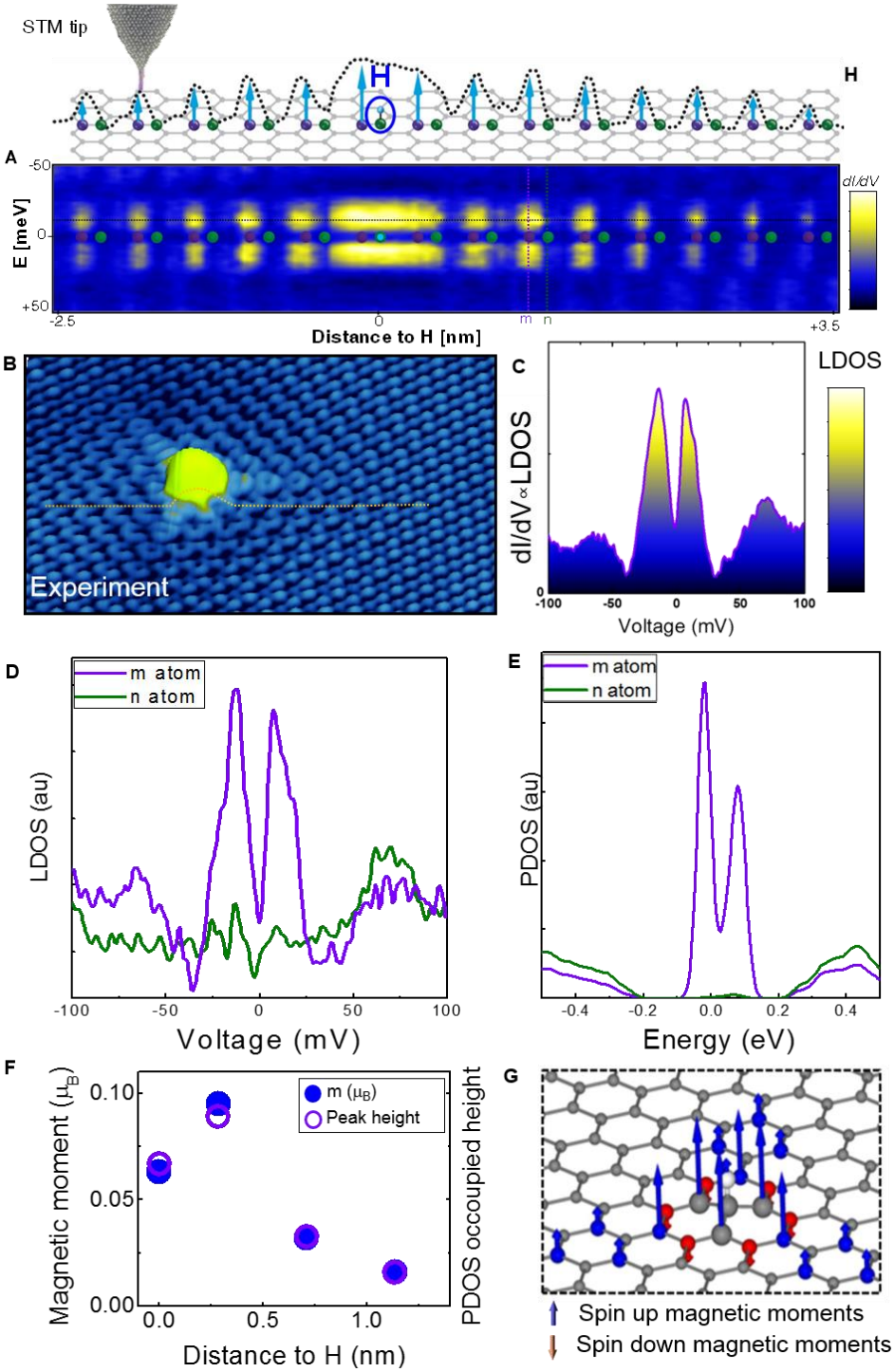

Figure 2.14: Spatial extension of the spin-polarized electronic state induced by H atoms in graphene. (A) Spatially resolved conductance map - dI/dV(x, E) - along the dashed line drawn in (B). Green/purple balls indicate the positions of C atoms along the profile. (B) STM topography of a single H atom on graphene (0.2V, 0.1nA, 7x5nm²). (C) dI/dV curve measured on top of the hydrogen atom in (B) where the same colour code as the one in (A) has been used. (D) dI/dV curves measured on the m and n carbon atoms outlined in (A). (E) PDOS calculated on those m and n carbon atoms. (F) Comparison between local magnetic moment and occupied PDOS peak height calculated on different C atoms. (G) Calculated magnetic moments induced by H chemisorption. (H) Schematic diagram of the graphene structure along the profile drawn in (B), green/purple balls indicating the positions of C atoms belonging to the same/opposite sublattice with respect to H chemisorption. The dotted line shows the evolution of the occupied peak height and the arrows the relative magnetic moment contribution of each C atom, see text.

2.4.4 Confirming H magnetism by doping.

In this chapter we are making a big claim: The adsorption of a single H atom induces a local magnetic moment on graphene. Such claim is essentially supported by our observation of the appearance of two splitted peaks in the LDOS of graphene after adsorption of a single H atom. Thus, we believe it is important to provide an additional independent proof of the magnetic origin of the measured state.

The most traditional way of testing the magnetic origin of a STS signal is the use of an external magnetic field. Still, there is a major difficulty if one wants to measure this system with magnetic fields: the presence of Landau Levels at the same energy range as the split state. Even for the lowest magnetic fields, Landau levels emerge in graphene samples as peaks in the DOS in the same energy rage as the H induced split peaks [28, 47, 48], thus hampering the interpretation of the STS data. For higher fields the situation becomes even more complex, since due to the lifting of symmetry each Landau peak leads to a fourfold quartet [48]. In addition,

On the other hand, graphene offers a nice alternative: the use of electronic doping to change the occupation of the split states. In the introduction, we explained the origin of the H-induced graphene magnetic moment in terms of very simple arguments. There, we introduced the only formula we refer to $E_{\uparrow}=(n_{\downarrow}-1/2)$; $E_{\downarrow}=U(n_{\uparrow}-1/2)$ (see Figure 2.1), from which it is evident that being able to tune the occupation of the levels ($n_{\downarrow}$, $n_{\uparrow}$) would constitute a very natural way to proof its magnetic origin. Indeed, this was first proposed by P. W. Anderson in his seminal work ”Localized Magnetic States in Metals” [49], where he introduced a 2D-phase diagram “to trace out the transition curve from magnetic to non-magnetic behavior”, see Figure 2.15, with the two axes accounting for Δ, the width of the state, and for the energy position of the impurity level with respect to the Fermi level. Following Anderson model, the transition from a magnetic state to a non-magnetic one can be realized by tuning the energy position of the impurity level via graphene-doping (this would correspond to moving along a vertical line (at a fixed value $\pi\Delta$/U) in the original phase diagram proposed by Anderson. Applying the Anderson impurity model to the specific electronic structure of graphene also leads to the conclusion that the magnetic moments of adatoms could be controlled by doping [50].

In this section, we illustrate the influence of doping on localized magnetic moments in terms of the mentioned Anderson Impurity model to then continue with more realistic DFT calculations showing similar results. Finally, we present our experimental results on doped graphene to confirm the validity of these models.

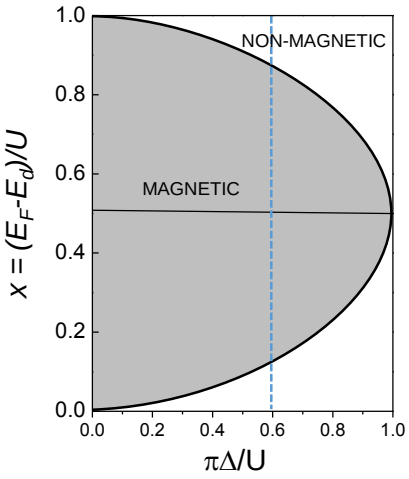

Figure 2.15: Regions of magnetic (grey shadow) and nonmagnetic (white) behaviour. Vertical dashed line outlines the magnetic-nonmagnetic transition due to electronic doping for a fix $\pi\Delta/U = 0.6$ value. Figure adapted from Fig 4 of ref [49].

The Anderson model contains the main ingredients required for an intuitive understanding of the charge tuning of magnetism in graphene after H adsorption. The model considers an impurity atom (described by a single electronic state "d" in the simplest case) in a host material (a metal with a featureless density of states). Anderson identified three important parameters which define the conditions for the existence or absence of localized magnetic states on this impurity: the energy position of the impurity level E_D with respect to the metal Fermi level E_F, the energy width of this state Δ(which results from its coupling with the host material), and the intra-atomic Coulomb repulsion U in the impurity state (Figure 2.16).

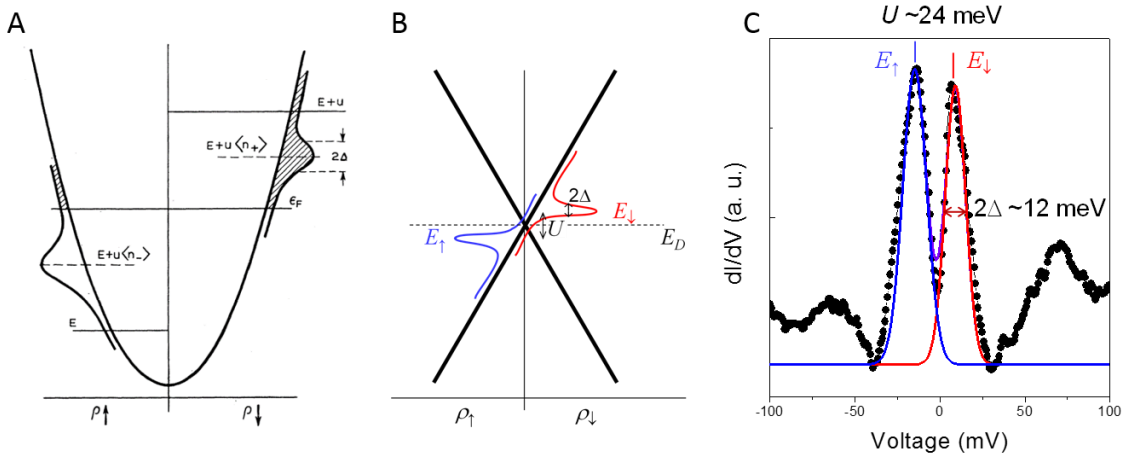

Figure 2.16: Anderson model for H on graphene. (A) Density of state distributions for a local magnetic moment in a magnetic case. The "humps" at E+U(n_-) and E+U(N_+) are the virtual d "levels" of width 2Δ, for up and down spins, respectively (extracted from ref [49]). (B) Schematic illustration of the adaptation of (A) to our specific system. (C) Illustration showing how we extracted the values of U and Δ from our dI/dV curves.

In the 2D-phase diagram of Figure 2.15, a magnetic moment only develops when U is significantly larger than Δ ($\pi\Delta/U<1$). In this case, the behavior depends on the position of E_F with respect to E_D and E_D +U: the magnetic moment, and thus the splitting, is suppressed when E_D +U<E_F or E_D >E_F whatever the value of Δ. For a given Δ value (in our system Δ is fixed by the coupling of the H induced impurity states with the host graphene substrate), the transition from a magnetic state to a non-magnetic one can be realized via electronic doping: this would correspond to moving along a vertical line at a fixed $\pi\Delta/U$ value in the original phase diagram proposed by Anderson (see vertical dashed line in Figure 2.15).

To illustrate this behaviour, we plot in Figure 2.17 the (local) density of states for the two spin components of the impurity resonance (panels Figure 2.17 (a) to (e)) together with the splitting of the two spin components (central panel Figure 2.17 (f)) as a function of (E_F- E_D). The energy of the peaks for majority (spin ↑) and minority (spin ↓) components of the resonance are given by $E_{\uparrow(\downarrow)}$= E_D +U$n_{\uparrow(\downarrow)}$, where $n_{\uparrow(\downarrow)}$ are the occupation of the majority (minority) states (their splitting being U($n_\uparrow$-$n_\downarrow$)) [49]. The origin of the energy is set at the Fermi level for the plots in panels (a) to (e) in Figure 2.17, and a value of $\pi\Delta/U$ =0.6 is chosen to mimic our dI/dV spectra measured for H monomers on neutral graphene. The maximum splitting of the majority and minority spin components of the impurity resonance (and accordingly the maximum spin imbalance $n_\uparrow$-$n_\downarrow$) is obtained for x=0.5 (Figure 2.17 (a)), when the Fermi level is located halfway between the two ↑ and ↓ peaks. When the Fermi level is shifted upwards (x>0.5) or downwards (x<0.5) with respect to E_D, the splitting first decreases (Figure 2.17 (b) and (c)) and eventually disappears (i. e. the local magnetic moment vanishes) for large or small enough x values (Figure 2.17 (d) and (e)).

In other words, starting from the “optimum” situation x=0.5 (maximum splitting or magnetic moment), doping the host material with electrons or holes will initially reduce the splitting (and moment) until it vanishes for sufficient strong doping.

A similar result is obtained by analysing the evolution of the peak splitting with graphene doping using more realistic DFT calculations. DFT calculations corroborate the results of the Anderson impurity model, showing that the splitting of the DOS polarized peak and the associated magnetic moment gradually decreases as we increase the electron doping of the graphene layer. When we add one electron (or hole) per super-cell -and thus per H atom-, only one occupied peak is observed in the DOS with the system becoming non-magnetic (see Figure 2.18). Further electron (hole) doping just shifts the position of the DOS single peak to more negative (positive) energy values, following the change in E_D position. This implies that the first extra-electron (hole) available in the system is used to fill-up (empty) the unpaired electron originated upon H chemisorption and the additional ones for overall electron (hole) doping. If the

split-state had a different non-magnetic (i.e. “one electron”) origin, as it happens for the non-magnetic AB dimer shown in Figure 2.19 (see section 2.6) , we should observe a rigid variation of the peak positions with doping and both of them should still be observed even when the Dirac point is far away from E_F (see Figure 2.19). Our results are consistent with the case of sp^3 defects in graphene, where it was shown that the magnetism could be controlled by doping [18].

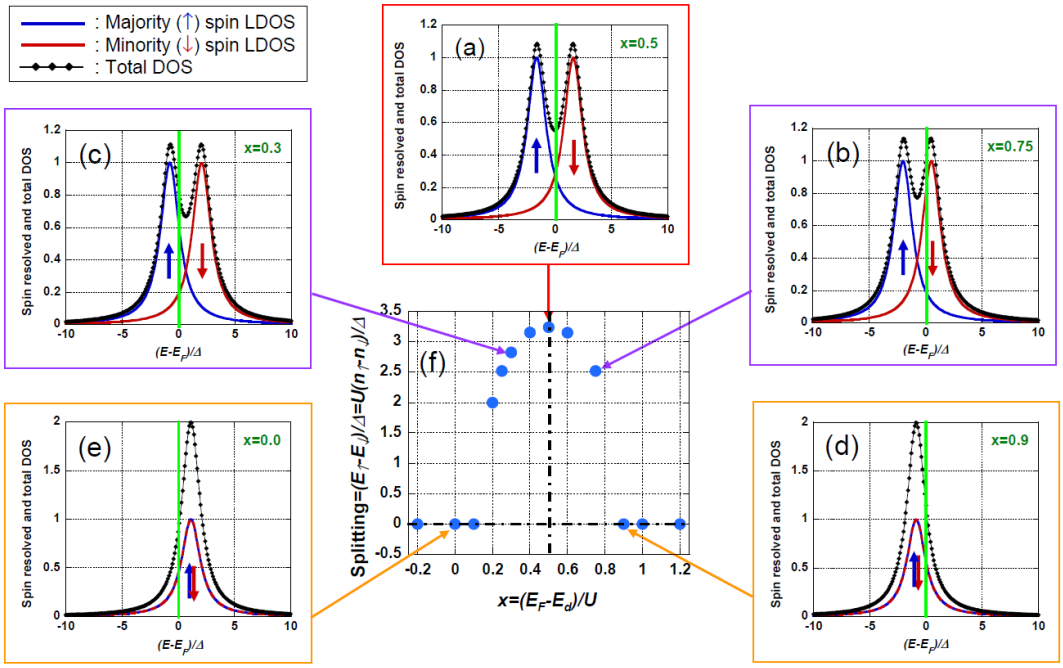

Figure 2.17: Evolution of the peak splitting with doping according to the Anderson impurity model. Here we used $\pi\Delta/U=0.6$. $x=(E_F- E_D)/U$ describes the doping of the host material. x= 0.5, corresponds to the “optimum” case for which states $E_\uparrow$ and $E_\downarrow$ are symmetrically placed about E_F. For large electron or hole doping of the host material, the splitting of the states ($E_\uparrow$ and $E_\downarrow$) vanishes, corresponding to a transition to a non-magnetic state. The spin-resolved and total LDOS on the impurity is plotted in (a) to (e) for selected x values. The splitting between the majority and minority components (in units of Δ), as a function of doping x, is shown in (f).

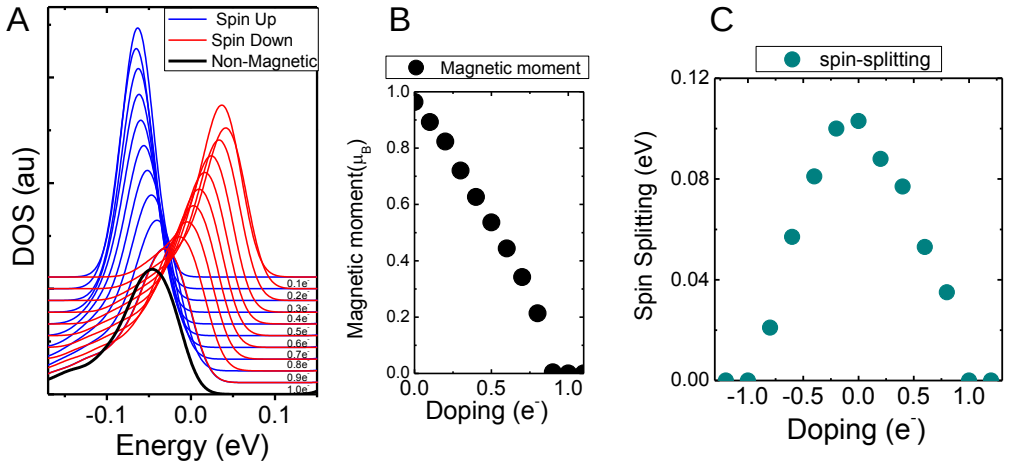

Figure 2.18: Graphene doping with DFT. (A) Calculated DOS for an H atom on graphene for different electronic dopings between 0 and 1.0 electrons per super-cell. (B) Calculated magnetic moment induced by the H atom as a function of electron-doping (C) Calculated spin-splitting induced by the H atom as a function of electron and hole doping.

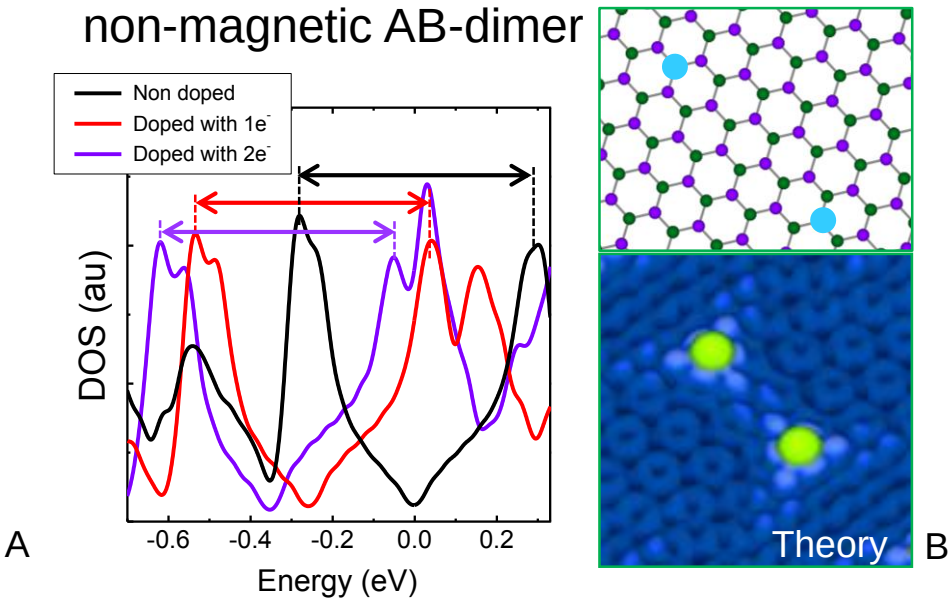

Figure 2.19: Evolution of the DOS of a non-magnetic dimer. (A) Calculated DOS for a non-magnetic AB dimer on graphene for different electronic dopings of 0, 1 and 2 electrons per super-cell. A rigid shift of the two peaks in the DOS associated to the "bonding antibonding" states can be appreciated. (B) Calculated STM image and the corresponding schematic diagram showing the H adsorption sites (blue balls) on graphene (purple and green balls) for the AB dimer calculated in (A).

In order to prove this scenario, we also investigated the spectroscopic signature of single H atoms deposited on top of p- and n-doped graphene layers. The n-doped layer was prepared by growing a "thinner" graphene sample. Due to a small charge transfer from the substrate, the first graphene layers grown on SiC(000-1) are known to be slightly electron doped. Therefore, our n-doped graphene samples had only 2-3 layers, exhibiting n-doping. The p-doped sample was obtained after several cycles of H deposition and further annealing on a 5-7 graphene layers SiC(000-1) sample.

Figure 2.20 A, shows 3 single H atoms adsorbed on a 3-layers thick graphene island on SiC(000-1). Far enough from the H atoms our STS data show a featureless V shape with its minimum, marking the position of E_D, at -0.14eV confirming that the graphene sheet is electron doped (see Figure 2.20 B). We have obtained the same doping level by the analysis of the quasiparticle interferences (QPIs) generated in the vicinity of atomic-size impurities such as the H adatoms [51-53]. STS spectra consecutively measured with the same tip on top of single H atoms show the appearance of a single occupied sharp peak, whose maximum is essentially located at the Dirac point position (see Figure 2.20 B).

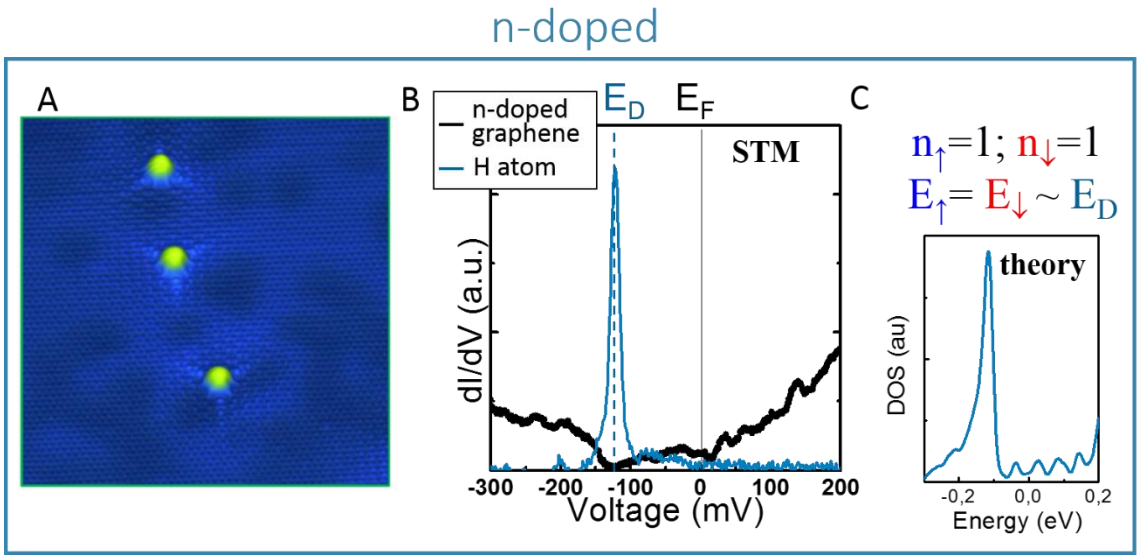

Figure 2.20: H atoms on electron-doped graphene. (A) STM topography showing three single H atom chemisorbed in 3-layers thick graphene on SiC(000-1) (-0.4V, 0.04nA, 20x20nm²). (B) dI/dV spectra measured on single H atoms, purple curve, and clean graphene, black curve. (C) Calculated DOS for the case of a n-doped graphene layer.

As shown by our STS data, graphene hole-doping was achieved after exposing our samples to many cycles of H dosing and further annealing. Our STS data on hole-doped graphene (far enough from any H atom) showed a featureless V shape with its minimum, marking the position of E_D, at positive energies. E_D values between +0.02eV and +0.1eV were typically achieved. Our dI/dV spectra consecutively measured on H atoms chemisorbed on those hole-doped graphene layers, showed the appearance of a single occupied sharp peak at the Dirac point position, see Figure 2.21.

Our dI/dV spectra demonstrate in perfect agreement with the Anderson model, that both n- and p-type doping cause the splitting of the H-induced state to vanish, leading to the appearance of only one sharp peak at ED, as corresponds to a transition to the non-magnetic state. Our results are consistent with the case of sp^3 defects in graphene, where it was shown that the magnetism could be controlled by doping [18].

To summarize, in this section we studied how the adsorption of a single H atom on top of graphene leads to the creation of a magnetic moment of $1\mu_B$ according to theoretical calculations. This magnetic state extends over several nanometres and presents a corrugated texture at the atomic scale. In the following sections we will study how these results are affected by the underlying layers and the impact of the long spatial extension of the state in the interaction between H atoms.

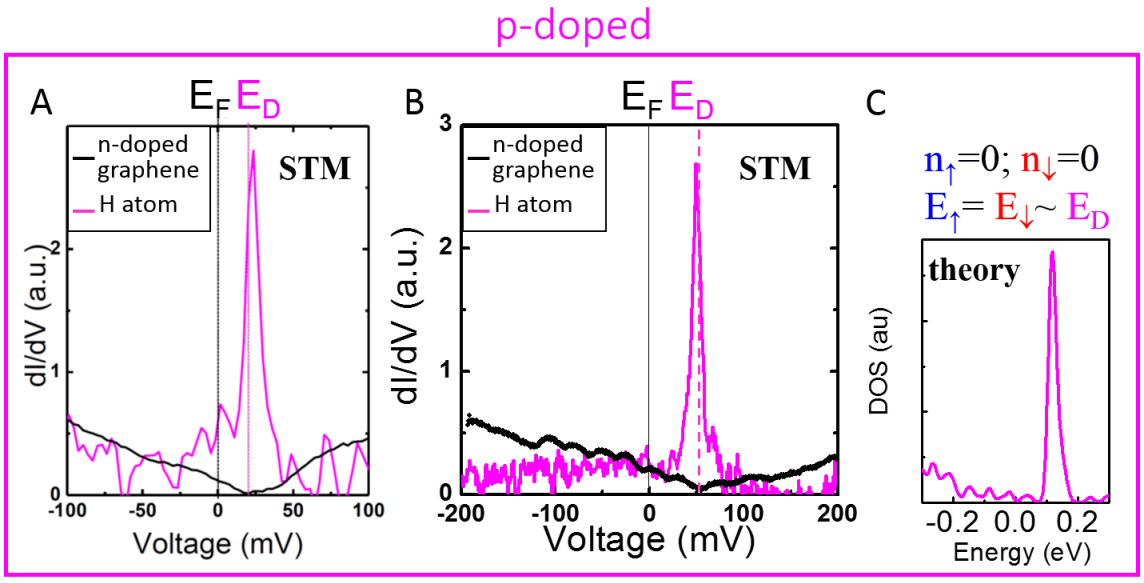

Figure 2.21: H atoms on hole-doped graphene. (A, B) dI/dV spectra measured on single H atoms (pink curve) and clean graphene (black curve) on graphene layers with different hole-doping levels. The graphene layer are hole-doped with ED at +0.025eV (A) and E_D at +0.050eV (A). For both doping levels, dI/dV spectra on H atoms show a single occupied peak at ~E_D position. (C) Calculated DOS for a p-doped graphene layer.

2.5 Influence of the underlying graphene layers.

As we commented in the sample preparation section, to ensure the charge neutrality of the surface graphene layer, a “thick” (5-7 graphene layers) multilayer graphene sample was grown. Although rotational disorder leads to the decoupling of the topmost layer, influence of the underlying layers in the LDOS of isolated H atoms has to be taken into account.

In our sample, for regions presenting large rotation angles (>10 °) between the two upmost graphene layers, the surface graphene layer can essentially be considered as a free standing graphene layer. In Figure 2.22 we present two dI/dV curves obtained in two isolated H atoms in a region where the rotation angle is >15° making the perception of the moiré pattern really difficult. Consecutive spectra measured with the same tip on the two atoms show that in this case there is only some residual influence of the underlying graphene layer, which is reflected in small variations of the relative amplitude between the empty and occupied peaks depending on the actual H atom we are measuring (most likely due to a different C-C stacking for the C atom on top of which the H is chemisorbed).

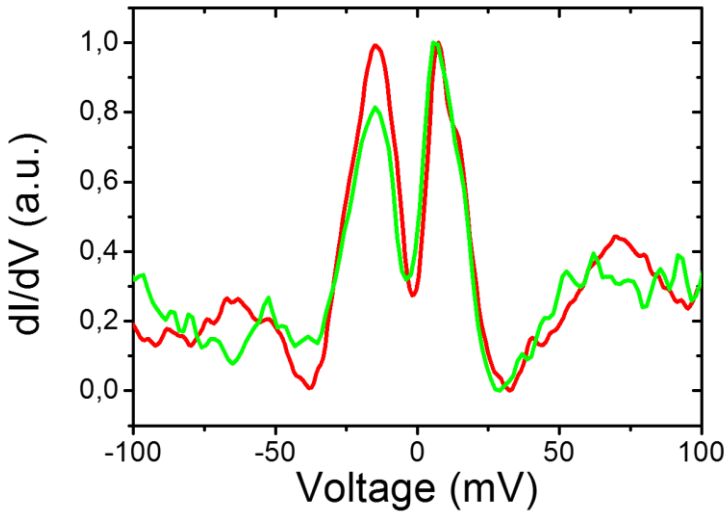

Figure 2.22: Influence of the underlying layer. dI/dV spectra consecutively measured on two isolated H atoms adsorbed on different positions of the same graphene sample terrace. The spectra were acquired at a nominal junction impedance of 2 gigaohm (-100 mV, 50 pA).

For small rotation angles (<10°) between the two upmost graphene layers, the influence of the underlying graphene layer is a bit more perceptible, since the difference in the C-C stacking sequence can even modify slightly the peak-splitting. In Figure 2.23 A we present two single hydrogen atoms adsorbed in a terrace where a moiré pattern arising from a ~5° rotation can be observed. If we now focus on the position with respect to the moiré pattern of our two hydrogen atoms (Figure 2.23 B) we notice that the atom A is in a bright position of the moiré

while the atom B is in a dark region. In Figure 2.23 C we present the dI/dV curves of both hydrogen atoms, showing a slight change in the splitting of the peaks. The fact that our results are not really affected by the underlying layers, makes us believe that the validity of our results can be extended to multi-layer graphene structures (i.e. independently of the stacking sequence) as long as the graphene surface remains neutral.

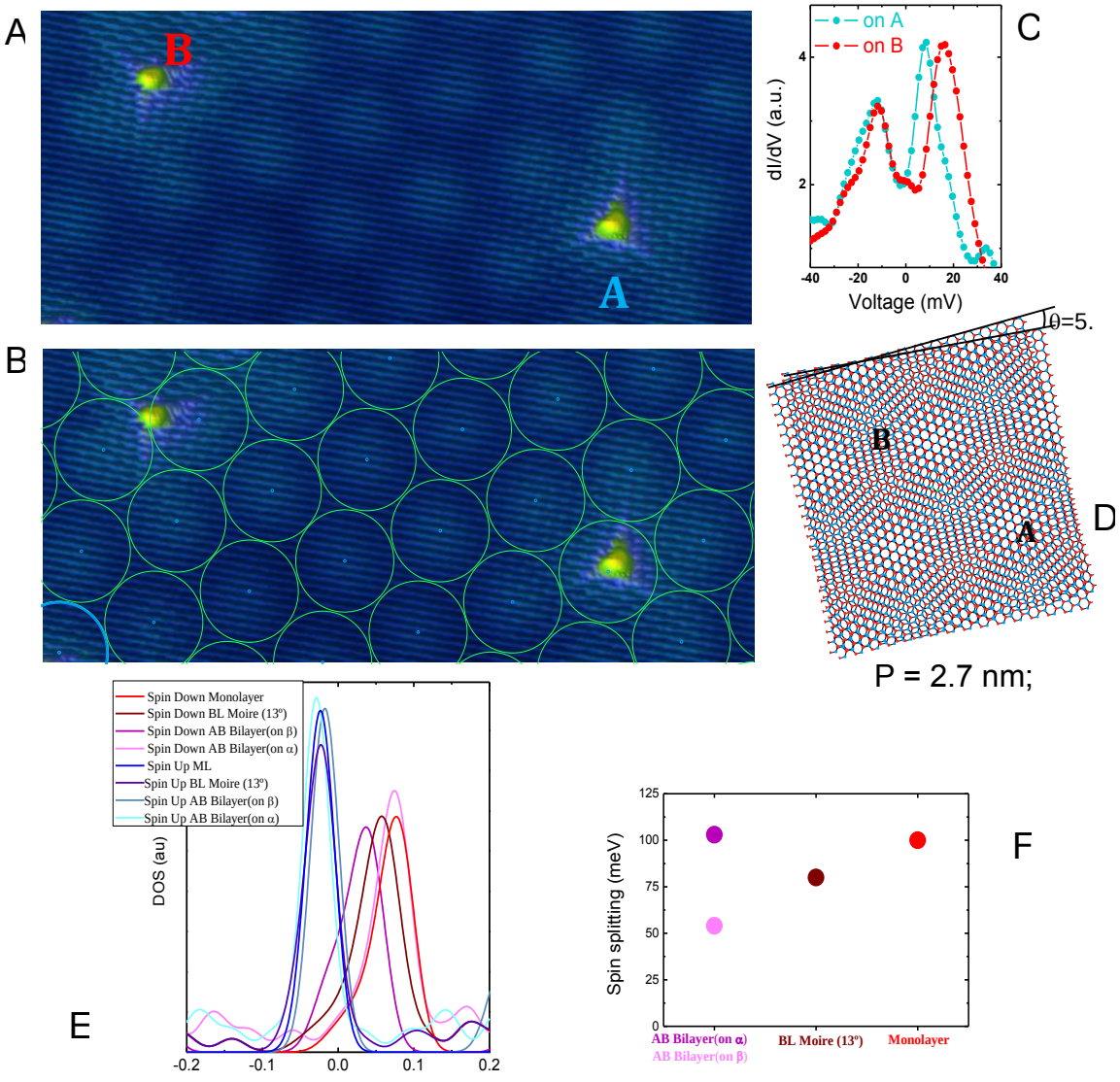

Figure 2.23: DOS of single H atoms on a moiré. A) STM topography of a graphene moiré pattern arising from a θ = 5.3° rotation angle between the two upmost graphene layers (0.2V, 50 pA, 19x8nm²). Two single H atoms chemisorbed on the bright (H atom A) and dark (H atom B) part of the moiré, which correspond to AA and AB stacking regions respectively see panel (D), can be observed. B) Same image as (A) with a schematic moiré (2.7nm periodicity, θ = 5.3°) outlined to better appreciate H adsorption site inside the moiré. C) dI/dV spectra on each single H atom, showing the slightly energy difference in the splitting of the polarized peak. The spectra were acquired consecutively at a nominal junction impedance of 4 gigaohm (-200 mV, 50 pA). D) Illustration of a moiré pattern arising from a θ = 5.3° rotation angle; letters indicate that H atom A is on an AA stacking region and H atom B is on an AB region. E,F) DFT simulated DOS (E) and energy spin splittings (F) for H atoms chemisorbed on graphene with different stackings.

Our results are consistent with calculations from our coworkers where they have shown that as in the case of single layer graphene, the adsorption of H on bilayer graphene or graphite also induces a magnetic moment of $1\mu_B$, mainly, on the host monolayer (see Figure 2.24) [54]. Therefore, we don't expect a big influence of the underlying layers on our results.

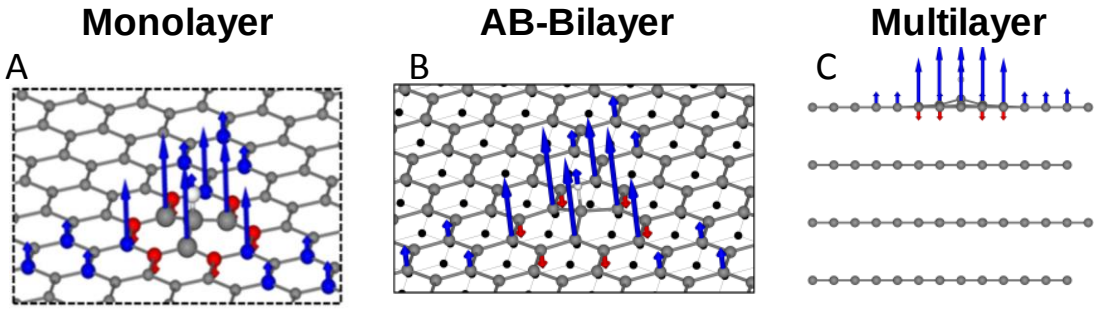

Figure 2.24: Magnetic moment of single H atom on different stackings. A-C) DFT calculations of the relaxed atomic structure and spin polarization around an adsorbed H atom on monolayer, AB stacked bilayer and multilayer graphene respectively. As shown, in all cases, magnetic moments - depicted by blue(red) arrows for spin-up(spin-down)- are induced in the upmost graphene layer. Calculation are used with the same methodology as in this work [54].

However, we performed further DFT calculations, which also show that the underlying graphene layers have little influence with respect to H induced magnetism. In addition, we have calculated the DOS for H atoms chemisorbed on C graphene atoms presenting different C-C stackings, in particular for H on top of α and β C atoms on BL graphene and for 13° twisted bilayer graphene. As shown in Figure 2.23 E, all calculated spectra show the spin polarization of the state independently of the stacking sequence, which only affects to the actual value of the energy spin splitting, see Figure 2.23 F.

2.6 Hydrogen-Hydrogen interaction.

The large extension of the local magnetic moments associated with H chemisorption measured in section 2.4.3, suggests that long-range magnetic interactions mediated by direct exchange should take place. This is different from substrate-mediated interactions such as the Ruderman-Kittel-Kasuya-Yosida interaction, because in this case the coupling results from the direct overlap of magnetized graphene states. In addition, the critical sublattice dependence that we observed for the spin-polarized peak implies that the magnetic coupling should be radically different depending on whether H atoms are adsorbed on the same or different sublattices [55]. Consistent with this expectation, our DFT calculations reveal that two H atoms chemisorbed on the same sublattice (AA dimer) show ferromagnetic coupling with a total spin S = 1, whereas for H atoms on different sublattices (AB dimer), the solution is nonmagnetic. This result is reproduced for all possible H-H arrangements up to the largest distances (~1.5 nm) achievable with our super cell sizes (Figure 2.25). The computed exchange energy for two hydrogen atoms in AA sites at a distance 14.96 Å is: E_{ex} = [(2H in AA with spin 1)-(2H in AA forced to spin 0)] = 35 meV. Furthermore, the total energy of all H dimers that we studied is lower than that of two isolated atoms, confirming the observed tendency of H to form dimers on graphene surfaces at high enough H concentrations [34-36].

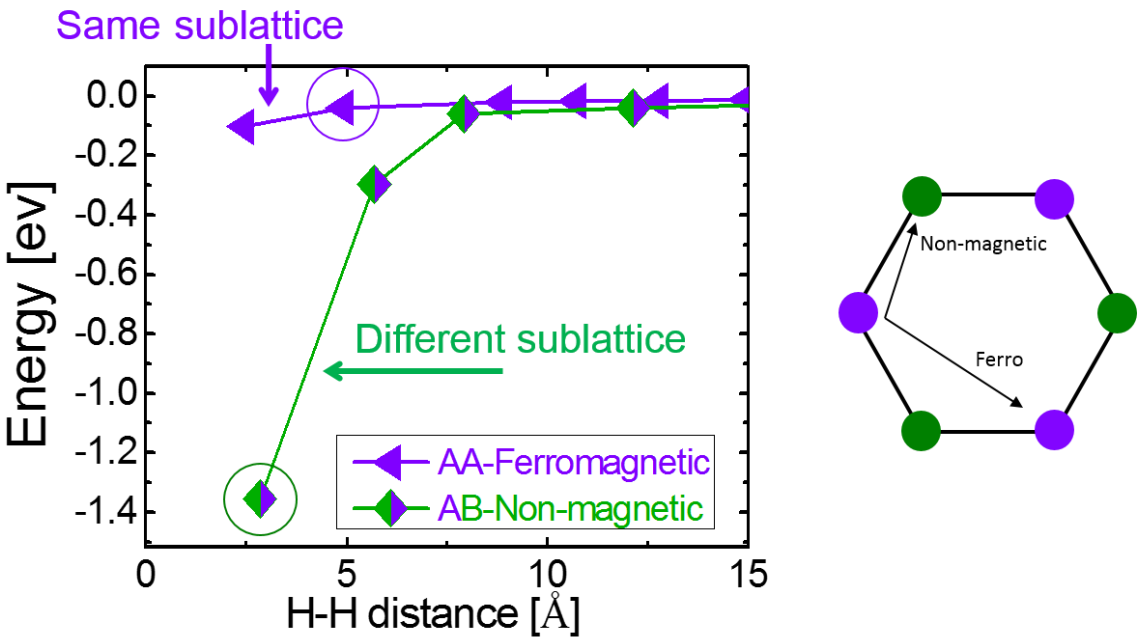

Figure 2.25: H-H dimer interaction. Left panel: Calculated total energy, relative to twice the adsorption energy of a single H atom, and magnetic state of a pair of H atoms adsorbed on the same (AA dimer) and different (AB dimer) sublattices, plotted as a function of the H-H distance. Right panel: Sketch of the magnetic interaction depending on the sublattice.

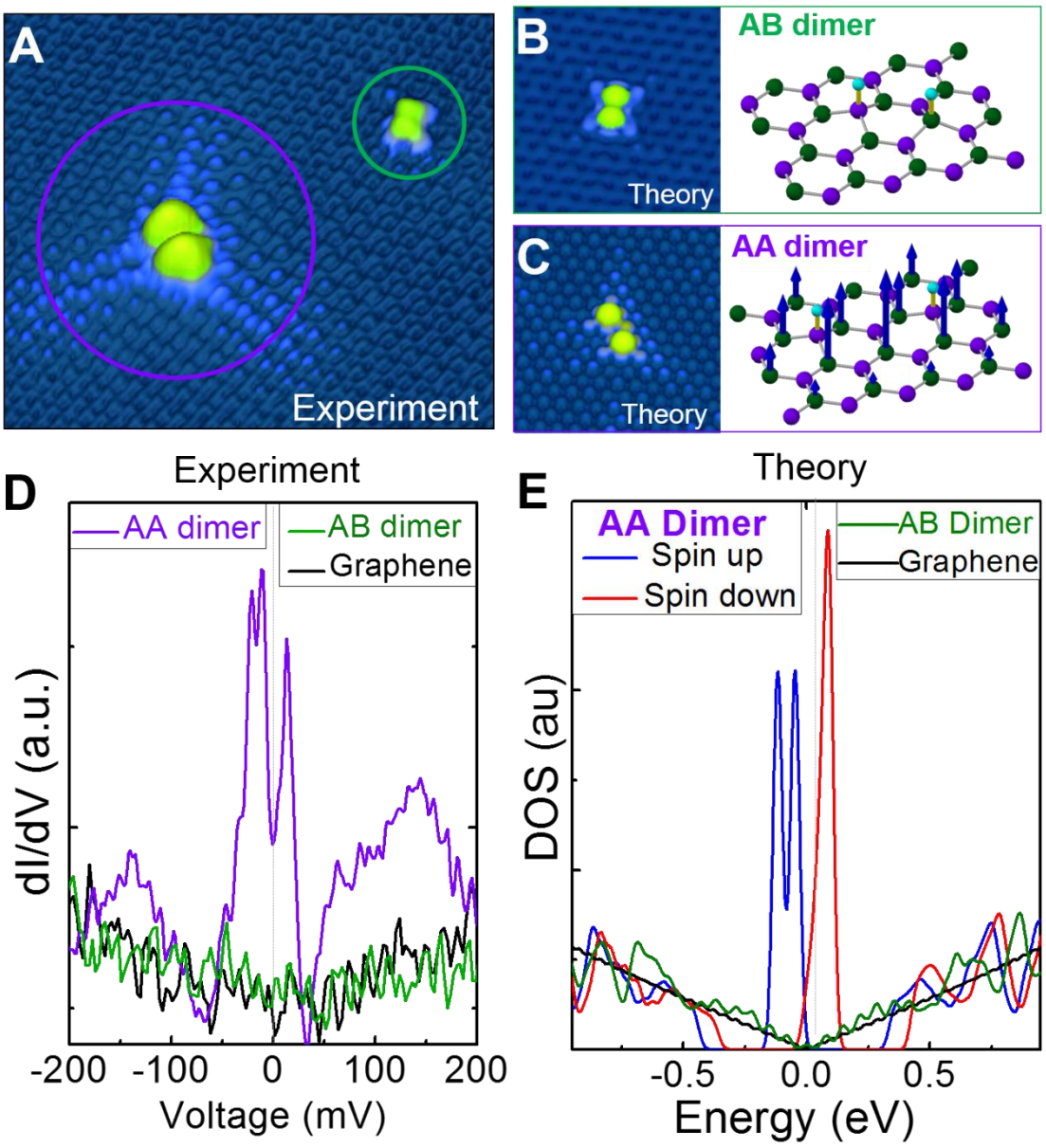

Figure 2.26: Sublattice dependence of the magnetic coupling between neighboring H atoms. (A) STM image showing two different pairs of H atoms, with one pair in an AA (purple circle) and the other pair in an AB (green circle) configuration (0.2 V, 0.1 nA, 7.8 × 6.6 nm²). (B) Calculated STM image of the AB dimer and (C) the AA dimer, with the corresponding diagrams for H atoms (blue balls) on graphene (purple and green balls). (D) Experimental dI/dV spectra and (E) calculated DOS for the AA dimer, AB dimer, and clean graphene. The spectra were acquired at a nominal junction impedance of 8 gigaohms (–400 mV, 50 pA).

To test this scenario experimentally, we explored the local electronic structure of many different H dimers with high-resolution scanning tunneling spectroscopy (STS). The STM image in Figure 2.26 A shows two H dimers in AA (purple circle) and AB (green circle) configurations; the corresponding calculated STM images are shown in Figure 2.26 B and C. The dI/dV spectra acquired on the AB dimer (green line in Figure 2.26 D) show a featureless local DOS that is indistinguishable from that measured on bare graphene (black), as would be expected for a nonmagnetic configuration. In contrast, dI/dV spectra measured

on the AA dimer (purple) show the split state in the vicinity of E_F, as expected for a ferromagnetic coupling between the H atoms. As shown in Figure 2.26 E, our calculated DOS reproduce these observations, confirming the ferromagnetic (nonmagnetic) nature of the AA (AB) dimer. For all H dimers measured in this study, AA dimers presented a fully split state close to E_F, which was absent in AB dimers. Our STS data show that this sublattice-dependent magnetic coupling persists for very long distances, even for H dimers separated by more than 1 nm (see Figure 2.27).

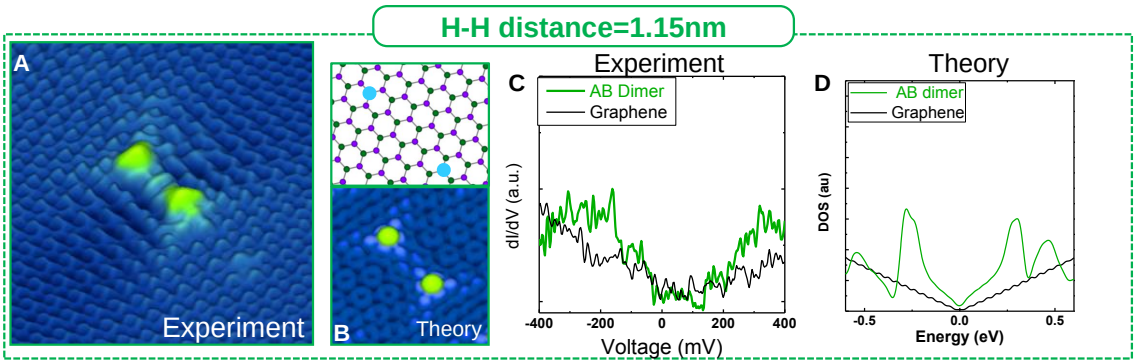

Figure 2.27: H-H coupling at large distances. (A) STM topography of an AB dimer separated by 1.15 nm (-0.2V, 0.05nA, 10×10nm²). (B) Calculated STM image, within the Tersoff-Hamann approximation, and the corresponding schematic diagram showing the H adsorption sites (blue balls) on graphene (purple and green balls) for the AB dimer shown in (A). (C, D) Experimental (C) and calculated (D) DOS generated by the AB dimer and clean graphene.

2.7 Manipulating hydrogen magnetism by STM.

The different magnetic behaviour of AA and AB dimers we have observed, together with the STM ability to perform precise and reproducible atomic manipulations, will allow us to induce magnetic moments on selected graphene regions [56-58]. As we mentioned in chapter 1, section 13, the number of experiments showing STM manipulation of single atoms in graphene are really low. Most of these experiments involve the manipulation of Co atoms. In this section, we will prove for the first time how individual H atoms can manipulated. Indeed, we were able to perform three different kind of manipulations: removing hydrogen atoms, laterally move them, and deposited them on graphene with atomic precision to ultimately tailor their local magnetic state.

Figures 2.28 and 3.29 shows two representative examples of these manipulation experiments, in which the local graphene magnetism was selectively switched on and off. The graphene region in Figure 2.28 A shows two H atoms in an AB dimer configuration. Our STS data measured on those H atoms (Figure 2.27 C) show that this AB dimer configuration does not induce any magnetism on the graphene layer, in good agreement with the coupling rules previously discussed. Figure 2.28 B shows the same graphene region as in Figure 2.28 A, after the controlled extraction of one H atom by carefully approaching it with the STM tip. As shown in Figure 2.28 D, a spin-split state immediately emerges on the graphene layer after the H removal, confirming the creation of a local magnetic moment in graphene. The insets show the corresponding DFT calculations of the resulting magnetic moment for each situation.

We next performed a lateral manipulation on the H dimer, shown in the central region of Figure 2.29 E. Initially, the dimer was in an AA configuration, with both H atoms chemisorbed on the same carbon sublattice. The STS spectrum for that configuration (Figure 2.29 G) shows the presence of a spin-split state, as expected for ferromagnetic coupling. To switch off the graphene magnetic moments induced by this H dimer, we turned it into a nonmagnetic AB dimer configuration by laterally moving one of its H atoms to the opposite sublattice. Figure 2.29 F shows the same graphene region after the H manipulation (the AB dimer in the upper part of the image serves as reference). The STS spectrum measured on the constructed AB dimer shows the disappearance of the polarized peaks, indicating that local graphene magnetism was effectively switched off.

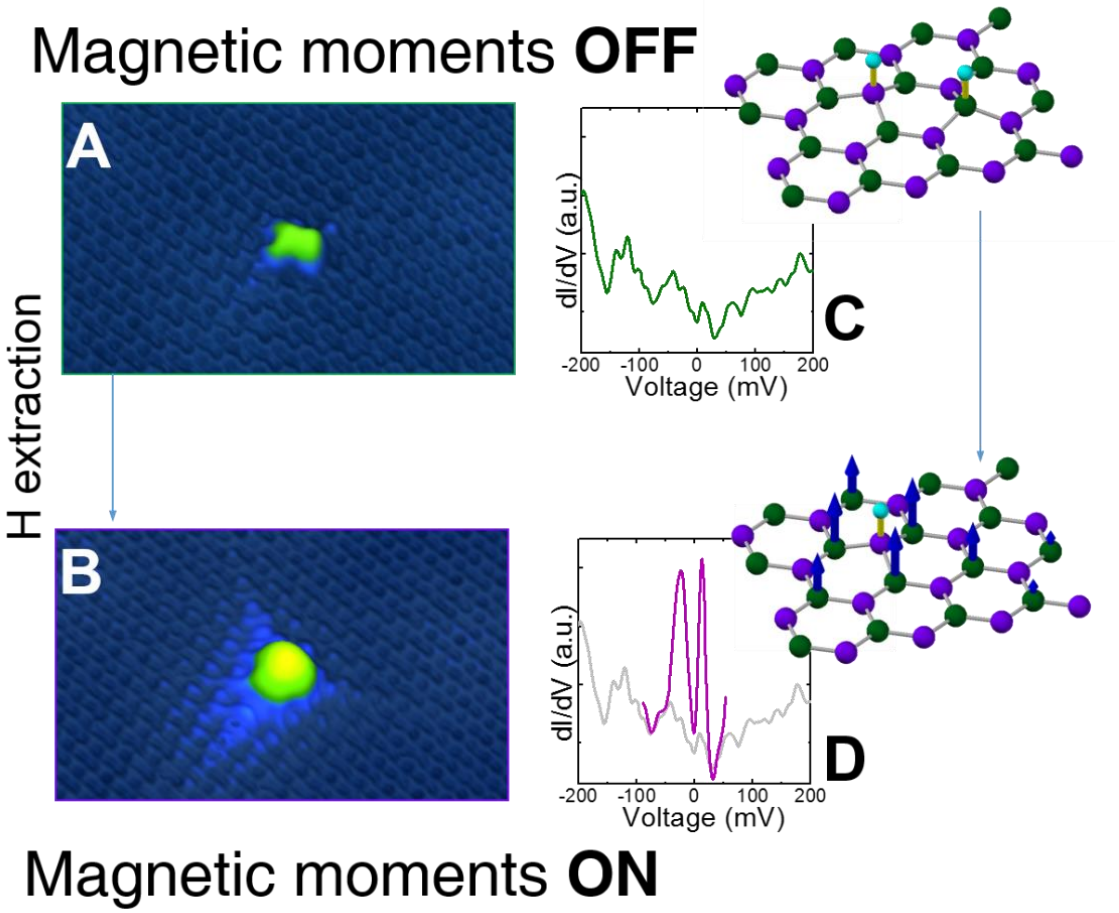

Figure 2.28. Manipulation of graphene local magnetic moments H extraction. (A) STM image of an H dimer in an AB configuration. (B) STM image after the removal of one H atom. (C) dI/dV spectra measured on the AB dimer in (A) and (D) the single H atom in (B).The spectra were acquired at a nominal junction impedance of 4 gigaohms (200 mV, 50 pA). The insets present the corresponding DFT calculations for H atoms (blue balls) on graphene (purple and green balls), with blue arrows being the magnetic moments induced on graphene.

Up to now, we have just showed how to change the graphene magnetic moment using H atoms that are already present in the sample. In the following we present a manipulation experiment, where we deliberately deposited hydrogen atoms with our STM tip in order to perform manipulations involving a larger number of spins. By doing so, one can explore the possibility of selectively tuning the collective magnetic moment in a graphene region by inducing an imbalance between H atoms on opposing sublattices A and B. In order to perform this complex manipulation experiments, three different manipulation processes need to be used: removing hydrogen atoms, depositing hydrogen atoms and laterally moving hydrogen atoms. So we will first detail the experimental methodology to perform each of the processes and then proceed with the real experimental realization.

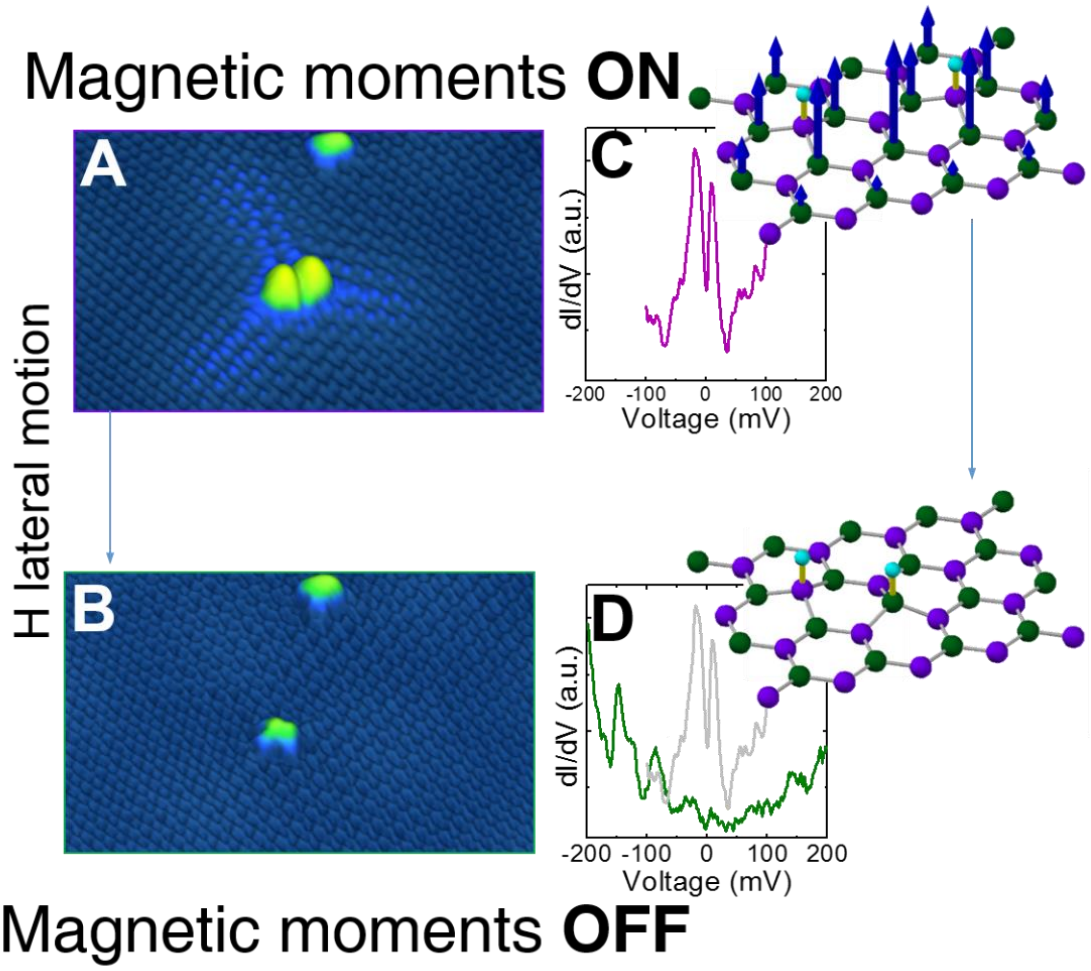

Figure 2.29. Manipulation of graphene local magnetic moments by H lateral motion. (A) STM image of an H dimer in an AA configuration. (B) STM image after laterally moving one H atom. (C) dI/dV spectra measured on the AA dimer in (A) and (D) the AB dimer in (B). The spectra were acquired at a nominal junction impedance of 4 gigaohms (200 mV, 50 pA. Tunneling parameters were 0.2 V, 0.1 nA, and 6.5 × 4.0 nm² for (A) and (B); 0.2 V,0.1 nA, and 9.5 × 5.5nm² for (E) and (F).

To selectively remove H atoms from the graphene sample we approached the STM tip towards the sample. This can be done by continuously increasing, under feedback control, the set point tunneling current on top of the selected H atom until it is desorbed, or by switching the feedback off and slightly decreasing the tip-sample distance on top of it. It is also possible to completely remove all H atoms from a graphene region by imaging it at high currents. The precise tunneling values for the manipulation depend on each specific tip apex, but for the same tip apex those values are very reproducible. As a rough guide, for removing H atoms it is usually enough to approach the STM tip by 1-2 Å.

The deposition of H atoms is done by applying negative sample voltages pulses. In order to deposit H atoms, we first need to pick them up from the graphene surface, so the tip can act as an H reservoir. Then by applying negative sample voltages pulses the H atoms are deposited on the selected graphene

region under the tip position (see Figure 2.29 B). Again, the voltage threshold for H deposition might vary from tip to tip, but values of around -5 V are usually enough for H deposition.

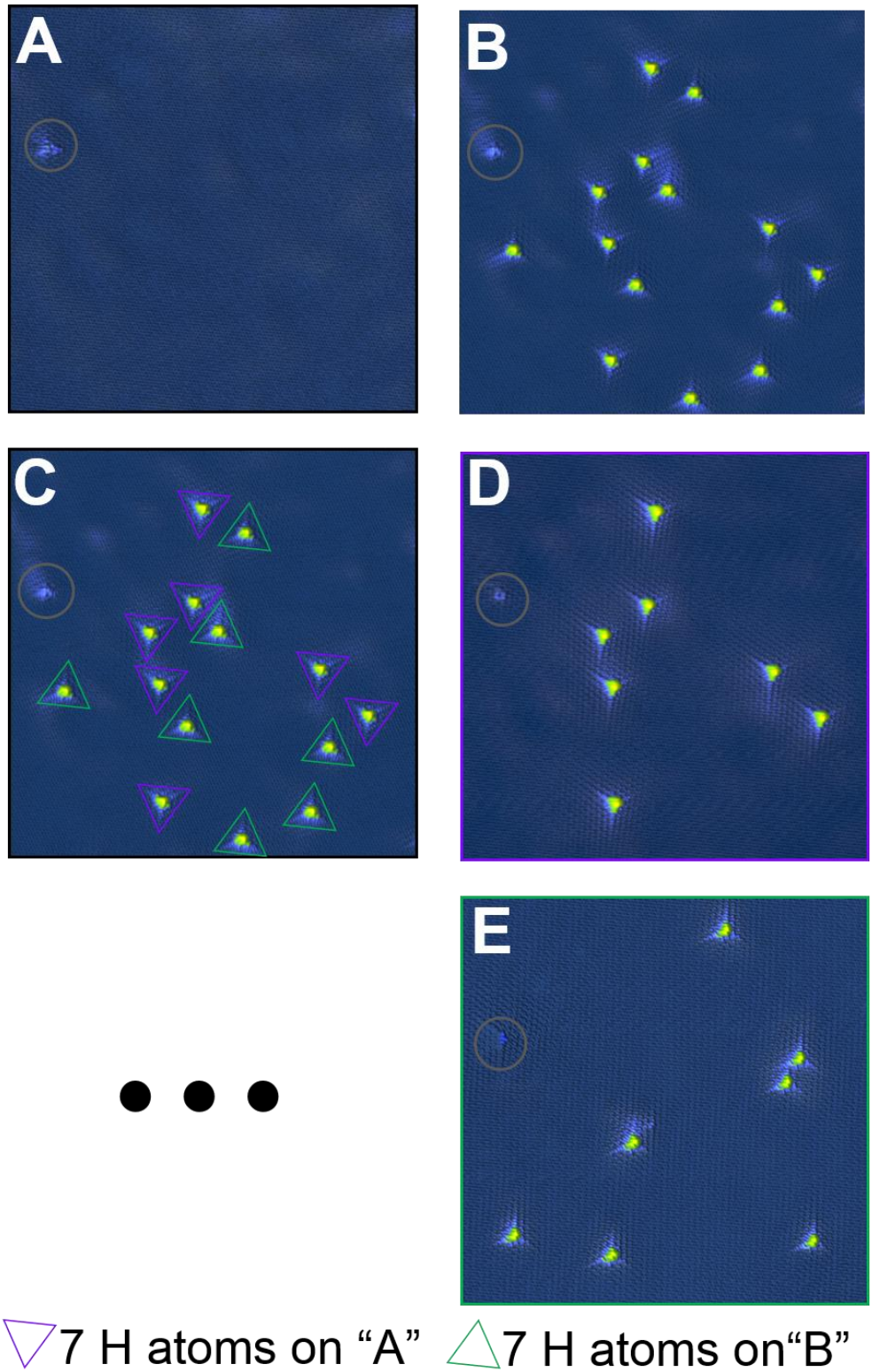

Figure 2.30: Manipulations involving 14 H atoms. (A to E) STM images showing the same graphene region during different steps of a manipulation experiment involving a large number of H atoms. The point defect outlined with a gray circle is used as a reference. Tunneling parameters were 0.4 V,0.03 nA, and 28 × 28 nm².

To laterally move hydrogen atoms, small positive sample voltages are used while measuring close to the hydrogen atoms.

With this methodology, we can now proceed to perform more sophisticated manipulations involving a greater number of H atoms. In Figure 2.29 A to E, we present an example in which we first removed all H atoms from a graphene region by using the STM tip (Figure 2.30 A). Then, we selectively deposited 14 H atoms on this same region to reach a configuration with seven H atoms chemisorbed on each graphene sublattice (Figure 2.30 B). Our experimental findings and existing calculations [9, 14] indicate that a very low (if any) net magnetic moment should be expected on this region, because of these equal sublattice populations. Next, by selectively removing all the H atoms chemisorbed on sublattice B, we created a ferromagnetic configuration with the seven remaining H atoms on sublattice A (Figure 2.30 D). As the final step, we combined several manipulation processes to reverse the situation and construct an H arrangement with all seven H atoms chemisorbed on sublattice B (Figure 2.30 E). The degree of complexity shown in our manipulation experiments demonstrates the high reproducibility of the procedure, which paves the way to the realization of atomically controlled experiments in graphene magnetism, an area that has thus far been restricted to a purely theoretical framework.

Due to the low number of manipulation experiments in graphene, we believe it is important to understand the process behind our hydrogen manipulation. In order to get a deeper comprehension, we asked our collaborators from the group of J.J. Palacios to perform some calculations. The results can be observed in Figure 2.31. They consist of a pyramidal Pt tip approaching a H atom adsorbed on graphene. The calculated adsorption energy of a H atom on the Pt tip apex is around 2.8 eV. Because of the difference between the adsorption energy for H on graphene (around 1 eV) and that on the Pt tip, it can be inferred that H prefers to adsorb on the Pt tip, the only obstacle being the desorption barrier. This barrier can be suppressed by approaching progressively the tip to the deposited H. Figure 2.31 shows the evolution of the binding energy curve of the H atom in between the tip and graphene. When the tip gets closer, both adsorption energy minima merge at some point. When retracting the tip the desorption barrier builds up again, but now with the H adsorbed on the Pt tip. The blue and red arrows indicate the spin density on the atoms. The Pt tip apex also develops a magnetic moment, but it is not depicted for clarity.

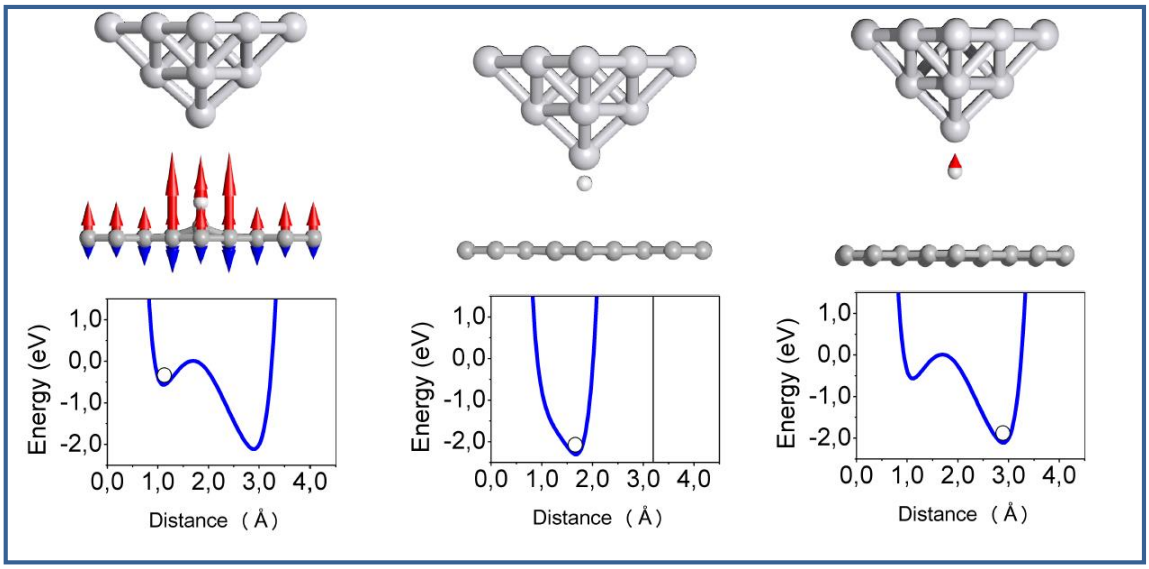

Figure 2.31: Hydrogen manipulation by DFT. DFT calculation of the evolution of the binding energy of the H atom in between the tip and graphene as a function of tip-sample distance.

The manipulation of H with the Pt tip has been modelled through the DFT+ Green's function methodology as implemented in ANT.G [59-61]. The DFT part in this code is performed by Gaussian [62]. Only the electrons from the $5s^2$, $5p^6$, $5d^9$ and $6s^1$ shells of Pt were treated explicitly, while the shells below these were replaced by Effective Core Potentials (ECP), as is the case of the LanL2DZ basis set in the Gaussian code. In the case of H, the same type of basis set reproduces the complete electronic structure without the need of ECP potentials. Finally, the bonding carbon atom was treated with the complete basis set LanL2DZ describing the six electrons, while the other carbon atoms were described by the minimum basis set CRENBS in which only the $2s^2$ and $2p^2$ shells are treated explicitly, with the others replaced by an ECP potential. The functional used was BLYP, which typically leads to proper results for covalent and metallic bonds in both organic and metallic elements. The functional used was BLYP [63] , which typically leads to proper results for covalent and metallic bonds in both organic and metallic elements, complemented with dispersion forces through the GD3 Grimme implementation [64].

2.8 Conclusions.

In this chapter, we have investigated the possibility to induce local magnetic moments on graphene by adsorbing single H atoms. From the experimental results, obtained on our UHV-LT-STM, together with DFT calculations, the main conclusions we can extract are:

-By means of thermal dissociation of H_2, single hydrogen atoms can be deposited on the surface of graphene grown on SiC(000-1). The trigonal symmetry and their characteristic $\sqrt{3}\times\sqrt{3}$ interference pattern in the STM images, have allowed us to identify them as well as their adsorption site.

-The STS spectra acquired at 5K on top of single hydrogen atoms has shown, for the first time, the existence of a spin-splitted peak ~20 meV at the Fermi level. This agrees with existing theoretical calculations which predicted a moment of $1\mu_B$ associated to H adsorption.

-The spatial extension of the spin-splitted state has been studied by means of STS experiments. It extends over several nanometres and presents strong atomic-scale modulation of the peak height. The state is essentially localized on the carbon atoms belonging to the opposite sublattice where the hydrogen atom was adsorbed. DFT calculations corroborate the sublattice dependence as well as the slow decay of the state.

-Using the Anderson model, together with DFT calculations we studied the evolution of the spin-splitted peaks depending on the doping of the graphene layer. These calculations showed that if our two peaks have a magnetic origin, for high enough doping they should turn into one peak situated at the energy of the Dirac point. Our STS measurements on single hydrogen atoms in both n- and p-doped graphene samples, confirmed the calculations, exhibiting one peak at the Dirac point energy. These results represent an independent proof of the magnetic origin of the splitted state measured in our experiments.

- The magnetic interaction induced by neighbouring H atoms on graphene has been studied, showing that dimers where the two H atoms are adsorbed in the same sublattice have a ferromagnetic coupling while the magnetism is suppresed for hydrogen atoms adsorbed in opposite sublattices.

-We have demonstrated the possibility to extract, move and deposit hydrogen atoms. Using the STM ability to perform manipulations at the atomic scale, we showed how to modify the magnetic moment of dimers or how to create controlled arrangements of hydrogen atoms.

References

1. Tombros, N., et al., *Electronic spin transport and spin precession in single graphene layers at room temperature.* Nature, 2007. **448**(7153): p. 571-U4.
2. Han, W. and R.K. Kawakami, *Spin Relaxation in Single-Layer and Bilayer Graphene.* Physical Review Letters, 2011. **107**(4).
3. Fujita, M., et al., *Peculiar localized state at zigzag graphite edge.* Journal of the Physical Society of Japan, 1996. **65**(7): p. 1920-1923.
4. Vozmediano, M.A.H., et al., *Local defects and ferromagnetism in graphene layers.* Physical Review B, 2005. **72**(15).
5. Edwards, D.M. and M.I. Katsnelson, *High-temperature ferromagnetism of sp electrons in narrow impurity bands: application to CaB 6.* Journal of Physics: Condensed Matter, 2006. **18**(31): p. 7209.
6. Han, W., et al., *Graphene spintronics.* Nat Nano, 2014. **9**(10): p. 794-807.
7. Lehtinen, P.O., et al., *Irradiation-induced magnetism in graphite: A density functional study.* Physical Review Letters, 2004. **93**(18): p. 187202.
8. Fernandez-Rossier, J. and J.J. Palacios, *Magnetism in graphene nanoislands.* Physical Review Letters, 2007. **99**(17): p. 177204.
9. Yazyev, O.V. and L. Helm, *Defect-induced magnetism in graphene.* Physical Review B, 2007. **75**(12): p. 125408.
10. Palacios, J.J., J. Fernández-Rossier, and L. Brey, *Vacancy-induced magnetism in graphene and graphene ribbons.* Physical Review B, 2008. **77**(19): p. 195428.
11. Yazyev, O.V., *Emergence of magnetism in graphene materials and nanostructures.* Reports on Progress in Physics, 2010. **73**(5): p. 056501.
12. Pereira, V.M., et al., *Disorder induced localized states in graphene.* Physical Review Letters, 2006. **96**(3): p. 036801.
13. Santos, E.J.G., A. Ayuela, and D. Sanchez-Portal, *Universal magnetic properties of sp(3)-type defects in covalently functionalized graphene.* New Journal of Physics, 2012. **14**.
14. Lieb, E.H., *2 Theorems on the Hubbard-Model.* Physical Review Letters, 1989. **62**(10): p. 1201-1204.
15. Ugeda, M.M., et al., *Missing Atom as a Source of Carbon Magnetism.* Physical Review Letters, 2010. **104**(9).
16. Nair, R.R., et al., *Spin-half paramagnetism in graphene induced by point defects.* Nature Physics, 2012. **8**(3): p. 199-202.
17. McCreary, K.M., et al., *Magnetic Moment Formation in Graphene Detected by Scattering of Pure Spin Currents.* Physical Review Letters, 2012. **109**(18): p. 186604.
18. Nair, R.R., et al., *Dual origin of defect magnetism in graphene and its reversible switching by molecular doping.* Nature Communications, 2013. **4**: p. 2010.
19. Balakrishnan, J., et al., *Colossal enhancement of spin-orbit coupling in weakly hydrogenated graphene.* Nature Physics, 2013. **9**(5): p. 284-287.
20. Kohler, U., et al., *On the road to an all-oxide spin-transistor: study of magnetotransport properties of magnetite/Nb : STO interfaces.* Journal of Magnetism and Magnetic Materials, 2004. **272**: p. E1437-E1438.
21. Han, K.H., et al., *Ferromagnetic spots in graphite produced by proton irradiation.* Advanced Materials, 2003. **15**(20): p. 1719-+.
22. Esquinazi, P., et al., *Induced magnetic ordering by proton irradiation in graphite.* Physical Review Letters, 2003. **91**(22).
23. Ugeda, M.M., et al., *Point Defects on Graphene on Metals.* Physical Review Letters, 2011. **107**(11).
24. Ugeda, M.M., et al., *Electronic and structural characterization of divacancies in irradiated graphene.* Physical Review B, 2012. **85**(12).

25. Latil, S., V. Meunier, and L. Henrard, *Massless fermions in multilayer graphitic systems with misoriented layers: Ab initio calculations and experimental fingerprints.* Physical Review B, 2007. **76**(20).
26. Hass, J., et al., *Why multilayer graphene on 4H-SiC(000(1)over-bar) behaves like a single sheet of graphene.* Physical Review Letters, 2008. **100**(12): p. 125504.
27. Shallcross, S., S. Sharma, and O.A. Pankratov, *Quantum interference at the twist boundary in graphene.* Physical Review Letters, 2008. **101**(5).
28. Miller, D.L., et al., *Observing the Quantization of Zero Mass Carriers in Graphene.* Science, 2009. **324**(5929): p. 924-927.
29. Sadowski, M.L., et al., *Landau level spectroscopy of ultrathin graphite layers.* Physical Review Letters, 2006. **97**(26).
30. Sprinkle, M., et al., *First Direct Observation of a Nearly Ideal Graphene Band Structure.* Physical Review Letters, 2009. **103**(22).
31. Zhou, S.Y., et al., *Departure from the conical dispersion in epitaxial graphene.* Physica E-Low-Dimensional Systems & Nanostructures, 2008. **40**(7): p. 2642-2647.
32. Varchon, F., et al., *Rotational disorder in few-layer graphene films on 6H-SiC(000-1): A scanning tunneling microscopy study.* Physical Review B, 2008. **77**(16): p. 165415.
33. Hiebel, F., et al., *Structure and stability of the interface between graphene and 6H-SiC(000-1) (3 x 3): an STM and ab initio study.* Journal of Physics D-Applied Physics, 2012. **45**(15).
34. Balog, R., et al., *Atomic Hydrogen Adsorbate Structures on Graphene.* Journal of the American Chemical Society, 2009. **131**(25): p. 8744-+.
35. Hornekaer, L., et al., *Clustering of chemisorbed H(D) atoms on the graphite (0001) surface due to preferential sticking.* Physical Review Letters, 2006. **97**(18): p. 186102.
36. Sljivancanin, Z., et al., *Extended atomic hydrogen dimer configurations on the graphite(0001) surface.* Journal of Chemical Physics, 2009. **131**(8): p. 084706.
37. Hohenberg, P. and W. Kohn, *INHOMOGENEOUS ELECTRON GAS.* Physical Review B, 1964. **136**(3B): p. B864.
38. Kohn, W. and L.J. Sham, *Self-Consistent Equations Including Exchange and Correlation Effects.* Physical Review, 1965. **140**(4A): p. 1133-&.
39. Ordejón, P., et al., Physical Review B, 1996. **53**: p. R10411.
40. Soler, J.M., et al., *The SIESTA method for ab initio order-N materials simulation.* Journal of Physics-Condensed Matter, 2002. **14**(11): p. 2745-2779.
41. Sankey, O.F. and D.J. Niklewski, *Abinitio Multicenter Tight-Binding Model for Molecular-Dynamics Simulations and Other Applications in Covalent Systems.* Physical Review B, 1989. **40**(6): p. 3979-3995.
42. Perdew, J.P. and W. Yue, *Accurate and Simple Density Functional for the Electronic Exchange Energy - Generalized Gradient Approximation.* Physical Review B, 1986. **33**(12): p. 8800-8802.
43. Methfessel, M. and A.T. Paxton, *High-precision sampling for Brillouin-zone integration in metals.* Physical Review B, 1989. **40**(6): p. 3616-3621.
44. Hornekaer, L., et al., *Metastable Structures and Recombination Pathways for Atomic Hydrogen on the Graphite (0001) Surface.* Physical Review Letters, 2006. **96**(15): p. 156104.
45. Mizes, H.A. and J.S. Foster, *Long-Range Electronic Perturbations Caused by Defects Using Scanning Tunneling Microscopy.* Science, 1989. **244**(4904): p. 559-562.
46. Ruffieux, P., et al., *Hydrogen atoms cause long-range electronic effects on graphite.* Physical Review Letters, 2000. **84**(21): p. 4910-4913.
47. Li, G.H., A. Luican, and E.Y. Andrei, *Scanning Tunneling Spectroscopy of Graphene on Graphite.* Physical Review Letters, 2009. **102**(17).
48. Song, Y.J., et al., *High-resolution tunnelling spectroscopy of a graphene quartet.* Nature, 2010. **467**(7312): p. 185-189.

49. Anderson, P.W., *Localized magnetic states in metals.* Physical Review, 1961. **124**(1).
50. Uchoa, B., et al., *Localized magnetic states in graphene.* Physical Review Letters, 2008. **101**(2): p. 026805.
51. Rutter, G.M., et al., *Scattering and interference in epitaxial graphene.* Science, 2007. **317**(5835): p. 219-222.
52. Brihuega, I., et al., *Quasiparticle Chirality in Epitaxial Graphene Probed at the Nanometer Scale.* Physical Review Letters, 2008. **101**(20): p. 4.
53. Mallet, P., et al., *Role of pseudospin in quasiparticle interferences in epitaxial graphene probed by high-resolution scanning tunneling microscopy.* Physical Review B, 2012. **86**(4): p. 14.
54. Moaied, M., J.V. Alvarez, and J.J. Palacios, *Hydrogenation-induced ferromagnetism on graphite surfaces.* Physical Review B, 2014. **90**(11): p. 12.
55. Ferro, Y., et al., *Stability and magnetism of hydrogen dimers on graphene.* Physical Review B, 2008. **78**(8).
56. Eigler, D.M. and E.K. Schweizer, *Positioning Single Atoms with a Scanning Tunneling Microscope.* Nature, 1990. **344**(6266): p. 524-526.
57. Shen, T.C., et al., *Atomic-Scale Desorption through Electronic and Vibrational-Excitation Mechanisms.* Science, 1995. **268**(5217): p. 1590-1592.
58. Khajetoorians, A.A., et al., *Current-Driven Spin Dynamics of Artificially Constructed Quantum Magnets.* Science, 2013. **339**(6115): p. 55-59.
59. Palacios, J.J., et al., *Fullerene-based molecular nanobridges: A first-principles study.* Physical Review B, 2001. **64**(11): p. 115411.
60. Palacios, J.J., et al., *First-principles approach to electrical transport in atomic-scale nanostructures.* Physical Review B, 2002. **66**(3): p. 035322.
61. Jacob, D. and J.J. Palacios, *Critical comparison of electrode models in density functional theory based quantum transport calculations.* The Journal of Chemical Physics, 2011. **134**(4): p. 044118.
62. Frisch, M.J., et al., *Gaussian 09*. 2009, Gaussian, Inc.: Wallingford, CT, USA.
63. Miehlich, B., et al., *RESULTS OBTAINED WITH THE CORRELATION-ENERGY DENSITY FUNCTIONALS OF BECKE AND LEE, YANG AND PARR.* Chemical Physics Letters, 1989. **157**(3): p. 200-206.
64. Grimme, S., et al., *A consistent and accurate ab initio parametrization of density functional dispersion correction (DFT-D) for the 94 elements H-Pu.* Journal of Chemical Physics, 2010. **132**(15).

Chapter 3: Adsorption mechanism of hydrogen on Gr/SiC(000-1)

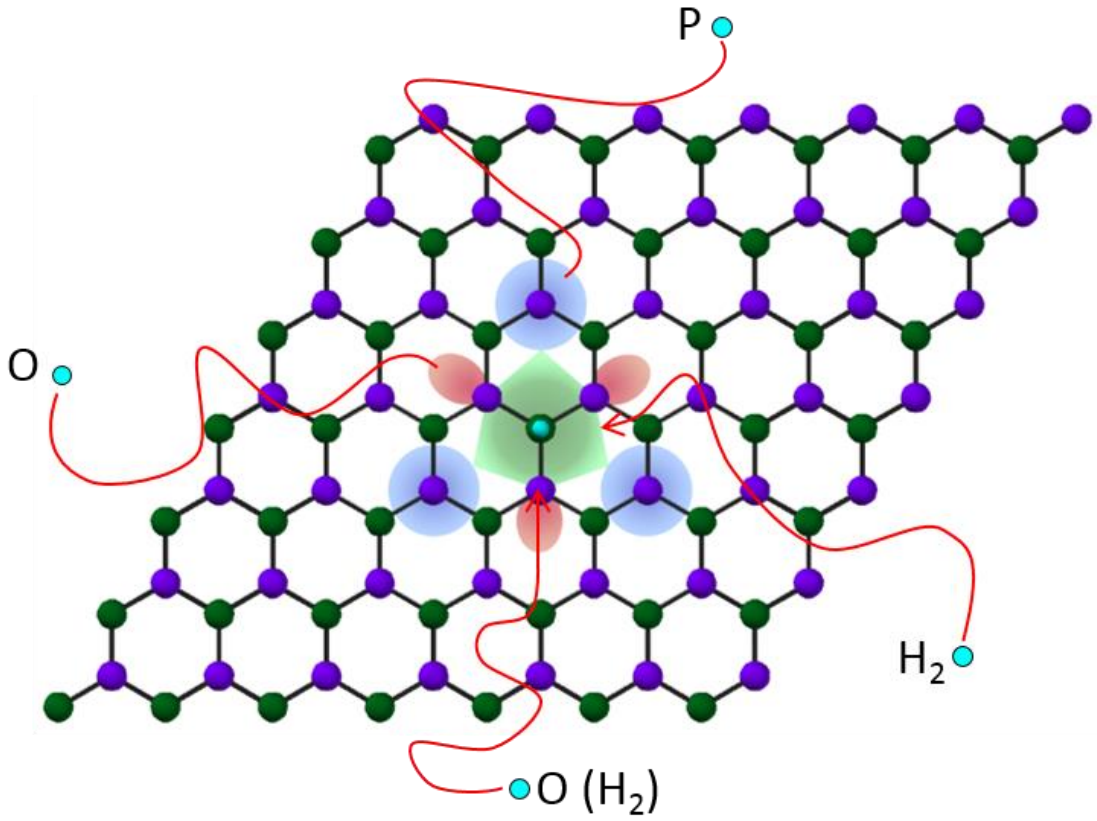

3.1 Introduction.

Hydrogen adsorption and interaction on graphitic surfaces has been extensively studied both from a theoretical and experimental point of view in the last 35-40 years in different areas [1-3]. Fields such as interstellar chemistry, where the formation of molecular hydrogen in carbonaceous surfaces is of great interest [4, 5], hydrogen storage to use it as a synthetic fuel in future technology [6, 7] and plasma/fusion physics where hydrogen trapping plays an important role [8], have investigated this issue. The field has gained new interest in recent years due to the apparition of graphene [9]. As we showed in chapter 2, the adsorption of a single hydrogen atom on top of graphene leads to the emergence of a magnetic moment of 1 Bohr magneton. Moreover, we also showed the existence of very particular coupling rules between the magnetic moments generated by neighbouring H atoms, 2 on the same sublattice (AA dimer) exhibit a ferromagnetic coupling, 2 on opposite sublattice (AB dimer) are non-magnetic. Thus, a natural question that arises is whether it is possible to induce a large magnetic moment in graphene by the simple adsorption of a large number of H atoms. Previous STM studies have shown the formation of different dimers and clusters in the surface of graphite and graphene when adsorbed at room temperature [10-12]. In these works, together with theoretical calculations, non-magnetic AB dimers have been found and predicted to be the most stable [13-15].

The aim of this chapter is to understand the adsorption process of H on graphene surfaces. To this end, we investigate the adsorption of hydrogen on graphene grown on SiC(000-1). Using our high resolution STM images we study which hydrogen configurations are present in our samples providing a detailed STM image library for the different H dimers and whether they contribute to create a magnetic moment or not. Our H adsorption experiments at RT and 140K show that it is necessary to reconsider the present understanding for H adsorption. With the help of new DFT calculations, we provide a comprehensive picture for the H adsorption on graphene. As our results show, the existence of a physisorption channel where the H is freely to move over the graphene surface, is crucial to understand the final configuration of H atoms on graphene.

3.2 Sample preparation.

The samples used in this chapter are multi-layer graphene grown on SiC(000-1). They were prepared by our French collaborators Jean Yves Veuillen and Pierre Mallet from the Néels Institute in Grenoble. Just as in the case of the previous chapter, the SiC(000-1) samples were prepared under UHV by graphitization of a 6H-SiC(000-1) surface [16, 17] (see chapter 2.2). For the hydrogen deposition the only difference is that we have also prepared our samples at low temperature (~140K). In order to cool down the sample, we made used of the continuous-flow cryostat installed in our manipulator. While depositing hydrogen, our SiC(000-1) sample is grabbed by the tweezers placed at the end of the manipulator. If liquid helium or nitrogen flows through the cryostat of the manipulator, the temperature of the tweezers (that can be measured with a thermocouple) can be lowered down to 140K. By grabbing the sample and waiting for 1 hour, our sample reaches an equilibrium temperature with the tweezers.

As in chapter 2.2, the deposition of atomic hydrogen was done following the procedure of refs [12, 18, 19], i.e. by the thermal dissociation of H_2 on a home-made hot hydrogen atom beam source. The pristine graphene substrate is placed 10 cm away from the filament, held at RT or LT during atomic H deposition and subsequently cooled down to 5K (after deposition, it takes ~6 minutes to introduce the sample in the STM chamber where the 4K cryostat is placed), the temperature at which we carried out all STM/STS experiments presented here. H_2 pressure is fixed to 3·10-7 torr as measured in the preparation chamber. The atomic H coverage was adjusted by changing the deposition times between 200-60s which corresponded to final coverages between 0.10-0.03 H atoms/nm² (or equivalently, 0.0026-0.0008ML; 1ML= 38 atoms/nm² = $3.8 \cdot 10^{15}$ atoms/cm², referred to carbon atoms in graphene layers). After the H deposition the graphene surface presents several bright features (see Figure 3.1) addressed as hydrogen atoms.

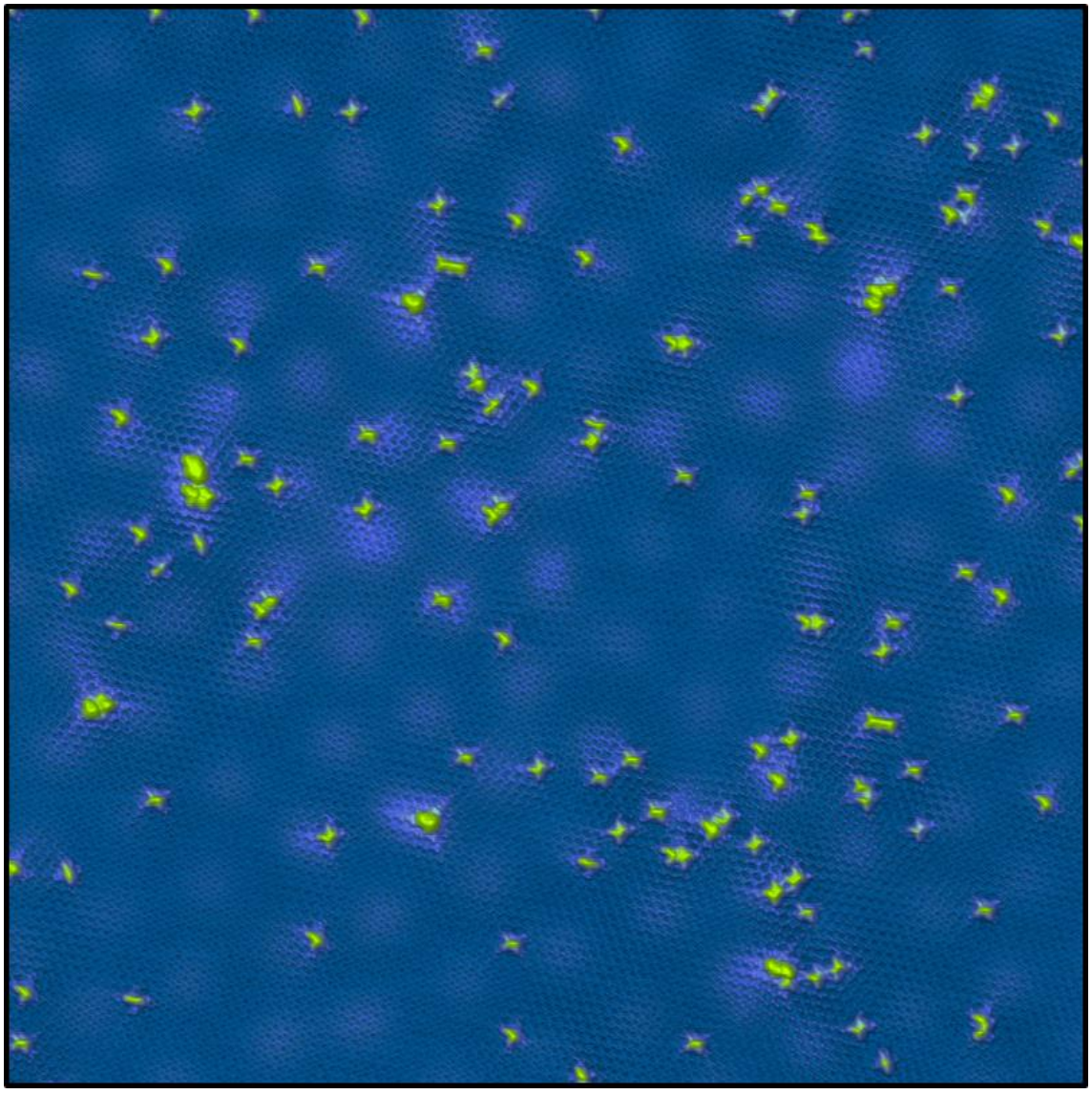

Figure 3.1: Gr/SiC(000-1) after hydrogen deposition. 40x40 nm² image of our graphene sample after hydrogen deposition. Different bright protrusion, attributed to hydrogen atoms, are observed. Tunneling parameters: -0.4V, 0.05 nA.

3.3 Identifying atomic H adsorption site by STM: An STM library for H dimers on graphene.

Due to the experimental challenge to get high resolution STM images of H adsorbates on graphene, assignments about the nature of H related STM features are frequently quite "debatable" in the literature. Here we aim to provide a clear guide to help identifying by STM the different H dimers that appear on graphene surfaces. In chapter 2.4 we already described how to identify a single H atom in our images as well as it adsorption site. Since the ability to identify and classify dimers will be an important part of the chapter, we will briefly describe the single hydrogen atom identification again to then continue with the dimer configurations. Just to remember, when we talk about two hydrogen atoms forming a dimer, and both of them are adsorbed on the same sublattice, we call it an AA pair. If they are on different sublattice, we address them as AB pair. AA pairs are magnetics, while AB pairs not (see chapter 2.6).

Single H atoms are visualized by STM as bright protrusions surrounded by a threefold $\sqrt{3}\times\sqrt{3}R30°$ pattern (Figure 3.2a) [20, 21]. This pattern presents three "arms" at 120° each (see Figure 3.2c). Using these "arms" as guidelines, the exact position of the hydrogen adsorption site is given by the intersection of them (Figure 3.2b). When adsorbed on an opposite lattice atom, the three "arms" will be rotated by 60° and the threefold induced pattern will appear with different orientation (Figure 3.2c). Therefore, when we have multiple single hydrogen atoms adsorbed on our graphene sample, we can easily discern how many of them are placed on each sublattice just by looking at the $\sqrt{3}\times\sqrt{3}R30°$ pattern (Figure 3.2d).

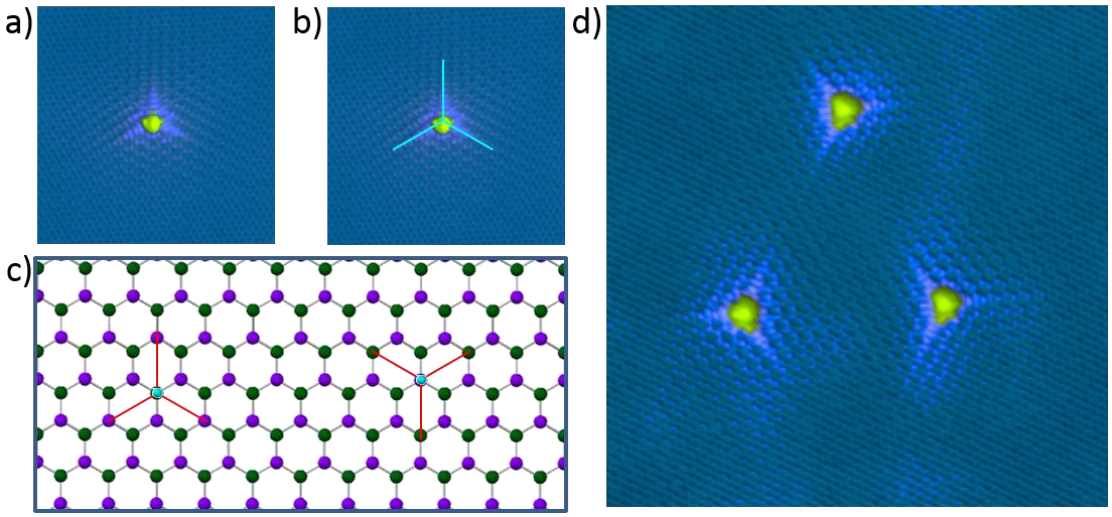

Figure 3.2: Identifying a single H atom. a) STM topography of a single H atom chemisorbed on graphene (0.4V, 0.045nA, 8×8nm^2). b) Same image as a) but with the 3 "arms" marked with lines for better differentiation c) Schematic diagram showing the corresponding H adsorption site (blue ball) on both graphene sublattices (purple and green balls). The three lines, at 120º each, correspond to the threefold ($\sqrt{3}\times\sqrt{3}R30°$) patterns generated on graphene by the H atom. d) STM topography of 3 single H atoms (-0,1V, 0,055nA, 14×14 nm^2)

If we now have two atoms closer to each other, things get more difficult. As a first approach there is a fast way to classify pairs in AA dimers or AB dimers: looking at their apparent height. For AA dimers the height measured by STM for the same tunnelling conditions is ~0.5-1 Å larger than the one for AB dimers (this criterion applies for bias voltages Vb ~-400/400 mV), see profile on Figure 3.2 a-b). The reason behind this difference on apparent height comes from the existence of the polarized state in the vicinity of E_F for the case of the AA dimer due to the ferromagnetic coupling. This height difference offers the possibility to visually differentiate AA dimers from AB dimers by just choosing the right colour code for our STM images. In Figure 3.3D we modified the palette to show a cyan tone on AA dimers and a red tone on AB dimers. After this first identification, there are some differences when it comes to find the exact atomic configuration of the dimers.

For AA dimers, the three “arms” of each atom are still visible. Therefore using images with atomic resolution, we can draw the “arms” and superimpose a honeycomb lattice to find out the adsorption position (Figure 3.4A). For the AB dimers, the three “arms” are not visible anymore and only some of them show some “arms” (for high-resolution images) depending on the configuration. Hence, for the closest AB atoms, even when we draw the perceivable “arms” and superimpose the honeycomb lattice, clear identification becomes more difficult (Figure 3.4B). In these cases, and especially if no “arms” are visible at all, we can make use of simulated images to get further information. It is important to remark that independently on which kind of dimer we are looking at, simulated STM images can be used as a support for identification. In Figure 3.4, we can observe how our simulated images for the 3 dimer configurations show good resemblance with our STM images.

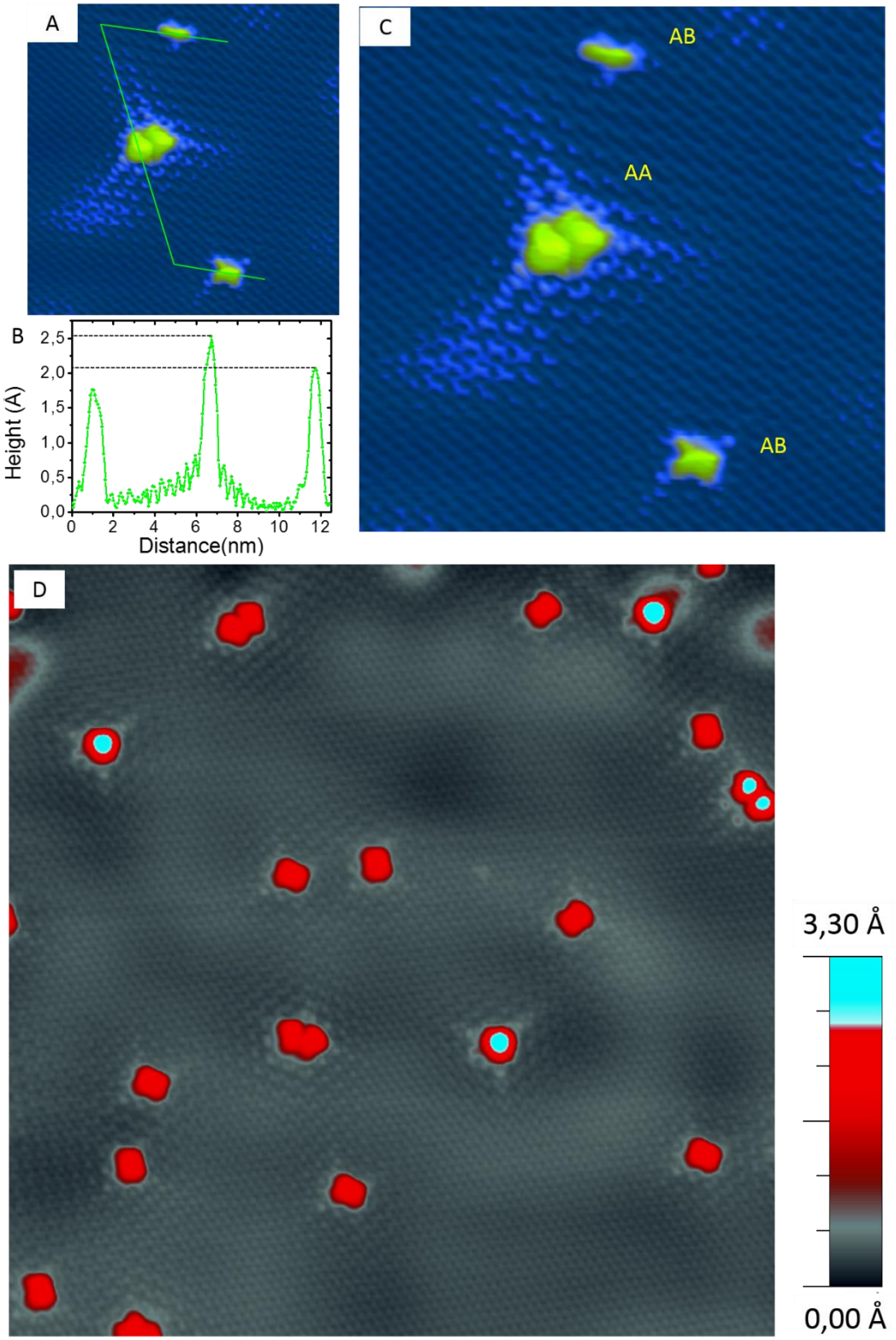

Figure 3.3: Identifying dimers by height. A) STM image showing three dimer configuration. B) Height profile along the green line showed in A). C) Same STM image as A where the three dimers have been classified into AA or AB (-0.4V, 0.05nA, 8,3×8,3nm^2). D) STM image with color code to easily distinguish AA and AB dimers

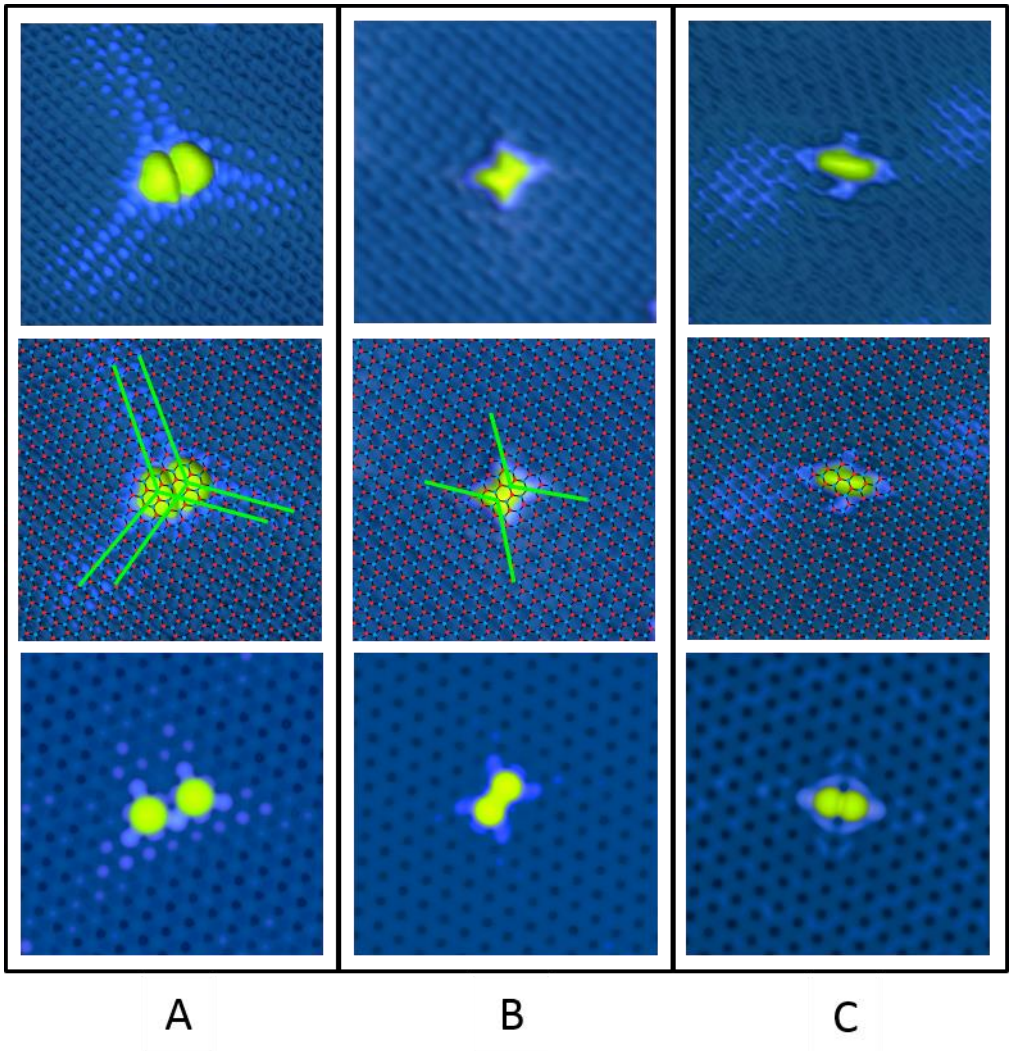

Figure 3.4: High resolution images to identify H dimers. A) AA dimer on Figure 3.3C (top) with the three “arms” on every H atom and honeycomb lattice drawn (middle) and the simulated image (down) to compare. B) AB dimer on botton part of Figure 3.3C (top) with only two “arms” per H atom drawn together with the honeycomb lattice (middle) and the simulated image (down) to compare. C) Different AB dimer on top part of Figure 3.3C (top) with the lattice drawn (middle) and the simulated image (down) to compare.

Applying these guidelines, we can now take our STM images and identify the different hydrogen configurations on our sample. In order to name the dimers, we have used the following nomenclature: Using the ortho, para and meta positions, any other configuration can be addressed using a combination of the three of them (see Figure 3.5 and [12]).

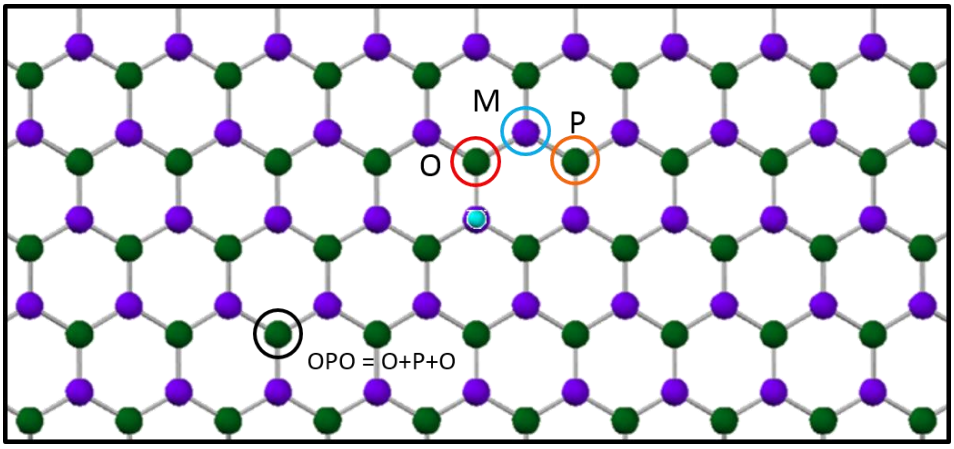

Figure 3.5: Schematic explanation of the nomenclature used to name the dimers. The blue ball represents the adsorbed hydrogen atom. Circled in red, blue and orange, the three different positions used to name any other configuration. In black, another position with its corresponding name according to our nomenclature.

We were able to identify up to 10 different dimer conformations in our STM images. In Figure 3.6 we can observe the schematic, STM and simulated image of all of them. This figure is meant to serve as a dimer library for anyone working with hydrogen atoms on graphene surfaces, and hopefully it will keep on increasing. It has to be pointed out that 5 out of the 10 dimers here presented, are reported for the first time by us (highlighted in grey in Figure 3.6). In addition, the MMM pair was only observed after atomic manipulation of hydrogen atoms and was never found naturally in the sample [22].

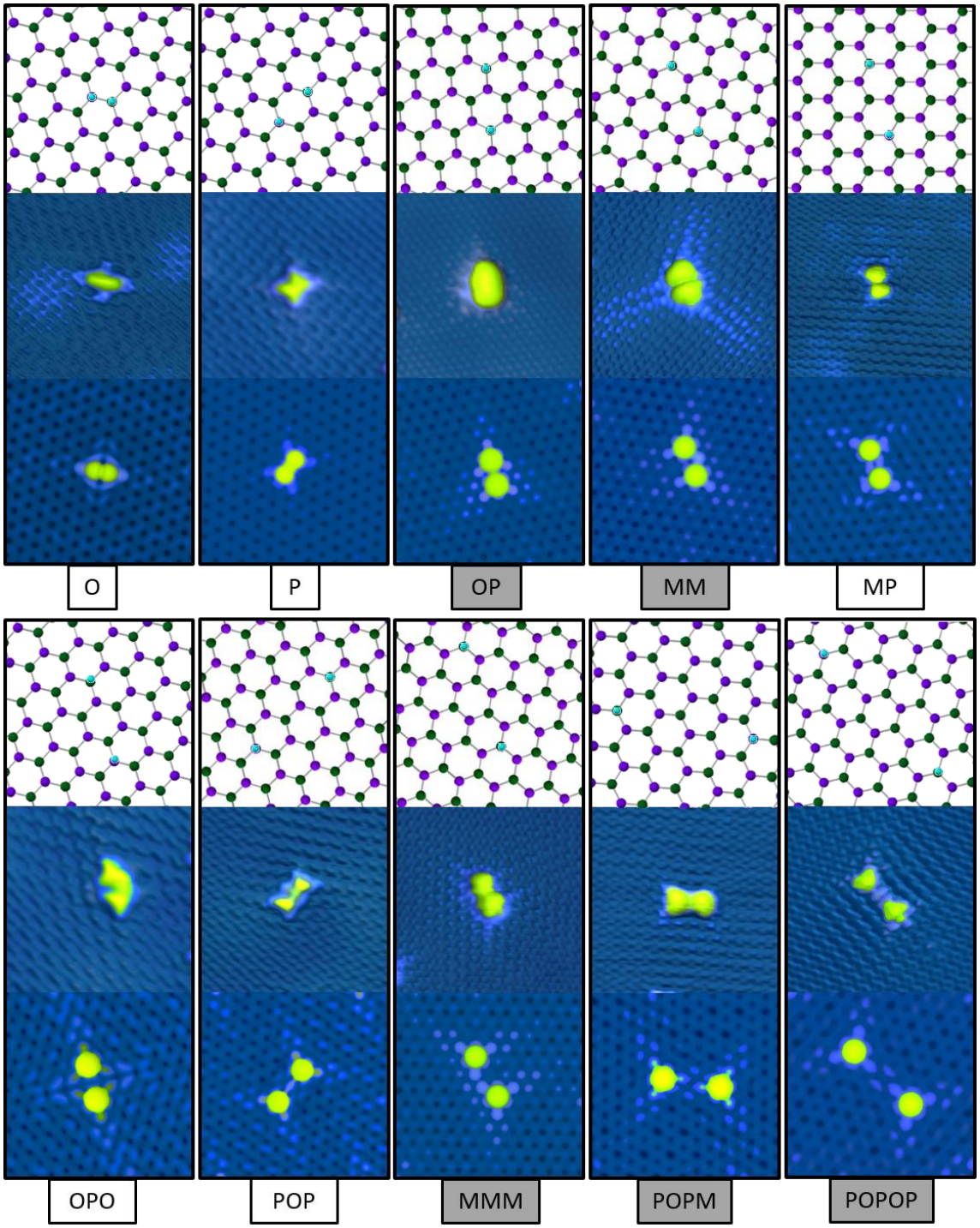

Figure 3.6: H dimers library. STM images of all the dimers found in our sample with an schematic configuration on a graphene lattice and it simulated STM image. This figure is intended to serve as a library to identify H dimers on graphene. All these images were taken at Vt= -200/-400 mV and It $\approx$ 0.05 nA.

3.4 H adsorption at RT.

Figure 3.7 shows an STM image of a graphene region after hydrogen deposition at room temperature. In the image, and using the catalogue of Figure 3.6, we have highlighted some of the identified dimers. Thanks to our high resolution images, we were able to characterize and make a quantitative study of the % of hydrogen atoms forming various conformations in different terraces of the sample. In Figure 3.7 we also present the statistical distribution of the different configurations we found. The dimers where the two hydrogen atoms are placed in the same sublattice and therefore should exhibit magnetic properties, are represented in cyan. Similar to previous studies, the most common dimmers on the surface are the O and P configurations. However, this is the first time that a statistical analysis about the abundance of each H dimer has been performed. The analysis was performed using 10 different STM images. After identification of the number and percentage of the different H configurations present in each image, a weighted arithmetic mean was used in order to take into account the inhomogeneous density of H atoms of the sample (the minimum density found in our images was 0.07 H atoms/nm^2 and the maximum one 0.15 H atoms/nm^2). The errors were calculated using the standard deviation. An important outcome from our study, is that only a 5% of the hydrogen atoms deposited on the sample ended up in magnetic configurations and therefore contributing to the magnetic moment induced in the surface.

According to the present understanding about the H adsorption on graphene, a good strategy to increase the number of single H atoms in the graphene sample would be to carry out the H deposition at lower temperatures. So let us first review the current understanding of hydrogen adsorption on graphene (see Figure 3.8 extracted from [19]). The chemisorption of a hydrogen atom on graphene, leads to a reconstruction due to the sp^2-sp^3 rehybridization. This reconstruction consists on the puckering of the carbon atom underneath the hydrogen. As a consequence of this puckering, the apparition of an adsorption barrier of ~0.20 eV occurs (see Figure 3.18) [12, 23-25], making the chemisorption of hydrogen a thermally active process at room temperature. However, while the hydrogen atom tries to jump over the barrier, it also has a finite probability of desorbing. Once the atom overcomes the barrier it gets chemisorbed with a biding energy ~0.7-1.0 eV (see Figure 3.18) [12, 19, 23, 25-29]. The binding energy, together with the adsorption barrier lead to a desorption energy ~1-1.2 eV [25, 29, 30] which is similar but slightly lower than the migration one [29-32]. At room temperature this means that our single hydrogen atoms will most likely desorb rather than diffuse. The predominance of the desorption process prevents the formation of dimers via diffusion leaving the adsorption of a second hydrogen atom close to the previous one as the most likely possibility.

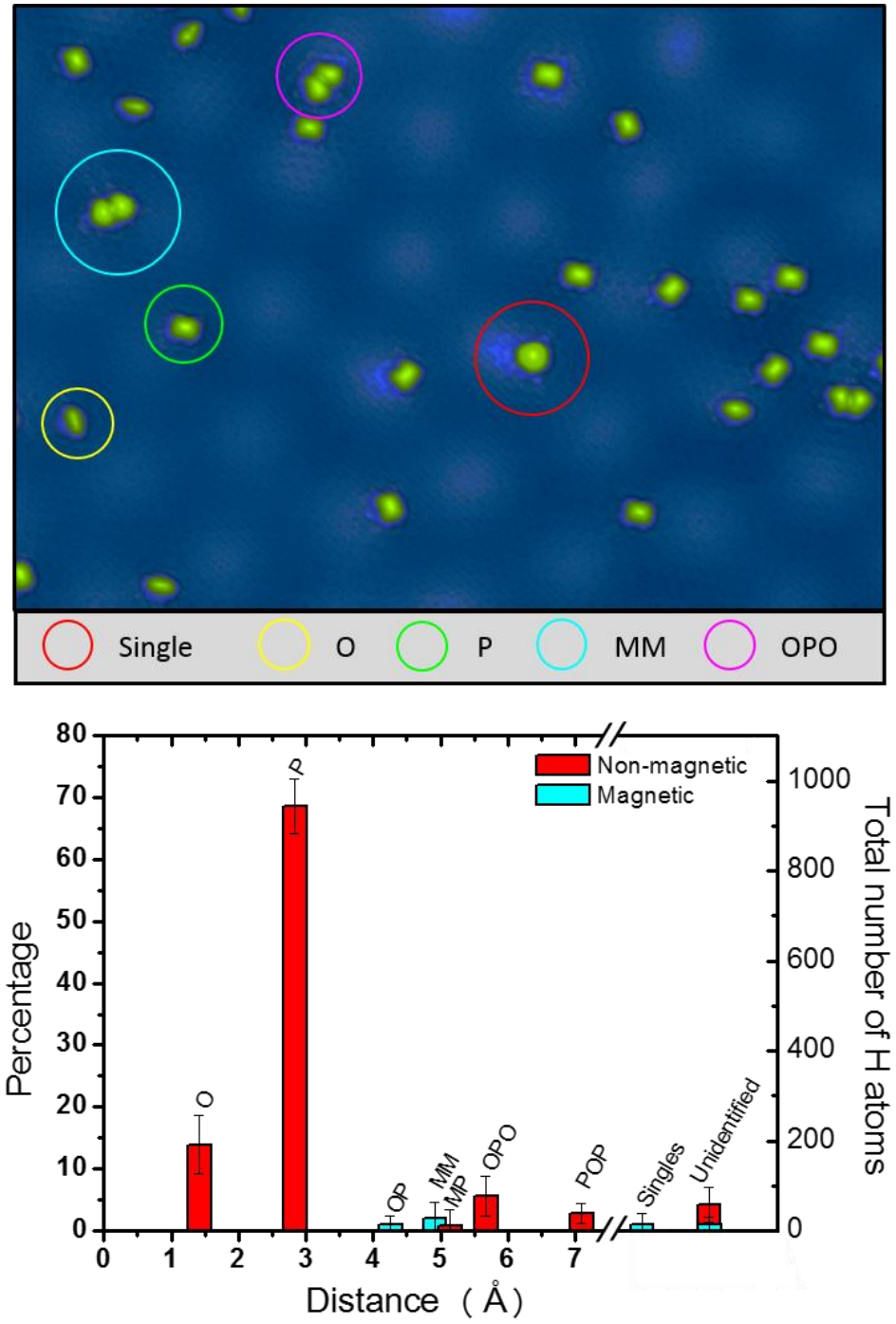

Figure 3.7: Graphene hydrogenation at room temperature. Top: STM image of our graphene sample where some hydrogen configurations have been highlighted to guide de eye. Size 25×25 nm², Vbias=-0,4eV, It=50 pA. Bottom graph: average concentration of atoms in each dimer configuration found in our images out of the total number of atoms. "Unidentified" refers to clusters of H atoms or some pairs which were not distinguishable. Within these unidentified objects some of them were clearly in magnetic configuration.

Calculations show that the adsorption of the first hydrogen atom causes a change on the energy landscape around it, decreasing the adsorption barriers in its vicinity. Then, if a second hydrogen reaches the surface close enough to the chemisorbed hydrogen atom, its probability of adsorbing will be higher and the formation of a dimer will occur. Indeed, although the O and P dimer have a similar

adsorption energy (~2 eV) (see Figure 3.9) [12-15, 19], more P dimers can be found, which was explained in terms of the stronger reduction of the barrier for chemisorption in the case of the P dimer (see Figure 3.8). This larger adsorption energy explain why H dimers exhibit a higher thermal stability compared with single hydrogen.

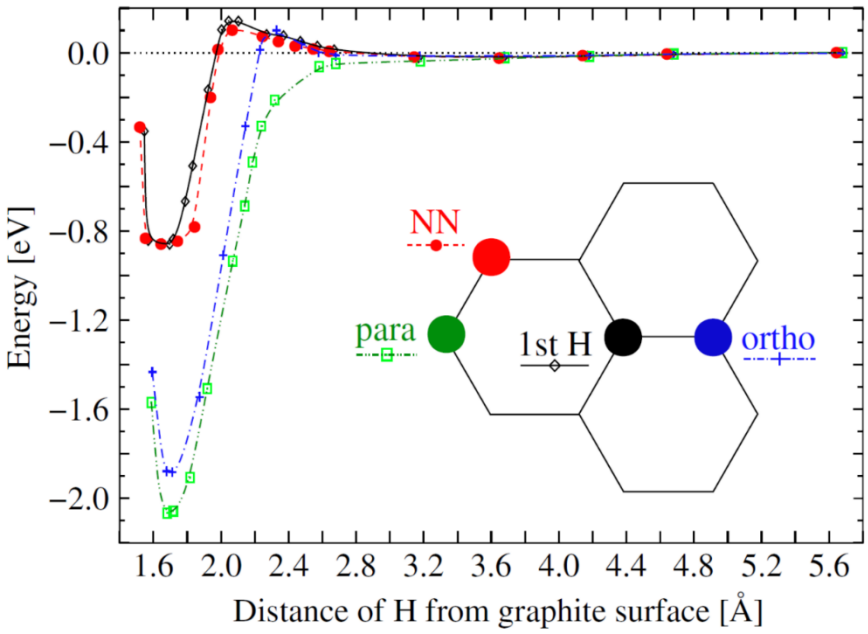

Figure 3.8: Previous calculations for the adsorption energy of a single and a second H atom. Potential energy curves for adsorption of a single H atom monomer (solid line), and for three dimer configurations the orthodimer (dash-dotted line), the next neighbor site (dashed line), and the paradimer (dash-double dotted line) (extracted from [19]).

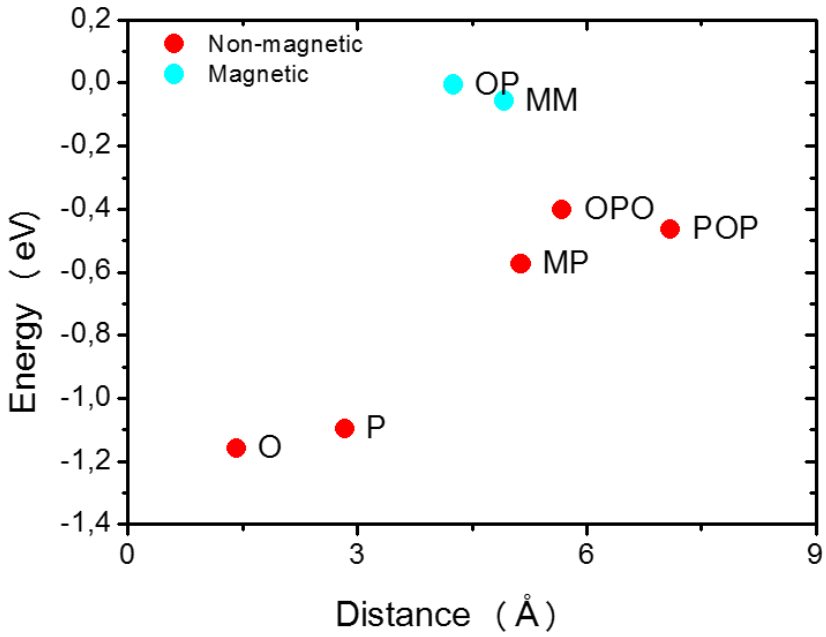

Figure 3.9: Calculated total energy of hydrogen dimers. Calculated total energy relative to twice the adsorption energy of a single H atom, and magnetic state of a pair of H atoms adsorbed on the different dimers configurations found in our sample. In red, non-magnetic configurations (AB dimers), in cyan, magnetic ones (AA dimers).

3.5 Lowering the temperature: Statistical study of hydrogen dimers adsorbed at 140K.

As mentioned before, according to the just described scenario, one possible approach to maximize the number of single hydrogen atoms on our sample would be the hydrogenation of graphene while keeping the sample at a lower temperature. The lower temperature will decrease the desorption probability of the single hydrogen atoms and therefore, our graphene should present a higher number of monomers compared with the experiments performed at room temperature. In Figure 3.10 we present a topography image of a hydrogenated graphene sample at 140K. Contrary to our expectations, the number of single hydrogen atoms does not increase significantly, and we mostly observe dimers. This can be observed in greater detail in the statistic study in Figure 3.10. The analysis was done following the same method as for the RT experiments. We basically observe ortho and para dimers and the ratio para/ortho has increased. These results go against the adsorption process for hydrogen on graphene previously described.

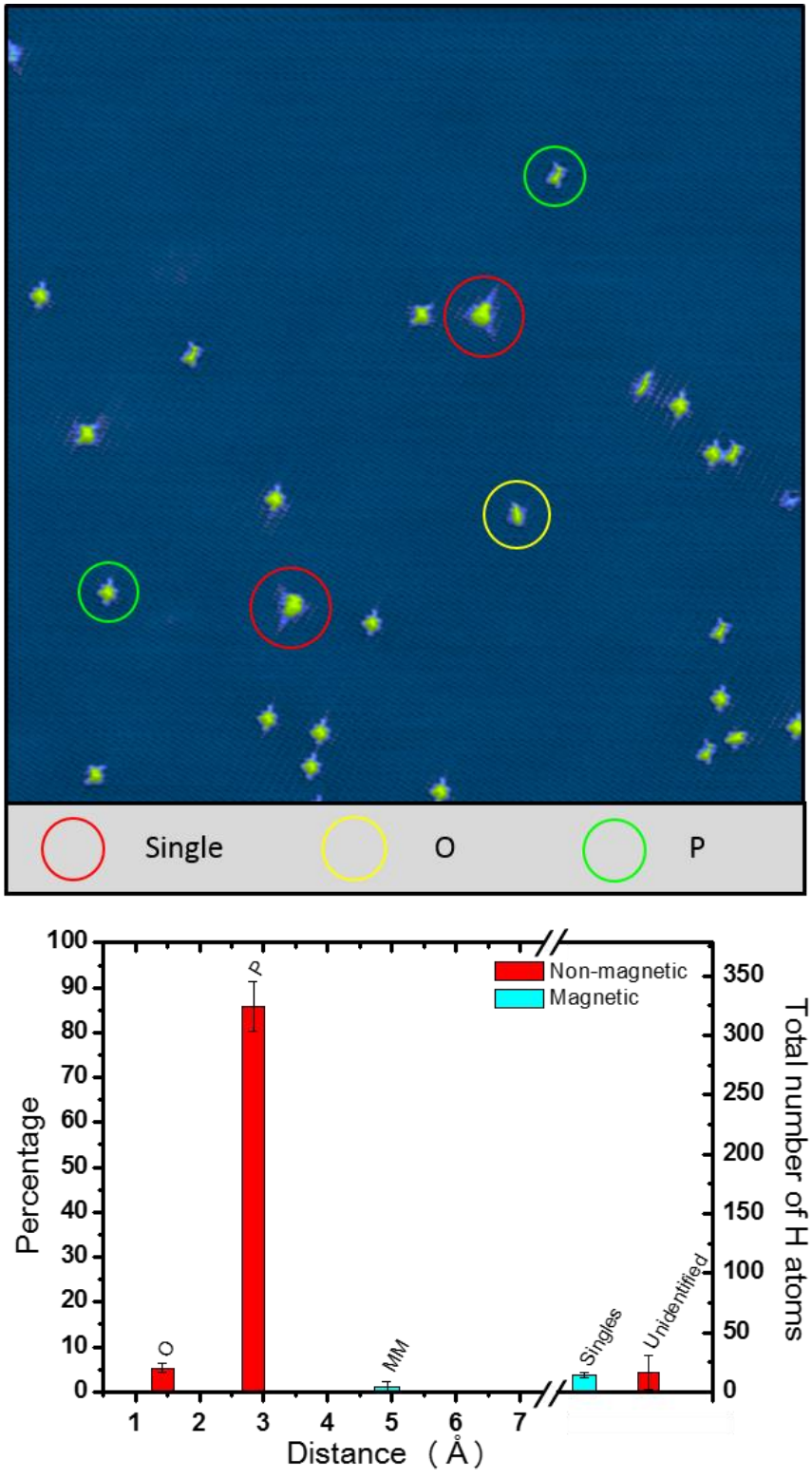

Figure 3.10: Graphene hydrogenation at 140K. Top: STM image of our graphene sample where some hydrogen configurations have been highlighted to guide de eye. Size 25×25 nm², Vbias=-0,4eV, It=50 pA. Bottom: Average concentration of atoms in each dimer configuration found in our images out of the total number of atoms. “Unidentified” refers to clusters of H atoms or some pairs which were not distinguishable.

3.6 Understanding H adsorption on graphene.

In order to shed light to the dynamical processes leading to the adsorption of hydrogen on graphene, we collaborate with Prof. Félix Ynduráin and the group of Prof. Juan José Palacios who performed DFT calculations including the latest van der Waals functionals. All the calculations here presented were performed in a 7x7 graphene cell using a double-zeta polarized basis set and a lattice constant of 1.428 Å. The DRSLL functional, proposed by Dion et al. is used to include van der Waals interactions [33, 34]. A mesh cut off of 400 Ryd and residual forces lower than 0.02 Ryd/Bohr are applied. Due to the rapid variation of the density of states at the Fermi level, a polynomial smearing method was used [35]. During the calculations,the only carbon atoms not allowed to relax are the ones located at the edge of the cell.

With this model, they calculated again the potential energy curves for the adsorption of a single hydrogen in three different high symmetry positions of the graphene lattice: on-top, saddle and hollow. The result can be seen in Figure 3.11. The main feature of these three curves, is the existence of a physisorption well for all the three positions. A closer look to the shape of the physisorption channel presented in the inset of Figure 3.11 shows that it is almost equal for the three positions presenting a minimum at ~100 meV. This means that once our hydrogen atom enters the physisorption channel, it will be able to freely move laterally along the sample without feeling the presence of the carbon lattice underneath. The existence of this physisorption channel has already been considered in the formation of molecular hydrogen in the interstellar medium, where the low temperatures would deactivate the chemisorption process. Two physisorbed hydrogen atoms would form a hydrogen molecule when they get close enough while moving on the surface (Langmuir-Hinshelwood mechanism). In fact the physisorption channel was measured by means of H and D scattering experiments in 1980, obtaining a value around 40 meV [36] and some previous DFT calculations also obtained a physisorption minimum with values ~ 60 meV [24]. However, this physisorption channel has not been considered as relevant when addressing the hydrogenation of graphene at higher temperatures.

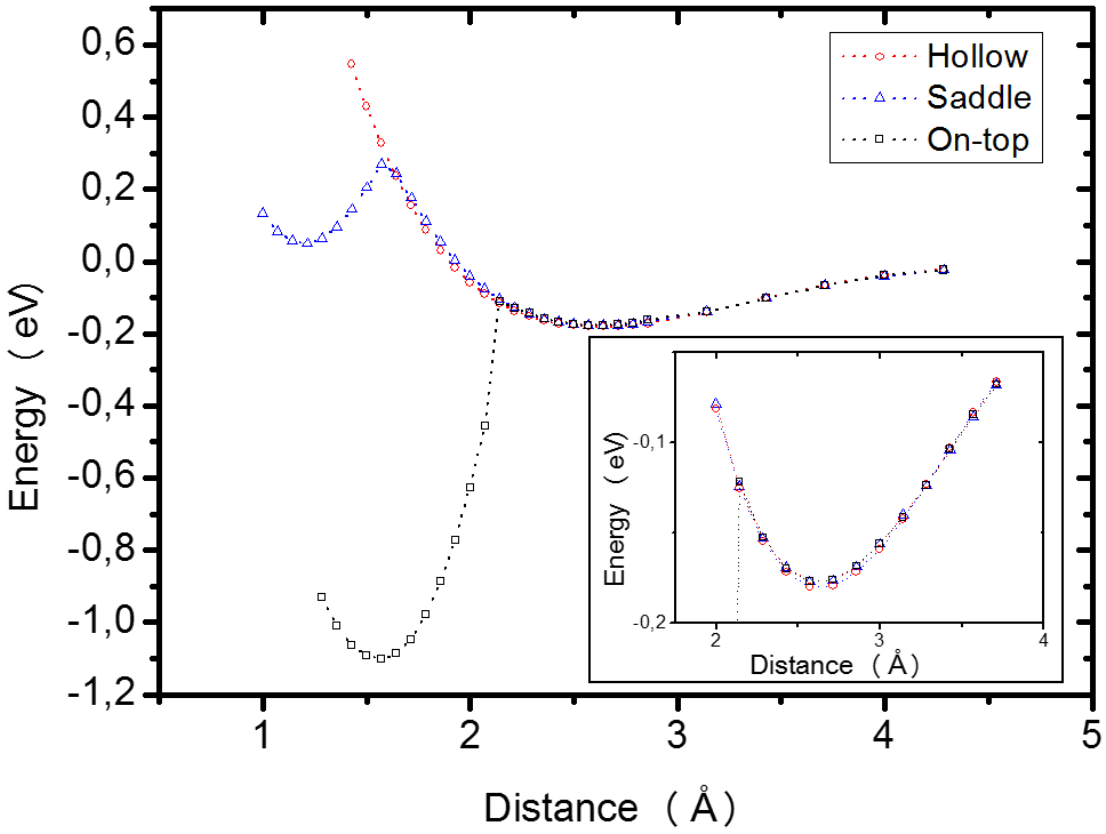

Figure 3.11: Hydrogen adsorption on graphene. Energy-distance curves of the adsorption of a single hydrogen atom on 3 different positions of the graphene latticeS: On-top, hollow and saddle. Inset: Zoom in of the physisorption well.

If we now take into account the existence of an active physisorption channel as our DFT calculations point out, the process by which the formation of hydrogen dimers would happen, leading to the final configuration of our samples, will be different to the one described before. First, a hydrogen atom reaches the surface and enters the physisorption channel. Once it is physisorbed, it moves over the surface at high velocity. While the H atom is moving it can either overcome the adsorption barrier after some attempts or end up desorbing. Indeed the calculated barrier for desorption is slightly higher than the one for entering the chemisorption well. When the hydrogen atom is chemisorbed, the adsorption energy barriers around it will be affected, reducing their value and even disappearing for some positions [12, 19]. Therefore, when a second hydrogen atom enters the physisorption channel, three cases have to be considered: a) It desorbs before finding any other H atom. b) It finds another physisorbed H atom forming a H_2 molecule and desorbs [37]. c) The hydrogen atom gets close to the chemisorbed atom and hence the probability to be adsorbed will be higher due to the reduced barriers and the formation of a dimer will take place.

The position dependant changes in the adsorption barrier can be seen as an increment of the reactivity of the graphene region surrounding the hydrogen atom. In order to check whether this changes would explain the distribution of configurations on our sample, we calculated the adsorption energy curves of a

second hydrogen atom on different carbon atoms close to the already chemisorbed one. Three different positions where calculated: ortho, para and POP (see Figure 3.12). In Figure 3.12 we can observe the results. In the case of the ortho dimer, there is still an adsorption barrier but its value has been decreased, facilitating the chemisorption and formation of the dimer. For the case of the para dimer, the adsorption barrier disappears meaning that once a hydrogen atom gets close enough to the para position, it will be chemisorbed. This absence of adsorption barrier would be in good agreement with the para dimer being the most observed in our samples. This reduction of the adsorption barrier for the O and P dimer had already been already calculated in previous works (see ref [19] and Figure 3.8). In those works, calculations were performed for the vertical adsorption of a second H atom.

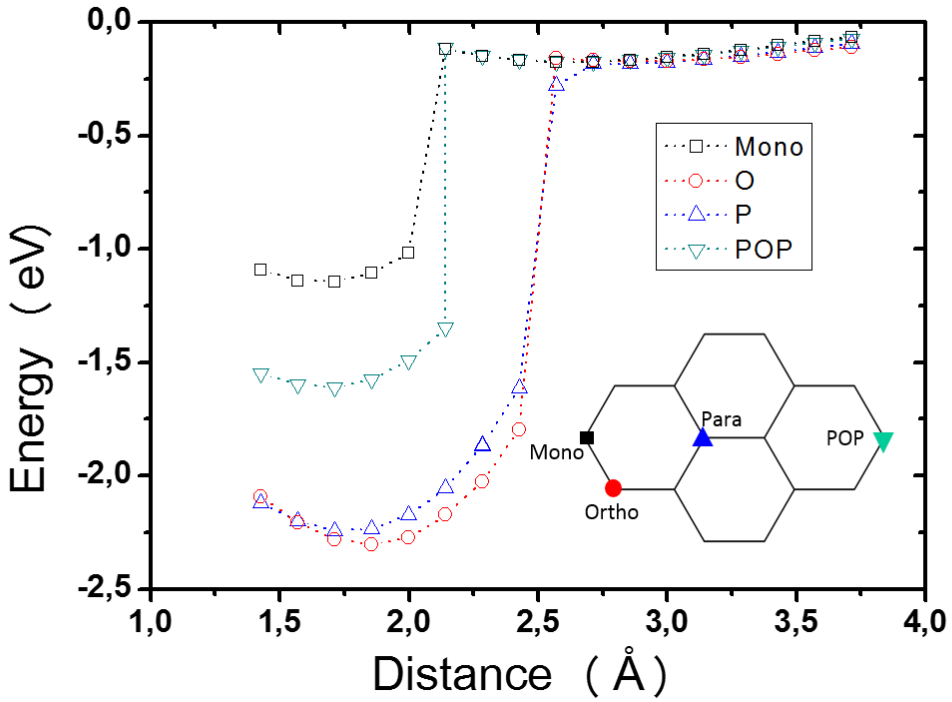

Figure 3.12: Adsorption of a second hydrogen atom. Energy-distance curves of the adsorption of a second hydrogen atom on 3 different carbon atoms.

Since the height and even the existence of the adsorption barrier changes depending on the position of the graphene lattice around the hydrogen atom, the probability for the formation of each type of dimer will greatly depend on the trajectory described by the second hydrogen atom along the surface. For long distances, the barriers seen by the H atom are basically the same as for the case of the single hydrogen. Only when it gets closer to the chemisorbed H atom the energy landscape will change and the second H atom will feel the perturbation of the chemisorbed one. To qualitatively illustrate the processes taking place, we made Figure 3.13. In this figure we have represented a graphene 7x7 cell where the blue ball represents the chemisorbed hydrogen atom. Around the ortho and

para positions we have drawn the region where a physisorbed hydrogen atom would feel the reduced barrier and could be adsorbed. Surrounding the hydrogen atom in green, we have the area where the two atoms would bind, forming a hydrogen molecule and desorbing. With arrows, we have depicted 4 representative paths: one reaching the para region, two in the ortho region and a last one where the hydrogen atom gets closer to the chemisorbed H atom avoiding both the O and P regions.

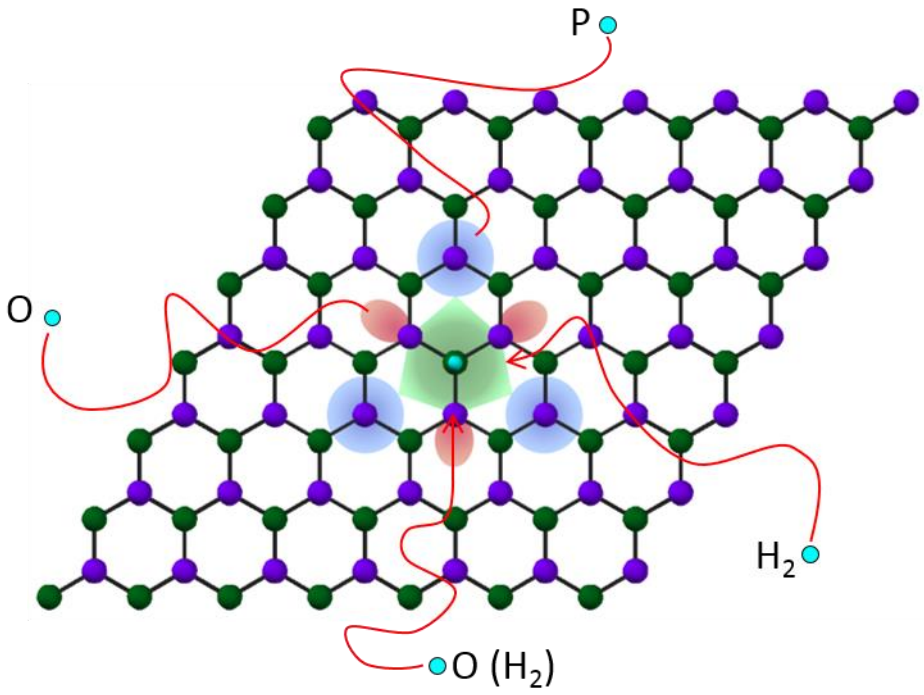

Figure 3.13: Adsorption of a second hydrogen atom in the vicinity of a chemisorbed atom. In red, four different paths for the hydrogen atom to get close to the chemisorbed one. Depending on the trajectory, orthodimer, paradimer or even desorption after the formation of a molecule of hydrogen can result.

If the hydrogen atom does not cross neither the para nor the ortho region while getting closer to the chemisorbed atom, it will reach the green area where our calculations show that the two hydrogen atoms will interact, form a hydrogen molecule and desorb (see H_2 in Figure 3.13). If the hydrogen atom enters through the physisorption channel the blue region around the para position, if feels the disappearance of the adsorption barrier, leading to the formation of the dimer with essentially 100% probability (see P in Figure 3.13). If the hydrogen atom gets close to the red region around the O position, we have to discern two possibilities, which we named O and O(H_2) in Figure 3.13. In the first case (O), the hydrogen atom reaches the red area and overcomes the reduced adsorption barrier being chemisorbed and forming the dimer. In the second case (O (H_2)) the hydrogen atoms does not surpass the adsorption barrier and therefore continues towards the green region surrounding the chemisorbed hydrogen atom where it ends forming a hydrogen molecule and desorbing. In Figure 3.14 we show the calculations performed for these two last cases (O and O(H_2)). We have

calculated a hydrogen atom moving from the hollow position towards a chemisorbed hydrogen atom through the ortho site. Both O and O(H_2) possibilities are considered: in red, the hydrogen atom overcomes the adsorption barrier and gets chemisorbed (O). In green, the H atom continues on the physisorption state without overcoming the barrier for chemisorption. For the first case, red curve, the hydrogen atom will form an ortho dimer where the equilibrium position would be the H3 position. For the second case, green curve, the hydrogen atom continues on the physisorption channel till it reaches the ortho site. At this point, the hydrogen atom reacts with the chemisorbed one forming a hydrogen molecule and thus desorbing. These results are also compatible with the higher number of para dimers at 140K compared with ortho dimers. The lower thermal energy would decrease the probability of the second hydrogen atom to overcome the adsorption barrier and form the ortho dimer while the probability to form the P dimer will be essentially unaltered.

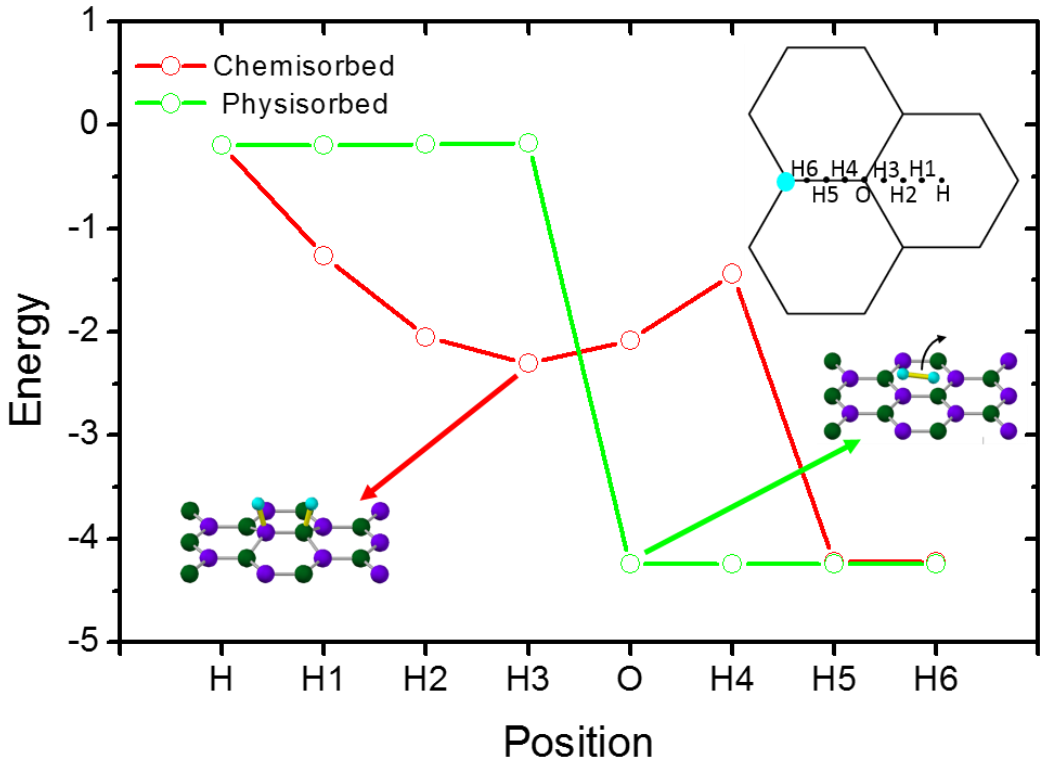

Figure 3.14: Formation of an O dimer or a H_2 molecule. Energy of a second hydrogen atom as it approaches to the nominal O position *via* physisorption or chemisorption channel.

An additional evidence we found during our experiments pointing to the existence of the diffusion channel for hydrogen atoms on graphene, was the observation of a great number of atoms on grain boundaries and defects even for low coverage in the terraces (see Figure 3.15). It is well known that these kind of defects increase the reactivity of the carbon atoms involved making those position more stable. In that sense, the physisorbed hydrogen atoms would get trapped by the grain boundaries while diffusing on the surface.

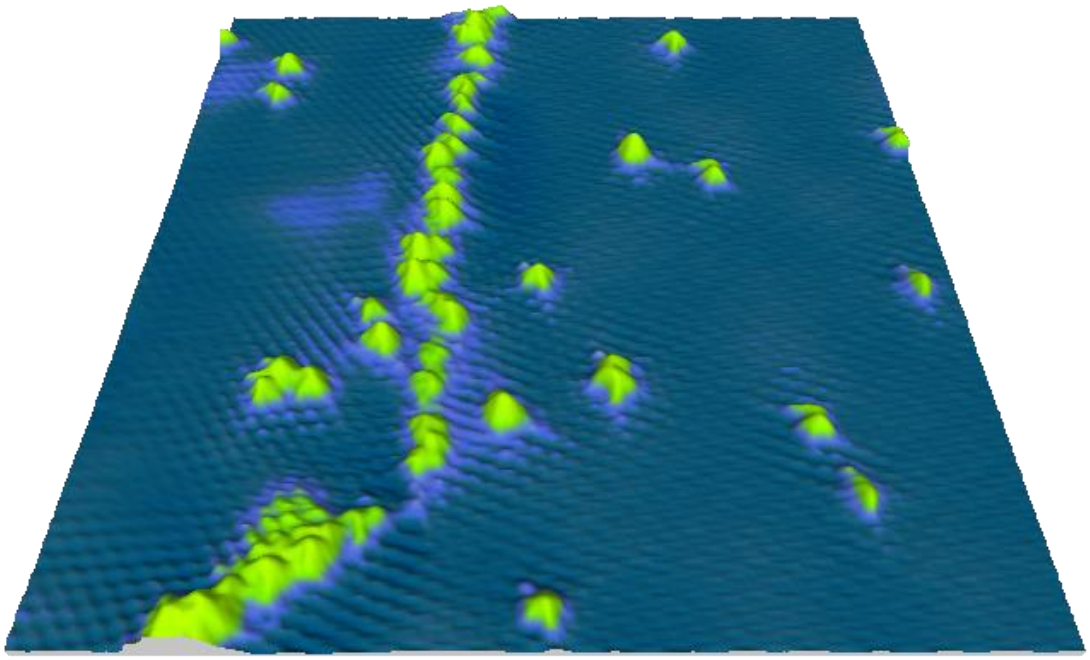

Figure 3.15: Hydrogen on grain boundaries. 36×36 nm^2 STM image showing a graphene terrace where a grain boundary can be observed. The grain boundary is decorated with hydrogen atoms, suggesting the diffusion of the atoms. Vbias=-0,4eV, It=70 pA.

All the results presented in this chapter were measured in multilayer graphene samples. Experiments performed using other weakly coupled graphene systems as monolayer and bilayer graphene grown on SiC(0001), 2-3 layers graphene on SiC(000-1) and graphite during this thesis, have shown similar behaviour. Interestingly, as we will present in chapter 4, in the case of graphene grown in the (111) face of copper, we mostly find single hydrogen atoms.

3.7 Conclusions.

In this chapter we have studied in detail the adsorption of hydrogen on graphene grown on SiC(000-1) in order to learn how we can create magnetic graphene by hydrogenation. We found that hydrogen atoms tend to form dimers in our multilayer graphene samples. From our STM results together with the theoretical DFT calculations, the main conclusions we obtained are:

- We found a methodology to study and identify the atomic position of hydrogen atoms forming dimers on graphene grown on SiC (000-1). Combining high-resolution STM images and simulated STM images, we identified ten different dimers (5 were reported for the first time) and statistically studied the abundance of them in our sample.

- The adsorption of hydrogen atoms on graphene at room temperature results in the formation of mostly non-magnetic dimers. From our statistical study, only a 5% of the hydrogen atoms are arranged in magnetic configurations. After considering the adsorption process present in the literature, we tried a different approach to increase the number of single hydrogen atoms in the sample: performing the hydrogen deposition at lower temperatures. Our hydrogenation experiments at 140K present basically the same tendency as the ones at room temperature. This fact, made us reconsider the adsorption process of hydrogen on graphene.

- Our DFT calculations including van der Waals interactions for the adsorption curve of a single hydrogen atom on graphene, point to the existence of a physisorption well of ~100 meV prior to the chemisorption one. This physisorption well is the same all over the graphene atomic lattice allowing hydrogen atoms to freely move for long distances. Such a physisorption channel had never been considered for the adsorption and formation of hydrogen dimers on graphene.

- This possibility for the hydrogen atom to “freely” move over the graphene layer, together with the change in the energy landscape for the adsorption of a second hydrogen atom in the vicinity of an already chemisorbed hydrogen atom, goberns the formation of dimers found in our sample and explains the dimer distribution observed in our experimental measurements even at low temperatures.

References

1. Finzel, H.U., et al., *ATOM-SURFACE SCATTERING WITH VELOCITY-SELECTED H AND D-ATOMIC BEAMS FROM LIF AND NAF(001).* Surface Science, 1975. **49**(2): p. 577-605.
2. Dovesi, R., et al., *REGULAR CHEMISORPTION OF HYDROGEN ON GRAPHITE IN CRYSTALLINE ORBITAL NDO APPROXIMATION.* Journal of Chemical Physics, 1976. **65**(8): p. 3075-3084.
3. Pirronello, V., et al., *Laboratory synthesis of molecular hydrogen on surfaces of astrophysical interest.* Astrophysical Journal, 1997. **475**(1): p. L69-L72.
4. Hornekær, L., et al., *Importance of Surface Morphology in Interstellar H2 Formation.* Science, 2003. **302**(5652): p. 1943-1946.
5. Pirronello, V., et al., *Measurements of molecular hydrogen formation on carbonaceous grains.* Astronomy & Astrophysics, 1999. **344**(2): p. 681-686.
6. Schlapbach, L. and A. Zuttel, *Hydrogen-storage materials for mobile applications.* Nature, 2001. **414**(6861): p. 353-358.
7. Meregalli, V. and M. Parrinello, *Review of theoretical calculations of hydrogen storage in carbon-based materials.* Applied Physics a-Materials Science & Processing, 2001. **72**(2): p. 143-146.
8. Mayer, M., et al., *Hydrogen inventories in nuclear fusion devices.* Journal of Nuclear Materials, 2001. **290**: p. 381-388.
9. Novoselov, K.S., et al., *Electric field effect in atomically thin carbon films.* Science, 2004. **306**(5696): p. 666-669.
10. Hornekaer, L., et al., *Metastable Structures and Recombination Pathways for Atomic Hydrogen on the Graphite (0001) Surface.* Physical Review Letters, 2006. **96**(15): p. 156104.
11. Merino, P., et al., *Ortho and Para Hydrogen Dimers on G/SiC(0001): Combined STM and DFT Study.* Langmuir, 2014. **31**(1): p. 233-239.
12. Sljivancanin, Z., et al., *Extended atomic hydrogen dimer configurations on the graphite(0001) surface.* Journal of Chemical Physics, 2009. **131**(8): p. 084706.
13. Rougeau, N., D. Teillet-Billy, and V. Sidis, *Double H atom adsorption on a cluster model of a graphite surface.* Chemical Physics Letters, 2006. **431**(1â€“3): p. 135-138.
14. Ferro, Y., et al., *Stability and magnetism of hydrogen dimers on graphene.* Physical Review B, 2008. **78**(8).
15. Casolo, S., et al., *Understanding adsorption of hydrogen atoms on graphene.* Journal of Chemical Physics, 2009. **130**(5): p. 054704
16. Varchon, F., et al., *Rotational disorder in few-layer graphene films on 6H-SiC(000-1): A scanning tunneling microscopy study.* Physical Review B, 2008. **77**(16): p. 165415.
17. Hiebel, F., et al., *Structure and stability of the interface between graphene and 6H-SiC(000-1) (3 x 3): an STM and ab initio study.* Journal of Physics D-Applied Physics, 2012. **45**(15).
18. Balog, R., et al., *Atomic Hydrogen Adsorbate Structures on Graphene.* Journal of the American Chemical Society, 2009. **131**(25): p. 8744-+.
19. Hornekaer, L., et al., *Clustering of chemisorbed H(D) atoms on the graphite (0001) surface due to preferential sticking.* Physical Review Letters, 2006. **97**(18): p. 186102.
20. Mizes, H.A. and J.S. Foster, *Long-Range Electronic Perturbations Caused by Defects Using Scanning Tunneling Microscopy.* Science, 1989. **244**(4904): p. 559-562.
21. Ruffieux, P., et al., *Hydrogen atoms cause long-range electronic effects on graphite.* Physical Review Letters, 2000. **84**(21): p. 4910-4913.
22. González-Herrero, H., et al., *Atomic-scale control of graphene magnetism by using hydrogen atoms.* Science, 2016. **352**(6284): p. 437-441.

23. Sha, X. and B. Jackson, *First-principles study of the structural and energetic properties of H atoms on a graphite (0 0 0 1) surface.* Surface Science, 2002. **496**(3): p. 318-330.
24. Jeloaica, L. and V. Sidis, *DFT investigation of the adsorption of atomic hydrogen on a cluster-model graphite surface.* Chemical Physics Letters, 1999. **300**(1-2): p. 157-162.
25. Ivanovskaya, V.V., et al., *Hydrogen adsorption on graphene: a first principles study.* The European Physical Journal B, 2010. **76**(3): p. 481-486.
26. Moaied, M., J.V. Alvarez, and J.J. Palacios, *Hydrogenation-induced ferromagnetism on graphite surfaces.* Physical Review B, 2014. **90**(11): p. 12.
27. Borodin, V.A., et al., *Hydrogen transport on graphene: Competition of mobility and desorption.* Physical Review B, 2011. **84**(7): p. 075486
28. Lehtinen, P.O., et al., *Irradiation-induced magnetism in graphite: A density functional study.* Physical Review Letters, 2004. **93**(18): p. 187202.
29. Ferro, Y., et al., *Adsorption, diffusion, and recombination of hydrogen on pure and boron-doped graphite surfaces.* The Journal of Chemical Physics, 2004. **120**(24): p. 11882-11888.
30. McKay, H., et al., *Hydrogen on graphene under stress: Molecular dissociation and gap opening.* Physical Review B, 2010. **81**(7): p. 075425.
31. Wehling, T.O., M.I. Katsnelson, and A.I. Lichtenstein, *Impurities on graphene: Midgap states and migration barriers.* Physical Review B, 2009. **80**(8).
32. Moaied, M., et al., *Theoretical study of the dynamics of atomic hydrogen adsorbed on graphene multilayers.* Physical Review B, 2015. **91**(15): p. 155419.
33. Dion, M., et al., *Van der Waals density functional for general geometries.* Physical Review Letters, 2004. **92**(24): p. 246401
34. Román-Pérez, G. and J.M. Soler, *Efficient Implementation of a van der Waals Density Functional: Application to Double-Wall Carbon Nanotubes.* Physical Review Letters, 2009. **103**(9): p. 096102.
35. Methfessel, M. and A.T. Paxton, *High-precision sampling for Brillouin-zone integration in metals.* Physical Review B, 1989. **40**(6): p. 3616-3621.
36. Ghio, E., et al., *Vibrational spectrum of H and D on the (0001) graphite surface from scattering experiments.* The Journal of Chemical Physics, 1980. **73**(1): p. 556-561.
37. Morisset, S., et al., *Quantum dynamics of H2 formation on a graphite surface through the Langmuir Hinshelwood mechanism.* The Journal of Chemical Physics, 2004. **121**(13): p. 6493-6501.

Chapter 4: Graphene tunable transparency to tunnelling electrons as a tool to study the local electronic coupling of graphene with the underlying substrate.

4.1. Graphene on metallic substrates.

Graphene is known to exhibit notable differences in its electronic properties on top of different substrates. As graphene has been grown on diverse metallic substrates, a new collection of exciting properties such as band structure gaps, n- and p-type doping, magnetism, changes in Fermi velocity, or superconducting behaviour have been found [1-10]. This modifications on its properties appear as a direct consequence of the specific coupling between the graphene layer and its underlying host. Moreover, graphene-substrate interaction can be further modified by the intercalation, incorporation or adsorption of additional material. They locally induce gaps in the band structure of graphene, magnetic moments or decouple electronically the graphene layer [11-18]. Indeed, the specific graphene-substrate coupling also has an impact in the properties of adsorbates. This has been shown for the adsorption of magnetic atoms on various graphene systems. In the case of single Co atoms different magnetic moments and anisotropy have been found depending on the substrate used [19-22]. Moreover, we have also seen in the second chapter of this manuscript how by changing the number of layers of our SiC samples (and hence, the Dirac point energy) [23], the magnetic moment of our hydrogen atoms disappeared. In a similar way, the adsorption processes and interactions between hydrogen atoms that we discussed in chapter 3: physisorption channel, adsorption energy, diffusion barrier, changes in the energy landscape around the hydrogen atom, dimer formation, etc; will be probably affected by the graphene system coupling.

Therefore, gaining a detailed knowledge of the graphene-substrate coupling would make possible not only to characterize any novel property, but also to envision and design new ways of incorporating additional capabilities. A great experimental and theoretical effort is currently involved in measuring, understanding and controlling such interactions. From the experimental side, macroscopic techniques, such as ARPES or X-Ray Photoemission (XPS), can provide overall information about both the characteristics of the graphene layer and the underlying substrate [2, 8, 17, 24, 25], but lack the local resolution required to explore in detail the coupling of specific graphene regions. Local experimental techniques, such as STM or High-Resolution Transmission Electron Microscopy (HRTEM), can, on the other hand, characterize with atomic precision any modification on the graphene layer [12, 14, 26-31], but to date have provided very limited information about the underlying substrate. Such information is key to understand in depth the interactions at the local scale. In the literature there are a few STM works that have already indicated that under certain conditions the graphene layer is not visible in tunneling experiments, which directly allows to probe the underlying substrate. For example, in the SiC (0001) face, STM experiments have shown that for certain tunnelling conditions, the $(6\sqrt{3}\times6\sqrt{3})R30°$ interface reconstruction is visible through the graphene monolayer [32-34]. On graphene grown on Cu(111), the observation of standing

waves coming from the copper substrate underneath have been reported [35, 36] and also the herringbone reconstruction on graphene grown on Au(111) [36, 37]. For graphene islands grown on Ir(111) and Ag(111) confined states due to graphene states or the scattered surface state of the substrate have been observed depending on the tunnel conditions [38, 39]. In the case of intercalation experiments, STM measurements have also shown the capability to determine the order of the foreign species underneath the graphene layer [40-42].

From the theoretical side, calculations are rapidly progressing to understand this coupling, but to reach the insight required in the modelization, a complete experimental data set is necessary to ensure the consistency of the theory. The experimental results discussed above, were all obtained in low-interacting graphene-metal systems. In such weak graphene-substrate interaction systems, van der Waal forces play an important role. However, the functionals used now a days must be further optimized to accurately include van der Waal forces and be able to correctly describe these systems.

In this chapter, we aim to demonstrate the potential of graphene tunable transparency to probe local interactions by thoroughly characterizing the graphene/Cu(111) coupling using STM and Scanning Tunneling Spectroscopy (STS) experiments. We will show how to selectively modify the STM tip apex and/or the tunnel parameters to locally visualize, in the same energy range, either the graphene layer or the copper surface underneath, or even both at the same time. Our results, supported by ARPES and state of the art calculations (Density Functional Theory with van der Waals, DFT + vdW), yield a detailed picture of the existing electronic interactions and offer a clear explanation for the transparency mechanism. In addition, we show that this graphene tunable transparency can also be used to locally probe the interactions that adsorbates generate on the system. Structural or chemical modifications are frequently introduced in graphene layers to selectively modify its properties [11, 12, 14], but whether these novel properties will remain or not in the presence of an underlying substrate is a crucial but far from trivial question that needs to be solved for each specific system. In fact, even if the properties of graphene are weakly affected by a specific substrate, local modifications of the pristine graphene layer can noticeably modify its coupling to the substrate. This has been shown for the weakly interacting graphene/Pt(111) and graphene/Ir(111) systems, where the interaction with the graphene layer strongly increases after the introduction of single carbon vacancies in the graphene layer [43] or by the adsorption of H or Ir atoms [11, 44]. According to theoretical predictions, a strong local interaction between the graphene and the substrate develops where the vacancies or atomic adsorbates are located. In connection with the previous chapters of this thesis, it is important to understand how the local coupling modifies the properties of H atoms adsorbed on graphene layers. As we have already shown, H atoms are known to induce exciting changes in the electronic properties of isolated

graphene [45-47] and while for multilayer graphene grown on SiC(000-1) the apparition of a magnetic moment has been proven [23], for systems such as graphene/Ir(111) it was reported to give rise to the opening of a band gap due to a strong increase of the graphene-metal interaction at H sites [11]. Hence, as a proof of principle, we investigate atomic hydrogen adsorbed in our graphene/Cu(111) system and single C vacancies deliberately introduced on the graphene layer to show that graphene tunable transparency can reveal the local interactions between adsorbates with both the graphene layer and the substrate underneath.

4.2. Graphene on Cu(111)

We have chosen graphene on Cu(111) as a model system to understand graphene tunable transparency for three main reasons: i) It has a very weak graphene-metal interaction, which allows us to obtain the electronic properties of the graphene layer by visualizing the graphene quasiparticle dispersion; ii) The Cu(111) surface is a well-characterized substrate, so any modifications on its surface states induced by the interaction with the graphene layer can be easily identifiable; iii) Graphene on Cu is a very attractive system for practical applications since it enables the growth of high quality graphene films due to the low solubility of carbon in Cu [48] and can be transferred onto arbitrary substrates by chemical etching of the underlying metal [49, 50].

4.2.1 Gr/Cu(111) growth and characterization.

To grow monolayer graphene on Cu (111) we have used a technique developed in our laboratory by A.J. Martínez-Galera during his phD thesis [36, 51] that consists in the thermal decomposition of low energy ethylene ions irradiated on a hot copper surface. This technique allows growing very large graphene domains free of defects. This technique consists of three steps: 1) preparation of clean Cu(111) surface by the standard method of Ar^+ bombardment and annealing cycles, 2) ethylene irradiation, with an accelerated ion energy of 0.5 keV, keeping the Cu(111) substrate at around 800 °C, and 3) further annealing of the sample for 10 minutes at around 900°C.

The Cu(111) surface was prepared using cycles of Ar^+ bombardment with an ion energy of 0.5 keV during 20 minutes followed by 15 minutes annealing at ~625°C. In Figure 4.1 we can observe our typical Cu(111) sample prior to the growth of graphene, including atomic resolution. For the ethylene irradiation, a pressure of $1.5 \cdot 10^{-5}$ Torr of ethylene was used and the ions were accelerated with an energy of 0.5 keV while the sample was held at 800°C. After 20 minutes, the bombardment was turned off and the sample was annealed up to ~900°C for 10 minutes.

Due to its weak interaction, graphene usually grows on Cu(111) in several orientation domains, which leads to the formation of moiré patterns with different periodicity (see Figure 4.2) [36, 52, 53]. Our STM images show large regions covered by high quality graphene flakes (Figure 4.2a), where we can observe different moiré patterns depending on the relative rotation of the graphene sheet with respect to the Cu(111) substrate (Figures 4.2b-c). High resolution STM images, allow the geometric characterization of the graphene layer orientation with respect to the copper substrate by comparison with model sketches (Figure 4.2d).

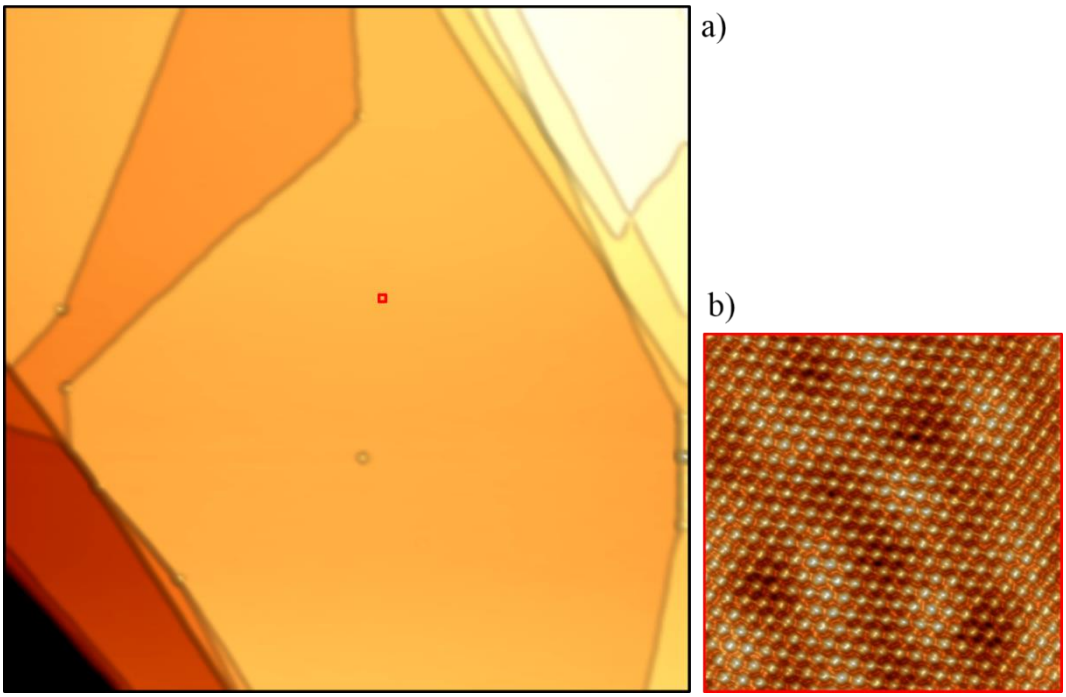

Figure 4.1: Cu(111) prior to graphene preparation. a) 900x900 nm² STM image showing the general morphology of the Cu(111) surface before the ethylene irradiation. b) Zoom in the red region marked in a) to appreciate the atomic resolution of Cu (111) (V=5V, I=0.1nA).

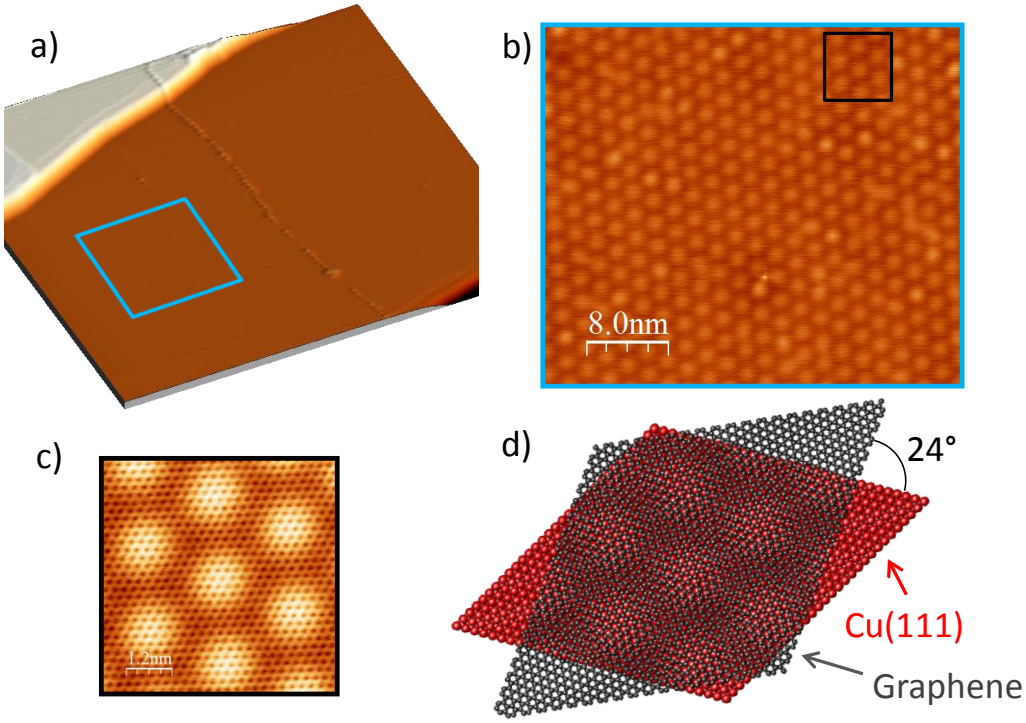

Figure 4.2: STM characterization of the general morphology of G/Cu(111) samples. a) 140x140 nm² region of graphene. b) 40x35 nm² zoom of a) where we can observe a moiré superstructure. c) 6x6 nm² zoom of previous image where atomic resolution on graphene can be observed. d) Schematic model of the moiré shown in c) where a graphene lattice (in black) is superposed onto the Cu(111) lattice (in red) with a rotation of 24°.

4.2.2 Tunable transparency: Seeing on and through graphene.

In order to study the electronic properties of our system, we have developed a new methodology that is illustrated in Figure 4.3, where we focus our attention into one specific terrace and image it using two different tip apex terminations but with identical scanning conditions. As it can be seen, thanks to graphene tunable transparency to tunneling electrons we can selectively visualize only the graphene layer as in Figure 4.3a, or tunnel through such overlayer revealing the modifications induced on the Cu (111) surface by the coupling with graphene as in Figure 4.3b. Such changes in the tip visualization mode are fully reversible and are deliberately introduced by controlled indentations of the STM tip onto the G/Cu(111) substrate.

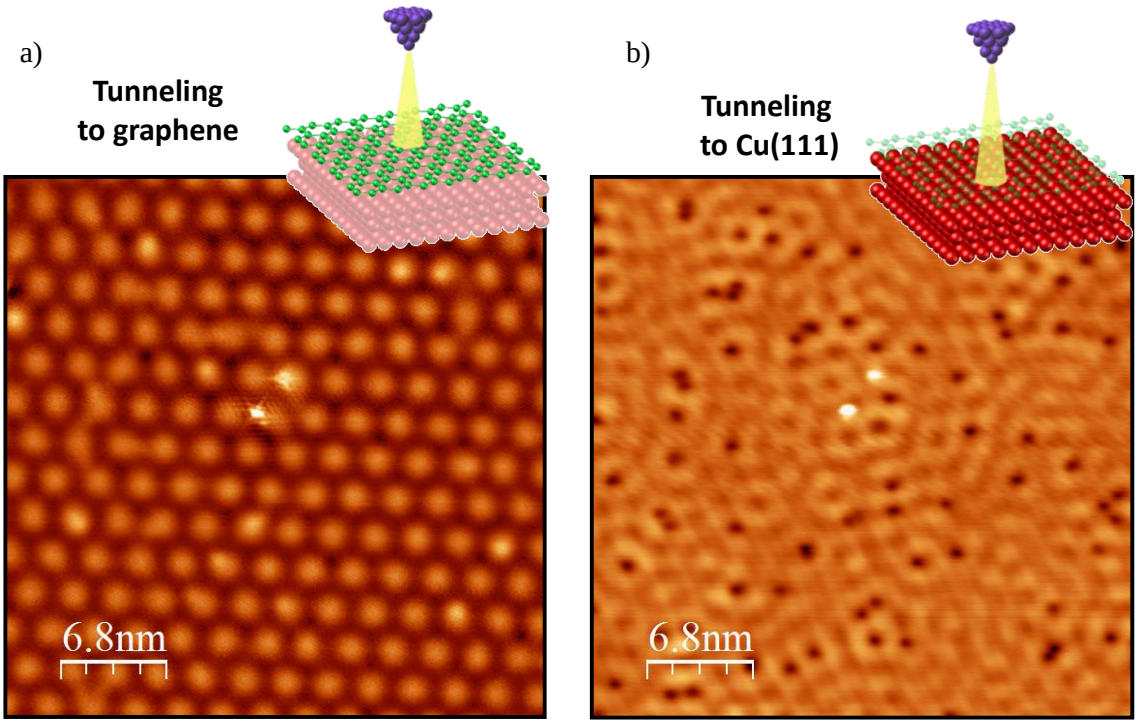

Figure 4.3: Gr/Cu(111) transparency. STM images showing the same graphene/Cu(111) sample region measured with different tip apex terminations, which enables to selectively visualize in the same energy range, graphene (a) or the Cu(111) substrate underneath (b). Image size: 34 × 34nm^2; sample bias: 50meV; tunnelling current: 0.4nA.

The actual procedure to selectively change the tip state was the following: We first imaged an specific G/Cu(111) region with a given tip, i.e. a tip probing either Cu surface states or graphene states. Then, we moved ~500 nm away from this region to modify the tip apex by the controlled indentation of the STM tip onto the substrate without affecting the region of interest. Typical indentation values were: z-displacement ~2-4 nm, bias voltage ~1-2V. After each indentation experiment we acquired a dI/dV spectrum to check the tip state. We found that by acquiring an STS spectrum we could quickly identify which kind of tip we had: tips probing graphene states have a reduced DOS in the vicinity of E_F (possibly

due to some contamination of the tip apex with electronegative impurities) while tips sensing Cu(111) surface states clearly see the onset of the Cu(111) surface state with a featureless DOS close to E_F (as expected from a purely metallic tip), see Figure 4.4. We systematically repeated this procedure until we obtained the desired tip-apex change. The exact number of indentations required varied from tip to tip, but after a few repetitions it was always possible to obtain the desired tip state. Then, we moved back to the initial region and measured it again with the modified tip to fully characterize it.

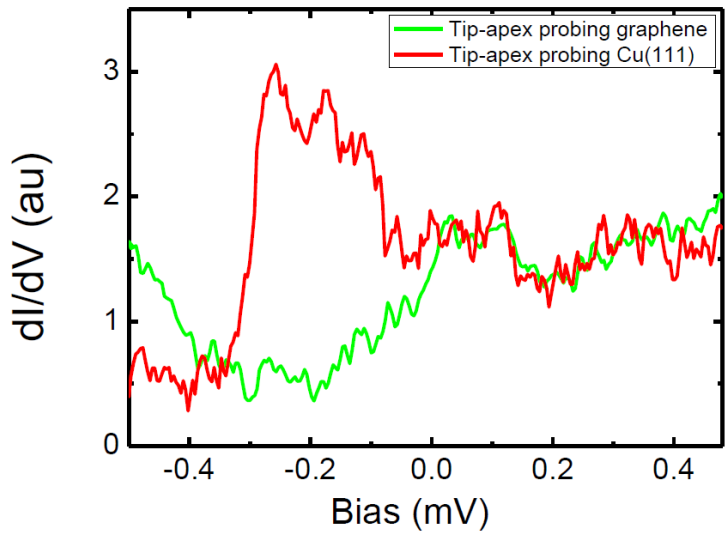

Figure 4.4: Tip state identification from dI/dV spectra. dI/dV curves measured on the graphene/Cu(111) sample region shown in Figure 4.3 with different tip apex terminations to selectively probe graphene (green curve) or the Cu(111) surface states (red curve). Green/red curve was obtained with the same tip apex termination than Figure 4.3 a-b. Both dI/dV curves were measured with the same tunneling parameters: nominal junction impedance of 1.2 GΩ (-500 mV, 0.4 nA).

4.2.3 Gr/Cu(111) electronic properties measured by STM

4.2.3.1 STS characterization of 2D electronic states: Cu(111) surface state, a model case.

Of particular interest for the present study is the characterization of 2D electronic states by STM. Pioneering STM works showed the possibility to visualize the elastic scattering of quasiparticles from these 2D electronic states with the different impurities of the system in the form of quantum interference patterns [54, 55]. The interference between incident and scattered 2D quasiparticles gives rise to LDOS spatial modulations related to the particular symmetry of the 2D constant-energy contour of the system (2D constant-energy contours present, in the reciprocal space, all the available electronic states for each energy). In a very simple picture, elastic scattering at impurities couple different states $\vec{k}(E)$ and $\vec{k'}(E)$ of the constant-energy contour, being more

probable the scattering processes corresponding to good nesting vectors. It was also shown [54, 55] that the 2D Fourier Transform (2D-FT) of STM dI/dV images is closely related to a map of the constant-energy contour of the 2D state since it reflects the possible scattering vectors of the system, being this an efficient method to directly obtain k(E).

One of the first systems where this was demonstrated was the Cu(111) surface [54]. Pristine Cu(111) presents a Shockley surface state characterized by a 2D free-electron like behaviour with an isotropic parabolic band dispersion given by: $E = E_0 + \hbar^2 k^2 / 2m^*$, where E_0 is the band edge and m* is the effective mass, see Figure 4.5a. The 2D constant-energy contours correspond then to a ring of radius k(E) centred at the Γ point of the Brillouin zone (see right panel in Figure 4.5a). Accordingly, as shown in Figure 4.5b, the 2D-FT of dI/dV maps, measured at energy E=e·V, show a central ring of radius $2\vec{k}(E)$ (here scattering between states $\vec{k}(E)$ and $\overrightarrow{k'}(E)$, with a scattering vector $2\vec{k}(E)$, are the most efficient processes as indicated in the right panel of Figure 4.5b). The energy dispersion k(E) of the clean Cu(111) surface is then obtained by performing the 2D-FT of dI/dV maps measured at different energies (see Figures 4.5c-g). The band edge can be determined from the energy position of the sudden step observed in dI/dV curves measured on clean terraces (Figure 4.5h) [56] .We obtained E_0=-430±10 meV and m*=0.390±0.01 m_e (m_e is the free-electron mass) for the Cu(111) surface state before graphene formation, in perfect agreement with the values reported in the literature [54, 57, 58] (see Figure 4.5i and Table 2).

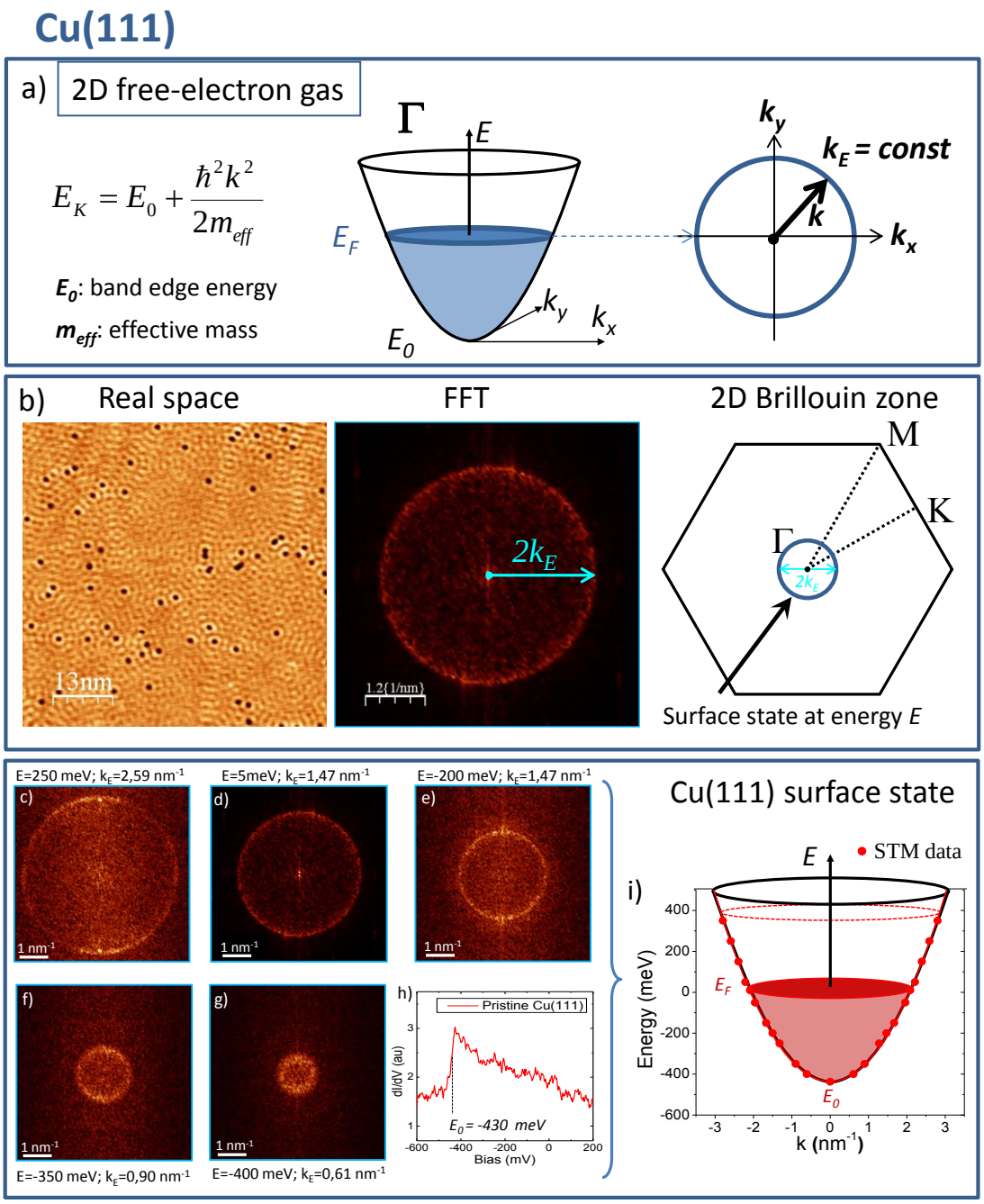

Figure 4.5: Characterization of 2D electronic states by STM/STS. a) 2D free-electron gas with its characteristic parabolic dispersion and the corresponding 2D constant energy contours. b) Left panel: STM dI/dV map where the standing waves are visible. Central panel: 2D-FT of the left image where a central ring of radius 2k can be observed. Right panel: 2D Brillouin zone of Cu(111). c-g) 2D-FT of dI/dV maps measured at different energies. h) dI/dV curve measured on clean Cu(111) where we can observe the sudden step related with the band edge of the surface state. i) Parabolic dispersion extracted from dI/dV maps and dI/dV curves as the ones shown in Figures 4.5 c-h.

4.2.3.2 STS characterization of the electronic states of Gr/Cu(111).

In the case of graphene, the low energy bands consist in cones at *K* and *K'* points of the Brillouin zone, named valleys, presenting a linear and isotropic dispersion. Accordingly, near E_F graphene constant-energy contours correspond to rings of radius *k*(E) centred at the *K* and *K'* points of the Brillouin zone (see Figure 4.6b). As mentioned in section 1.8, in monolayer graphene, due to the peculiar symmetry of quasiparticle wavefunctions, named pseudospin, two-dimensional Fourier Transform (2D-FT) of d*I*/d*V* maps essentially probe intervalley scattering processes [59, 60]. As depicted in Figure 4.6b, in those events graphene quasiparticles scatter between neighboring valleys, giving rise to scattering vectors *q(E),* which correspond to $(\sqrt{3} \times \sqrt{3})R30°$ interference patterns in the local density of states (LDOS). Thus, our 2D-FT (Figure 4.6a,c) shows ring-like features of radius *2k(E)* centred at *K* and *K'* points of the Brillouin zone.

By selecting the appropriate tunneling conditions, one can simultaneously image both the graphene layer and the underlying Cu(111) substrate. This is shown in Figure 4.6a presenting the 2D-FT of the LDOS measured at E_F on a 45x45nm^2 G/Cu(111) region. Scattering processes from graphene quasiparticles give rise to the aforementioned *K* and *K'* rings (green square), whereas scattering processes from Cu(111) surface quasiparticles generate the central, larger ring visible at Γ (red square). As shown in Figures 4.6c,e, the radius of the rings centered *K/K'* and Γ points correspond to twice the Fermi wave-vector of the graphene layer and the underlying Cu(111) surface state respectively. In the 2D-FT central zone, outlined by the red square, six points show up due to the moiré pattern originating from the existing rotation of 12° between the graphene layer and the Cu(111) surface.

The dispersion of both the graphene Dirac-like band and the Cu(111) surface state can be obtained from the 2D-FT in energy dependent d*I*/d*V* maps (see Figure 4.7c,f respectively and Tables 1 and 2 in section 4.6). A linear dispersion characterized by k_{FG}=0.55±0.03 nm^{-1} and v_{FG}= (1.1±0.1)·10 ^{6} m/s is obtained for graphene in the present case (see Figure 4.7c and Table 2). Our STS data show an upwards shift of +0.13 eV of the onset of Cu(111) (see d*I*/d*V* spectra in Figure 4.7d). Aside from this energy shift, the energy dispersion obtained from the 2D-FT of d*I*/d*V* maps shows a non-rigid upwards displacement of the Cu(111) surface state band, with an effective mass increase from 0.39m_e to 0.43m_e (Figure 4.7e). In Figure 4.7f we superimpose the central region of the 2D-FT of d*I*/d*V* maps measured at E_F on covered and uncovered Cu(111) regions. A smaller ring, corresponding to a smaller Fermi wave-vector in graphene covered areas, indicates the electron depletion of the Cu(111) surface state band. Earlier STM/STS experiments[61, 62] have reported similar modifications of the Cu(111) surface state in the presence of weakly interacting

overlayers, such as 1ML Xe or insulating NaCl, whose very low DOS at E_F enables the transparency of tunneling electrons.

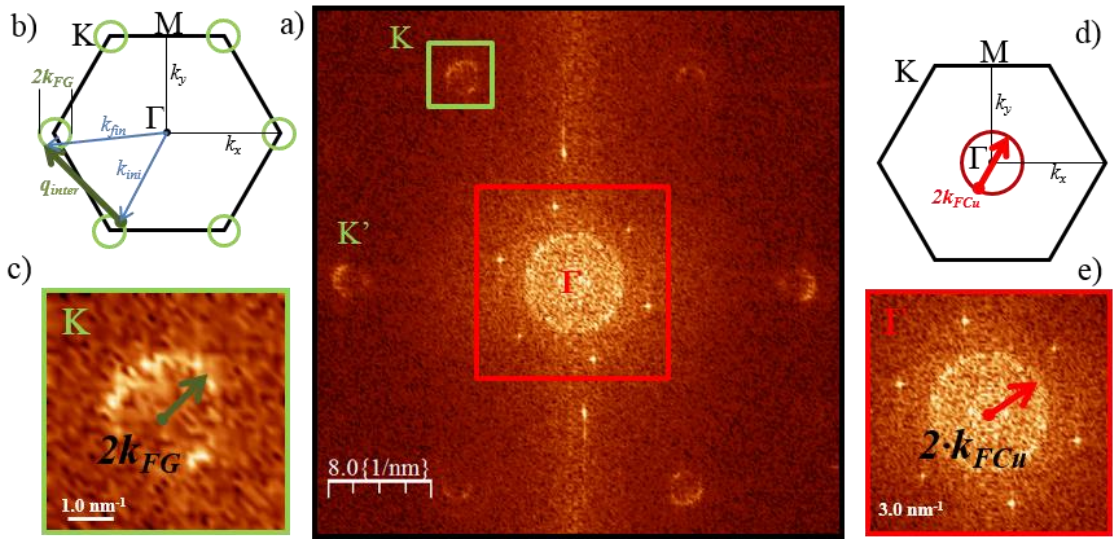

Figure 4.6 Electronic structure of the Gr/Cu(111) system by LT_STM. a) 2D-FT of the LDOS measured at EF on a 45 × 45 nm2 graphene/Cu(111) region, when the tip is tuned to visualize both graphene and Cu underneath. b) Schematic Fermi surface for electron-doped graphene, where arrows illustrate an elastic intervalley scattering process. c) Zoom-in on the outer ring centered at *K* point outlined in a) by the green square. d) Schematic Fermi surface of the Cu(111) surface state. e) Zoom-in on the central region outlined in a) by the red square.

Figure 4.8 qualitatively sketches the outcome of our measurements (for quantitative details see section 4.6). A graphene Fermi wave-vector of k_{FG}= 0.55 nm^{-1} is found in revealing an electron doping of $1.0 \cdot 10^{-3}$ e/Å^2 for the overlayer (the Dirac point is exactly at E_F, *i.e*, k_{FG}=0, for isolated graphene). This graphene doping is due to an electronic transfer from the Cu(111) surface state, whose Fermi wave-vector decreases from the value of k_F = 2.10 nm^{-1} of the pristine Cu(111) surface, to k_{FCu}=1.80 nm^{-1} found in the presence of the graphene overlayer. This corresponds to an electron lose of $-1.9 \cdot 10^{-3}$ e/Å^2. Therefore, as we explain in detail in section 4.3, not all the charge leaving the Cu(111) surface state is incorporated into the graphene layer.

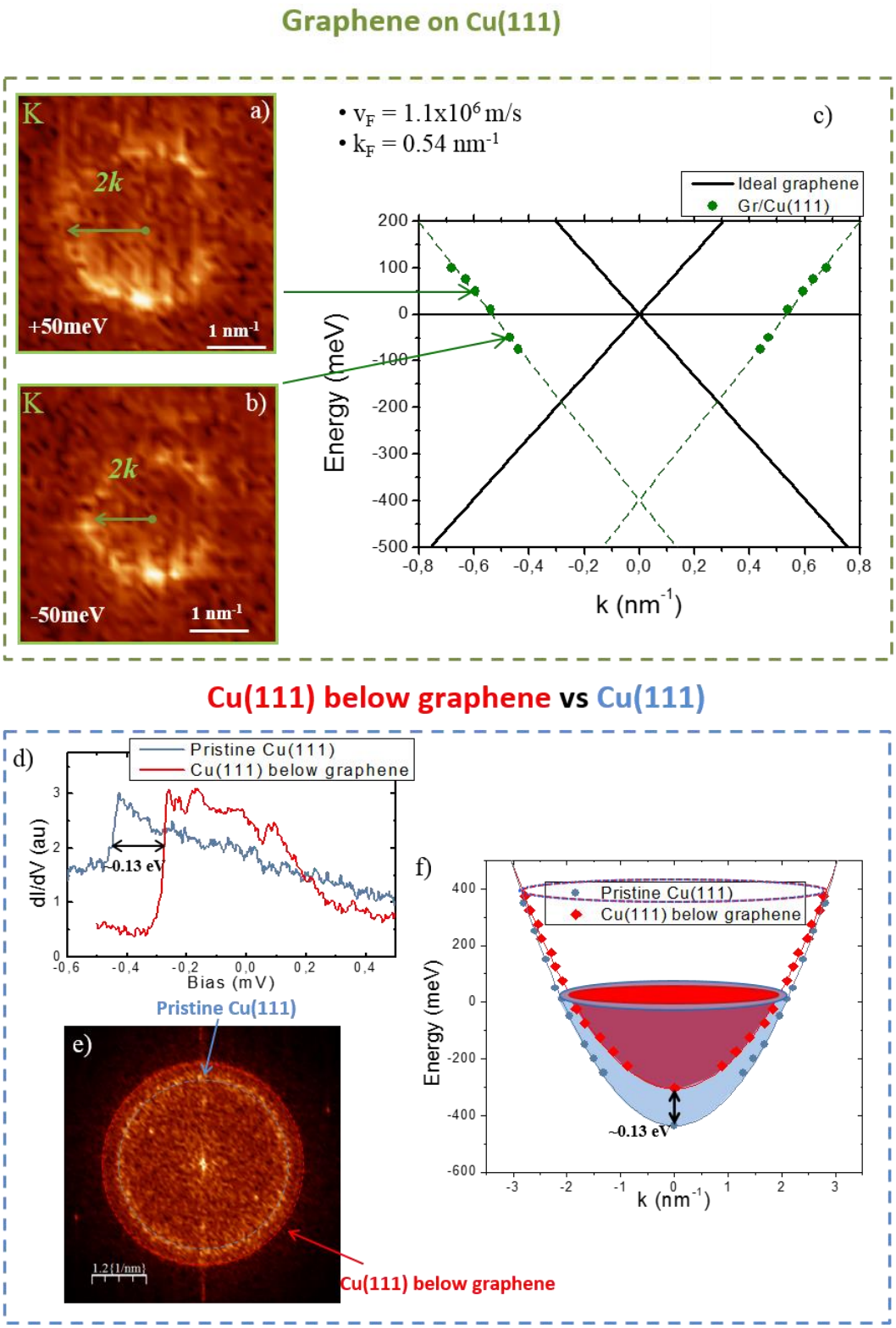

Figure 4.7: Graphene and Cu(111) energy dispersion on Gr/Cu(111). Energy dispersion of graphene π bands (c) is obtained from the energy dependence of the radius of the ring like features centered at *K* points of the Brillouin zone (a-b). d) dI/dV spectra showing the energy shift of the surface state band edge. e) Energy dispersion of the Shockley surface state (red) compared with the one of pristine Cu(111) (blue). f) Central region of two 2D-FT of dI/dV maps measured at E_F showing the different k_{FCu}, for pristine Cu(111) and Cu(111) below graphene.

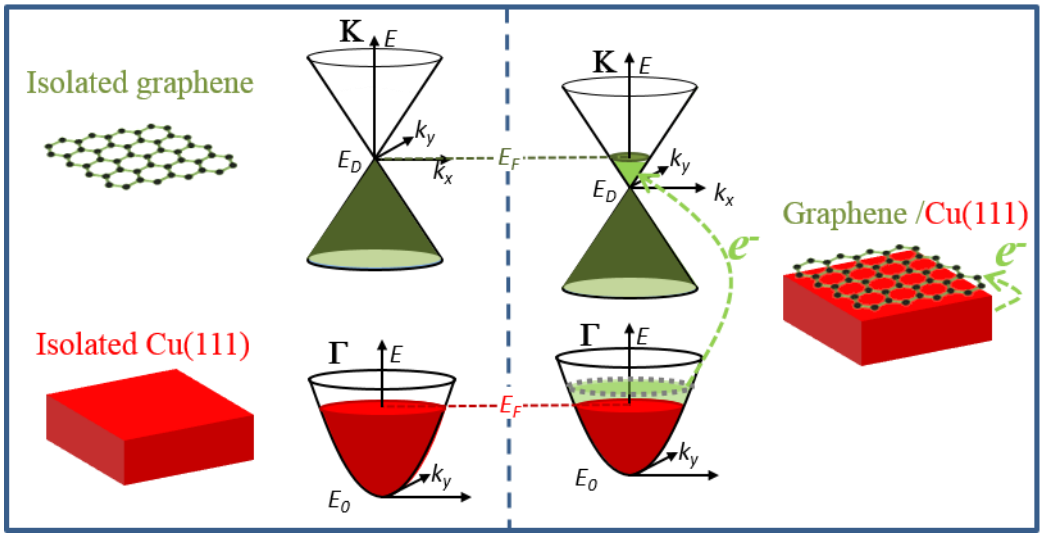

Figure 4.8: Schematic representation of our results. Left panel shows the isolated energy dispersion of graphene and Cu(111). Right panel shows the charge transfer occurring when graphene is placed on top of Cu(111)

It is noteworthy that the STM values have been obtained from over 50 graphene and Cu(111) regions exhibiting different orientations where practically identical doping level values are found (see Figure 4.9). The doping levels from Figure 4.9 are estimated from the change in the Fermi wave-vectors of the graphene and Cu(111) surface state by comparing values from the pristine systems and the coupled G/Cu(111) one. For graphene: $n=2\cdot2\cdot k_{Ffin}^2/4\pi=k_{Ffin}^2/\pi=+1.0\cdot10^{-3}$ e/Å^2; where k_{Ffin}= 0.55 nm^{-1} is the Fermi wave-vector of graphene in contact with the Cu(111) surface. For Cu(111): $n=2\cdot[k_{Ffin}^2-k_{Fini}^2]/4\pi$; $=[k_{Ffin}^2-k_{Fini}^2]/2\pi=-1.9\cdot10^{-3}$ e/Å^2;where k_{Ffin}= 1.80 nm^{-1} is the Fermi wave-vector of Cu(111) below the graphene layer and k_{Fini}= 2.10 nm^{-1} is the Fermi wave-vector of pristine Cu(111). Such constant experimental doping for the graphene/Cu(111) interface suggests that graphene doping is dominated by the nature of the underlying substrate with little influence of the specific arrangement of the graphene layer.

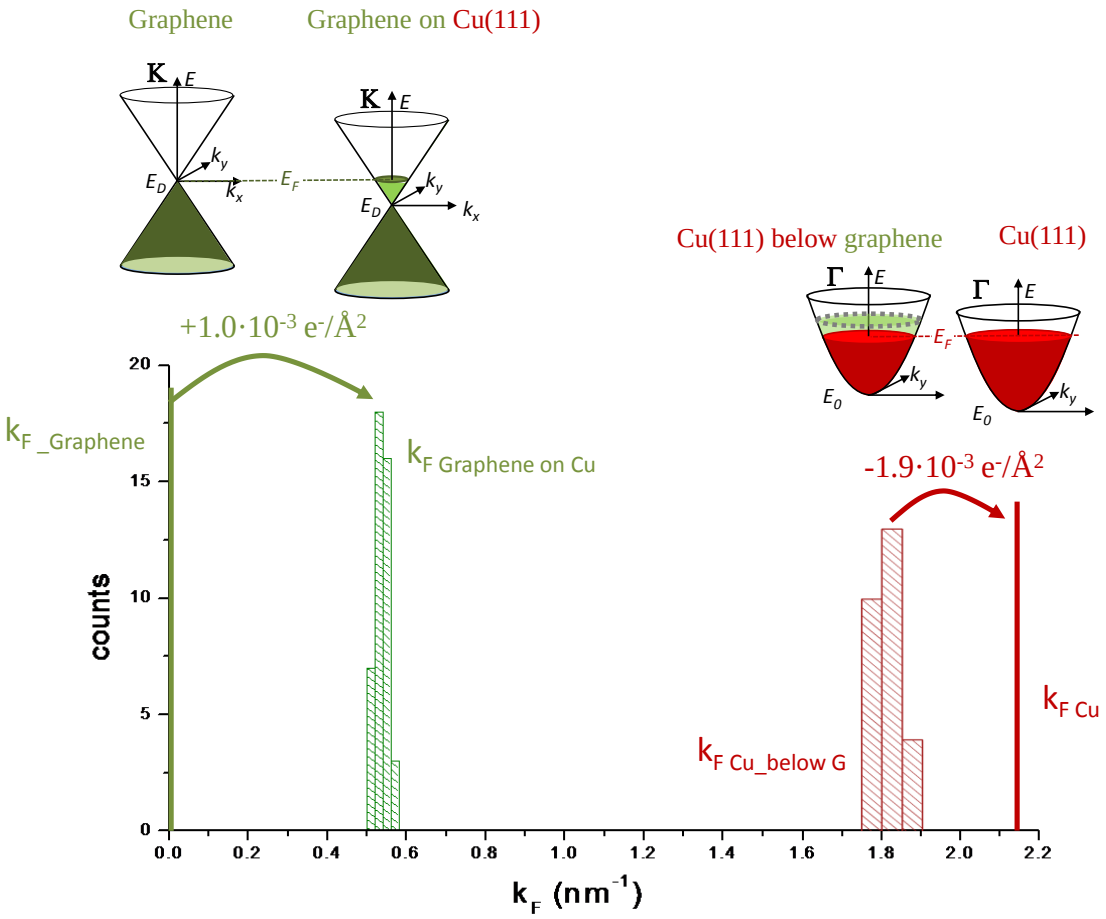

Figure 4.9: STM/STS measurements over more than 50 different graphene/Cu(111) regions. The lower part of the image shows the histograms for the the STM values obtained from over 50 graphene and Cu(111) regions exhibiting different orientations. Practically identical doping levels values are found. Such constant experimental doping for the graphene-Cu(111) interface suggests that graphene doping is dominated by the nature of the underlying substrate with little influence of the specific arrangement of the graphene layer. The schematic band dispersions of the upper part, qualitatively illustrate the outcome of our measurements.

4.3 Gr/Cu(111) coupling described by DFT methods

To get a better insight on the interaction that is taking place between our graphene layer and the substrate underneath, and aiming to fully understand our system, we started a collaboration with the group of Prof. Rubén Pérez. This group has been investigating graphene systems by means of DFT calculations and in the last years they have started to implement the impact of the van der Waals (vdw) interaction in their description of graphene/metallic systems. In addition, they can also combine first principle calculations with non-equilibrium Green's function formalism, allowing them to calculate transport properties.

In previous works, first principles calculations based on recent improvements on density functional theory (DFT) that include dispersion interactions [63, 64] have been extensively used [65] in order to shed light on the graphene-metal interaction. Although they have disclosed some of the fundamental properties of these systems, some theoretical approaches have not been conclusively validated. Main concerns lay on the van der Waals (vdW) interactions. Approaches for dispersive interactions have been well tested for molecule-molecule interactions or the absorption of small molecules on surfaces where more exact methods can be used [63, 64]. However, on extended systems, their size prevents the use of these accurate methodologies, so the validation of the theoretical results has to come exclusively from the comparison with experimental data. Graphene on metals is a prototypical example of extended system ruled by vdW interactions. There are already multiple references where DFT+vdW simulations in G-metal systems have been compared with the data measured with different structural and spectroscopic experimental techniques [66]. The experimental findings presented above, exploiting the tunable transparency, offer the quantitative information needed to further refine that comparison on several key parameters that characterize the G-metal coupling such as the G layer-metal distance, the graphene corrugation and the charge transfer within a single experimental technique.

Our collaborators used our experimental information to test the description of the G/Cu(111) interaction provided by first principle simulations that combine DFT with different theoretical approaches to describe vdW interactions. These methodologies include the use of the PBE [67] exchange-correlation (XC) functional supplemented by semi-empirical approaches like the popular Grimme D2 [68] (PBE-D2) and Grimme D3 (PBE-D3) [69], and recently proposed functionals that include the vdW interactions in the XC kernel (DFT-DF), like the optB86b-vdW functional proposed by Klimes et al. [70]. For all these calculations, VASP code [71] with a 400 eV cutoff for the plane wave basis set and PAW pseudopotentials was used [72]. The experiments show that the Cu surface state plays an important role on this system. An accurate description of this state with DFT simulations requires a slab with more than ~15 Cu layers in order to

decouple the surface states of both slab faces. Using a Cu slab consisting on a 1x1 surface cell and 15 layers, the onset of the surface state at ~ -0.39 eV with respect to the Fermi level and an effective mass m*/me of ~ 0.38 were obtained, in good agreement with our STM experiments and previous calculations. The addition of the graphene layer to the 1x1 Cu(111) slab results on a charge transfer between the graphene and the metal that shifts the Dirac point toward lower energies [73].

PBE-D2 calculations yield a graphene-surface average distance of ~2.9 Å, which translates into an unrealistic downward shift of the Dirac point of ~0.65 eV and an upward shift of the onset of the Cu surface state of ~0.4 eV with an effective mass of m^*/m_e ~ 0.48 (see Figure 4.10c,d). The comparison of these numbers with the local STM experimental information indicates that the charge transfer yielded by the simulation is much larger than the real one, i.e. the PBE-D2 method is overestimating the graphene-metal interaction. Calculations show that while the total binding energy, essentially controlled by the vdW forces, is quite flat, the resulting graphene-metal coupling, reflecting the overlap of the wavefunctions and described by DFT, strongly depends on the graphene-metal distance. From the comparison between theory and experiments, we can conclude that the graphene-metal coupling is correctly described by PBE at the 3.4 Å G-Cu distance. The discrepancies with the experiments can be indeed attributed to details in the description of the vdW interactions: further calculations show that more accurate approaches like PBE-D3 [69] and the DFT-DF optB86b-vdW functional [70] yield G-Cu distances of ~3.2 Å and ~3.3 Å respectively (see Figure 4.10d).

In this way a clear correlation between the shifts of the Dirac point and the onset of the Cu surface state with respect to the graphene-Cu distance was obtained (see Figure 4.10d). At an average distance of 3.4 Å, with an energy increase of just 45 meV per surface unit cell (with respect to 2.9 Å), the shift of the onset of the Cu surface state is +0.13 eV with an effective mass of m^*/m_e ~ 0.41 and the Dirac point is placed at -0.35 eV with k_{FG} ~ 0.6 nm^{-1}) all in excellent agreement with the experiments, see Figure 4.10 (notice that for the separation of 2.9 Å we get an unrealistic value of k_{FG} =1.3 nm^{-1}).

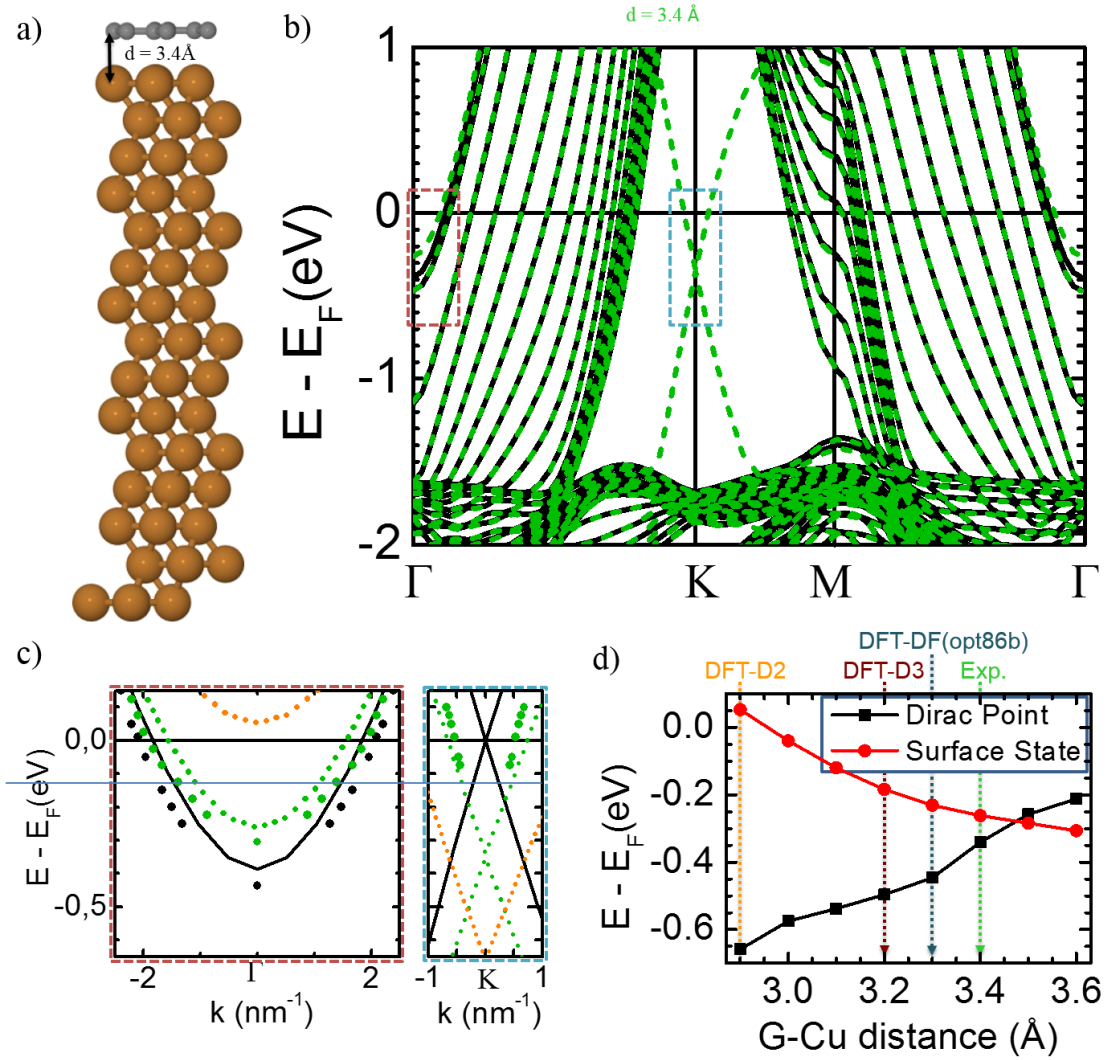

Figure 4.10: DFT+vdW calculations of the G/Cu(111) system. a) Ball-and-stick model of the (1x1) surface cell of graphene on Cu(111). b) Band structure of graphene on Cu(111) for the (1x1) surface cell with optimal empirical graphene-Cu distance of 3.4 Å (green dashed lines) and the isolated Cu slab bands (black lines). c) shows zooms of the G/Cu (green dashed lines and Cu (black lines) bands in the vicinity of E_F around Γ and *K* high symmetry points, which include the experimental results (dots). For comparison the bands for a 2.9 Å graphene-Cu separation (orange dot lines) are included. d) The graphene Dirac point (black line) and the Cu surface state (red line) positions as a function of the G-Cu distance. The equilibrium distances obtained with DFT-D2 (orange), DFT-D3 (purple), DFT-DF(opt86b) (blue) and the optimal empirical G-Cu (green) separations are marked.

This accurate description allows us to provide more trustful quantitative information on the graphene-Cu coupling. Aside from doping, calculations show that the graphene bands close to E_F practically do not interact with Cu bands keeping unmodified the graphene electronic properties (see Figure 4.10b). This doping is due to both work function differences of Cu and free-standing graphene (~0.2 eV) and the interaction between them [73] (see Figure 4.11). Our experiments show that the graphene is increasing its electronic charge by $1.0 \cdot 10^{-3} e/Å^2$ while the Cu surface state is transferring $1.9 \cdot 10^{-3} e/Å^2$. This suggests the presence of a charge dipole pointing from the G to the Cu. However, the

decrease in the work function of the G/Cu, 4.3 eV in the calculations (4.2 eV measured with ARPES), with respect to the Cu(111) surface, ~4.8 eV (4.9 eV measured with ARPES) requires a dipole in the opposite direction [73]. This dipole can be clearly observed in Figure 4.11, where the calculated plane-averaged differential electron density is represented.

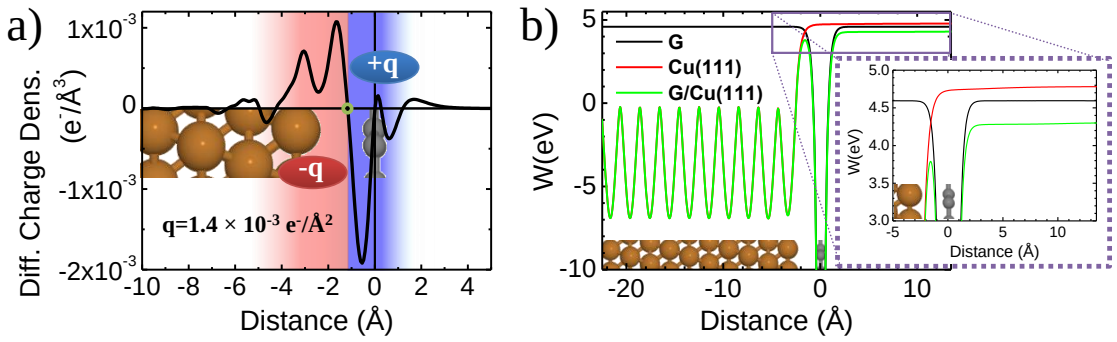

Figure 4.11: Charge density distribution and level alignment on G/Cu(111). a) Differential average plane charge density calculated as the difference between the charge density of the G/Cu system and the isolated G and Cu slabs. A dipole pointing out from Cu to G localized between the metal surface and the layer is clearly observed (red and blue areas show respectively excess and deficit of electron charge density). The charge, q, integrated from the nodal point (green circle) to the infinity is 1.4 × 10^{-3} e-/Å^2 (~1/2 of the dipole charge previously reported [73]). The formation of this dipole results on a reduction of the workfunction of the G/Cu respect of the G and Cu ones. b) Electrostatic potential of G (black line), Cu(111) (red line) and G/Cu(111) (green line) respect to their corresponding Fermi levels. The asymptotic value (4.6 eV, 4.8 eV and 4.3 eV for G, Cu, and G/Cu respectively) is the workfunction provided by the PBE calculation.

These results concerning the nature (n-doping) and distance dependence of the charge transfer to graphene from Cu are consistent with earlier calculations by Giovanetti et al. using the local density approximation (LDA) to the exchange correlation functional [5] and later work from some of those authors [73] using the PW91 GGA functional. Calculations also reproduce the prediction of ref. [5] of an interface dipole that tends to reduce the work function of the G/Cu system with respect to that of the clean metal. However, the orientation of this dipole (see Figure 5 in ref. [73]), with the positive charge close to the G sheet seems to be inconsistent with the G being n-doped (extracting electrons from the metal). Our detailed measurements of the Fermi wave vectors of G and the Cu confirm that this is indeed the case and identify one important contribution to the G doping, with electrons being transferred from the surface state to G. The way out of this puzzle is to abandon the naive view of charge being transferred and localized at the positions of the atoms and focus instead on the spatial extension of the electronic orbitals involved in the process. The Cu surface state extends through and beyond the G and its loss of charge in that area is larger than the charge gained by the pure G states that are significantly more localized. The 0.9·10^{-3}e/Å^2 of the charge left by the Cu surface state, which is not incorporated into the graphene layer, is located on the G-Cu coupling area to complete the dipole. The large extension of the Cu surface state is not only important to explain the puzzle

between n-doping and the interface dipole but provides the crucial hint to understand the tunable transparency of G, as discussed in the following section. The previous analysis has been possible due to the experimental ability to sense both the graphene and the substrate underneath.

One should notice that the theoretical results presented above have been calculated with a small 1x1 surface unit cell. Due to the lattice mismatch, imposing a 1x1 periodicity implies a strong deformation of either the G layer or the metal. In the present calculations, the Cu lattice parameter was used to correctly describe the surface state, thus the G layer has been stretched by 4.6%. This induced strain is so high, with such a large energy penalty that makes the 1x1 moiré unrealistic. This is consistent with the fact that the G/Cu moiré patterns observed in the experiments are much larger. Simulations with a $\sqrt{57}$x$\sqrt{57}$ moiré with respect to the G, one of the smallest observed experimentally, but with only 4 Cu layers have been performed (see Figure 4.12). Although this calculation cannot provide a proper description of the influence of G on the Cu surface state (the simulation with 15 Cu layers is beyond the current computing capabilities), it does shed light on the possible influence of strain in the results discussed above. In this moiré, the lattice mismatch is very small, only 0.3%, so the uncertainties coming from the choice of the lattice parameter are minimized. An average G-Cu distance of 3.0 Å, slightly larger than in the 1x1 case was found, and a topographic corrugation of the G layer of 9 pm. The areas with C atoms on top of the Cu atoms are the lowest ones, while the ones corresponding to hollow positions are the highest (see Figure 4.12b). Similarly to the 1x1 case, this moiré also shows a large downward shift of the Dirac point (0.6 eV), indicative again of a large G-Cu interaction. Furthermore, the Dirac point position coincides with the case of the 1x1 surface cell for the same G-Cu distance (see Figure 4.10d). These results show that the link between G-metal distances and energy shifts are essentially the same for the real $\sqrt{57}$x$\sqrt{57}$ moiré pattern and the 1x1 surface cell, and, thus, validate our previous discussion of the G-metal interaction on the properties of both graphene and the Cu surface state.

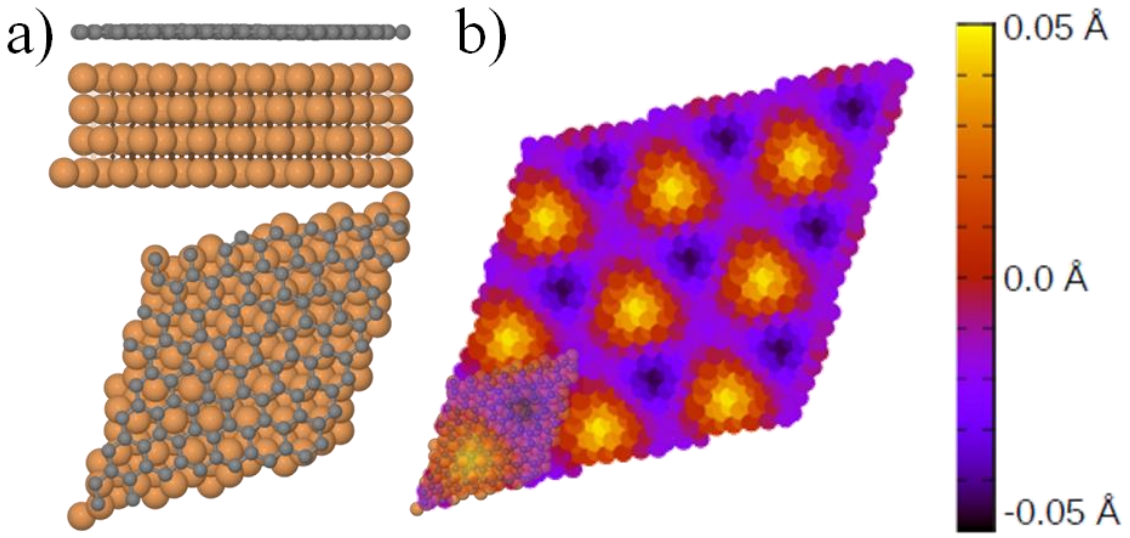

Figure 4.12 The √57x√57 moiré pattern. a) Ball-and-stick model of the atomic structure of G/Cu(111) forming a √57x√57 moiré pattern (respect to the G) calculated with PBE+D2. The average G-Cu distance is 3 Å. b) Color map of the corrugation of the G layer for his moiré pattern. Area with smaller G-Cu distance corresponds to C atoms stacking on the top of Cu atoms, while maximum separation corresponds to carbons staking on hollow positions. The layer is very flat with a corrugation of just 9 pm.

4.4 Explanation of graphene transparency

It is of paramount importance to understand the mechanism behind this graphene tunable transparency. Our results show that the answer lies in the difference in the decay lengths between the metal surface state and the graphene π-states, much larger in the first case. To demonstrate this, we present in Figure 4.13a the calculated plane–averaged electron density projected on the energy range -0.5 eV to E_F for an isolated Cu slab (red line), a free standing graphene layer (black line), and both together with the optimal separation of 3.4 Å (green line). The decay of the Cu surface state is slow compared to the graphene, which shows a more localized charge in space. For distances larger than ~ 4 Å from the graphene, the charge density coming from the Cu is prevailing over that of the graphene in spite that the metal surface is 3.4 Å deeper.

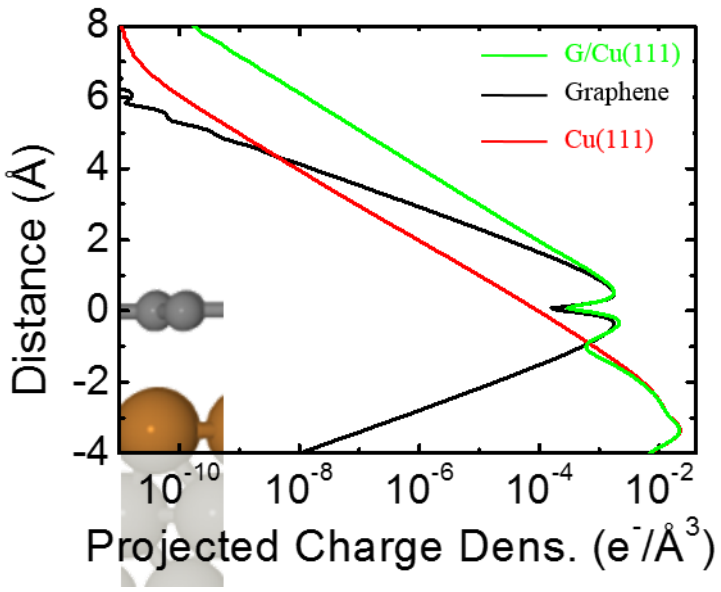

Figure 4.13: Projected charge density on the energy range from -0.5 eV. Projected charge density on the energy range from -0.5 eV to E_F integrated in the xy plane as function of perpendicular position for graphene on Cu (green line), for a Cu(111) slab (red line) and for an isolated graphene (black line). Note that all curves share the same relative positions, being graphene its distance origin. We observe that the Cu surface state decay length is larger than graphene, so for graphene on Cu, the charge at larger distances is dominated by Cu.

To substantiate these simple arguments and to identify the nature of the tips that allow the imaging of both G and the Cu surface state, our theoretical collaborators combined first principles simulations with Non Equilibrium Green Function calculations [74] to determine the electronic current between the STM tip and the G/Cu(111). A simulation of the Cu surface standing waves observed on the STM experiments, created by the scattering of a low density of point defects and extending for several nanometres, would require extremely large cells. In order to capture this effect with a reasonable use of computational resources, they introduced an artificial electronic modulation on the Cu surface with a line defect: they replace an entire row of Cu surface atoms on the [1$\bar{1}$0]

direction by oxygen atoms, and repeat this process with a periodicity of ~ 2 nm, large enough to accommodate the lateral decay of the real standing waves. This can be simulated with a 9x1 surface cell and a slab that includes the 15 Cu layers required to properly describe the Cu surface state. A G layer at the distance of 3.4 Å following a 1x1 moiré pattern was also included (see Figure 4.14a)

In the experiments, we found two different kinds of tips. After preparation by soft contact with the G/Cu(111) substrate, most of the tips easily image the Cu standing waves, but only few are able to provide atomic resolution on G. Playing with these last tips, we discovered that a reduction on the set point (an increase of the tip-surface distance) resulted on a change of contrast from the graphene to the Cu. In order to understand this behavior, the STM contrast obtained with two different models for tip apexes was theoretically analysed: A pure Cu (111)-oriented tip with 10 atoms (Cu10 tip), and an O-contaminated tip, where the Cu atom at the apex was replaced by an O atom (CuO tip). Both structures are stable and have been used in previous studies of STM/AFM imaging on CuO_2 surfaces by our collaborators [75]. In the context of the G/Cu system, the O atom mimics the possible contamination of the tip with electronegative impurities with similar chemical properties, like S, that are known to be abundant in Cu [36, 76], and thought to be a local source of scattering that contributes to the observed standing wave pattern. Note that metal tips are very reactive and thus prone to contamination.

Figure 4.14 compares constant current profiles calculated with the purely metallic Cu10 tip and the contaminated CuO tip. At large distances (d > 4 Å), both tips are sensing the charge modulations originated in the Cu surface states by defects on its surface, confirming the key role of the different decay lengths of Cu surface states and G π states in the imaging of the Cu substrate, that almost any tip is able to capture. At closer distances (d =3 Å), the contrast of the Cu tip is still dominated by the metal states, while there are already clear features that reveal atomic contrast in G with the CuO tip.

Figure 4.15a-c shows experimental data confirming this change of visualization of graphene or the copper underneath by approaching a non-reactive tip towards the sample. For currents around 0.5 nA, STM images basically visualize the graphene honeycomb (see Figure 4.15a) while for lower current values (and therefore, larger tip-sample distances) STM images on the same region show the predominance of the standing waves of the Cu(111) surface state (see Figure 4.15b). Comparison with theoretical constant current STM line profiles including multiple scattering effects [74] for four tip-surface distances, using the CuO tip, are presented in Figure 4.15d . At d=4 Å (black line) only the modulation induced by the defects on the Cu surface is observed. Upon tip approach, atomic corrugation in the G is obtained, while the electronic modulation of the Cu surface gets reduced, becoming negligible at d=2 Å.

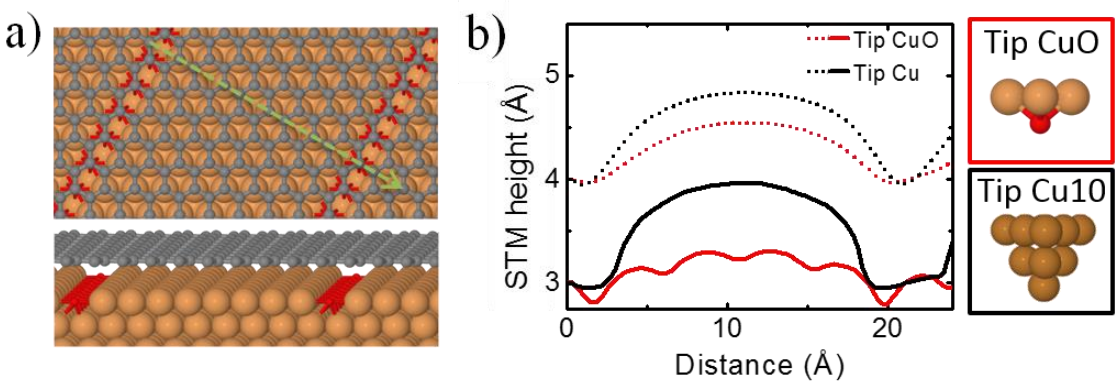

Figure 4.14 Comparison between the constant current profiles calculated with the purely metallic Cu10 tip and the contaminated CuO tip. a) Stick-and-ball model of the atomic configuration of a graphene layer on a Cu surface tailored with an oxygen row substituting Cu surface atoms. b) Simulated constant current STM profiles along the green line marked on a) for different tip sample separations and at a -0.1 V bias.

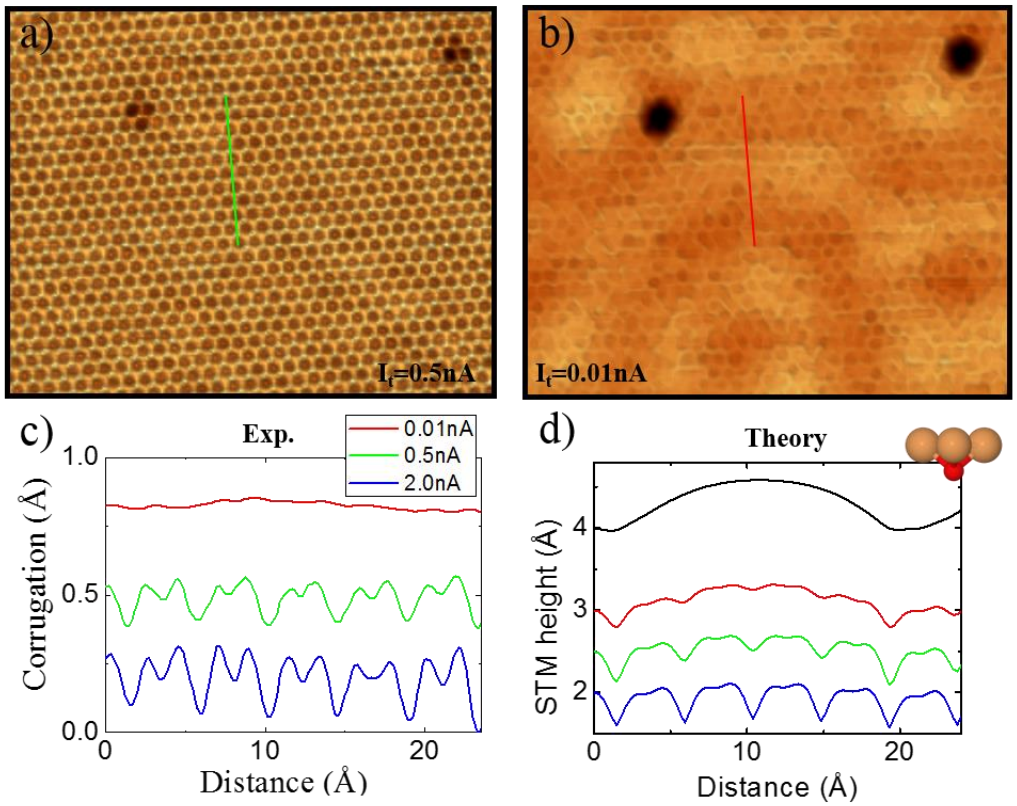

Figure 4.15: Changing from graphene visualization to Cu(111) imaging by changing the tunnel current. a) and b) show experimental constant current STM images at two different current set points (I=0.5 nA and I=0.01 nA, respectively); c) compares the same line profile (outlined by the green and red line in a) and b)) at different constant current set points. d) Simulated constant current STM profiles along the green line marked on Figure 4.14a at different tip sample separations and at a -0.1 V bias Notice that both experimental and simulated STM profiles show the Cu surface state modulation at larger tip-sample distances while the graphene atomic contrast is disclosed for closer tip-graphene separation.

For close enough distances, the Cu tip -as representative of any metal tip- would also show atomic contrast on G, but we can discard it as a suitable candidate to explain the experiments for two reasons: (i) the interaction of the Cu tip with the substrate is very strong, particularly at the rather small surface distances required to get atomic resolution on G ruling, making stable operation very challenging; (ii) In that short distance range, due to multiple scattering effects [77], those metal tips would provide an inverted contrast image with hexagonal (not honeycomb) symmetry, where the maxima of the current are on the hollow sites not on the atoms.

In essence, the excellent agreement between experiments and simulations validates our explanation for the transparency of the STM on graphene on metal in terms of the extension of the metal surface state versus the spatial localization of the graphene charge density in the normal direction, and allow us to identify a metal tip contaminated with electronegative species as representative of the experimental tips that are able to image both the Cu substrate and the G honeycomb lattice.

4.5 ARPES measurements on Gr/Cu(111)

Our calculations have shown that to access to the electronic properties of graphene by STM we need a weakly reactive tip enabling operation at small tip-sample distances. Therefore, it is important to rule out any spurious influence of the STM tip in our data. To this end, we contacted the group of Prof. Enrique Ortega to perform additional ARPES experiments.

The graphene on Cu(111) sample used for the ARPES measurements was grown using the standard ethylene cracking method reaching temperatures close to the Cu melting point [25, 52]. ARPES is highly complementary to STM since it measures in the reciprocal space and therefore has direct access to the electronic structure of the system (no 2D-FT required). The important differences with STM are that only the DOS of the sample are probed (no tip involved) and ARPES averages over the whole illuminated region (non-local technique). Therefore, an important drawback is that ARPES demands an excellent surface preparation. However, as we have seen in our measurements, the ethylene cracking method allows to achieve homogeneous, single domains extending over large sample areas. The data in Figure 4.16 indicate the presence of a dominant graphene domain over the area sampled by the light spot size of 0.25 mm². The angle resolved photoemission (ARPES) setup consisted of a display type hemispherical analyser (Phoibos150) with an energy/angle resolution of 40 meV/0.1° and a monochromatized source Helium I ($h\upsilon$ = 21.2 eV) source. The channel plate slit lies along the rotation axis of the manipulator. All the presented data were recorded approximately at 180 K.

In our ARPES experiments, Fermi surfaces and band dispersions close to the centre (Γ) and edge (*K*) of the Brillouin Zones are readily probed, as shown in Figure 4.16. The Fermi surface portion displayed in Figure 4.16c shows both, the graphene π-bands surrounding the *K* point, and the modified Cu(111) Shockley state around the Γ point. A zoom-out view at both symmetry points are shown in Figures 4.16 b and e, whereas the respective band dispersions are shown in Figures 4.16 a and d. The excellent agreement with the STM and DFT+vdW results shown in tables 1 and 2 excludes any tip-influence in our measurements confirming graphene tunable transparency as an ideal tool to probe graphene-substrate interactions.

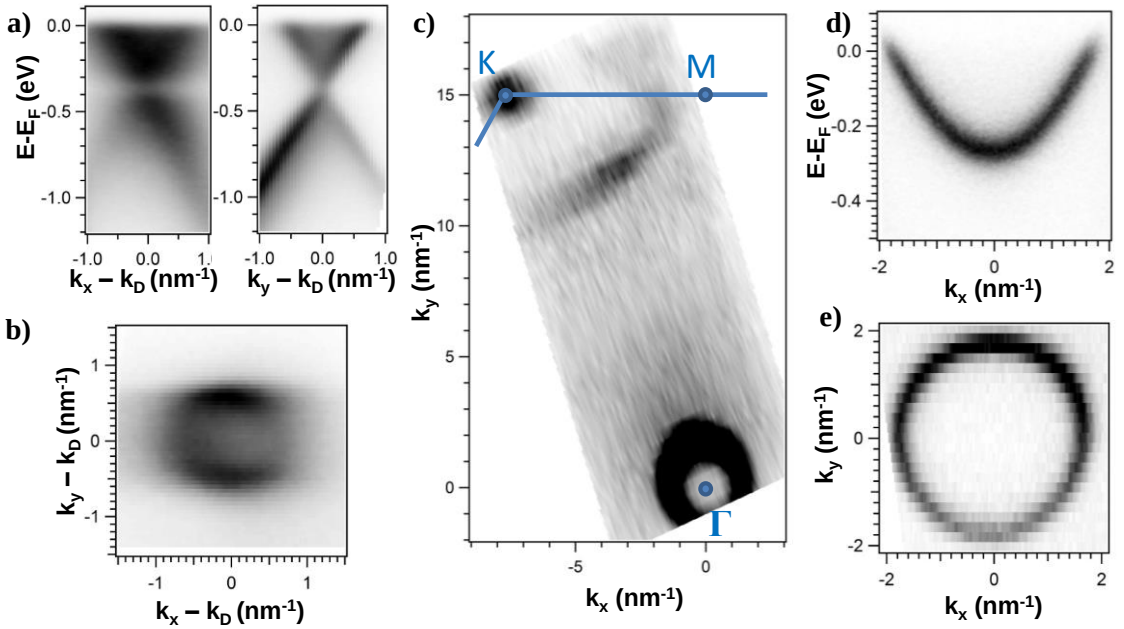

Figure 4.16: Experimental electronic structure of graphene on Cu(111) as obtained from ARPES. The raw data is represented in grayscale, being darker more intense. It clearly shows the graphene π band around the Γ point (panels (a) and (b)) as well as the modified Cu(111) Shockley state in the proximity of the Γ point (panels (d) and (e)). Panel c) presents a section of the Fermi Surface where the blue line shows the edge of the Brillouin zone and relevant high-symmetry points. The feature away from the high-symmetry points (close to 11 nm^{-1}) corresponds to the Fermi energy crossing of the Cu sp-bulk band. The graphene π band is scaled in reference to the Dirac point position (found at E_B = 0.38 eV and $k_{||}$ = 16.8 nm^{-1}). The Shockley state is symmetric around Γ with a rigid shift of ~140 meV when compared to pristine Cu(111) (Panels (d) and (e)).

4.6 Summary of the electronic properties of Gr/Cu(111) by STM, DFT+vdW and ARPES.

In the two tables that we present in this section, we gathered and organized in a comprehensive way all the results obtained by the three techniques used along this chapter, in order to fully characterized our Gr/Cu(111) system. In Table 1 we summarized all the results regarding the Cu(111) surface stat both for the clean system and after the growth or a graphene layer on top of it. Table 2, on the other hand, condenses all the key parameter to describe the linear dispersion of a graphene layer grown on Cu(111).

	STM (5K)		ARPES (180K)		DFT+vdW		
	Cu(111)	Cu(111) below graphene	Cu(111)	Cu(111) below graphene	Cu(111)	Cu(111) below graphene (3.4 Å)	Cu(111) below graphene (2.9 Å)
E_0 (meV)	- 430 ± 10	-300± 10	- 400 ± 10	- 263 ± 10	-390	-260	0
m^*/m_e	0.39± 0.01	0.43± 0.01	0.41± 0.01	0.43 ± 0.01	0.38	0.41	0.48
k_F (nm^{-1})	2.10± 0.05	1.80± 0.04	2.05± 0.05	1.75 ± 0.05	1.97	1.70	0

Table 1: Parameters obtained for STM, ARPES and DFT+vdW for the Cu(111) surface state on the pristine surface and graphene covered. Notice that the temperatures for STM and ARPES are different, which translates in a rigid shift of the parabola towards E_F as the temperature is raised [78, 79].

	Graphene on Cu(111)			
	STM (5K)	ARPES (180 K)	DFT+vdW (3.4 Å)	DFT+vdW (2.9 Å)
E_D (meV)	-400± 20*	- 380 ± 10	-350	-650
v_F (m/s)	$(1.1\pm 0.1)\cdot 10^6$	$1.0\cdot 10^6$	$0.89\cdot 10^{6}$ **	$0.76\cdot 10^{6}$ **
k_F (nm^{-1})	0.55±0.03	0.60 ± 0.06	0.6	1.3

Table 2: Parameters obtained for STM, ARPES and DFT+vdW for the graphene π bands of the graphene layer on the vicinity of the *K* and *K'* points. (*E_D value from STM data is estimated from the linear fit of STS data near E_F, see green dotted line in Figure 4.7c. ** Graphene strain and e-e interactions could slightly affect calculated v_F values).

4.7 Interaction of point defects with Gr/Cu(111)

One of the mayor strengths of our method stems in its ability to locally probe the graphene/metal interactions. In this way, graphene tunable transparency can be further exploited as an extraordinary tool capable of tracking new local interactions introduced in the system. As a case example we will consider the adsorption of dilute atomic hydrogen on G/Cu(111) and the introduction of C vacancies in the graphene layer.

4.7.1 H atoms on Gr/Cu(111)

In chapter 2, we showed that the adsorption of atomic H on graphene layers induce a local magnetic moment. It has also been reported that atomic H on isolated graphene layers induces changes in the electronic properties, such as the opening of band gaps [11, 46]. For the weakly interacting G/Ir(111) system, it was reported that it gave rise to the opening of a band gap in graphene due to a strong increase of the graphene-metal interaction mediated by the local re-hybridization of C atoms from sp^2 to sp^3 bonding, with H binding on top of a C atom as in the isolated graphene layer and the surrounding C atoms binding to an Ir atom below [11]. Such sp^3 hybridization is possible only in hcp or fcc regions, where every other C atom is placed above a surface Ir atom. In the case of G/Cu(111) we have carried out such study by depositing atomic hydrogen at RT. The deposition was made following the same procedure as for H on SiC(000-1), i.e., by thermal dissociation of H_2 on a home-made hot hydrogen atom beam source. A molecular H_2 beam is passed through a hot W filament held at 1900K. The pristine graphite surface is placed 10 cm away from the filament and held at RT during atomic H deposition. H_2 pressure is regulated by a leak valve and fixed to $3{\cdot}10^{-7}$ Torr as measured in the preparation chamber for the present experiments. A low final coverage of 0.2 H atoms/nm² (or equivalently, 0.005ML; 1ML= 38 atoms/nm2 = $3.8{\cdot}10^{15}$ atoms/cm², referred to carbon atoms in graphene layers) is achieved ensuring an average first neighbours H-H distance ~1nm. Control experiments where the sample was exposed to the same $3{\cdot}10^{-7}$ Torr H_2 pressure and deposition times keeping the W filament cold and experiments with the W filament at the same 1900K temperature without molecular H_2, did not show any trace of H (no triangular bright features could be observed) or any other atomic adsorbate on the surface.

Figure 4.17 shows a large STM image, revealing both the graphene layer and the underlying Cu(111) surface after the atomic hydrogen exposure. Hydrogen atoms on the graphene layer appear as bright triangular-shaped features pointing to opposite directions depending on its sublattice adsorption site. Using the graphene transparency to tunneling electrons, we can check the local coupling of the H impurities with the metallic interface following the Cu(111) surface quasiparticles scattering. We observe in Figure 4.17 the presence of

standing wave patterns generated by the existence of intercalated impurities on the Cu(111) surface. Such impurities, appearing as dark round features, always occupy minima of the LDOS modulation and act as scattering centres for the Cu(111) surface state. In contrast the H triangular bright features can be independently found both over bright and dark regions of the Cu(111) standing wave patterns, suggesting a lack of interaction with the Cu(111) surface quasiparticles. But this is not the case when considering the interaction with the graphene overlayer: The high resolution STM image of Figures 4.18a-d shows that H atoms act as scattering centres for graphene quasiparticles. Thanks to the STM sensitivity to both the overlayer and Cu surface state, R3 patterns originated from the intervalley scattering of graphene quasiparticles are observed, independently of the standing waves underneath.

The absence of a strong H interaction can be unambiguously demonstrated experimentally based on the atomic manipulation capabilities of the STM [80, 81]. As we showed in chapter 2, by choosing the appropriate tunneling parameters atomic H can be removed from graphene with atomic precision. The role played by the STM tip is to selectively modify the binding energy landscape of H atoms to produce the required H manipulation. To selectively remove H atoms from the graphene sample we approached the STM tip towards the sample. This can be done by continuously increasing, under feedback control, the set-point tunneling current on top of the selected H atom until it is desorbed, or by switching the feedback off and slightly decreasing the tip-sample distance on top of it. It is also possible to completely remove all H atoms from a graphene region by imaging it at high currents. The precise tunneling values for the manipulation depend on each specific tip apex, but for the same tip apex those values are very reproducible. As a rough guide, for removing H atoms it is usually enough to approach the STM tip by 2-3 Å (opening the feedback loop at a nominal junction impedance of 20 MΩ; Vbias =0.01 V, It=0.5 nA). Figures 4.18a-d show how we can subsequently remove 3 H atoms in a controlled way. After each single H atom removal, the same sample region is imaged back to check for any difference arising in the scattering patterns originated by both graphene -R3 patterns- and Cu(111) -standing waves patterns- quasiparticles.

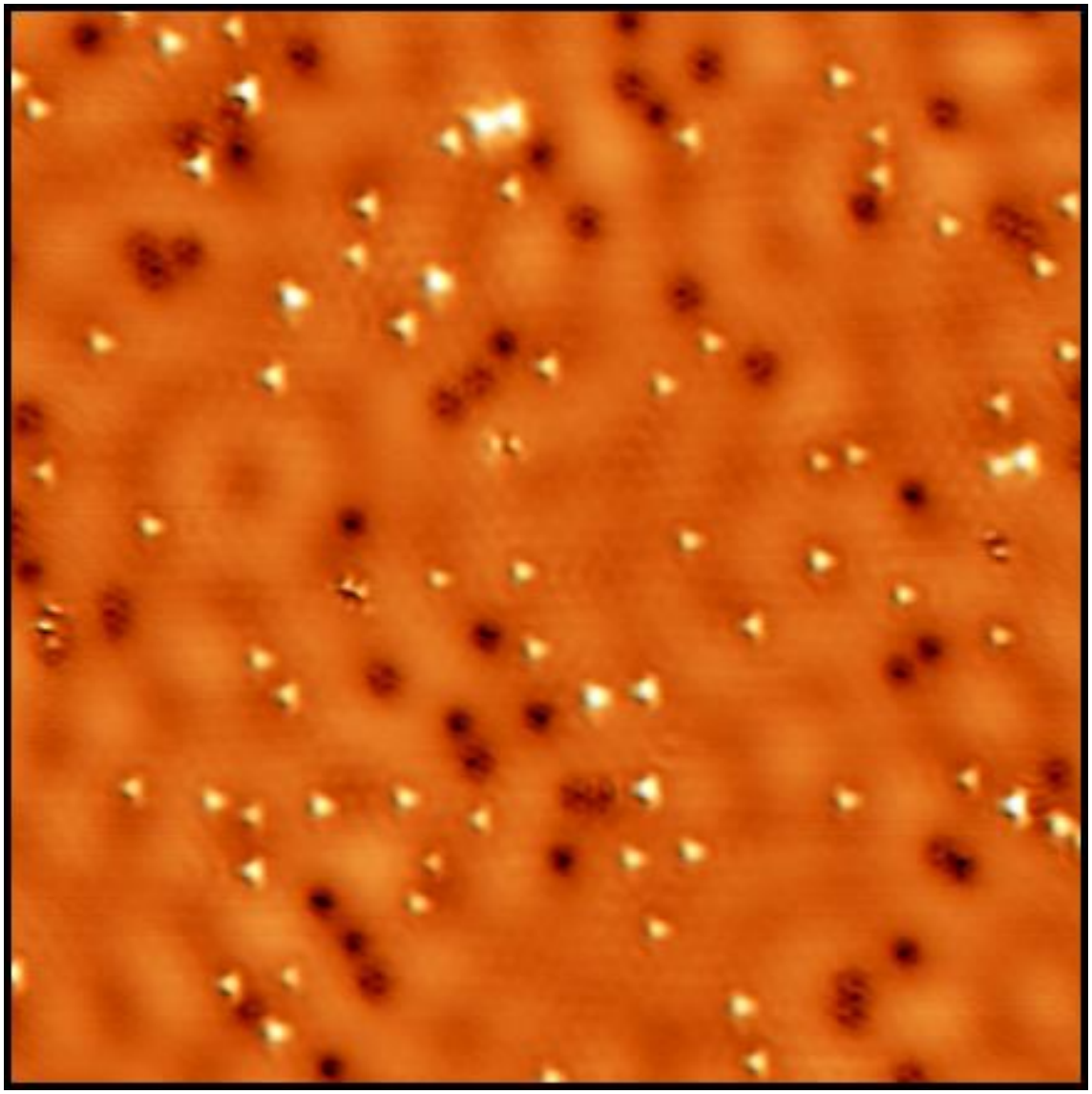

Figure 4.17: Hydrogen atoms adsorbed on Gr/Cu(111). 19×19 nm² STM image showing the general morphology of the G/Cu(111) surface after H deposition. Triangular bright features correspond to single H atoms on the graphene layer. Small dark rounded features are Cu(111) surface impurities. Standing waves from the Cu(111) surface are also observed (Vbias =0.010 V, It=0.2 nA).

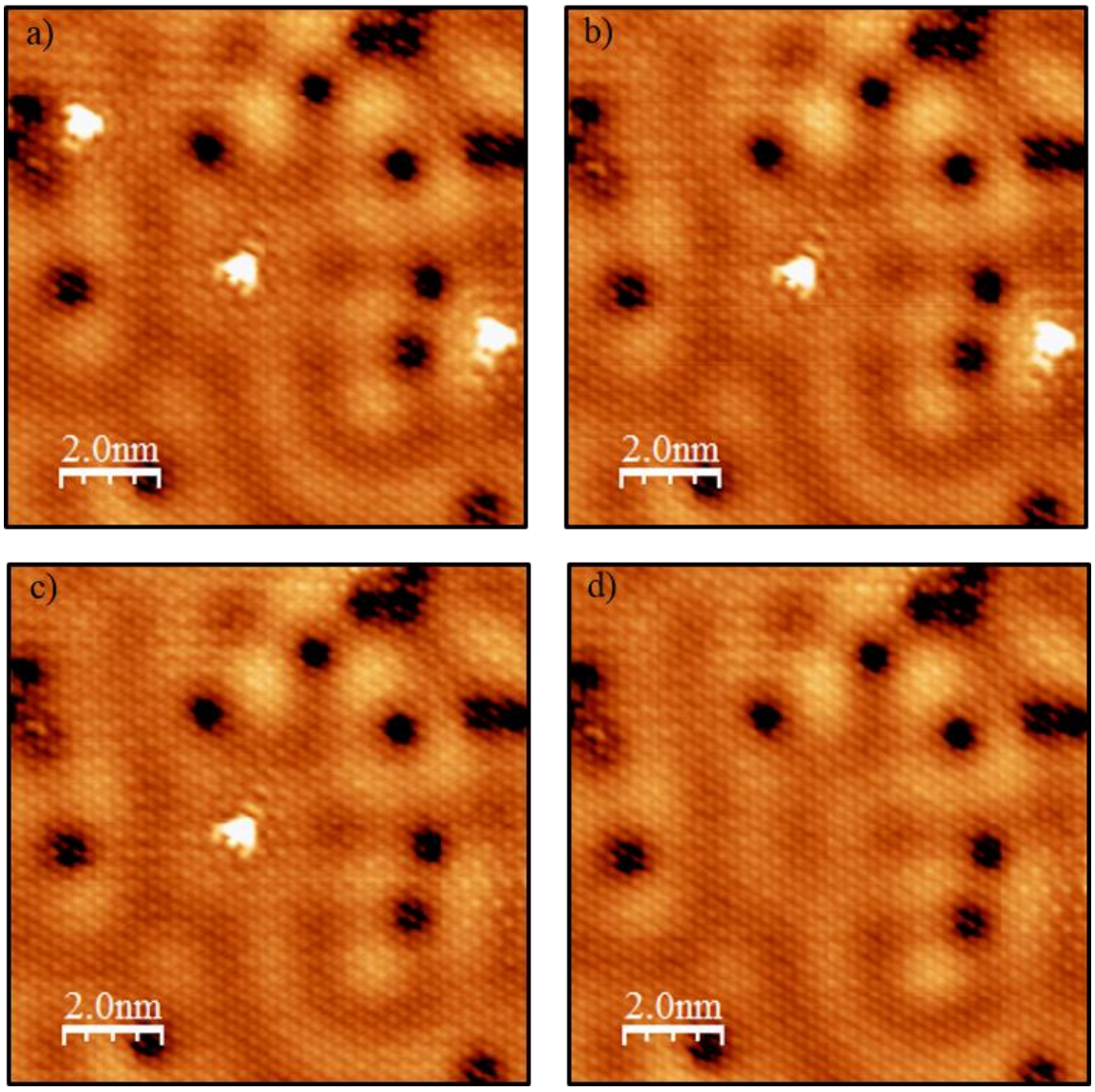

Figure 4.18: Use of the tunable transparency as a tool to follow the interaction between atomic hydrogen adsorbed onto G/Cu(111). a) High resolution STM image showing a 10 × 10 nm² sample region with 3 H atoms. b-d) STM images of the same sample region as in (a) showing that the removal of H atoms does not affect the Cu(111) standing waves patters. (Vbias =-0.01V, It=0.5nA).

The sequence of STM images obtained after each H atom removal clearly show that while graphene R3 patterns surrounding H atoms vanish, the Cu(111) standing waves patterns are not affected at all by any H atom removal. This can be further observe in Figure 4.19, where profiles before and after the removal are presented. This confirms that H atoms adsorbed on the graphene layer do not induce any local interaction between the C atoms of the graphene layer and the underlying Cu(111) substrate.

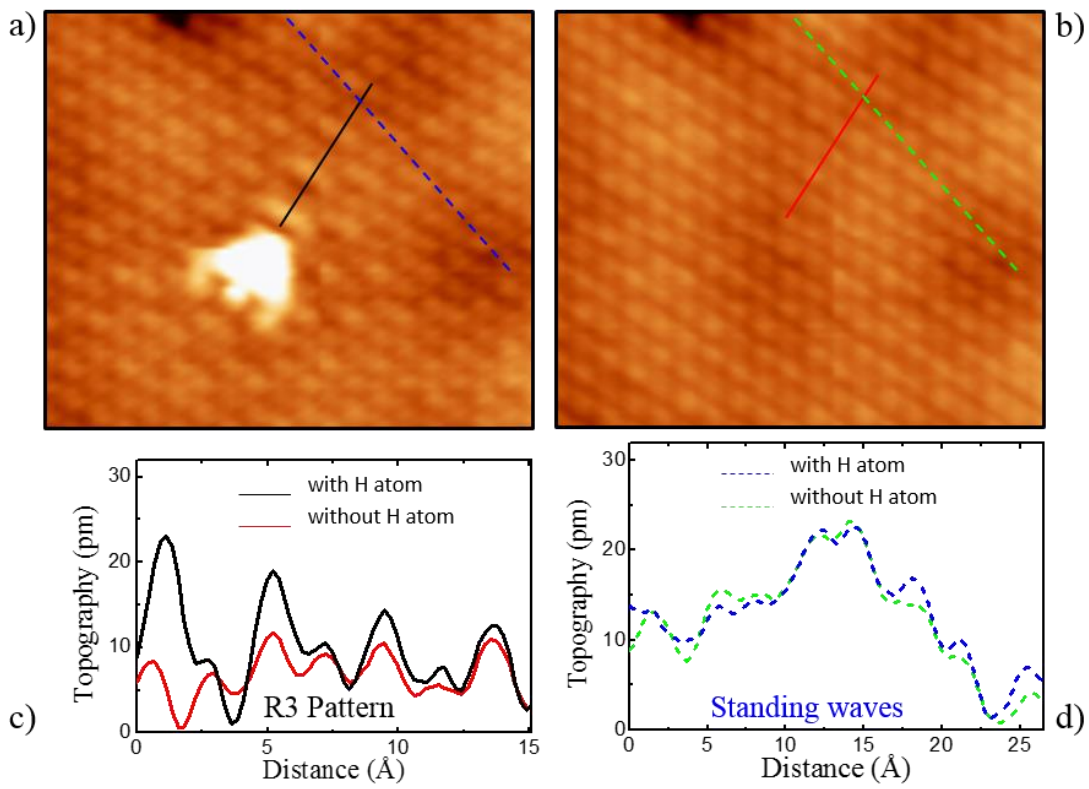

Figure 4.19: Impact of a single hydrogen atom on Gr/Cu(111). a, b) Zoom-in of the central region of Figure 4.18c-d respectively to show the effect of removing a H atom on graphene R3 patterns -see line profiles in c- and standing waves -see line profiles in d).

Regarding the LDOS of single hydrogen atoms adsorbed on Gr/Cu(111), our STS experiments found the apparition of a broad peak around ~ -0.36 eV, which correspond to the energy of the Dirac point of our graphene layer (see Figure 4.20a). This is what we would expect from the adsorption of a hydrogen atom on a n-doped graphene layer. As in the case of our doped SiC(000-1) samples in chapter 2, theoretical calculations predict no magnetic moment arising from H atoms [23]. Our DFT+D2 calculations support the negligible modification on the G-Cu interaction upon H adsorption. The simulation of the adsorption of a H atom in a $\sqrt{57}$ x $\sqrt{57}$ moiré (respect to the G) shows that the atomic configuration of the G (see Figure 4.20b) is very similar to the one obtained on free standing layers [23, 45, 47, 82], moreover, no significant variations neither on the average G-Cu distance nor the position of Cu atoms are found.

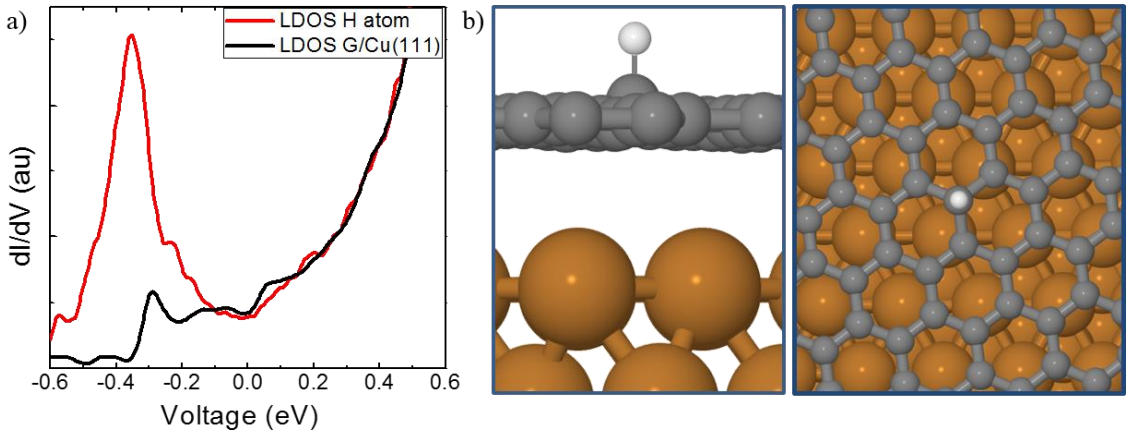

Figure 4.20: DFT calculations on hydrogen adsorption. a) 5 K STS measurements of the LDOS on a H atom (red curve) and on pristine G/Cu(111) (black curve). b) Side and top view of the DFT calculation for the adsorption of a H atom in a $\sqrt{57}$ x $\sqrt{57}$ moiré.

In order to test the possible influence of the adsorption site in the LDOS of hydrogen atoms, we measured dI/dV curves on different single hydrogen atoms in the same terrace. As it can be seen in Figure 4.21, the spectra show a broad peak independently of the position of the hydrogen atom. The only changes are variations in their height and small changes in the energy position of the peaks (~-0.36/-0.32).

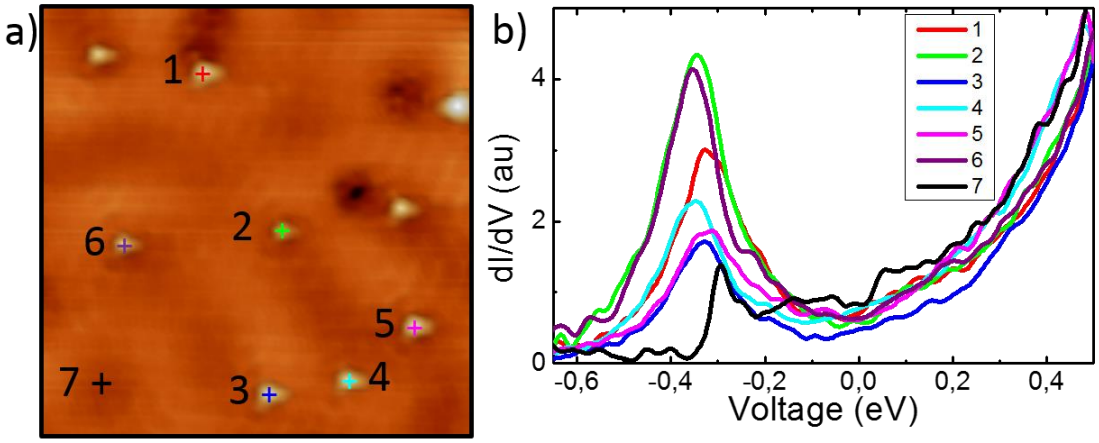

Figure 4.21: STS on hydrogen atoms. a) Graphene terrace where 6 hydrogen atoms have been probed using STS. b) dI/dV spectra obtained on top of hydrogen atoms enumerated on a).

Our results imply that the G/Cu(111) system essentially behaves as an electron-doped graphene layer for atomic hydrogen adsorbates. On doped enough graphene layers, the energy shift of E_D prevents the spin-polarization of the state, which is predicted to show up in the LDOS as a single peak at the new normal E_D energy position. Above H atoms the emergence of a single broad peak in the LDOS located around E_D (-0.36/-0.40 eV) is observed, excluding thus the formation of a H induced magnetic moment, as expected for H adsorption on an electron-doped graphene layer. Such single broad electronic resonance was

observed for all single H atoms independently of their position inside the moiré, which points to a small influence of the moiré superstructure on their properties. The only influence detected was the variation of the resonance height for H atoms on different moiré positions. Interestingly, our results show that the measurement of the LDOS peak energy position after the adsorption of H atoms could be used to determine E_D in some graphene systems-. Our STS data show that for H atoms the only role played by the Cu substrate is to electron-dope the graphene layer, in agreement with the lack of direct coupling observed between the H adsorbates and the metal interface.

4.5.2 C vacancies on Gr/Cu(111)

As we have commented along this manuscript, another interesting route to modify graphene properties is the introduction of single C vacancies in graphene layers [14, 43, 47]. When generated in HOPG surfaces [14] they essentially retain the main properties expected for C vacancies in free-standing graphene [47]. However, it has been shown that the situation is very different for the weakly interacting G/Pt(111) system, where the interaction with the graphene layer strongly increases after the introduction of single carbon vacancies [43]. According to DFT calculations, a strong local interaction between the graphene and substrate develops where the vacancies are located [43]. Thus, C vacancies appears as an optimal system to test the potential of the graphene tunable transparency.

We have deliberately introduced C vacancies into the graphene layer by irradiating the surface with 140eV Ar^+ ions, which are known to mainly generate singe C vacancies in graphite surfaces and in G/Pt(111) [14, 43]. Our STM measurements after the irradiation procedure reveal the appearance of almost identical bright features on the previously pristine graphene layer, in a number almost equal to the number of Ar^+ ions impacting the surface, see Figure 4.22.

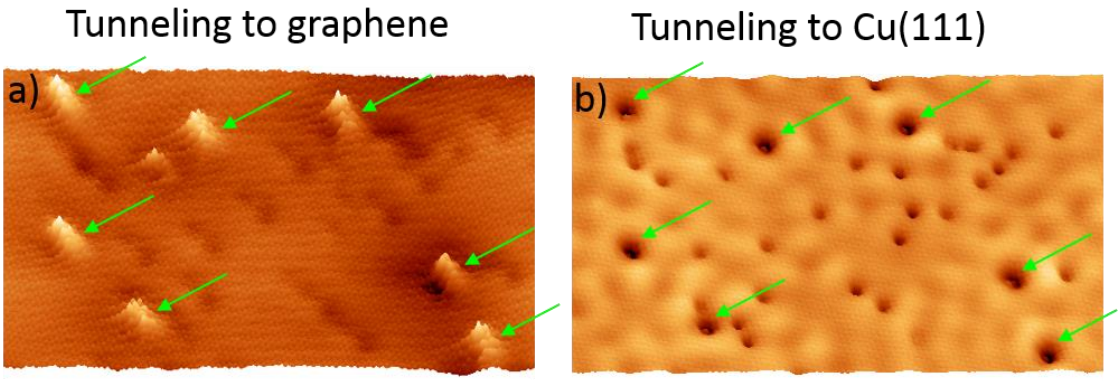

Figure 4.22: Vacancies on Gr/Cu(111). a) 17x10nm^2 STM image showing a G/Cu(111) sample region with several C –bright protrusions- deliberately introduced on the graphene layer by Ar^+ irradiation (V=0.01V, I=0.5 nA). b) Same region as a) measured a lower current (I=0.1nA) to probe the underlying Cu(111) surface.

Thanks to the graphene tunable transparency we can probe the impact of the C vacancies both in the graphene layers and in the Cu(111) surface underneath. This is demonstrated in Figures 4.23 a,b which show exactly the same G/Cu(111) region, with two C vacancies, for high (I=0.5nA) and low (I=0.1 nA) tunneling currents to probe the graphene layer and Cu(111) surface respectively. When probing the graphene layer, C vacancies appear in STM images as bright protrusions surrounded by R3 patterns, see Figure 4.23a. When probing the underlying Cu(111) substrate as in Figure 4.23b, in the position of C vacancies small round features surrounded by Cu(111) standing waves appear, which implies that C vacancies located in the graphene layer act as scattering centres for the Cu(111) surface state quasiparticles. This indicates that, contrary to the case of H atoms, C vacancies do strongly interact with the metal substrate underneath.

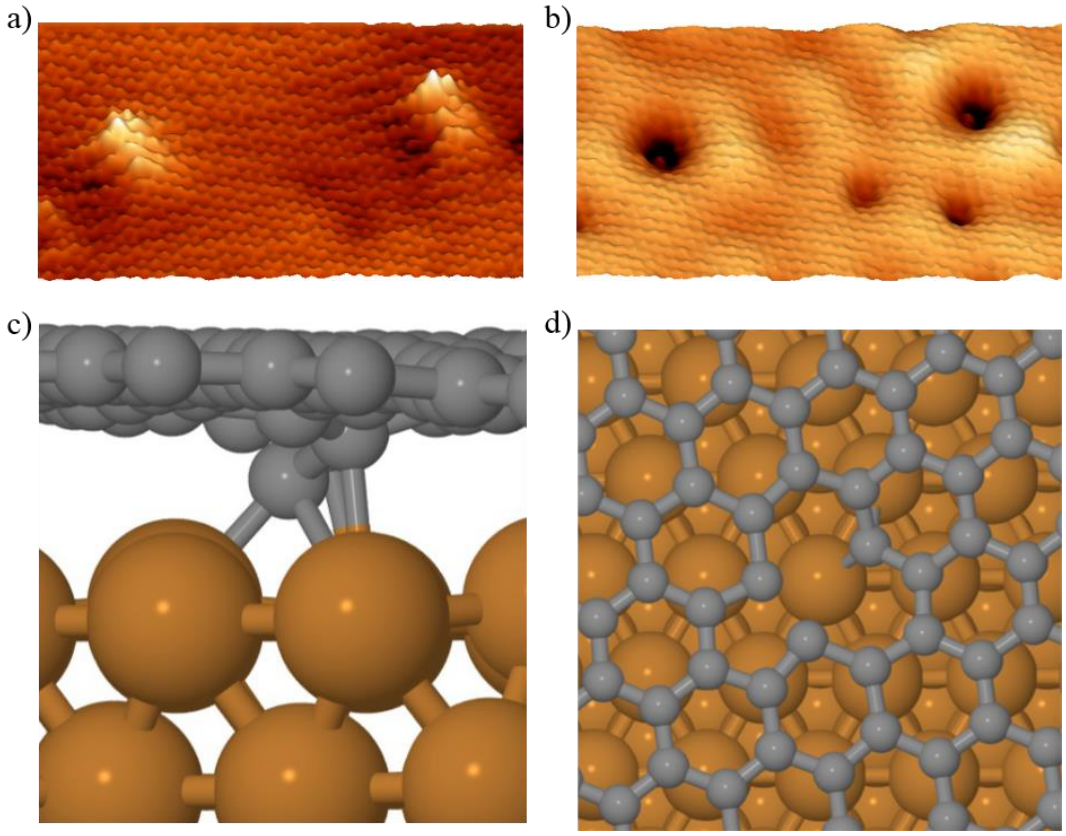

Figure 4.23: Use of the tunable transparency to follow the interaction between graphene C vacancies and the Cu(111) substrate underneath. a) STM image showing a G/Cu(111) sample region with two single C vacancies deliberately introduced on the graphene layer by Ar irradiation (Vbias =0.010 V; I=0.5 nA). b) Same sample region measured at a lower current (I= 0.1 nA) to probe the underlying Cu(111) surface. C vacancies in graphene act as scattering centers for the Cu(111) surface quasiparticles generating standing waves below them. c, d) Top (c) and side (d) view of the ball-and-stick model of the atomic structure calculated with DFT of a G monovacancy in the $\sqrt{57}$ x $\sqrt{57}$ moiré pattern. The characteristic 2+1 reconstruction of the C vacancy in graphene is obtained, with two C atoms forming a soft bond and the remaining C atom strongly interacting with the Cu surface.

We have also carried out a DFT simulation of a monovacancy in the G on Cu on the $\sqrt{57}$ x $\sqrt{57}$ moiré pattern (Figures 4.22c-d). The vacancy reconstructs with the same Jahn-Teller distortion that has been identified in free-standing graphene [47], with two of the three C atoms forming a soft bond. The reactive dangling bond of the third C atom strongly interacts with the underneath metal. The bonds between the carbon atom and the Cu surface atoms induce a significant out-of-plane distortion of the G layer in the neighborhood of the vacancy (more than 1 Å). The final structure is very similar to the one found for single-atom vacancies in G on Pt [43]. Adsorbates are well recognized as scattering centers for the Cu surface state. As confirmed by our STM measurements, due to the strong interaction with the substrate, this carbon atom acts effectively as an adsorbate for the Cu surface inducing the observed standing wave pattern.

4.8 Conclusions

Over the development of this chapter, we have presented our results concerning the study and characterization of the Gr/Cu(111) system. In this system, previous experiments had shown that under certain conditions, the Cu(111) surface state was visible with STM. By combining our STM/STS measurements with DFT calculations and ARPES experiments we have been able to get a fully understanding of our graphene/metal system. The principal conclusions extracted from our results are:

- We learnt how to visualized in a controlled way either the graphene layer, the Cu(111) surface state underneath or both at the same time. This was done by learning how to modify the tunnelling parameters or by changing the tip apex.

- Thanks to that tunable transparency, we have been able to characterize the electronic properties of both the graphene layer and the substrate underneath. Our graphene layer is n-doped with a Dirac point energy of ~ -400 meV and presents a linear dispersion around the Fermi energy with a Fermi velocity ~ $1.1 \cdot 10^6$. On the other hand, the Cu(111) surface states, presents an upward shift of its energy onset of ~ 130 meV and a change in the effective mass from 0.39 m_e to 0.43 m_e when compared with the clean Cu(111) surface state.

- DFT+vdW calculations found a graphene/metal distance of ~3.4Å and how the main effect of this distance is the charge transfer that takes place between the graphene layer and the Cu substrate.

- Further calculations demonstrated that the transparency we observe in our system is due to the difference in decay length of the surface state of the Cu(111) underneath compared with the more localized π states of graphene. On top of that, they also showed that only tips contaminated with electronegative species are able to visualize the graphene layer.

- Additional ARPES experiments were carried out, finding similar results as the ones obtained by STM, discarding any influence of our STM tip in the measurements.

- We used graphene's transparency to study the impact of single hydrogen atoms and carbon vacancies in Gr/Cu(111). While H atoms just interact with the graphene layer, carbon vacancies act as scattering centres for the Cu(111) surface state showing interaction with both the graphene layer and the substrate.

References

1. Ohta, T., et al., *Controlling the electronic structure of bilayer graphene.* Science, 2006. **313**(5789): p. 951-954.
2. Ohta, T., et al., *Interlayer interaction and electronic screening in multilayer graphene investigated with angle-resolved photoemission spectroscopy.* Physical Review Letters, 2007. **98**(20).
3. Zhou, S.Y., et al., *Substrate-induced bandgap opening in epitaxial graphene.* Nature Materials, 2007. **6**(10): p. 770-775.
4. Craciun, M.F., et al., *Trilayer graphene is a semimetal with a gate-tunable band overlap.* Nature Nanotechnology, 2009. **4**(6): p. 383-388.
5. Giovannetti, G., et al., *Doping graphene with metal contacts.* Physical Review Letters, 2008. **101**(2).
6. Decker, R., et al., *Atomic-scale magnetism of cobalt-intercalated graphene.* Physical Review B, 2013. **87**(4).
7. Wintterlin, J. and M.L. Bocquet, *Graphene on metal surfaces.* Surface Science, 2009. **603**(10-12): p. 1841-1852.
8. Pletikosic, I., et al., *Dirac Cones and Minigaps for Graphene on Ir(111).* Physical Review Letters, 2009. **102**(5).
9. Hwang, C., et al., *Fermi velocity engineering in graphene by substrate modification.* Scientific Reports, 2012. **2**.
10. Heersche, H.B., et al., *Bipolar supercurrent in graphene.* Nature, 2007. **446**(7131): p. 56-59.
11. Balog, R., et al., *Bandgap opening in graphene induced by patterned hydrogen adsorption.* Nature Materials, 2010. **9**(4): p. 315-319.
12. Zhao, L., et al., *Visualizing Individual Nitrogen Dopants in Monolayer Graphene.* Science, 2011. **333**(6045): p. 999-1003.
13. Nair, R.R., et al., *Dual origin of defect magnetism in graphene and its reversible switching by molecular doping.* Nature Communications, 2013. **4**.
14. Ugeda, M.M., et al., *Missing Atom as a Source of Carbon Magnetism.* Physical Review Letters, 2010. **104**(9).
15. Riedl, C., et al., *Quasi-Free-Standing Epitaxial Graphene on SiC Obtained by Hydrogen Intercalation.* Physical Review Letters, 2009. **103**(24).
16. Gierz, I., et al., *Electronic decoupling of an epitaxial graphene monolayer by gold intercalation.* Physical Review B, 2010. **81**(23).
17. Varykhalov, A., et al., *Electronic and Magnetic Properties of Quasifreestanding Graphene on Ni.* Physical Review Letters, 2008. **101**(15).
18. Calleja, F., et al., *Spatial variation of a giant spin-orbit effect induces electron confinement in graphene on Pb islands.* Nature Physics, 2015. **11**(1): p. 43-47.
19. Eelbo, T., et al., *Adatoms and Clusters of 3d Transition Metals on Graphene: Electronic and Magnetic Configurations.* Physical Review Letters, 2013. **110**(13): p. 5.
20. Eelbo, T., et al., *Influence of the degree of decoupling of graphene on the properties of transition metal adatoms.* Physical Review B, 2013. **87**(20): p. 4.
21. Donati, F., et al., *Tailoring the Magnetism of Co Atoms on Graphene through Substrate Hybridization.* Physical Review Letters, 2014. **113**(17): p. 6.
22. Donati, F., et al., *Magnetic Moment and Anisotropy of Individual Co Atoms on Graphene.* Physical Review Letters, 2013. **111**(23): p. 5.
23. González-Herrero, H., et al., *Atomic-scale control of graphene magnetism by using hydrogen atoms.* Science, 2016. **352**(6284): p. 437-441.
24. Grueneis, A. and D.V. Vyalikh, *Tunable hybridization between electronic states of graphene and a metal surface.* Physical Review B, 2008. **77**(19).

25. Walter, A.L., et al., *Electronic structure of graphene on single-crystal copper substrates.* Physical Review B, 2011. **84**(19).
26. Gomez-Navarro, C., et al., *Atomic Structure of Reduced Graphene Oxide.* Nano Letters, 2010. **10**(4): p. 1144-1148.
27. Hashimoto, A., et al., *Direct evidence for atomic defects in graphene layers.* Nature, 2004. **430**(7002): p. 870-873.
28. Li, G., et al., *Observation of Van Hove singularities in twisted graphene layers.* Nature Physics, 2010. **6**(2): p. 109-113.
29. Meyer, J.C., et al., *The structure of suspended graphene sheets.* Nature, 2007. **446**(7131): p. 60-63.
30. Rutter, G.M., et al., *Scattering and interference in epitaxial graphene.* Science, 2007. **317**(5835): p. 219-222.
31. Zhang, Y., et al., *Origin of spatial charge inhomogeneity in graphene.* Nature Physics, 2009. **5**(10): p. 722-726.
32. Berger, C., et al., *Electronic confinement and coherence in patterned epitaxial graphene.* Science, 2006. **312**(5777): p. 1191-1196.
33. Brar, V.W., et al., *Scanning tunneling spectroscopy of inhomogeneous electronic structure in monolayer and bilayer graphene on SiC.* Applied Physics Letters, 2007. **91**(12).
34. Rutter, G.M., et al., *Imaging the interface of epitaxial graphene with silicon carbide via scanning tunneling microscopy.* Physical Review B, 2007. **76**(23).
35. Jeon, I., et al., *Passivation of Metal Surface States: Microscopic Origin for Uniform Mono layer Graphene by Low Temperature Chemical Vapor Deposition.* Acs Nano, 2011. **5**(3): p. 1915-1920.
36. Martinez-Galera, A.J., I. Brihuega, and J.M. Gomez-Rodriguez, *Ethylene Irradiation: A New Route to Grow Graphene on Low Reactivity Metals.* Nano Letters, 2011. **11**(9): p. 3576-3580.
37. Leicht, P., et al., *In Situ Fabrication Of Quasi-Free-Standing Epitaxial Graphene Nanoflakes On Gold.* Acs Nano, 2014. **8**(4): p. 3735-3742.
38. Altenburg, S.J., et al., *Local Gating of an Ir(111) Surface Resonance by Graphene Islands.* Physical Review Letters, 2012. **108**(20).
39. Jolie, W., F. Craes, and C. Busse, *Graphene on weakly interacting metals: Dirac states versus surface states.* Physical Review B, 2015. **91**(11).
40. Meng, L., et al., *Silicon intercalation at the interface of graphene and Ir(111).* Applied Physics Letters, 2012. **100**(8).
41. Schumacher, S., et al., *The Backside of Graphene: Manipulating Adsorption by Intercalation.* Nano Letters, 2013. **13**(11): p. 5013-5019.
42. Petrovic, M., et al., *The mechanism of caesium intercalation of graphene.* Nature Communications, 2013. **4**.
43. Ugeda, M.M., et al., *Point Defects on Graphene on Metals.* Physical Review Letters, 2011. **107**(11).
44. Rusponi, S., et al., *Highly Anisotropic Dirac Cones in Epitaxial Graphene Modulated by an Island Superlattice.* Physical Review Letters, 2010. **105**(24).
45. Boukhvalov, D.W., M.I. Katsnelson, and A.I. Lichtenstein, *Hydrogen on graphene: Electronic structure, total energy, structural distortions and magnetism from first-principles calculations.* Physical Review B, 2008. **77**(3).
46. Elias, D.C., et al., *Control of Graphene's Properties by Reversible Hydrogenation: Evidence for Graphane.* Science, 2009. **323**(5914): p. 610-613.
47. Yazyev, O.V. and L. Helm, *Defect-induced magnetism in graphene.* Physical Review B, 2007. **75**(12).
48. Bartelt, N.C. and K.F. McCarty, *Graphene growth on metal surfaces.* Mrs Bulletin, 2012. **37**(12): p. 1158-1165.

49. Bae, S., et al., *Roll-to-roll production of 30-inch graphene films for transparent electrodes.* Nature Nanotechnology, 2010. **5**(8): p. 574-578.
50. Li, X., et al., *Large-Area Synthesis of High-Quality and Uniform Graphene Films on Copper Foils.* Science, 2009. **324**(5932): p. 1312-1314.
51. Martínez-Galera, A.J., *Nucleación, crecimiento y nanoestructuración en grafeno epitaxial sobre metales.* Tesis doctoral Departamente de Fïsica de la Materia Condensada Universidad Autónoma de Madrid, Junio 2012.
52. Gao, L., J.R. Guest, and N.P. Guisinger, *Epitaxial Graphene on Cu(111).* Nano Letters, 2010. **10**(9): p. 3512-3516.
53. Nie, S., et al., *Origin of the mosaicity in graphene grown on Cu(111).* Physical Review B, 2011. **84**(15).
54. Crommie, M.F., C.P. Lutz, and D.M. Eigler, *Imaging Standing Waves in a 2-Dimensional Electron-Gas.* Nature, 1993. **363**(6429): p. 524-527.
55. Hasegawa, Y. and P. Avouris, *Direct Observation of Standing-Wave Formation at Surface Steps Using Scanning Tunneling Spectroscopy.* Physical Review Letters, 1993. **71**(7): p. 1071-1074.
56. Hörmandinger, G., *Imaging of the Cu(111) Surface-State in Scanning-Tunneling-Microscopy.* Physical Review B, 1994. **49**(19): p. 13897-13905.
57. Petersen, L., et al., *Direct imaging of the two-dimensional Fermi contour: Fourier-transform STM.* Physical Review B, 1998. **57**(12): p. R6858-R6861.
58. Reinert, F., et al., *Direct measurements of the L-gap surface states on the (111) face of noble metals by photoelectron spectroscopy.* Physical Review B, 2001. **63**(11): p. 115415.
59. Mallet, P., et al., *Role of pseudospin in quasiparticle interferences in epitaxial graphene probed by high-resolution scanning tunneling microscopy.* Physical Review B, 2012. **86**(4): p. 14.
60. Brihuega, I., et al., *Quasiparticle Chirality in Epitaxial Graphene Probed at the Nanometer Scale.* Physical Review Letters, 2008. **101**(20): p. 4.
61. Park, J.Y., et al., *Modification of surface-state dispersion upon Xe adsorption: A scanning tunneling microscope study.* Physical Review B, 2000. **62**(24): p. 16341-16344.
62. Repp, J., G. Meyer, and K.H. Rieder, *Snell's law for surface electrons: Refraction of an electron gas imaged in real space.* Physical Review Letters, 2004. **92**(3).
63. Grimme, S., *Density functional theory with London dispersion corrections.* Wiley Interdisciplinary Reviews-Computational Molecular Science, 2011. **1**(2): p. 211-228.
64. Klimes, J. and A. Michaelides, *Perspective: Advances and challenges in treating van der Waals dispersion forces in density functional theory.* Journal of Chemical Physics, 2012. **137**(12).
65. Batzill, M., *The surface science of graphene: Metal interfaces, CVD synthesis, nanoribbons, chemical modifications, and defects.* Surface Science Reports, 2012. **67**(3-4): p. 83-115.
66. Iannuzzi, M., et al., *Moire beatings in graphene on Ru(0001).* Physical Review B, 2013. **88**(12).
67. Perdew, J.P., K. Burke, and M. Ernzerhof, *Generalized gradient approximation made simple.* Physical Review Letters, 1996. **77**(18): p. 3865-3868.
68. Grimme, S., *Semiempirical GGA-type density functional constructed with a long-range dispersion correction.* Journal of Computational Chemistry, 2006. **27**(15): p. 1787-1799.
69. Grimme, S., et al., *A consistent and accurate ab initio parametrization of density functional dispersion correction (DFT-D) for the 94 elements H-Pu.* Journal of Chemical Physics, 2010. **132**(15).
70. Klimes, J., D.R. Bowler, and A. Michaelides, *Van der Waals density functionals applied to solids.* Physical Review B, 2011. **83**(19).

71. Kresse, G. and J. Furthmuller, *Efficient iterative schemes for ab initio total-energy calculations using a plane-wave basis set.* Physical Review B, 1996. **54**(16): p. 11169-11186.
72. Kresse, G. and D. Joubert, *From ultrasoft pseudopotentials to the projector augmented-wave method.* Physical Review B, 1999. **59**(3): p. 1758-1775.
73. Khomyakov, P.A., et al., *First-principles study of the interaction and charge transfer between graphene and metals.* Physical Review B, 2009. **79**(19).
74. Blanco, J.M., F. Flores, and R. Pérez, *STM-theory: Image potential, chemistry and surface relaxation.* Progress in Surface Science, 2006. **81**(10–12): p. 403-443.
75. Moenig, H., et al., *Understanding Scanning Tunneling Microscopy Contrast Mechanisms on Metal Oxides: A Case Study.* Acs Nano, 2013. **7**(11): p. 10233-10244.
76. Hollen, S.M., et al., *Modification of electronic surface states by graphene islands on Cu(111).* Physical Review B, 2015. **91**(19).
77. Ondracek, M., et al., *Forces and Currents in Carbon Nanostructures: Are We Imaging Atoms?* Physical Review Letters, 2011. **106**(17).
78. Paniago, R., et al., *TEMPERATURE-DEPENDENCE OF SHOCKLEY-TYPE SURFACE-ENERGY BANDS ON CU(111), AG(111) AND AU(111).* Surface Science, 1995. **336**(1-2): p. 113-122.
79. Reinert, F., et al., *Direct measurements of the L-gap surface states on the (111) face of noble metals by photoelectron spectroscopy.* Physical Review B, 2001. **63**(11).
80. Eigler, D.M. and E.K. Schweizer, *POSITIONING SINGLE ATOMS WITH A SCANNING TUNNELING MICROSCOPE.* Nature, 1990. **344**(6266): p. 524-526.
81. Shen, T.C., et al., *ATOMIC-SCALE DESORPTION THROUGH ELECTRONIC AND VIBRATIONAL-EXCITATION MECHANISMS.* Science, 1995. **268**(5217): p. 1590-1592.
82. Yndurain, F., *Effect of hole doping on the magnetism of point defects in graphene: A theoretical study.* Physical Review B, 2014. **90**(24).

Conclusiones generales

A lo largo de este manuscrito, he presentado los resultados más importantes obtenidos durante mi tesis. Uno de los principales objetivos de mi trabajo ha sido el estudio del impacto de átomos individuales de hidrógeno en las propiedades del grafeno. Estudios teóricos habían predicho que estos defectos puntuales debían inducir un momento magnético neto en grafeno. Pese a que ciertas técnicas microscópicas habían medido señales magnéticas en muestras de grafeno hidrogenadas, hasta la fecha no había ninguna prueba directa de la repercusión de un átomo de hidrógeno individual adsorbido en grafeno. Gracias a nuestras medidas con STM combinando ultra alto vacío y bajas temperaturas (~5K), esta última prueba ha sido conseguida. En acuerdo con las predicciones teóricas, nuestros espectros dI/dV demuestran la existencia de un estado spliteado en spin con una distancia en energía entre picos de ~20meV. El origen de dicho splitting se debe a la interacción Coulombiana que tiene lugar en dicho estado. Valores tan bajos de esta interacción implican un estado altamente deslocalizado. Nuestras medidas de la extensión espacial del estado mediante STS confirman la deslocalización y muestran una fuerte modulación de la intensidad de los picos a la escala atómica así como una localización dependiente de la subred: átomos de carbono en la misma subred en la que el átomo de hidrógeno ha sido adsorbido no presentan rastro de los dos picos, mientras que átomos de carbono en la subred opuesta sí. De igual forma, nuestros resultados muestran como esta extensión espacial del estado da lugar a interacciones magnéticas de largo alcance mediadas por interacción de canje directa. Además, la localización del estado magnético en una subred determina dos tipos diferentes de interacción entre dos átomos de hidrógeno cercanos. Si los dos átomos están adsorbidos en la misma subred, un acoplo ferromagnético tiene lugar. Si los dos átomos están adsorbidos en distinta subred, el resultado es no magnético. Esto ofrece la posibilidad de controlar el momento magnético en grafeno de forma controlada como hemos demostrado mediante la manipulación selectiva de la posición de adsorción de átomos de hidrógeno con precisión atómica. Finalmente, como demostración independiente del origen magnético de nuestro estado, hemos estudiado la adsorción de átomos de hidrógeno en muestras de grafeno dopadas con electrones y huecos. Si tal como afirmamos, los dos picos observados en la densidad de estado son resultado del Coulomb splitting, el valor de la separación U entre ellos debería depender de la ocupación del estado, es decir, del dopaje. Para dopajes suficientemente altos, los dos picos deberían volverse uno, siguiendo la posición en energía del punto de Dirac. Nuestros resultados usando STS mostraron la aparición de un único pico a la energía del punto de Dirac para ambos tipos de dopaje, confirmando el origen magnético del estado spliteado en spin. Todos nuestros resultados experimentales fueron respaldados con exhaustivos cálculos teóricos.

Tras demostrar que un átomo de hidrógeno individual induce un momento magnético local en grafeno, estudiamos la posibilidad de obtener el mayor número de átomos de hidrógeno individuales en nuestra muestra mediante hidrogenación. Nuestro objetivo era conseguir un método que permitiese crear muestras magnéticas de grafeno de forma sencilla. Mediante imágenes de STM de alta resolución, fuimos capaces de desarrollar una metodología para identificar dímeros de hidrógeno. Usando este método, identificamos 10 configuraciones diferentes de dímeros y estudiamos la concentración de cada una de ellas en nuestras muestras. Sorprendentemente, nuestros experimentos a temperatura ambiente y 140K mostraron una tendencia de los átomos de hidrógeno a organizarse formando dímeros no magnéticos. A pesar de que el hecho de la formación de dímeros ya había sido observado en experimentos anteriores a temperatura ambiente, nuestros resultados a 140K parecían estar en contradicción con el mecanismo de adsorción propuesto para el hidrógeno en grafeno. Por lo tanto, revisamos el proceso de adsorción para átomos de hidrógeno en grafeno y encontramos la existencia de un canal de fisisorción previo al pozo de quimisorción. Nuestros cálculos muestran que este pozo de fisisorción tiene un valor de ~100 meV y es igual en toda la superficie del grafeno, lo que permite a los átomos de hidrógeno moverse largas distancias libremente sobre la superficie. Cálculos teóricos teniendo en cuenta este canal de fisiorción junto a los cambios en las barreras de quimisorción alrededor de un átomo de hidrógeno ya adsorbido, nos permitieron explicar la distribución de dímeros encontrada en nuestras muestras. Tal y como muestran nuestros resultados obtenidos con STM, la existencia de un canal de fisisorción es crucial para el entendimiento de las configuraciones finales de los átomos de hidrógeno adsorbidos a temperatura ambiente en capas de grafeno desacopladas. Para sistemas donde el acoplo es algo mayor, la situación cambia. En el caso de grafeno crecido en Ir(111), los átomos de hidrógeno se agrupan en partes concretas del moiré mientras que para grafeno crecido en Cu(111), se encuentran principalmente átomos individuales de hidrógeno tras depositar el mismo a temperatura ambiente.

En la última parte del manuscrito nos hemos centrado en entender las interacciones que ocurren cuando se contacta el grafeno con un substrato. La posibilidad de modificar las propiedades del grafeno al crecerlo en diferentes superficies ha sido estudiada extensamente. En nuestro caso, nos hemos centrado en el grafeno crecido en Cu(111). En este sistema, la visualización de las ondas estacionarias del estado de superficie del Cu(111) a través de la capa de grafeno había sido reportada. Sin embargo, no había un entendimiento real de a qué se debía dicha transparencia. Nuestros experimentos demuestran que cambiando de forma selectiva los parámetros túnel, es posible caracterizar mediante STM/STS simultáneamente la capa de grafeno y el substrato que se encuentra debajo. Mediante medidas de STS/STM a baja temperatura, mostramos que la transparencia del grafeno permite medir las propiedades

electrónicas locales del grafeno y el Cu(111) en la misma zona y en el mismo rango de energías. El principal efecto del crecer una capa de grafeno sobre Cu(111) es una trasferencia de carga electrónica desde el estado de superficie del Cu(111) hacia la capa de grafeno. El buen acuerdo entre nuestras medidas de STM y datos obtenidos mediante ARPES excluyen artefactos de la punta y refuerzan nuestra confianza en los resultados obtenidos. Además, nuestros resultados han sido complementados con cálculos DFT-vdW, que ofrecen una explicación realista a la transparencia del grafeno en función del decaimiento de las funciones de onda del grafeno y el Cu(111). Nuestro método se puede extender también al estudio de láminas modificadas de grafeno. En particular, hemos visto como la adsorción de hidrógeno atómico en nuestro Gr/Cu(111) no modifica la interacción entre el grafeno y el Cu(111). Sin embargo, tras introducir monovacantes en nuestra muestra, observamos que éstas interaccionan fuertemente con el substrato metálico. La posibilidad de caracterizar de forma independiente cada parte del sistema es clave para poder alcanzar un entendimiento completo de las interacciones locales y en particular en las cercanías de partículas intercaladas o adsorbidas.

General conclusions.

In the present manuscript, I have presented the most important findings obtained during my phD thesis. One of the main goals of this work, was the study of the impact of hydrogen atoms on graphene properties. These punctual defects, had been predicted to induce a net magnetic moment on graphene and while some microscopic techniques had measured magnetic signals coming from hydrogenated graphene samples, a direct proof of the repercussion of a single hydrogen atom adsorbed on graphene was lacking. Thanks to our STM measurements combining UHV and low temperatures (~5K), this missing proof was achieved. As predicted by theory our dI/dV spectra show the existence of a spin-splitted state with a peak energy separation of ~20 meV. The origin of this splitting was attributed to the Coulomb interaction taking place in the state. Such a low value of the Coulomb splitting implies a very delocalized state. Our measurements on the spatial extension of the state by means of STS confirmed this delocalization and found a strong atomic-scale modulation of the peak intensity together with a sublattice localization: Carbon atoms in the same sublattice as the adsorbed hydrogen atom showed no trace of the two peaks, while carbon atoms in the opposite sublaticce did. As our results show, the spatial extension of the state leads to a long-range magnetic interaction mediated by direct exchange. In addition, the sublattice localization of the magnetic state determines two kind of possible interactions between two adjacent hydrogen atoms. If both atoms are adsorbed in the same sublattice, a ferromagnetic coupling takes place. If the two atoms are adsorbed in opposite sublattices, the result is non-magnetic. This also opens the possibility to control the magnetic moment of graphene regions in a controlled way as we demonstrated by selectively manipulating the hydrogen adsorption position with atomic precision. Finally, in order to prove in an independent way the magnetic origin of our state, we deposited hydrogen atoms in n- and p-doped graphene layers. If as we claimed, the two peaks observed in the density of states were a result of the Coulomb splitting, then the value of U should depend on the occupation of the state i.e., the doping level. For high enough doping, the two peaks should turn into one peak following the Dirac point energy. Our STS results showed the appearance of such a single peak at the Dirac point energy for both n- and p-doped samples, confirming the magnetic origin of the spin-splitted state. All our experimental results, were supported with extensive theoretical calculations.

After proving that a single hydrogen atom induces a local magnetic moment on graphene, we studied the possibility to obtain the largest amount of single hydrogen atoms in our graphene sample by just hydrogenation. Our aim was to find a method to easily achieve magnetic graphene. Using high-resolution STM images we were able to develop a methodology to identify hydrogen dimers. This method allowed us to identify up to 10 different dimers configurations and, consequently, study the concentration of each one. Surprisingly, our deposition

experiments at room temperature and 140K showed a tendency of the hydrogen atoms to form non-magnetic dimers. Despite the fact that dimer formation had already been observed in previous RT experiments, our low temperature results seemed to be in contradiction with the proposed adsorption mechanism of hydrogen on graphene. Therefore, we revisited the adsorption process of hydrogen on graphene, finding the existence of a physisorption channel prior to the chemisorption well. Our calculations showed that this physisorption well has a value of ~100 meV, which is the same all over the graphene layer, allowing hydrogen atoms to freely move for long distances over the surface. Further calculations taking into account the physisorption channel together with the changes in the energy landscape around an already chemisorbed hydrogen, explain the experimental dimer distribution we find in our samples. As our STM results show, the existence of this physisorption channel seems to be crucial for understanding the final configuration of hydrogen atoms after RT deposition on well decoupled graphene layers. For slightly higher coupled systems the situation turns out to be quite different. In the case of graphene grown on Ir(111), hydrogen atoms form clusters in selective regions of the moiré pattern and for graphene grown on Cu(111), isolated hydrogen atoms are observed after hydrogen deposition at room temperature.

In the last part of this manuscript we focused in understanding the interactions that take place when graphene is in contact with a substrate. The possibility to modify graphene properties by growing it in different surfaces has been extensively studied. Here, we focused on graphene grown on Cu(111). This system was known to exhibit certain transparency when performing STM measurements, allowing the visualization of the Cu(111) surface state standing waves through the graphene layer. However no real understanding of the reasons behind that transparency existed. Our experiments showed that the selective modification of the tunnelling parameters in STM experiments, opens the possibility to simultaneously characterize by STM/STS a graphene layer and the substrate underneath. By performing low temperature STS/STM experiments on a graphene monolayer grown on a Cu(111) surface, we showed that this graphene tuneable transparency enables the accurate measure of the local electronic properties of both graphene and Cu(111) surface at the same sample region and within the same energy range. We found that the main impact of the Cu(111) substrate on the graphene layer is an electronic charge transfer from the Cu(111) surface state towards the graphene layer. The exceptional agreement between the STM results and ARPES data excludes tip artefacts and strengthens the confidence in the obtained results. In addition, our experimental findings are complemented by DFT–vdW calculations, which offer a realistic explanation to the graphene tuneable transparency in terms of the different wave functions that spill out of the graphene and Cu(111) surface state. The versatility of our approach can be further exploited by extending the method to modified graphene layers. In particular, we proved that the diluted adsorption of atomic H on top of

the graphene layer on Cu(111) does not increase the local coupling between the C atoms surrounding the H adsorbates and the metal underneath. In contrast, C vacancies introduced in the graphene layer do strongly interact with the metal substrate underneath. The possibility of characterizing independently each system part is key to achieve a detailed understanding of the local interactions, in particular in the vicinity of intercalated or adsorbed particles.

List of publications

Atomic scale control of graphene magnetism by using Hydrogen atoms.
H. González-Herrero, J.M .Gómez-Rodríguez, P. Mallet, M. Moaied, J.J. Palacios, C. Salgado, M.M. Ugeda, J.Y. Veuillen, F. Ynduráin and I. Brihuega
Science 352, 437 (2016)

Graphene Tunable Transparency to Tunneling Electrons: a Direct Tool to Measure the Local Coupling.
H. González-Herrero , P. Pou J. Lobo-Checa , D. Fernández-Torre , F. Craes, A. J. Martínez-Galera, M. M. Ugeda, M. Corso, J. E. Ortega, J. M. Gómez-Rodríguez, R. Pérez and I. Brihuega.
ACS NANO 10, 5131 (2016)

Unraveling the Intrinsic and Robust Nature of van Hove Singularities in Twisted Bilayer Graphene by Scanning Tunneling Microscopy and Theoretical Analysis
I. Brihuega, P. Mallet, H. González-Herrero, G.T. de Laissardière, M.M. Ugeda, L. Magaud, J.M. Gómez-Rodríguez, F. Ynduráin & J-Y. Veuillen
Phys. Rev. Lett. 109, 196802 (2012)

Physisorption highway for the formation of hydrogen dimers on graphene.

H. González-Herrero, E. Cortés, J.M .Gómez-Rodríguez, P. Mallet, J.J. Palacios, J.Y. Veuillen, I. Brihuega and F. Ynduráin.
In preparation